Spring 2024

Design, synthesis, and characterization of complex chalcogenides for energy storage and energy conversion applications

Srikanth Balijapelly
Missouri University of Science and Technology

Department: Chemistry

DESIGN, SYNTHESIS, AND CHARACTERIZATION OF COMPLEX CHALCOGENIDES FOR ENERGY STORAGE AND ENERGY CONVERSION APPLICATIONS

by

SRIKANTH BALIJAPELLY

A DISSERTATION

Presented to the Graduate Faculty of the

MISSOURI UNIVERSITY OF SCIENCE AND TECHNOLOGY

In Partial Fulfillment of the Requirements for the Degree

DOCTOR OF PHILOSOPHY

in

CHEMISTRY

2022

Approved by:

Dr. Amitava Choudhury, Advisor
Dr. Jay Switzer
Dr. Pericles Stavropoulos
Dr. Manashi Nath
Dr. Aleksandr V. Chernatynskiy

TO

MY FAMILY

PUBLICATION DISSERTATION OPTION

This dissertation consists of the following eight papers formatted in the style used by the Missouri University of Science and Technology:

Paper I, found on pages 26-54, is intended for submission to *Journal of the American Chemical Society*.

Paper II, found on pages 55-82, has been published in *Dalton Transactions*.

Paper III, found on pages 83-123, has been published to *ACS Applied Energy Materials*.

Paper IV, found on pages 124-157, has been published in *Inorganic Chemistry*.

Paper V, found on pages 158-182, has been published in *Chemical Communications*.

Paper VI, found on pages 183-213, has been published in *Journal of Alloys and Compounds.*

Paper VII, found on pages 214-250, has been published in *Journal of Materials Chemistry C.*

Paper VIII, found on pages 251-271, is intended for submission to *ACS applied energy materials.*

ABSTRACT

Through this investigation, complex chalcogenides with the combination of main group metals, transition metals, and rare earth metals have been synthesized using the building block approach and their structure-property relationships are evaluated. The main emphasis of research is on rationally designing new materials for applications in sodium and lithium ion conducting solid electrolytes, cathodes, thermoelectrics, and nonlinear optics. Along with the experimental studies, theoretical calculations are also employed to better understand the physicochemical properties of the synthesized compounds.

The first part of the research will discuss designing alkali ion containing complex chalcogenides using the building block approach. This investigation resulted in the discovery of several new compounds with unique crystal structures and fascinating physicochemical properties namely, facile sodium ion diffusion with ionic conductivities reaching up to 0.12 mS/cm in interpenetrated structure Na_3ZnGaQ_4 (Q = S, Se), metamagnetic behavior in $LiMnPS_4$, promising harmonic signals with high laser-induced damage threshold in $Na_8Mn_2(Ge_2Se_6)_2$.

The second part of the research will discuss the synthesis and characterization of complex chalcogenides for thermoelectric applications. In this study, interplay between composition and disorder in tuning thermoelectric properties is investigated in the makovickyite and pekoite-aikinite family of compounds. Through this investigation ultra-low thermal conductivities (<0.7 W/m.K) are achieved, which in combination with high Seebeck coefficients led to moderate zT values (0.1 – 0.2).

ACKNOWLEDGMENTS

There are many people whom I would like to thank for their contributions, both directly and indirectly, to this dissertation. I would first like to express my sincere gratitude to my advisor, Dr. Amitava Choudhury, who made this work possible. The training I received from Dr. Choudhury made me to “hit the ground running” beginning synthesis experiments in my first semester of Ph.D. Without his support, I could not have done what I was able to do. He spent countless nights reviewing and proofreading my research papers, seeking topics and new problems for me to improve my dissertation. I will always remember his patience and the time he dedicated in the X- ray lab teaching single crystal X-ray crystallography.

I also thank my collaborator, Dr. Aleksandr Chernatynskiy, who always helped me in understanding Density Functional Theory (DFT) calculations.

Besides my advisor, I would like to thank the rest of my dissertation committee members, Dr. Jay A. Switzer, Dr. Pericles Stavropoulos, and Dr. Manashi Nath, for their time and valuable feedback.

I would like to acknowledge the department of chemistry for their financial support during my course of Ph.D. in the form of graduate teaching assistantship.

I sincerely thank all my past, present lab-mates, and friends, Prashanth, Bhushan, Santhosh, Harish, and Sutapa, for creating a friendly atmosphere in the laboratory.

Finally, my deep and sincere gratitude to my mom, dad for their unparalleled love and support. I am forever thankful to my brothers, who always believed in me and supported me through all my life.

TABLE OF CONTENTS

Page

LIST OF ILLUSTRATIONS

SECTION Page

PAPER II

PAPER III

PAPER V

PAPER VI

LIST OF TABLES

PAPER V

PAPER VI

PAPER VII

1. INTRODUCTION

Technological innovation is driven by the discovery and characterization of materials. More specifically, solid state compounds have been the foundation of electronics industry and many emerging technologies.[1] For example, $LiCoO_2$ revolutionized Li-ion batteries that are now essential to portable electronics such as laptops and cell phones.[2] Semiconductors such as Si and GaAs which improved telecommunication systems and led to discovery of transistors, LEDs, and lasers.[3] While some of these materials found potential applications immediately after their discovery, others had to wait for a long time before an application was identified. As such every new material has some value for future research, even when an immediate application is not found. Therefore, it is not surprising that new materials discovery remains an extremely active field of research.[4-8] The potential to tailor the materials properties towards target application is the basis of modern materials design and engineering, which is often limited by our accessible materials space. In recent years, there has been a growing interest on moving away from the historical, traditional, slow, and serendipitous trial-and-error methods of discovering and developing new materials.[9-17] To accelerate the pace of materials discovery, fundamental understanding on materials formation chemistry needs to be strengthened. Any solid-state synthetic chemist must chase some of these fundamental questions: How to rationally form target materials? What critical factors lead to the formation of these materials? How to target materials for specific application?

In general, experimental chemists rely on theory-based calculations to synthesize phases that have been predicted to be stable instead of wasting time chasing compositions

which may or may not lead to a new phase formation under any achievable conditions. Figure 1.1. shows the comparison between computational databases and number of publications resulted from experiments.[18] It is clear that only a small portion of computationally discovered phases are experimentally realized.

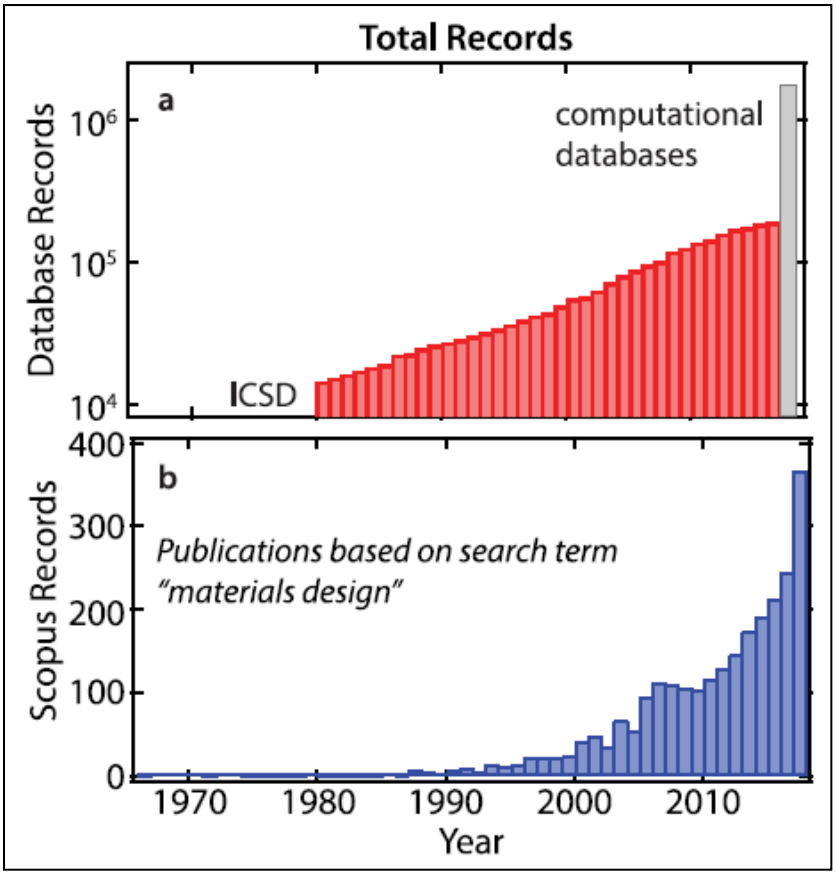

Figure 1.1. (a) Total number of compounds contained within the Inorganic Crystal Structure Database (ICSD) and computational databases. These values do not reflect the extent of the information in each entry. (b) The number of publications returned in from a Scopus search using query terms 'materials design'. (Reprinted with permission from ref 18. Copyright 2018 IOP Publishing Ltd)

However, computational difficulty in *ab initio* structure prediction for complex systems (ternary and quaternary) is a major limitation in predicting stable phases. High-throughput calculations often take cues from a library of known structures and compositions that are calculated to be stable. These computationally predicted stable phases may not be synthesizable for a variety of reasons. The incomplete library with one stable structure missing, would fail to predict the compositions that are stable in the missing structure. This approach leads to an inaccurate result as it ignores the possibility of forming the competing phases resulting from the missing compounds.

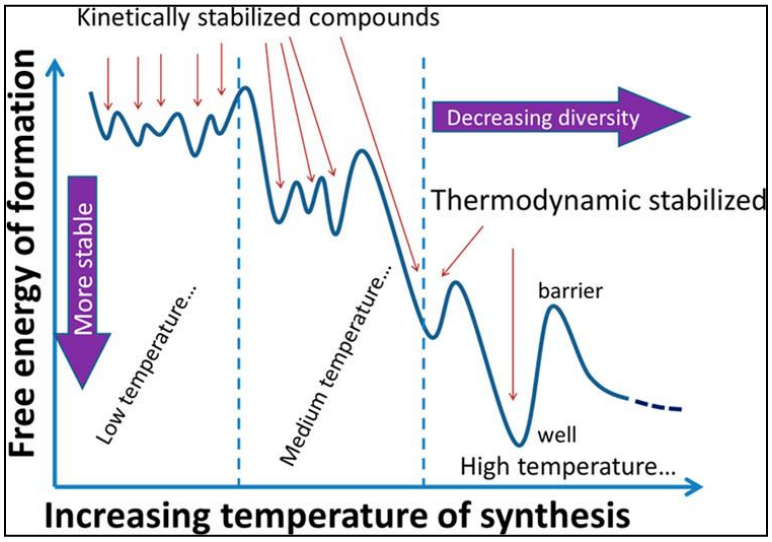

Figure 1.2. Energy landscape of phases that are stabilized in different temperature regimes. (Reprinted with permission from ref 9. Copyright 2017, American Chemical Society)

However, there exists many challenges in this materials discovery approach. First, lack of close integration between the exploratory synthesis and computational design of materials; second, complex chemistries between the reactants and the reaction pathways

that often depend on thermodynamic and kinetic factors. Identification of reaction mechanism in solid state compounds is extremely difficult but is an important step towards rational design of materials.[9]

Organic chemists use certain well-known reaction types to install functional groups or form specific bonds. Whereas such option is not applicable in extended solid-state materials because of the limited predictive tools in synthesis methods used. In a traditional solid-state synthesis, the reaction partners must come sufficiently close to react. But this diffusion process in solid media requires high thermal activation, resulting no control over the reaction and the product formation. Traditional solid-state reactions involve continuous change of atomic positions until a thermodynamic equilibrium is reached. During this process, many metastable phases with various lifetimes may form and disappear before a thermodynamically stable product forms (Figure 1.2). In molecular chemistry, short-lived intermediates form from the elementary reactions before the final product is formed. In case of a solid-state reactions, prolonged reaction time at high temperatures limit the control over the reaction products. Because of this predominant thermodynamic control of the reaction processes, the possibilities for a rational design of synthesis towards a target compound appears to be severely limited. Solid state synthetic chemistry has not developed to the extent to rationally synthesize an unknown solid compound with a prescribed structure and target properties.

While realization of new crystal structures is an important goal of solid state chemistry, synthesizing new compounds in a rational manner for possible application is considered the ultimate objective of modern solid state chemistry. To achieve this goal, it is important to understand the structure and bonding of solid state materials.[17] In this

context, solid state chemists are in pursuit of modifying and evolving new synthetic approaches. Intuition driven new synthetic approaches can potentially pursue discovery of materials that may have been overlooked by computational approaches.

Chalcogenides constitute compounds with diverse structures and compositions and considered as important class of compounds after organic compounds and metal oxides. Compounds containing chalcogen atom (S, Se , or Te) and metal atom are called Chalcogenide compounds. Semiconducting to metallic nature induced by lower electronegativity of S, Se, Te makes this class of compounds scientifically interesting for diverse applications.[19-23] Depending on the number of metal atoms, the chalcogenide can be binary, ternary, or quaternary compounds. Main group and transition metal chalcogenides exhibit scientifically and technologically interesting properties.

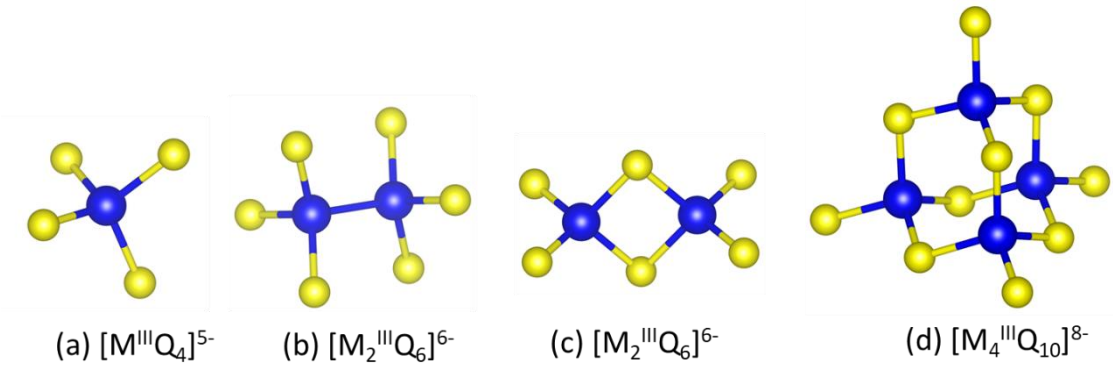

Figure 1.3. Chalcometallate building units that serve as building blocks in complex chalcogenides

The combination of chalcogen and main group metal results in covalently bonded complex anions usually called chalcometallates. Species, such as chalcophosphates $(P_xQ_y)^{n-}$, chalcogermanates $(Ge_xQ_y)^{n-}$, chalcostannates $(Sn_xQ_y)^{n-}$, chlacogallates $(Ga_xQ_y)^{n-}$

(Q = S, Se, Te) as shown in Figure 1.3. are examples of chalcometallates.[9,24] These chalcometallate moieties can serve as building blocks to form a vast set of compounds (ternary and quaternary) with unique structures and properties. For example, $Li_4MgGe_2S_7$, a diamond like semiconductor display high laser induced damage threshold.[25] Piezoelectricity and ferroelectricity in $Sn_2P_2S_6$,[26] good optical transmission and low acoustic velocity in $TlPSe_4$,[27] and frustrated magnetism in interpenetrated Na_3MGaS_4 (*M* = Fe, Mn, Co).[28] These above mentioned materials contain a corner-shared tetrahedra (Ge_2S_7), ethane-like ($P_2S_6^{4-}$), simple tetrahedral (PSe_4^{3-}) and complex super-tetrahedral units, respectively, as their structural building blocks.

Several ternary and quaternary chalcogenides are being extensively investigated for their use as solid ion conductors in solid state batteries. For example, Li_3PS_4, Li_7PS_5X (X = halogen), Li_4SnS_4, $Li_{10}GeP_2S_6$, and $Na_{11}Sn_2PS_6$ display room temperature ionic conductivities reaching a value above 0.5 mS/cm, on par with liquid electrolytes.[29-31]

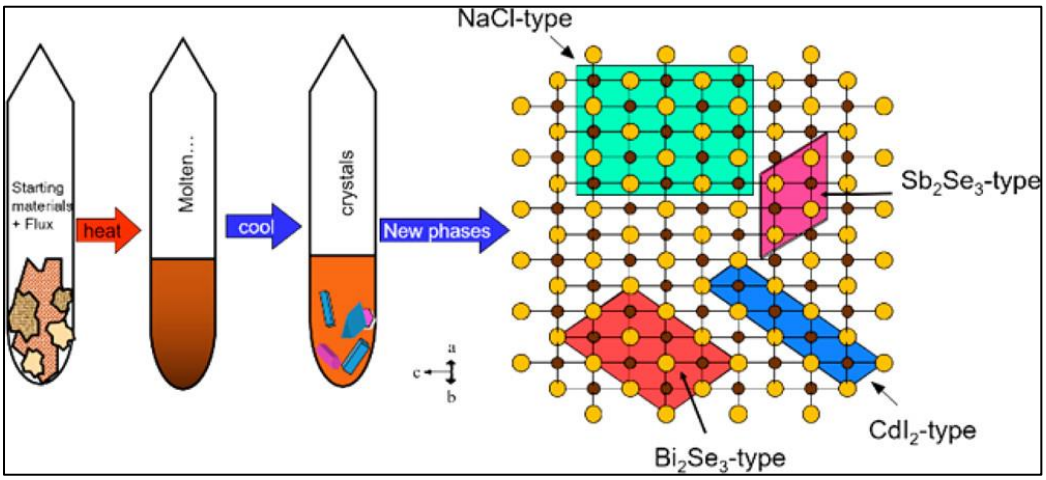

Figure 1.4. Schematic showing polychalcogenide flux as reaction media for directed synthesis. (Reprinted with permission from ref 9. Copyright 2017, American Chemical Society)

1.1. SYNTHESIS OF COMPLEX CHALCOGENIDES

There are several methods to synthesize crystalline chalcogenide materials. For example, conventional solid-state synthesis (direct combination reactions at high temperature), molten flux synthesis, and hydro (solvo) thermal synthesis. The conventional approach of solid-state synthesis is to mix stoichiometric quantities of pure elements or binaries and react them at high temperatures typically in the range of 800 – 1000 °C. Generally, a silica or quartz ampoule, sealed under vacuum (ca. 10^{-3} mbar) is used as a reaction vessel. New compound is formed as a result of diffusion between the reactants exposed to high temperatures. Sometimes carbon coating on the inner walls of the ampule is necessary to prevent side reaction with the quartz tube walls.

This classical method requires long periods of annealing to overcome the diffusion barriers between the reactants and to grow large crystals resulting from thermodynamically stable products, which limit the access to metastable phases. Most of these compounds that are formed at high temperatures are thermodynamically stable. Therefore, the synthesis of new multinary, complex phases (ternary and quaternary) become difficult as they are often not the most thermodynamically stable product. Because of that, alternative approaches, such as molten salt flux has been explored. Kanatzidis has explored and discovered many metastable complex metal chalcogenides using flux reactions which allowed access to new compounds at low and intermediate temperatures.[32-34] In this method, reactive polychalcogenide salts such as alkali metal polychalcogenides, A_xQ_y (A = Li, Na, K, Rb, and Cs; Q = S, Se, and Te) fluxes act as solvent, which can dissolve the reactants (Figure 1.4.) at relatively low temperatures. This flux reactions facilitates better diffusion between the reactants and lead to new framework assembly followed by crystal growth at

moderately low temperatures. Hydrothermal and solvothermal synthesis methods have also been extensively investigated. In this method polar solvents such as H_2O, CH_3CN, CH_3OH, NH_3 and organic amines have been employed as reaction media at temperatures between 120 to 200 °C in a closed vessel. The enhanced solubility of reactants in this solvent medium increases the ion diffusion followed by product formation. However, reaction parameters such as time, temperature, and the molar ratio of reactants play critical role in the final product formation.

1.2. SOLID STATE METATHESIS REACTIONS

Traditional solid-state reactions are considered as universal tool to synthesize inorganic solid-state materials. Until now, only this method could manage a vast portfolio of functional materials across periodic table comprising wide variety of compositions. Solid state reactions usually involve reactions of solids at sufficiently high temperatures (800 – 1000 °C) for long durations, typically hours to days, until a stable equilibrium state is reached. During this type of reactions, diffusion-controlled reorganization of the reactants takes place between the reactant mixture to form a product. However, the use of high temperatures limits the discovery of thermally labile metastable compounds. Synthetic solid-state chemistry research led by the groups of Parkin (London)[27] and Kaner (Los Angeles)[35,37] have demonstrated the synthesis of refractory materials, such as metal borides, nitrides, carbides, and other compounds using solid-state metathesis reactions.

Solid state metathesis reactions are stoichiometrically-balanced and these reactions are performed by gradually heating up the reaction mixture to initiate an exchange of ions

or group of atoms between the reactants as shown in Eqn 1.[38,39] However, the concept of solid-state metathesis has never been used in complex chalcogenide chemistry.

$$MCl_3 + A_3N \rightarrow MN + 3\ ACl\ (A = \text{Alkali ion}) \quad (1)$$

The focus of this research is to investigate and incorporate solid state metathesis concept for the first time in designing complex chalcogenide-based compounds. In this approach, a hypothesis that alkali metal chalcometallates (Figure 1.3.) when heated in combination with metal halides will promote compound formation between the metal of the metal halide and chalcometallate unit with the generation of alkali halide by-product. The high enthalpy of formation of alkali halides will drive the reaction in the forward direction as shown below in a general equation (Eqn. 2).

$$A_x(\text{Building unit}) + yMCl_n \rightarrow A_{x-ny}M(\text{Building unit}) + nyACl \quad (2)$$

(A = Na, Li; M = Main group metal, transition metal, or rare-earth metal, n = charge on the metal)

The final product should contain the intact building unit as backbone framework and the metal atom of choice (from metal halide source) will connect them together. Since the covalently bonded molecular building units present in the starting precursor are retained in the final product, a more suitable term namely ‘building block approach’ is coined. One can choose appropriate building unit and the desired metal halide to create quaternary/ternary chalcogenides for specific applications.

In this context, our research is focused on designing complex chalcogenides using building block approach with an eye on applications primarily in lithium and sodium solid ion conductors, cathodes for lithium and sodium ion batteries, magnetic semiconductors, thermoelectrics, and nonlinear optics.

1.3. SOLID ELECTROLYTES AND ALL SOLID-STATE BATTERIES

In recent years the demand for clean energy options compared to traditional fossil fuel sources has increased dramatically. Though there are other clean energy options such as solar and wind energy, however, batteries play a very important role in current energy storage industry.[2, 40, 41] The demand for high performance battery continue to rise due to the manyfold growth of electric vehicle industry and smart grid in the last few years. Though the current battery technology provides high energy density, it still does not satisfy all kinds of applications due to several safety concerns associated with the flammable liquid electrolytes. Safe battery technology with higher energy density, faster charge/discharge rate, and longer cycle life is desired.[42]

Solid-state electrolytes offer one possible solution for higher safety.[43-45] Compared to liquid electrolytes, solids typically have better mechanical, thermal, and chemical stability. However, finding solids which possess all these above-mentioned properties and have useful ionic conductivities at practical temperatures has been challenging. Furthermore, interfacial impedance between electrolyte grains; and between electrolyte and electrodes have become limiting factors in the commercialization of solid-state electrolytes. Though often the diffusion within the grain is fast enough but the inter-grain diffusion becomes a limiting factor for the overall conductivity. Hence densification of the electrolyte layer is important to overcome the grain boundary resistances.[46]

Due to the low elastic moduli, chalcogenide-based compounds require very low sintering temperature as compared to oxide-based ceramics, which require high-temperature sintering steps to minimize grain boundary impedance.[47,48, 31, 50]

Table 1.1. Ionic conductivity and activation energy of the reported chalcogenide-based inorganic solid-state electrolytes.[49] Adapted from Jia, H.; Peng, L.; Yu, C.; Dong, L.; Cheng, S.; Xie, J. *J. Mater. Chem. A* **2021**, *9*, 5134– 5148

Compound	σ (S.cm^{-1})	T	E_a
t-Na_3PS_4	4.17×10^{-6}	50	0.4
c-Na_3PS_4	2×10^{-4}	25	0.28
c-Na_3PS_4	4.6×10^{-4}	25	0.2
Na_3PSe_4	1.16×10^{-3}	25	0.21
$Na_3P_{0.62}As_{0.38}S_4$	1.46×10^{-3}	25	0.26
t-Na_3PS_4	3.39×10^{-3}	25	0.17
t-$Na_{2.9375}PS_{3.9375}Cl_{0.0625}$	1.14×10^{-3}	30	0.25
$Na_{3.1}Ti_{0.1}P_{0.9}S_4$	2.3×10^{-4}	RT	0.2
$Na_{3.1}Ge_{0.1}P_{0.9}S_4$	2.12×10^{-4}	RT	0.21
$Na_{3.1}Sn_{0.1}P_{0.9}S_4$	2.5×10^{-4}	RT	0.18
c-$Na_{2.70}Ca_{0.15}PS_4$	0.94×10^{-3}	RT	0.49
t-$Na_{3.0}PS_{3.8}Cl_{0.2}$	1.96×10^{-3}	25	0.19
t-$Na_{2.9375}SbS_{3.9375}Cl_{0.0625}$	2.9×10^{-3}	RT	0.24
$Na_{2.9}P_{0.9}W_{0.1}S_4$	13.0×10^{-3}	25	
t-Na_3SbS_4	3×10^{-3}	25	0.25
t-Na_3SbS_4	1.1×10^{-3}	25	0.2
t-Na_3SbS_4	1.05×10^{-3}	25	0.22
c-Na_3SbS_4	2.8×10^{-3}	RT	0.06
t-Na_3SbSe_4	3.7×10^{-3}	RT	0.19
$Na_{2.9}Sb_{0.9}W_{0.1}S_4$	41×10^{-3}	25	
$Na_{2.88}Sb_{0.88}W_{0.12}S_4$	32×10^{-3}	25	0.18
$Na_{10}SnP_2S_{12}$	0.4×10^{-3}	25	0.36
$Na_{10}GeP_2S_{12}$	1.2×10^{-5}	RT	0.46
$Na_{11}Sn_2PS_{12}$	1.4×10^{-3}	25	0.25
$Na_{11}Sn_2PS_{12}$	3.7×10^{-3}	25	0.39
$Na_{3.75}Sn_{0.75}Sb_{0.25}S_4$	$(2–5) \times 10^{-4}$	30	—
$Na_{11.1}Sn_{2.1}P_{0.9}Se_{12}$	3×10^{-3}	25	0.3

Table 1.1. Ionic conductivity and activation energy of the reported chalcogenide-based inorganic solid-state electrolytes.[49] Adapted from Jia, H.; Peng, L.; Yu, C.; Dong, L.; Cheng, S.; Xie, J. *J. Mater. Chem. A* **2021**, *9*, 5134– 5148 (cont.)

Compound	σ (S.cm^{-1})	T	E_a
$Na_4Sn_{0.67}Si_{0.33}S_4$	1.23×10^{-5}	27	0.56
$Na_{3.75}[Sn_{0.67}Si_{0.33}]_{0.75}P_{0.25}S_4$	1.61×10^{-3}	27	0.26
$Na_{3.67}[Sn_{0.67}Si_{0.33}]_{0.67}P_{0.33}S_4$	6.55×10^{-4}	27	0.3
$Na_{3.6}[Sn_{0.67}Si_{0.33}]_{0.6}P_{0.4}S_4$	5×10^{-4}	27	0.31
$Na_{3.8}[Sn_{0.67}Si_{0.33}]_{0.8}Sb_{0.2}S_4$	1.75×10^{-4}	26	0.31
$Na_{3.57}[Sn_{0.67}Si_{0.33}]_{0.67}P_{0.33}S_{3.9}Cl_{0.1}$	9.4×10^{-4}	27	0.28
$Na_{3.57}[Sn_{0.67}Si_{0.33}]_{0.67}P_{0.33}S_{3.9}Br_{0.1}$	9.2×104	27	0.28
$Na_{3.57}[Sn_{0.67}Si_{0.33}]_{0.67}P_{0.33}S_{3.9}I_{0.1}$	1.08×103	27	0.24

The depleting Li resources due to ubiquitous use of Li-ion batteries, alternative energy storage technologies are much sought after. Sodium, on the other hand, is the sixth most abundant element on Earth.[40] Grid-scale energy storage applications place large emphasis on the cost effectiveness, safety, and longevity of the batteries making sodium all-solid-state batteries a promising alternative. Nevertheless, the ionic radius of Na^+ is larger than that of Li^+, making the task of finding a material with superionic conductivity in sodium system more challenging. Ionic conduction in solids is the movement of ions by hopping to adjacent stable sites.[47] Ionic conductivity is governed by the following equation:

$$\sigma = ne\mu \tag{3}$$

where n is the charge carrier concentration and μ is the ion mobility. In the design of electrolytes, the charge carrier concentration can be increased through the formation of defects, such as vacancies or interstitials. Because Na^{1+} is a larger ion, the channel size

needs to be large enough to allow its passage through it. Designing materials with complex structures possessing multi channels and voids can help ion mobility. Ion conduction is also a thermally activated process, and its temperature dependence follows the Arrhenius equation:

$$\sigma_T = \sigma_o \exp(-E_a/k_B T) \quad (4)$$

where σ_T is the intrinsic ionic conductivity, E_a is the activation energy, k_B is the Boltzmann constant, and T is the absolute temperature. Therefore, as the temperature increases, the ionic conductivity increases.

Though chemical modifications like doping and substitutions are known to improve ionic conductivities, new material discovery with targeted property has the capability to move the boundaries beyond known existing materials.[51, 52] Only handful of compounds with high ionic conductivity are reported so far which are listed Table 1.1, so there is plenty of room to search for the new materials through building block approach using chemical intuition and basic solid state chemistry principles.

Through this investigation, using the basic solid state chemistry principles in the realm of building block approach, several new ternary and quaternary chalcogenide compounds are discovered. Concept of building block approach along with *in situ* synchrotron powder X-ray diffraction studies are reported in Paper I. *In situ* synchrotron powder X-ray diffraction studies of reactions between chalcometallate units and metal chlorides prove instant formation of crystalline product at a particular temperature without the destruction of chalcometallate building blocks. Two new ternary alkali ion thiogallates A_5GaS_4 (A = Li, Na) with tetrahedral building units are synthesized. Both the compounds show modest ionic conductivities. More importantly, these materials can serve as starting

precursor building units to design several quaternary chalcogenide compositions in combination with different transition metal and rare-earth metal ions. Structure, optical properties along with ion transport properties are investigated in Paper II. Two new quaternary chalcogenides Na_3ZnGaQ_4 (Q = S, Se) with supertetrahedral secondary building units are obtained using building block approach by taking advantage of hard and soft acid base theory (HSAB). Both the compositions show excellent ionic conductivity and can have potential applications in sodium ion solid-state batteries. Detailed structural investigation, ion transport properties along with theoretical insights are reported in Paper III. In Paper IV, synthesis of a quaternary chalcogenide, $Na_{15}Cu_3Ga_6S_{18}$, using building block approach has been reported. The compound possesses open framework structure built with unusual linear Cu(I) linkages. Detailed structural investigations, ion transport properties along with insights on bonding are reported. Paper V describes the discovery of first ever olivine-type lithium manganese thiophosphate, $LiMnPS_4$, using building block approach. The natural tendency of chalcogenide compounds to crystallize in non-centrosymmetric space group has been exploited for nonlinear optical applications. In Paper VI, synthesis of a polar chalcogenide, $Na_8Mn_2(Ge_2Se_6)_2$, using building block approach is reported. $Na_8Mn_2(Ge_2Se_6)_2$ exhibits promising harmonic generation signals with a high laser-induced damage threshold.

1.4. INTRODUCTION TO THERMOELECTRIC MATERIALS

Thermoelectric devices can be used to exploit the waste heat and directly convert to electricity. .[11, 53-55] Thermoelectric technology have many advantages such as longer life, no moving parts, and least maintenance. More than two third of the energy generated across

the globe is wasted in the form of heat. Combustion engines, power plants, automobiles, and computers are some of the sources for waste heat. Thermoelectrics can be used for energy harvesting wherever there is a source of waste heat.[56]

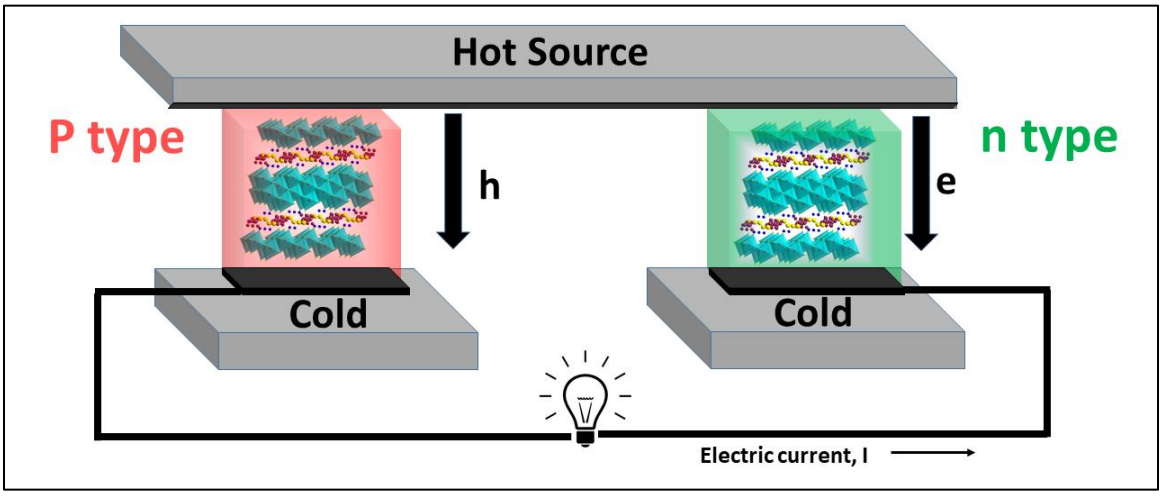

Figure 1.5. Thermoelectric couple made of an n-type and a p-type thermoelectric material.

A typical thermoelectric device is usually made of many thermoelectric modules, which are connected thermally in parallel and electrically in series. A thermoelectric module is made of two semiconducting materials, an *n*- and a *p*-type. A typical thermoelectric module is illustrated in Figure 1.5. A temperature gradient across a thermoelectric module causes the diffusion of charge carriers: electrons in *n*-type semiconductor and holes in *p*-type semiconductor. An electric field is created as a result of diffusion of charge carriers.[57] The choice of thermoelectric module depends on the temperature gradient. The Seebeck effect which is the basis of thermoelectric phenomenon is described below.[58] Peltier effect is the result of opposite phenomenon of Seebeck effect

i.e if a voltage is applied across the thermoelectric module, then a temperature difference will be created providing cooling effect at one junction.

Thermoelectric phenomenon was discovered by Seebeck in 19th century. Seebeck observed that when two dissimilar materials are joined together with temperature gradient (T and T+ΔT), a voltage difference (ΔV) develops between them, which is proportional to the temperature difference. The proportionality constant is called Seebeck coefficient (S or α).[58]

$$S = -\frac{\Delta V}{\Delta T} \tag{5}$$

The Seebeck coefficient is negative for electrons and positive when holes are charge carriers. Ten years later, Peltier discovered that when electric current is passed through two dissimilar materials, heating or cooling effect would be produced at the junction. Thermoelectric effect arises because of the charge carriers diffuse from hot end to cold end when a temperature difference is applied. The net charge build-up at the cold end results in electrostatic potential. The relationship of Seebeck coefficient to the carrier concentration (n) is given by;

$$S = \frac{8\pi^2 k_B}{3eh^2}\, m^* T\left(\frac{\pi}{3n}\right)^{2/3} \tag{6}$$

1.4.1. Figure of Merit of Thermoelectric Materials. The efficiency of single thermoelectric material can be expressed by the dimensionless thermoelectric figure of merit, *z*T, which characterizes the thermoelectric properties of a given material,

$$zT = \frac{S^2 \sigma T}{k} \tag{7}$$

where S, T, σ, and κ are the Seebeck coefficient, absolute temperature, electrical conductivity, and thermal conductivity, respectively.

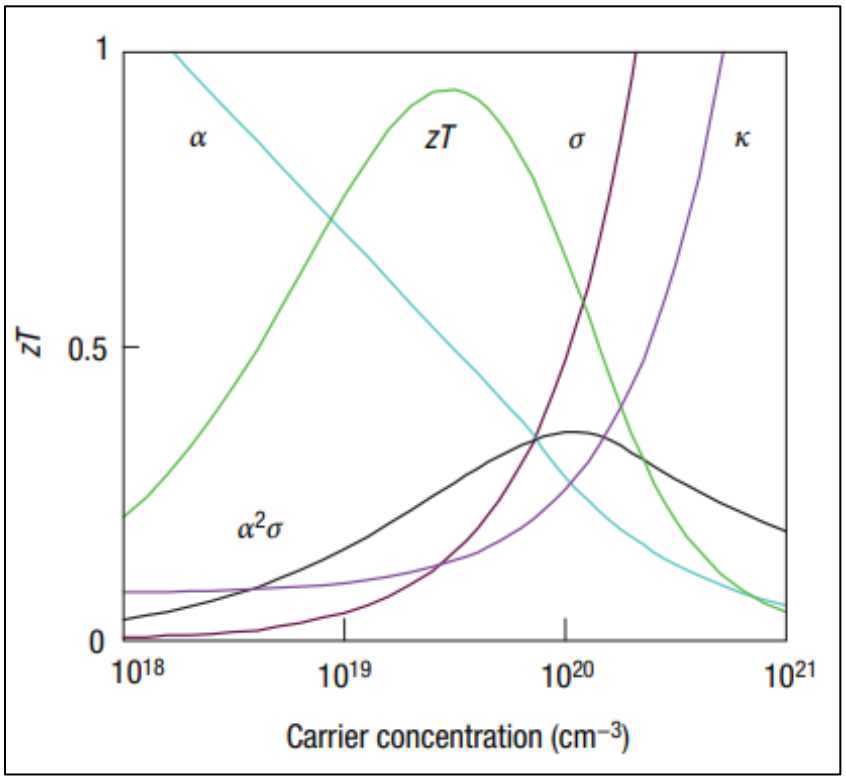

Figure 1.6. Complex dependance of thermoelectric properties on carrier concentration. (Reprinted with permission from ref 64. Copyright 2008, Nature Publishing Group)

To achieve high *z*T, material should have high Seebeck coefficient like in insulators and semiconductors, high electrical conductivity like in metals, low thermal conductivity like in amorphous materials. All these properties are function of charge carriers and strongly coupled with each other. While the Seebeck coefficient generally decreases with *n* (charge carrier density), both the electrical and the thermal conductivity increase with *n*. These relationships can be better illustrated by the following formula

$$\sigma = ne\mu \tag{8}$$

$$\kappa = \kappa_l + \kappa_e \tag{9}$$

$$\kappa_e = L\sigma T \tag{10}$$

where σ is electrical conductivity, μ is mobility, κ_L is lattice thermal conductivity, κ_e is electronic contribution of thermal conductivity, L is Lorentz factor which is 2.4×10^{-8} $W\Omega K^{-2}$ for free electrons. Complex dependencies of one property on other properties makes it difficult to optimize one property without negatively affecting another property as shown schematically in Figure 1.6. The optimum zT occurs in the range of semiconductor to metallic carrier concentration i.e. degenerate semiconductors.

1.4.2. Complex Chalcogenides as Thermoeletrics. Since the thermoelectric field has become one of the main focus areas of research, numerous thermoelectric materials have been developed and investigated like skuttrudites,[59] clathrates, halfheusler intermetallics,[60] oxides,[61] zintl phases,[62] and chalcogenides.[19] Skuttrudites are compounds that crystallize in $CoAs_3$ structure type with a void space at body centered position. Void filling with other guest metal ions has been proven to be an effective approach called "rattling effect" to suppress the lattice thermal conductivity. However, limited filling fraction constrains the performance of the material. Several oxide-based materials have shown good thermoelectric performance but the strong ionic character results in poor electronic conductivity due to weak orbital overlap.[61] Rare-earth intermetallic compounds shows very high Seebeck coefficients due to formation of 4*f* states near fermi level, unfortunately these compounds possess large thermal conductivities. Zintl phases possess properties intermediate to intermetallics and insulators and considered good candidates for

high temperature thermoelectric device applications. $Yb_{14}MnSb_{11}$ showed *z*T of 0.95 in the temperature range of 975 –1275 K outperforming the superior SiGe alloy and currently being used in NASA deep space probes.[65] However, studies are in progress to boost the *z*T further. Chalcogenide compounds comprise a large family of materials because of the ability of the chalcogen atoms to combine with several other metal atoms. Chalcogenides often form predominantly semiconductor to metallic compounds. Due to small variation in the electronegativity among S, Se, and Te, it is possible to fine tune the band gaps accordingly.[19] Chalcogen atoms form softer bonds compared to oxides, which can scatter the heat carrying phonons thereby reducing the lattice thermal conductivity.

Though new material synthesis is highly anticipated to boost the current *z*T limits, a significant number of existing materials with appropriate attributes for high *z*T have not been investigated. Mineralogy is an unexploited area of research for a materials chemist to investigate the properties of several mineral materials for technological applications. Among several minerals, sulfosalts constitute a very large proportion of minerals and exhibit interesting properties due to the semiconducting nature. Sulfosalts containing group V semimetals (As, Sb, Bi) exhibit very diverse superstructures and modulated structures with interesting physicochemical properties.[66] These numerous structure types can be a good prototype for a synthetic solid-state chemist to form synthetic analogues with interesting properties.[67] For example several Li ion conductors (Li argyrodytes) have been originated from the mineral argyrodite, Ag_8GeS_6, with exceptional Li ionic conductivity.[68] Kagomé lattice, a structure type that many minerals adopt are well known to show magnetic frustration phenomenon originating from alternating arrangement of neighboring spins in a triangular topology.[69] Another sulfosalt, Kawazulite, a mineral with composition

Bi_2Te_2Se which showed topological insulating properties may find potential applications in spintronics.[70] One of the important advantages of mineral materials being their abundance and low processing cost and can be directly applied to practical purposes. More importantly one can use that as a model to derive several homologous series and investigate the physicochemical properties for several scientific applications like thermoelectrics, photo-voltaics, superconductors and ionic conductors. Often mineral formation takes place at geothermal conditions such as high temperatures and for long period of times. Therefore, it is challenging to synthesize them in pure crystalline form in the laboratory and study their properties. Among several complex chalcogenide structures, ternary and quaternary bismuth sulfides have become attractive for mid temperature thermoelectric applications due to their low lattice thermal conductivity resulting from the stereo-active lone pair of electrons.[71,72] Additionally, incorporating Cu atoms in the interstitial sites of bismuth sulfides would further reduce lattice thermal conductivity by effective scattering of phonons which was proven in the compositions, $Cu_{x+y}Bi_{5-y}Q_8$ (Q = S, Se) and $Cu_{1-x}\square_xPb_{1-x}Bi_{1+x}S_3$ series.[73,74]

Inspired by the wealth of sulfosalt mineral compositions, complex structures, and potential applications of bismuth sulfosalt compositions, we strategically attempted to synthesize several minerals and their corresponding homologous series and studied the physicochemical properties for thermoelectric applications.

Through this investigation, three quaternary complex chalcogenides, $Ag_{0.72}Bi_{5.48}Cu_{0.88}S_9$ (I), $Ag_{0.70}Bi_{5.30}Cu_{1.3}S_9$ (II), $Ag_{0.34}Bi_{4.54}Cu_{1.98}PbS_9$ (III) are synthesized by substituting Cu and Pb for Bi in the makovickyite family with general formula $Ag^{ab}{}_{n-1}Bi^{a}{}_4Bi^{ab}Bi^{b}{}_{n+2}S_{2n+10}$. Ultralow thermal conductivities in the range 0.75-0.45 $W.m^{-}$

$^{1}.K^{-1}$ are achieved through interplay between composition and disorder in makovickyite structure. A detailed structural investigation and correlation with thermoelectric properties are reported in Paper VII. Similar strategy has been successfully applied to another complex chalcogenide system where different amount of Cu/Pb substitution for Bi in Bi_2S_3 generates a series of structures, $Cu_xPb_xBi_{2-x}S_3$ (x = 0.2, 0.33, 1), with ultralow thermal conductivity conducive to achieve high *z*T (thermoelectric figure of merit). A detailed investigation of the interplay between composition and disorder has been reported in Paper VIII.

2. EXPERIMENTAL

The focus of this research is to discover new chalcogenide-based compounds using building block approach, which can be used as ion conductors, cathode materials in lithium and sodium ion batteries, and nonlinear optics. Therefore, a major part of the work consisted of synthesis, structural characterization, and various property studies (Figure 2.1.). In the following each of these experimental components are discussed briefly. The details of the experimental procedures are also outlined in the respective papers.

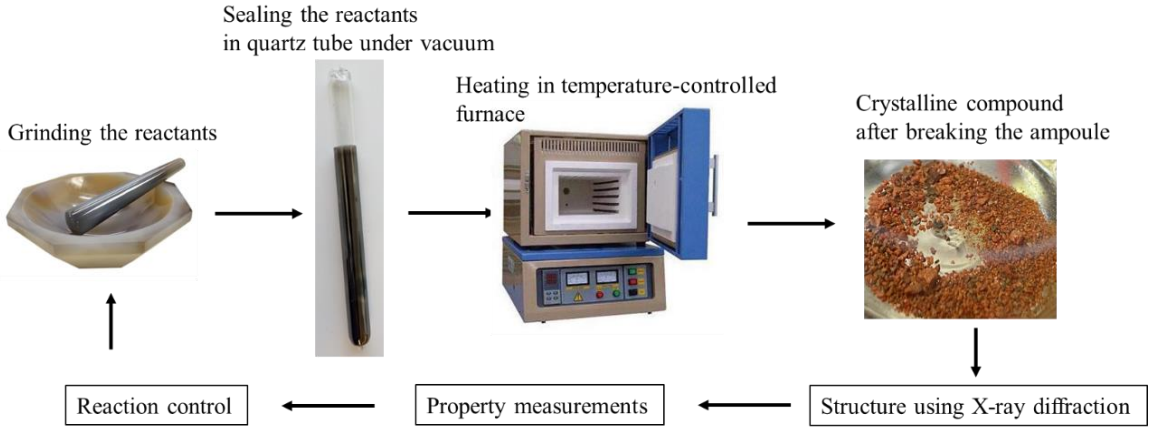

Figure 2.1. Schematic illustrating the general procedure followed for solid state synthesis and property measurements.

2.1. SYNTHESIS

All the main-group chalcometallate building units are synthesized by combining stoichiometric ratios of elements or binaries and subjected to heating at high temperature in a sealed quartz tubes. Metathetic reactions are performed with preformed

chalcometallate starting precursors and the metal chlorides to generate the quaternary compositions. After heating the reaction mixtures sealed in quartz tubes at various temperatures and dwelling times, the reaction products are retrieved by breaking the quartz ampoule in an argon filled glove box. The retrieved reaction products in the form of single crystals or powders are subjected to further characterizations.

2.2. CHARACTERIZATION

Crystallography played an important role in characterization of these solid state compounds. Single-crystal X-ray diffraction (SC-XRD) is used to solve the crystal structure for products, that yielded good quality single crystals suitable for diffraction data collection. The atomic coordinates from the fully solved crystal structure are used to generate a theoretical powder X-ray diffraction pattern of the compound. Experimental powder X-raydiffraction (PXRD) is used to verify sample purity with one-to-one matching

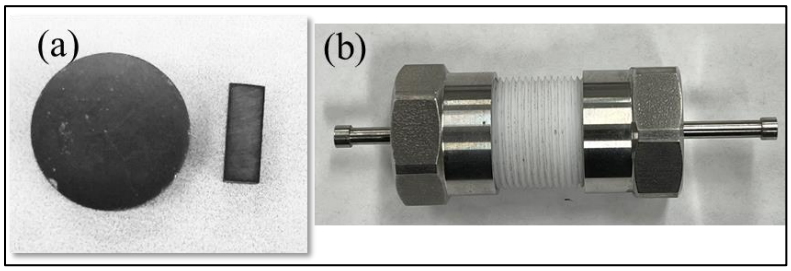

Figure 2.2. (a) A polished cylindrical pellet and a rectangular bar used for measuring thermoelectric properties, (b) An airtight swage lock cell used for measuring impedance data.

of theoretically simulated and experimentally obtained PXRD patterns. To track the stability of chalcometallate building units and the emergence of new product formation in

the *building block* approach, *in situ* synchrotron powder X-ray diffraction facility is used at advanced photon source (APS) in Argonne national laboratory.

The solved crystal structure is often the starting point for understanding of the structure model and used as a guide for many other complementary chemical analysis techniques. These include the IR spectroscopy, diffuse reflectance spectroscopy (DRS), thermogravimetric analysis (TGA), DC magnetization measurements, and SEM/EDS analyses.

Fourier-transformed infrared spectroscopy (FTIR) is used as a general tool for functional group characterization, mainly to realize the stability of as-synthesized compounds against the moisture. A combined thermogravimetric analysis and differential scanning calorimetry (TG-DSC) is used for thermal stability determination and also to follow thermally induced structural changes leading to phase transitions. The SEM/EDS analyses is utilized for morphological and elemental analysis studies. Diffuse reflectance spectroscopy is used to estimate the optical band gap of as synthesized compounds.

Electrochemical impedance spectroscopy (EIS) technique is used to evaluate the ionic and electronic conductivity properties. In this technique, alternating current (AC) voltage is applied on the system over a wide frequency range and the current output is recorded. Through this technique, Li^+ and Na^+ ionic conduction is assessed on candidate samples selected based on crystal structures from the as-synthesized materials. The sample preparation for ionic conductivity measurements involves intimate contact of conductive indium foil (blocking electrodes) on both sides of a pelletized sample (Figure 2.2.) and obtaining the impedance spectra at various temperatures.

DC magnetization measurements are used to investigate the magnetic interactions and magnetic phase transitions in samples. Oxidation state of metal atoms are also confirmed by magnetic measurements.

For measuring thermoelectric properties, polished cylindrical hot-pressed pellet samples are used for thermal conductivity measurements at different temperatures. Appropriately cut bars, from the same pellet on which thermal conductivity is measured, are used for electrical and Seebeck measurements. Details of the synthesis and experimental procedures are provided in the respective paper sections.

First principle density functional theory (DFT) calculations played an important role in understanding the electronic band structure, nature of bonding and ionic transport properties. Experimentally solved crystal structures from the single crystal X-Ray diffraction measurements are used as starting models for theoretical calculations. Detailed procedure of DFT calculations is explained in respective papers.

PAPER

I. BUILDING BLOCK APPROACH: A NEW SYNTHETIC TOOLBOX FOR DISCOVERY OF COMPLEX CHALCOGENIDES

*Srikanth Balijapelly,[a] Amitava Choudhury[a]**

[a]Department of Chemistry, Missouri University of Science and Technology, Rolla, Missouri 65409, United States

ABSTRACT

Lack of predictive tools in a typical solid state synthesis has been a limiting factor for the discovery of new targeted complex chalcogenides. Herein we report a new concept called building block approach of designing complex quaternary chalcogenides through metathesis reactions between alkali metal containing chalcometallate units and metal chlorides. The salt byproduct in the solid state metathesis reactions acts as a driving force to shift the equilibrium to the right and facilitates product formation. Through this unique approach, a library of new quaternary chalcogenides containing selenogeramate ($Ge_2Se_6^{6-}$) and thiophosphate (PS_4^{3-}) building units are discovered and structurally characterized. *In situ* synchrotron powder X-ray diffraction studies of reactions between chalcometallate units and metal chlorides reveal instant crystalline product formation at a particular temperature without the destruction of chalcometallate building blocks. This new approach can revolutionize the materials discovery process which is otherwise a slow and tedious process using conventional synthetic techniques.

1. INTRODUCTION

Synthesis of phase pure inorganic materials often serves as the first step towards unlocking the future potential hidden in them. The task of synthesizing a new inorganic solid material is in the hands of solid state synthetic chemists, who often play tricks of thermodynamic and kinetic controls to synthesize a particular target compound. While the synthesis of binary compositions is relatively easy compared to multicomponent systems such as ternary and quaternary phases as they often compete with the more thermodynamically stable binary phases.[1-3] The challenge lies in the synthesis of such multinary compounds where one needs to link together three or four different elements through ionic or covalent forces satisfying their unique coordination environment and oxidation states. For chalcogenides (compounds of sulfide, selenide, and tellurides) it is even more difficult to form a hypothetical multinary compounds as there exist a fierce competition from many binary phases. There is a severe lack of understanding of the materials formation mechanism as complete structural destruction of the reactants takes place at high temperatures and the resulting ions move through high diffusion barrier in a long transport path. Therefore, the synthesis of new materials often relies on exploratory routes such as molten polychalcogenide flux method. Flux method has been very successful in yielding new and complex structures,[4-9] however, it always posed difficulty in terms of predicting the oxidation states of the elements in the final product(s) and their structures. Hence search for a new synthetic approach is highly desired, which can offer better predictive tools for example, reliable formation of a specific structural moiety, control of

the oxidation state of elements involved, and shifting the thermodynamics to drive the chemical reaction towards target product.

To address this uncertainty in the synthesis of multinary chalcogenides we resort to an old concept, the so-called metathesis route. The concept of metathesis i.e exchange of atoms, atom groups, or functional groups is well known in both organic chemistry and inorganic chemistry. Metathesis reactions involving solid precursor is called solid state metathesis reaction (SSM). Groups of Parkin[10] and Kaner[11] have extensively investigated solid state metathesis reactions and made remarkable developments in the synthesis of refractory materials, such as borides, nitrides, and carbides. These solid-state metathesis reactions are salt balanced and the high enthalpy of formation of salt byproduct drives these reactions in the forward direction as shown below in a prototype example.

$$MCl_3 + A_3N \rightarrow MN + 3ACl \text{ (A = Li, Na, K, Rb, Cs)}$$

Generally, mononuclear negative anions of different charges (O^{2-}, S^{2-}, N^{3-}, P^{3-} and so on) are exchanged with equivalent amount of metal ions from the metal halides to obtain the desired binary compounds.[11] From the above reaction we envisage that if instead of a mononuclear anion, a relatively complex anion is used then a complex ternary or quaternary material can be generated if the structural integrity of the complex anion is retained during the metathesis reaction. The combination of chalcogen and main group metal results in structurally diverse, covalently bonded complex anions usually called chalcometallates for example, chalcophosphates $(P_xQ_y)^{n-}$, chalcogermanates $(Ge_xQ_y)^{n-}$, chalcostannates $(Sn_xQ_y)^{n-}$, and chalcogallates $(Ga_xQ_y)^{n-}$ (Q = S, Se, and Te).[4, 12] We hypothesize that alkali metal containing molecular building units when heated in conjunction with metal halides will undergo a rapid exothermic reaction due to the high

enthalpy of formation of the alkali halide salt byproduct to yield new crystalline products through the partial or full replacement of alkali ions by the metal ion of the metal halide precursor as shown below in a general equation.

$$A_x(\text{Building unit}) + yMCl_n \rightarrow A_{x-ny}M(\text{Building unit}) + nyACl$$

(*A* = Na, Li; *M* = Main group metal, Transition metal, or Rare-earth metal, n = charge on the metal)

To validate the hypothesis, we have selected an ethane like selenogermanate $[(Ge_2Se_6)^{6-}]$ and a tetrahedral ortho-thiophosphate $[(PS_4)^{3-}]$ unit as starting building block precursors and explored their reactions with a variety of metal chlorides employing metathesis reactions to generate a plethora of compounds.

Herein, we report the synthesis, structure, optical, and preliminary magnetic properties of a family of compounds containing $Ge_2Se_6^{6-}$ and PS_4^{3-} building units. Further insight into reaction mechanism of the building block approach has been garnered from *in situ* synchrotron powder X-ray diffraction method.

2. EXPERIMENTAL SECTION

First, different chalcometallate building units were synthesized using traditional solid state synthesis approach in evacuated sealed quartz ampoule. $Na_6Ge_2Se_6$ was prepared by combining a stoichiometric mixture of elements; 3 mmol of Na (Sigma, 99.9%), 1 mmol of Ge (Acros Organics, 99.9%) and 3 mmol of Se (Acros Organics, 99.5%). Li_3PS_4 was synthesized by reacting Li_2S and P_2S_5. Metathesis reactions were carried out by combining stoichiometric combination of preformed chalcometallate

building unit precursor and anhydrous metal chloride salt. The mixture was hand ground in a mortar pestle for 15 min and loaded into carbon coated quartz ampoule. The sealed ampoules were heated in a temperature-controlled furnace. The metathetic product containing crystals were found to be moderately stable in air but in some cases the crystals display sensitivity towards moisture. The bulk purity of chalcometallate building unit precursors was confirmed from laboratory-grade powder X-ray diffraction data. Details of synthesis and the heating protocol followed in each reaction is provided in Table S1.

2.1. X- RAY CRYSTALLOGRAPHY

Good quality crystal from each synthesis was chosen for single crystal X-ray diffraction data collection on a Bruker Smart Apex or Apex 2 CCD X-ray diffractometer equipped with a sealed tube X-ray source with Mo Kα radiation (λ = 0.71073 Å). Low-temperature data sets were collected at −53 °C with a step size of 0.3° in the ω scan and 20 s/frame exposure time using SMART software.[13] Data integration and absorption correction were done using the programs SAINT[14] and SADABS,[14] respectively. Atomic positions were determined from the difference Fourier syntheses using SHELXS-97. Full-matrix least-squares refinement against $|F^2|$ was carried out using the SHELXTL-PLUS suite of programs.[15] Final refinements including the anisotropic thermal parameters were carried out using SHELX 2018 with the ShelXle graphical user interface.[16] Crystal data and final refinement parameters are given in Tables S2-S7.

2.2. POWDER X-RAY DIFFRACTION

The laboratory-grade powder X-ray diffraction (PXRD) patterns were obtained using a PANalytical X′Pert Pro diffractometer equipped with a Cu Kα anode and a linear array PIXcel detector over a 2θ range of 5–90° with an average scanning rate of 0.0472° s^{-1}. Hand-ground samples were loaded into an air-tight cells covered with the Kapton film to collect the PXRD patterns.

2.3. OPTICAL BAND GAP MEASUREMENTS

Optical band gap measurements were performed on a Varian Cary 5000 UV−vis−NIR spectrophotometer equipped with a praying mantis set up. $BaSO_4$ powder (Fisher, 99.2%) was used as an ∼100% reflectance standard, and the Kubelka-Munk function was employed to transform the reflectance into absorption data to assess the band gap.[17]

2.4. MAGNETIC MEASUREMENTS

The variable temperature magnetic susceptibility data of the compounds were measured at 0.5 T over a temperature range of 1.8−300 K with a Quantum Design SQUID magnetometer. About 2-10 mg of samples were loaded in gelatin capsules and mounted in plastic straws for magnetic measurements.

2.5. IN-SITU POWDER X-RAY DIFFRACTION MEASUREMENTS

Stoichiometric ratios of reactants ($Na_6Ge_2Se_6$ and Metal chloride) were ground together using mortar and pestle for 30 min before loading into a 0.1 mm diameter quartz

capillary. These quartz capillaries were vacuum sealed using an inhouse adapter. The *in situ* synchrotron PXRD were taken at beamline 17-BM in the Advanced Photon Source at Argonne National Laboratory running at 51 keV (λ = 0.24145 Å). An electrical resistance furnace was used to heat the capillaries. The samples were heated to 450 °C at a rate of 15 °C/min then further heated to 700 or 800 °C at 10 °C/min. The capillaries were cooled from 800 °C to room temperature without any dwell time, at a rate of 20 °C /min. GSAS II software was used to process the raw data.[18]

3. RESULTS AND DISCUSSION

3.1. STRUCTURE DESCRIPTION

Depending on the nature of building units, the obtained compounds can be divided into two different families: compounds with selenogermanate containing $(Ge_2Se_6)^{6-}$ building unit and thiophosphates containing $(PS_4)^{3-}$ building units. Though all the compounds containing $(Ge_2Se_6)^{6-}$ building unit appear compositionally similar, there exist subtle structural differences. All the compounds with the general formula $Na_{12-nx}M'_x{}^{n+}(Ge_2Se_6)_2$ (*M′* = In^{3+}, La^{3+}, Ce^{3+}, Pr^{3+}, Nd^{3+}, Sm^{3+}, Gd^{3+}, Tb^{3+}, Dy^{3+}, Ho^{3+}, Yb^{3+}, Ca^{2+}, Sr^{2+}, Mn^{2+}, Pb^{2+}, Cd^{2+} and Eu^{2+}) crystallize in monoclinic crystal system in *C*2/*m* space group, except $Na_8Mn_2(Ge_2Se_6)_2$ which crystallizes in non-centrosymmetric space group *C*2 (Figure 1 and Table S2-S7).

Table 1. List of compounds formed by reacting the chalcometallate building block with metal chloride salts.

Building block precursor	Metal halide	Product
$Na_6Ge_2Se_6$	$InCl_3$	$Na_9In(Ge_2Se_6)_2$
	$LaCl_3$	$Na_9La(Ge_2Se_6)_2$
	$CeCl_3$	$Na_9Ce(Ge_2Se_6)_2$
	$PrCl_3$	$Na_9Pr(Ge_2Se_6)_2$
	$NdCl_3$	$Na_9Nd(Ge_2Se_6)_2$
	$SmCl_3$	$Na_9Sm(Ge_2Se_6)_2$
	$GdCl_3$	$Na_9Gd(Ge_2Se_6)_2$
	$TbCl_3$	$Na_9Tb(Ge_2Se_6)_2$
	$DyCl_3$	$Na_9Dy(Ge_2Se_6)_2$
	$HoCl_3$	$Na_9Ho(Ge_2Se_6)_2$
	$YbCl_3$	$Na_9Yb(Ge_2Se_6)_2$
	$CaCl_2$	$Na_8Ca_2(Ge_2Se_6)_2$
	$SrCl_2$	$Na_8Sr_2(Ge_2Se_6)_2$
	$MnCl_2$	$Na_8Mn_2(Ge_2Se_6)_2$
	$PbCl_2$	$Na_8Pb_2(Ge_2Se_6)_2$
	$CdCl_2$	$Na_8Cd_2(Ge_2Se_6)_2$
	$EuCl_2$	$Na_8Eu_2(Ge_2Se_6)_2$
Li_3PS_4	$MnCl_2$	$LiMnPS_4$
	$ZnCl_2$	$LiZnPS_4$
	CuCl	$Li_{1.5}Cu_{1.5}PS_4$

The crystal structure of these compounds can be explained in terms of anion close packing: hexagonal close packing (hcp) of anions, in which 5/6 of the octahedral holes are filled with Na and M atoms, the remaining octahedral holes are filled by Ge–Ge dimer

placed parallel or perpendicular to the anion layer. Such placement of the Ge–Ge dimer forces Ge to coordinate with the two opposite trigonal faces of the octahedron forming an ethane-like unit. The resulting $[Na(1)M(Ge_2Se_6)]^{3-}$ layers are separated by sodium atoms along the *c*-axis of the unit cell.

However, all the compounds with general formula $Na_8M_2(Ge_2Se_6)_2$ are not isostructural. While the Mn analogue crystallizes in noncentrosymmetric space group,[19] other divalent metal analogues (Ca, Sr, Pb, Cd, Eu) crystallize in centrosymmetric space group. In compounds with Ca, Sr, Pb, Cd, and Eu, the metal site is mixed occupied with sodium atom with 50:50 ratio (Na1/M1). These subtle differences in structure could arise from different ionic radii of the metal cations.

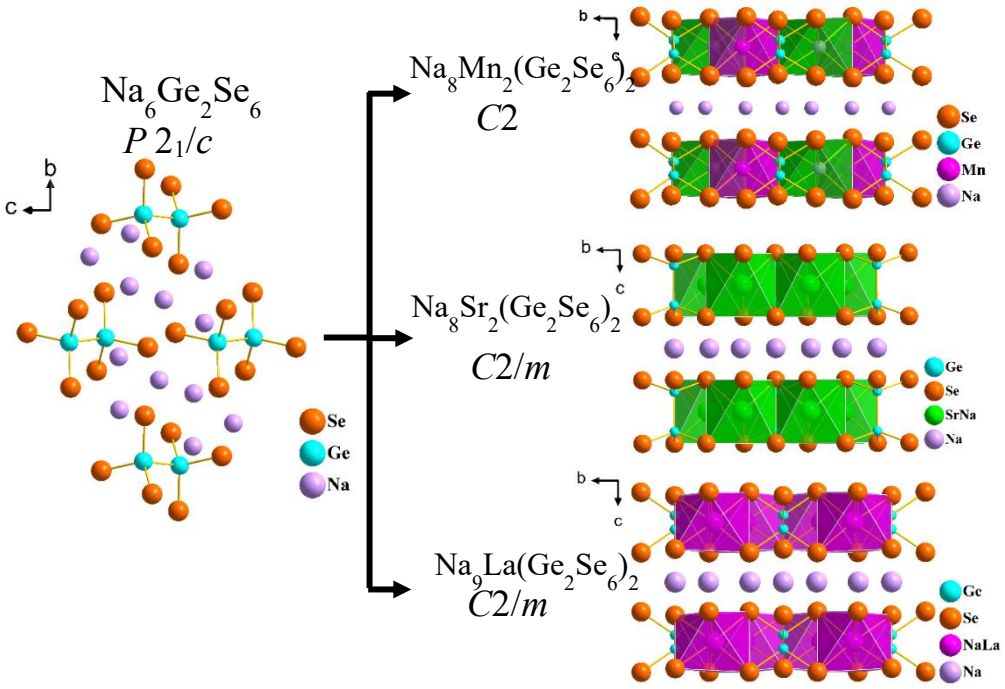

Figure 1. Illustrating the concept of building block approach scheme, using an ethane like $(Ge_2Se_6)^{6-}$ building unit as precursor and reaction with transition metal, main group metal, and rare earth metal chlorides, resulting in new quaternary complex chalcogenides.

Compounds that contain trivalent metal cation M^{3+} with general formula $Na_9M(Ge_2Se_6)_2$ have two Se (Se1 at 4*i* Wyckoff site, Se2 at 8*j* Wyckoff site), one Ge (Ge1 at 4*i* Wyckoff site), one mixed occupied M site (M1/Na1 = 25:75 ratio at 4*h* Wyckoff site), two Na atoms (Na2 at 2*a*, and Na3 at 4*g* Wyckoff site) present in the asymmetric unit. The key structural difference among these compounds is the orientation of Ge – Ge bond with respect to the close-packed Se-layer. The orientation of Ge – Ge bond with respect to Se-layer is listed in Table 2. It is important to note here that the common structural feature among all the compounds resulted from metathesis reactions using ethane like $(Ge_2Se_6)^{6-}$ is the integrity of the building unit in the final product. Also, note that the oxidation state of the metal ions (M^{2+}, M^{3+}) from the metal chloride precursors did not change in the final product. Hence, the building block approach as employed through solid state metathesis reaction can be a step forward towards a rational design of materials. To further test our building block approach hypothesis, a different chalcometallate building block precursor, Li_3PS_4, containing a tetrahedral thiophosphate-based building unit was used. Li_3PS_4 is a simple ternary thiphosphate based compound known for its good ionic conducting properties.[20] The room temperature polymorphs γ – Li_3PS_4 has isolated PS_4^{3-} building units

Table 2. Orientation of Ge – Ge bond in $Na_{12-nx}M_x^{n+}(Ge_2Se_6)$.

M in $Na_{12-nx}M_x^{n+}(Ge_2Se_6)_2$	M1/Na1	Ge - Ge bond angle
Mn^{2+}	100	18.54
Eu^{2+}, Pb^{2+}, Sr^{2+}	50:50	90
Ca^{2+}, Cd^{2+}	50:50	19.1
In^{3+}, La^{3+}, Ce^{3+}, Pr^{3+}, Nd^{3+}, Sm^{3+}, Gd^{3+}, Tb^{3+}, Dy^{3+}, Ho^{3+}, Yb^{3+}	25:75	19.2

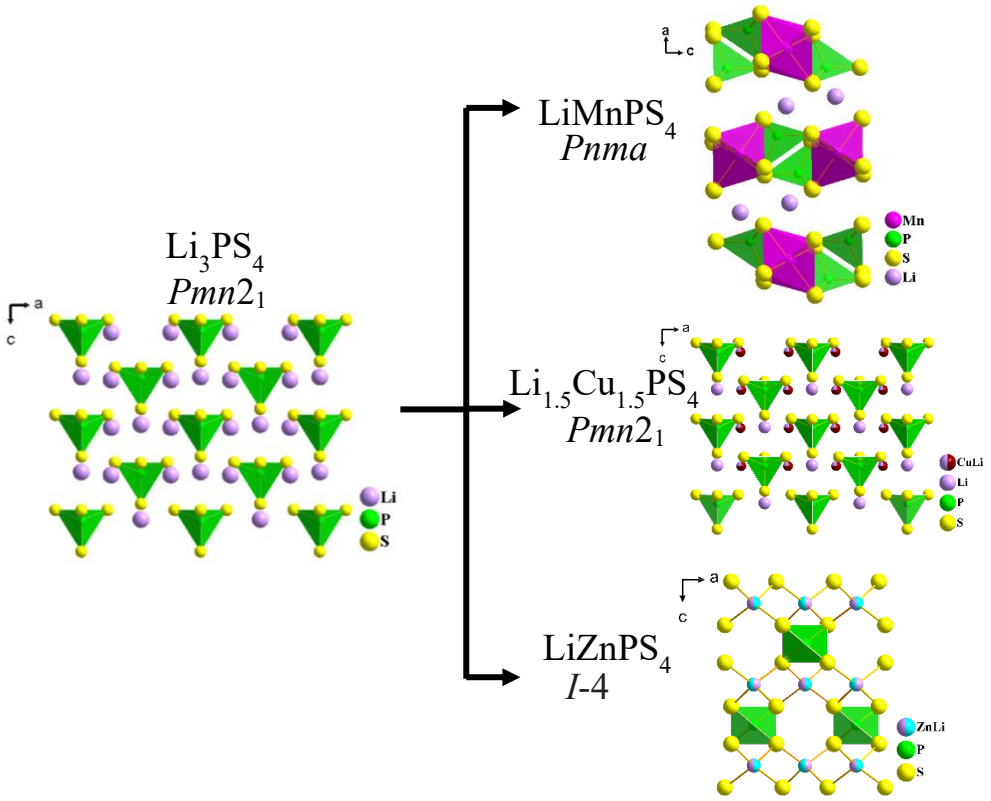

Figure 2. Illustrating the concept of building block approach, using orthothiophosphate $(PS_4)^{3-}$, a tetrahedral building unit and products formed by reaction with transition metal chlorides $MnCl_2$, CuCl, and $ZnCl_2$

separated by two crystallographically different Li ions in tetrahedral coordination. Metathesis reactions using preformed Li_3PS_4 and transition metal chloride salts $MnCl_2$, $ZnCl_2$, CuCl were performed. $LiMnPS_4$, an olivine-type compound synthesized through building block approach has been reported recently from our group.[21] The detailed structure description can be found in our recent publication, hence the crystal structure descriptions for $LiZnPS_4$ and $Li_{1.5}Cu_{1.5}PS_4$ are presented here (Figure 2). The hypothesis was to maintain the integrity of the $(PS_4)^{3-}$ building unit in the final product with the metal atom from the metal chloride salt forming a complex network by connecting the $(PS_4)^{3-}$ building units along with charge balancing Li ions. However, it is to be noted here that the high

temperature polymorph β – Li_3PS_4 and $LiMnPS_4$ are isostructural and can be formed topotactically by replacing 2 Li ions by Mn^{2+}. The detailed structural comparison is provided in our previous report. Similar metathesis reaction with monovalent cation Cu^{1+} using CuCl salt yielded a new solid solution series $Li_{3-x}Cu_xPS_4$ (x = 1, 1.5, 2.25). All the Cu substituted lithium thiophosphate compounds found to be isostructural to room temperature polymorph γ – Li_3PS_4. Monovalent cation Cu^{1+} generally prefers a tetrahedral coordination in chalcogenide matrix. Hence, increase in the amount of Cu increases the Cu occupancy on Li2 site making it a copper rich phase. To further validate our building block hypothesis, Zn^{2+}, a divalent cation, which also prefers a tetrahedral coordination in chalcogenide matrix similar to Cu^{+} was chosen. Reaction between γ – Li_3PS_4 and $ZnCl_2$ in 1:1 ratio resulted in the formation of $LiZnPS_4$,[22] a known structure type in which all the metal sites are tetrahedrally coordinated with sulfur atoms. However, in the metathesis product, Li and Zn found to occupy the same crystallographic site, whereas the reported $LiZnPS_4$ has ordered structure. These small structural differences can be ascribed to unique synthesis method adopted. It is important to note here that among all the thiophosphate-based compounds synthesized using building block approach, the PS_4^{3-} building unit is intact and the metal atom that connects these building units accommodates itself according to its own coordination and charge preference.

3.2. IN-SITU POWDER X-RAY DIFFRACTION MEASUREMENTS

There are few fundamental questions that we must chase to unravel the mechanism of product formation in our building block approach. First, whether the integrity of the chalcometallate building unit is maintained throughout the reaction. Second, is there

formation of any metastable phase(s) during the reaction, i.e before the product formation. Third, whether the transformation from the precursor mixture to the product is a solid state transformation or occurs through the melting of the charge. To answer these questions, we performed *in situ* powder X-ray diffraction measurements on the reaction mixture (building block precursor + metal chloride). In this technique, a powder X-ray diffraction pattern is collected at every 30 sec, while gradually heating up the reaction mixture in a sealed quartz capillary. Figure 3 shows the *in situ* powder X-ray thermodiffractogram of a selected reaction ($Na_6Ge_2Se_6$ + $SrCl_2$) performed at 17 BM, Advanced Photon Source (APS), Argonne National Laboratory. The thermodiffractograms of the other selected reactions are provided in SI (Figure S1, and S2).

Traditional solid-state reactions generally require high temperatures due to the limited diffusion between the reaction precursors in solid medium. However, solid-state metathesis reactions stand unique in this case, as these reactions are driven by the high enthalpy change through spontaneous formation of alkali halide salt (– 787 kJ mol^{-1} for NaCl) byproduct. From *in situ* measurements, it is evident that the crystalline product formation takes place at temperatures as low as 430 °C, without forming any intermediate phases. The formation of salt by product along with the metathetic product is also evident. This proves our hypothesis that the building block is in fact intact during the course of the reaction and product formation is very quick unlike typical solid state reaction. Similar observations were noted for other reactions as well, however, the formation of salt byproduct was not prominently seen in every reaction due to several experimental limitations, most notably, with the orientation of the sample holder.

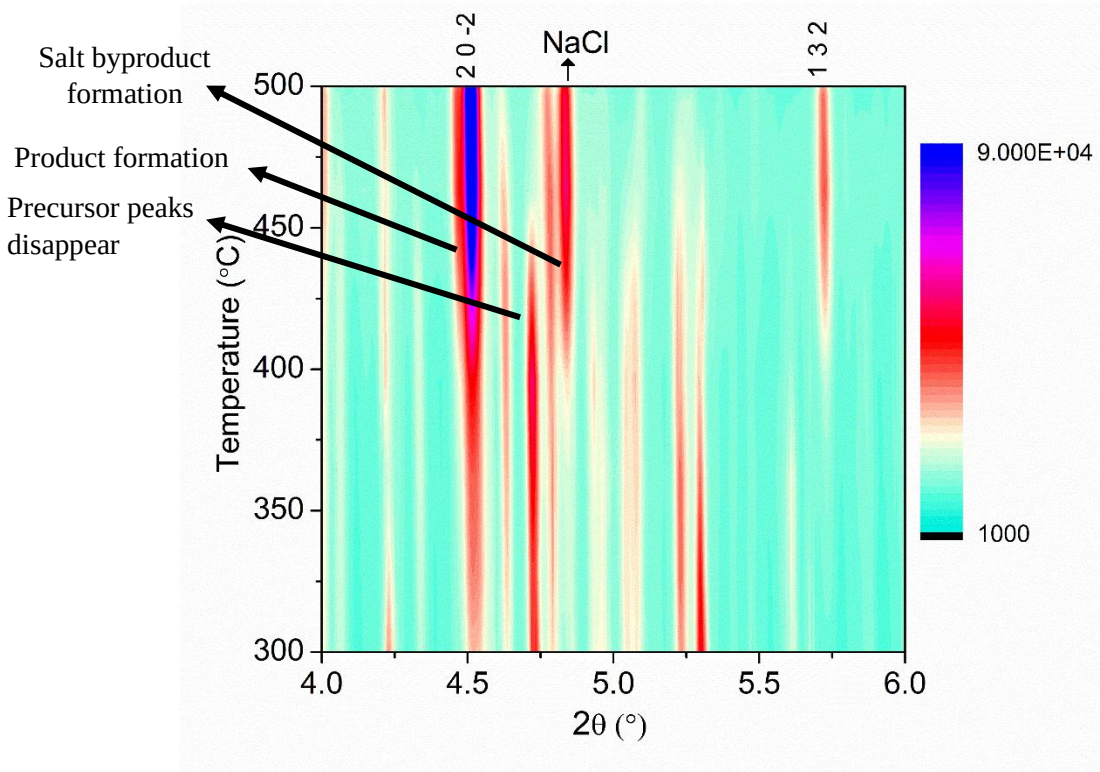

Figure 3. The *in situ* powder X-ray thermodiffractogram of the reaction mixture $Na_6Ge_2Se_6$ + $SrCl_2$ (1:1) to form the product $Na_8Sr_2(Ge_2Se_6)_2$. The arrows indicate the disappearance of the precursor peaks around the temperature 430 °C, and the emergence of product peaks followed by the formation of NaCl salt byproduct.

However, *in situ* studies confirmed the early formation of crystalline product before melting, directly from the reaction precursors, without passing through any secondary, or amorphous phases. Therefore, it is a truly a solid state transformation. Through this building block approach one can rationally synthesize a target composition with a prescribed structural moiety and choice of metal ion by bypassing all the competition from binary phases and nuisances of thermodynamic phase equilibrium. Predicting the structure type beforehand is challenging, if we are successful in doing so, it will be an ultimate achievement of synthetic solid-state chemistry. However, at this point predicting the presence of building unit in the final structure, the oxidation state of each element and

reliable formation of a target composition at relatively low temperature bear immense importance in rational design of solids. Since a wide variety of chalcometallate building blocks are available with various shapes, negative charges, and in combination with various alkali ions; a vast set of compounds (ternary and quaternary) with unique structures can be accessed in a predictive manner. As the covalently bonded molecular building units of the starting precursor are retained in the final product, this method is termed a 'building block approach'. In this approach, one has the advantage of choosing appropriate building unit and the desired metal halide to create quaternary/ternary chalcogenides for specific applications in semiconductor, magnetism, ionic conductor, cathodes in lithium and sodium ion batteries and nonlinear optics.

3.3. BAND GAP TUNING

One of the most useful applications of the building block approach of material synthesis is that it can provide ways the synthesize a series of isostructural compounds just varying the metals in the metal chloride or it can also afford a series of solid solutions by varying the ratio of metal/alkali ions in the metathetic reactions. Having such series of compounds provides a way to tailor the band gap of materials or provide a material with any band gap on demand. Several physicochemical properties of semiconductors are function of their optical band gap.[23] Tuning the band gap of a materials would provide control over several properties like electronic conductivity, optical transparency, photoelectric current, etc. Band gap tuning often involves doping with impurity elements in a specific crystallographic site within the solubility limit of that particular structure type. This is a strong limitation from experimental point of view because forming solid solutions

is often limited by thermodynamic stabilities of the end members in any solid solution series. In this scenario building block approach can have advantages in tuning the band gap as a function of metal ion used by keeping the structure type intact as the reactions are done at lower temperatures. Optical band gap values of the compounds $Na_{12-nx}M_x^{n+}(Ge_2Se_6)_2$ (M = Ca^{2+}, Sr^{2+}, Mn^{2+}, Pb^{2+}, In^{3+}, La^{3+}, Pr^{3+}, Sm^{3+}, Tb^{3+}) are provided in Table 3 and the diffuse reflectance plots are provided in Figure 4. Firstly, wide range of optical band gaps are observed within the same structure type with change of the metal ion. Band gap narrowing

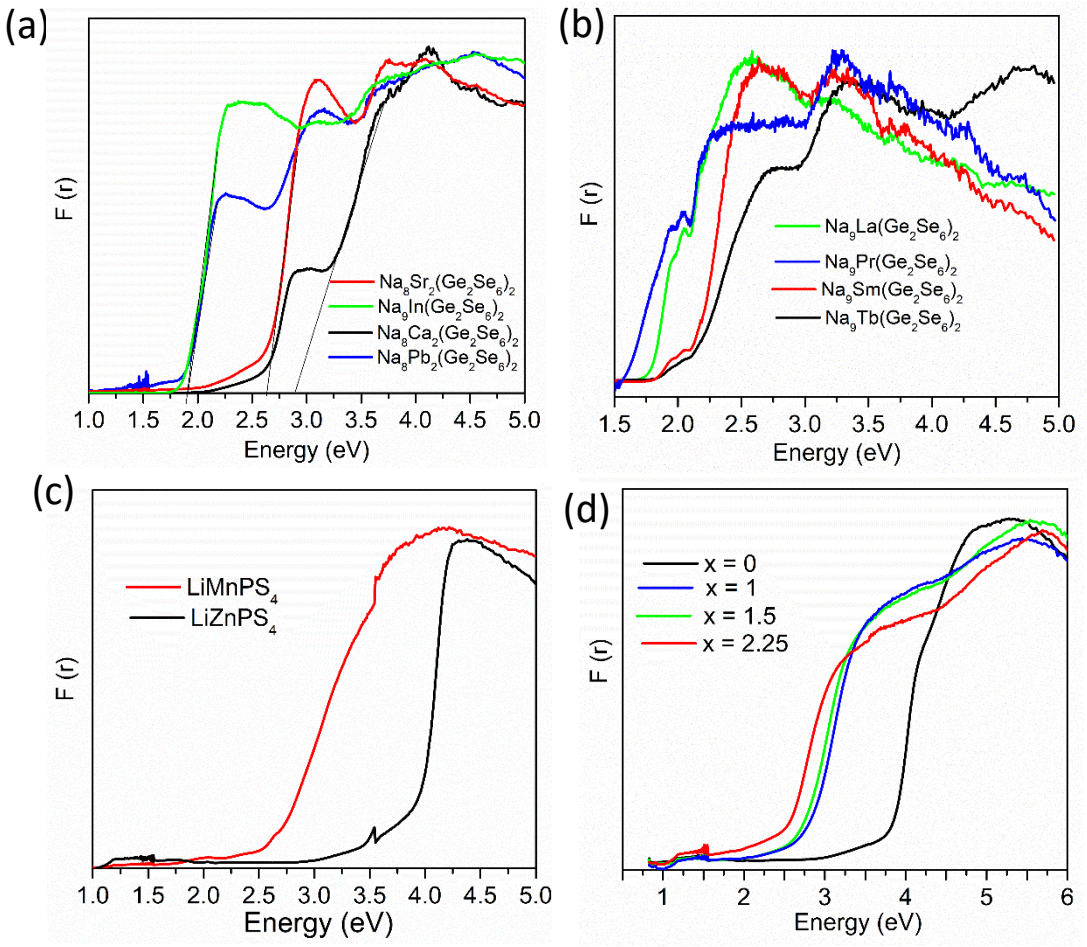

Figure 4. Diffuse reflectance spectra of compounds *M* in $Na_{12-nx}M_x^{n+}(Ge_2Se_6)_2$ where M is main group metals (a), rare earth metals (b); $LiMPS_4$ (M = Mn, Zn) (c), $Li_{3-x}Cu_xPS_4$ (x = 0, 1, 1.5, 2.25) (d).

is observed within the main group metals in moving from alkaline earth (Sr and Ca) to p-block element such as, In (Figure 4a), or 1st transition metal to rare earth metal (Figure 4b) analogues within the same structure type. Change of metal ion would change the overall orbital contribution to the valence and conduction bands, which ultimately modulates the band gap of the compound. In thiophosphate-based compounds, systematic decrease in the optical band gap is observed as a function of Cu content in the solid solution series $Li_{3-x}Cu_xPS_4$ (x = 1, 1.5, 2.25), (Figure 4c and 4d).

Table 3. Optical band gaps values of the compounds

M in $Na_{12-nx}M_x^{n+}(Ge_2Se_6)_2$	Band gap (eV)	M	Band gap (eV)
Ca	2.9	Li_3PS_4	3.8
Sr	2.6	$Li_{3-x}Cu_xPS_4$	2.8 (x = 1),
Mn	1.95	$Li_{3-x}Cu_xPS_4$	2.6 (x = 1.5),
In	1.9	$Li_{3-x}Cu_xPS_4$	2.4(x = 2.25)
Pb	1.9	$LiZnPS_4$	3.6
La	1.76	$LiMnPS_4$	1.95
Pr	1.59		
Sm	2.12		
Tb	2		

3.4. MAGNETIC STUDIES

To confirm the oxidation state of the metal and to study the magnetic properties, preliminary magnetic measurements were performed on as-synthesized powered samples. The experimental magnetic moments and theoretical magnetic moments are provided in Table 4. Magnetic susceptibility and inverse magnetic susceptibility plots are provided in Figure S3. The experimental magnetic moments are in very good agreements with the

theoretical magnetic moments, which confirms that the oxidation states assigned based on single crystal data are accurate.

Table 4. Experimental and theoretical magnetic moment values

Compound	Ion	Experimental (μ_β)	Theoretical (μ_β)
$Na_8Mn_2(Ge_2Se_6)_2$	Mn^{2+}	5.8	5.92[19]
$Na_8Eu_2(Ge_2Se_6)_2$	Eu^{2+}	6.99	7.93
$Na_9Gd(Ge_2Se_6)_2$	Gd^{3+}	8.2	7.94
$Na_9Tb(Ge_2Se_6)_2$	Tb^{3+}	10.1	9.72
$LiMnPS_4$	Mn^{2+}	5.69	5.92[21]

4. CONCLUSIONS

Herein, we report the building block approach, a new synthetic methodology to rationally design and synthesize complex quaternary chalcogenides with case studies using selenogermante, $Ge_2Se_6^{6-}$, and thiophosphate, PS_4^{3-}, building units. Several new quaternary chalcogenides are rationally synthesized using this building block approach. All the compounds are structurally characterized using single crystal and powder X-ray diffraction techniques. Further tracking of the building units in the reactive media using *in situ* synchrotron powder X ray diffraction method unleashed several findings on new phase formation through solid-solid diffusion in a solid-state metathesis mechanism. Building block approach also proved to be advantageous to tune the band gap of materials by keeping the structure type intact. This new synthetic approach can introduce high degree of rationality in solid state reactions in comparison to traditional solid-state process and can speed up the discovery of new materials in complex chalcogenide chemistry. The

building block approach can be further extended to other building units and different metal chloride salts across the periodic table to unlock the treasure of undiscovered materials and increase the materials space.

SUPPLEMENTARY INFORMATION

Table S1. Heating protocol followed for the metathesis reactions

Building block precursor	MCl3	Temp	heating rate	Dwell time	cooling rate	color	Product
$Na_6Ge_2Se_6$	$InCl_3$	700	25	96	30	orange yellow	$Na_9In(Ge_2Se_6)_2$
	$LaCl_3$	600	25	96	30	yellow	$Na_9La(Ge_2Se_6)_2$
	$CeCl_3$	600	25	96	30		$Na_9Ce(Ge_2Se_6)_2$
	$PrCl_3$	600	25	96	30		$Na_9Pr(Ge_2Se_6)_2$
	$NdCl_3$	600	25	96	30		$Na_9Nd(Ge_2Se_6)_2$
	$SmCl_3$	600	25	96	30		$Na_9Sm(Ge_2Se_6)_2$
	$GdCl_3$	600	25	96	30		$Na_9Gd(Ge_2Se_6)_2$
	$TbCl_3$	600	25	96	30		$Na_9Tb(Ge_2Se_6)_2$
	$DyCl_3$	600	25	96	30		$Na_9Dy(Ge_2Se_6)_2$
	$HoCl_3$	600	25	96	30		$Na_9Ho(Ge_2Se_6)_2$
	$YbCl_3$	600	25	96	30		$Na_9Yb(Ge_2Se_6)_2$
	$CaCl_2$	700	25	96	30	white	$Na_8Ca_2(Ge_2Se_6)_2$
	$SrCl_2$	700	25	96	30	pale yellow	$Na_8Sr_2(Ge_2Se_6)_2$
	$MnCl_2$	750	25	96	35	orange red	$Na_8Mn_2(Ge_2Se_6)_2$
	$PbCl_2$	650	20	120	30	red	$Na_8Pb_2(Ge_2Se_6)_2$
	$CdCl_2$	650	20	120	30	dark red	$Na_8Cd_2(Ge_2Se_6)_2$
	$EuCl_2$	600	25	96	30		$Na_8Eu_2(Ge_2Se_6)_2$
Li_3PS_4	$MnCl_2$	500	20	48	30	yellow	$LiMnPS_4$
	$ZnCl_2$	500	20	48	30	white	$LiZnPS_4$
	CuCl	700	25	48	30	yellow	$Li_{1.5}Cu_{1.5}PS_4$

Table S2. Crystal data and refinement details of $Na_8Ca_2(Ge_2Se_6)_2$, and $Na_8Sr_2(Ge_2Se_6)_2$

Empirical formula	$Na_8Ca_2(Ge_2Se_6)_2$	$Na_8Sr_2(Ge_2Se_6)_2$
Formula weight	1501.96	1597.04
Temperature	243(2) K	299(2) K
Wavelength	0.71073 Å	0.71073 Å
Crystal system	Monoclinic	Monoclinic
Space group	*C* 2/m	*C* 2/m
Unit cell dimensions	a = 7.8969(13) Å	a = 7.1529(13) Å
	b = 12.228(2) Å	b = 12.346(2) Å
	c = 7.1004(12) Å	c = 8.0299(15) Å
	b= 106.986(2)°	b= 107.275(2)°
Volume	655.72(19) $Å^3$	677.1(2) $Å^3$
Z	1	1
Density (calculated)	3.804 Mgm^{-3}	3.916 Mgm^{-3}
Absorption coefficient	21.709 mm^{-1}	24.540 mm^{-1}
R [$I>2\sigma(I)$]	1.163	1.078
R indices (all data)	$R1$ = 0.0293	$R1$ = 0.0458
R [$I>2\sigma(I)$]	$wR2$ = 0.0708	$wR2$ = 0.1161

Table S3. Crystal data and refinement details of $Na_9In(Ge_2Se_6)_2$, $Na_8Pb_2(Ge_2Se_6)_2$, and $Na_8Cd_2(Ge_2Se_6)_2$

Empirical formula	$Na_9In(Ge_2Se_6)_2$	$Na_8Pb_2(Ge_2Se_6)_2$	$Na_8Cd_2(Ge_2Se_6)_2$
Formula weight	1559.61	1836.18	1646.6
Temperature	243(2) K	223(2) K	300(2) K
Wavelength	0.71073 Å	0.71073 Å	0.71073 Å
Crystal system	Monoclinic	Monoclinic	Monoclinic
Space group	*C* 2/*m*	*C* 2/*m*	*C* 2/*m*
Unit cell dimensions	a = 7.8618(9) Å	a = 7.105(2) Å	a = 7.8306(14) Å
	b = 12.0825(14) Å	b = 12.269(4) Å	b = 12.040(2) Å
	c = 7.1007(8) Å	c = 7.993(4) Å	c = 7.1059(12) Å
	b= 106.8280(10)°	b= 107.158(4)°	b= 106.878(2)°
Volume	645.61(13) $Å^3$	665.8(4) $Å^3$	641.11(19) $Å^3$
Z	1	1	1
Density (calculated)	4.011 Mgm^{-3}	4.579 Mgm^{-3}	4.265 Mgm^{-3}
Absorption coefficient	22.539 mm^{-1}	33.578 mm^{-1}	23.417 mm^{-1}
Goodness-of-fit on F2	1.144	1.068	1.045
R [$I>2\sigma(I)$]	$R1$ = 0.0306	$R1$ = 0.0356	$R1$ = 0.0323
R indices (all data)	$wR2$ = 0.0756	$wR2$ = 0.0736	$wR2$ = 0.0850

Table S4. Crystal data and refinement details of $Na_9La(Ge_2Se_6)_2$, $Na_9Ce(Ge_2Se_6)_2$, and $Na_9Pr(Ge_2Se_6)_2$

Empirical formula	$Na_9La(Ge_2Se_6)_2$	$Na_9Ce(Ge_2Se_6)_2$	$Na_9Pr(Ge_2Se_6)_2$
Formula weight	1583.7	1584.91	1585.7
Temperature	298(2) K	293(2) K	293(2) K
Wavelength	0.71073 Å	0.71073 Å	0.71073 Å
Crystal system	Monoclinic	Monoclinic	Monoclinic
Space group	*C* 2/*m*	*C* 2/*m*	*C* 2/*m*
Unit cell dimensions	a = 7.9726(8) Å	a = 7.9629(10) Å	a = 7.8762(17) Å
	b = 12.3349(13) Å	b = 12.3133(16) Å	b = 12.185(3) Å
	c = 7.1121(7) Å	c = 7.1154(9) Å	c = 7.1165(15) Å
	β= 107.112(2)°	β= 107.072(2)°	β= 106.892(4)°
Volume	668.45(12) $Å^3$	666.92(15) $Å^3$	653.5(2) $Å^3$
Z	1	1	1
Density (calculated)	3.934 Mgm^{-3}	3.946 Mgm^{-3}	4.029 Mgm^{-3}
Absorption coefficient	22.482 mm^{-1}	22.639 mm^{-1}	23.226 mm^{-1}
Goodness-of-fit on F2	1.069	1.155	1.083
R [$I>2\sigma(I)$]	$R1$ = 0.0184	$R1$ = 0.0341	$R1$ = 0.0313
R indices (all data)	$wR2$ = 0.0369	$wR2$ = 0.0766	$wR2$ = 0.0923

Table S5. Crystal data and refinement details of $Na_9Nd(Ge_2Se_6)_2$, $Na_9Sm(Ge_2Se_6)_2$, and $Na_9Eu_2(Ge_2Se_6)_2$

Empirical formula	$Na_9Nd(Ge_2Se_6)_2$	$Na_9Sm(Ge_2Se_6)_2$,	$Na_8Eu_2(Ge_2Se_6)_2$
Formula weight	1589.03	1595.14	1725.72
Temperature	300(2) K	298(2) K	298(2) K
Wavelength	0.71073 Å	0.71073 Å	0.71073 Å
Crystal system	Monoclinic	Monoclinic	Monoclinic
Space group	*C* 2/*m*	*C* 2/*m*	*C* 2/*m*
Unit cell dimensions	a = 7.934(4) Å	a = 7.9158(15) Å	a = 7.1388(16) Å
	b = 12.282(6) Å	b = 12.244(2) Å	b = 12.334(3) Å
	c = 7.115(3) Å	c = 7.1048(13) Å	c = 8.0195(18) Å
	β= 107.052(6)°	β= 106.993(3)°	β= 107.267(4)°
Volume	662.8(5) Å3	658.6(2) Å3	674.3(3) Å3
Z	1	1	1
Density (calculated)	3.981 Mgm^{-3}	4.022 Mgm^{-3}	4.250 Mgm^{-3}
Absorption coefficient	23.020 mm^{-1}	23.428 mm^{-1}	25.295 mm^{-1}
Goodness-of-fit on F2	1.093	0.983	1.075
R [$I>2\sigma(I)$]	$R1$ = 0.0425	$R1$ = 0.0202	$R1$ = 0.0228
R indices (all data)	$wR2$ = 0.1107	$wR2$ = 0.0461	$wR2$ = 0.0564

Table S6. Crystal data and refinement details of $Na_9Gd(Ge_2Se_6)_2$, $Na_9Tb(Ge_2Se_6)_2$,and $Na_9Dy(Ge_2Se_6)_2$

Empirical formula	$Na_9Gd(Ge_2Se_6)_2$	$Na_9Tb(Ge_2Se_6)_2$	$Na_9Dy(Ge_2Se_6)_2$
Formula weight	1602.04	1603.71	1607.29
Temperature	293(2) K	293(2) K	293(2) K
Wavelength	0.71073 Å	0.71073 Å	0.71073 Å
Crystal system	Monoclinic	Monoclinic	Monoclinic
Space group	*C* 2/*m*	*C* 2/*m*	*C* 2/*m*
Unit cell dimensions	a = 7.9111(7) Å	a = 7.9004(6) Å	a = 7.8926(9) Å
	b = 12.2446(11) Å	b = 12.2327(10) Å	b = 12.2213(13) Å
	c = 7.1173(6) Å	c = 7.1129(6) Å	c = 7.1168(8) Å
	β= 106.9890(10)°	β= 106.9270(10)°	β= 106.924(2)°
Volume	659.35(10) $Å^3$	657.63(9) $Å^3$	656.74(13) $Å^3$
Z	1	1	1
Density (calculated)	4.035 Mgm^{-3}	4.049 Mgm^{-3}	4.064 Mgm^{-3}
Absorption coefficient	23.687 mm^{-1}	23.917 mm^{-1}	24.101 mm^{-1}
Goodness-of-fit on F2	1.078	1.086	1.037
R [$I>2\sigma(I)$]	$R1$ = 0.0165	$R1$ = 0.0164	$R1$ = 0.0185
R indices (all data)	$wR2$ = 0.0416	$wR2$ = 0.0455	$wR2$ = 0.0496

Table S7. Crystal data and refinement details of $Na_9Ho(Ge_2Se_6)_2$, and $Na_9Yb(Ge_2Se_6)_2$

Empirical formula	$Na_9Ho(Ge_2Se_6)_2$	$Na_9Yb(Ge_2Se_6)_2$
Formula weight	1609.72	1617.83
Temperature	293(2) K	293(2) K
Wavelength	0.71073 Å	0.71073 Å
Crystal system	Monoclinic	Monoclinic
Space group	*C* 2/*m*	*C* 2/*m*
Unit cell dimensions	a = 7.8960(14) Å	a = 7.9514(8) Å
	b = 12.222(2) Å	b = 12.3038(12) Å
	c = 7.1207(12) Å	c = 7.1159(7) Å
	β= 106.875(3)°	β= 107.060(2)°
Volume	657.6(2) $Å^3$	665.53(11) $Å^3$
Z	1	1
Density (calculated)	4.065 Mgm^{-3}	4.037 Mgm^{-3}
Absorption coefficient	24.238 mm^{-1}	24.489 mm^{-1}
R [$I>2\sigma(I)$]	1.052	1.111
R indices (all data)	$R1$ = 0.0353	$R1$ = 0.0358
R [$I>2\sigma(I)$]	$wR2$ = 0.0871	$wR2$ = 0.1014

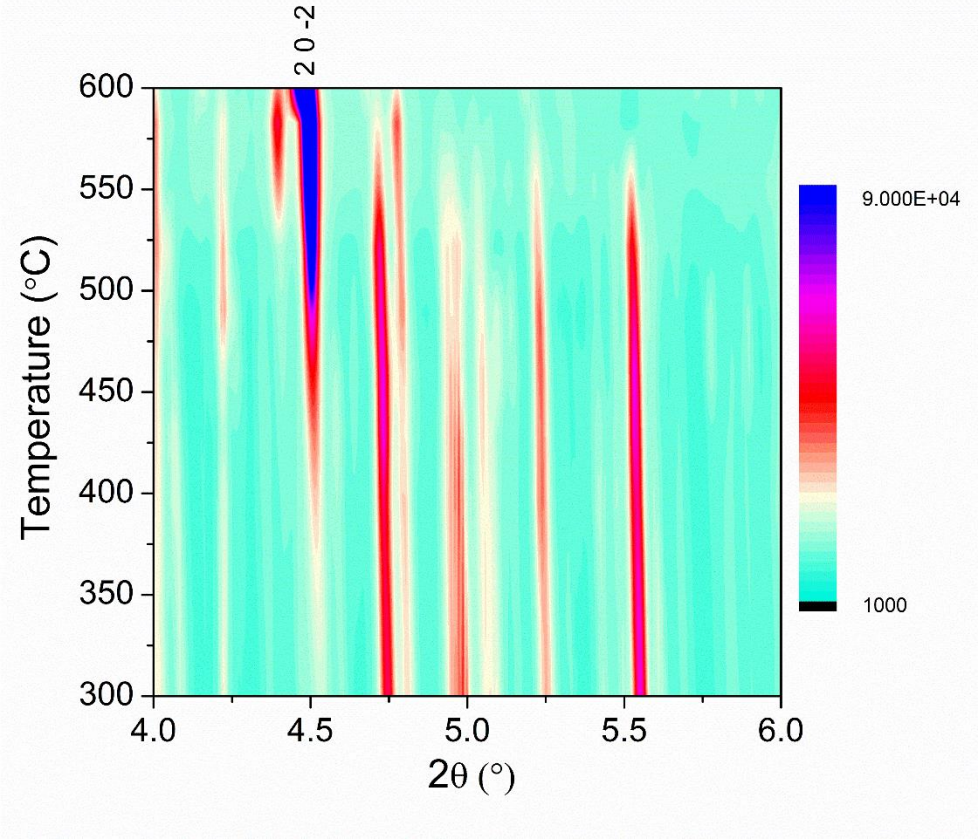

Figure S1. In situ powder X-ray thermodiffractogram of the reaction mixture $Na_6Ge_2Se_6$ + $CeCl_3$ (2:1) to form the product $Na_9Ce(Ge_2Se_6)_2$.

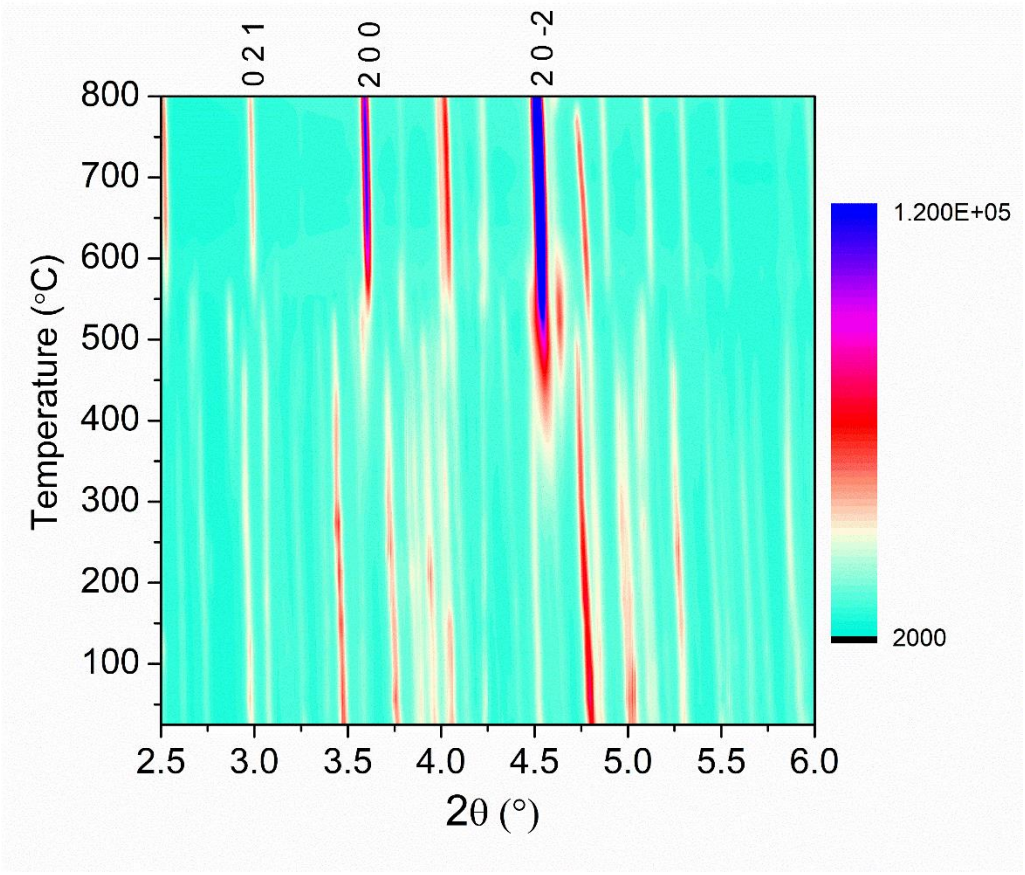

Figure S2. In situ powder X-ray thermodiffractogram of the reaction mixture $Na_6Ge_2Se_6$ + $CaCl_2$ (1:1) to form the product $Na_8Ca_2(Ge_2Se_6)_2$

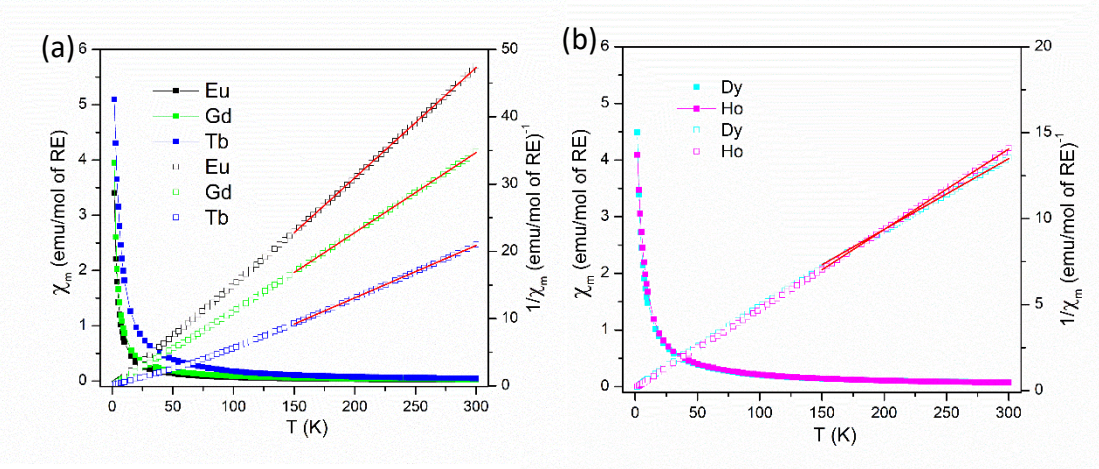

Figure S3. Temperature-dependent molar and inverse molar magnetic susceptibility of $Na_{12-nx}M_x^{n+}(Ge_2Se_6)_2$. (a) M = Eu, Gd, Tb (B) M = Dy, Ho

REFERENCES

1. Jansen M. A. Concept for Synthesis Planning in Solid-State Chemistry, *Angew. Chem., Int. Ed.*, **2002**, *41*, 3746 —3766.

2. Zunger, A. Inverse design in search of materials with target functionalities. *Nat Rev Chem,* **2018**, *2*, 1–16.

3. Bugaris, D. E.; zur Loye, H. C. Materials Discovery by Flux Crystal Growth: Quaternary and Higher Order Oxides. *Angew. Chem., Int. Ed*. **2012**, 51, 3780– 3811 DOI: 10.1002/anie.201102676

4. Kanatzidis, M. G. Discovery-Synthesis, Design, and Prediction of Chalcogenide Phases. *Inorg. Chem.* **2017**, *56*, 3158– 3173, DOI: 10.1021/acs.inorgchem.7b00188

5. Sunshine, S. A.; Kang, D.; Ibers, J. A. A New Low-Temperature Route to Metal Polychalcogenides: Solid-State Synthesis of $K_4Ti_3S_{14}$, a Novel One-Dimensional Compound. *J. Am. Chem. Soc*., **1987**, *109*, 6202 – 6204.

6. Cody, J. A.; Mansuetto, M. F.; Chien, S.; Ibers, J. A. Reactive flux syntheses at low and high temperatures. *Materials Science Forum*, **1994**, *152-5*, 35 - 42.

7. Kanatzidis, M.G. Molten Alkali-Metal Polychalcogenides as Reagents and Solvents for the Synthesis of New Chalcogenide Materials. *Chem. Mater*., **1990**, *2*, 353 – 363.

8. Palchik, O.; Marking, G. M.; Kanatzidis, M. G. Exploratory synthesis in molten salts: Role of flux basicity in the stabilization of the complex thiogermanates $Cs_4Pb_4Ge_5S_{16}$, $K_2PbGe_2S_6$, and $K_4Sn_3Ge_3S_{14}$. *Inorg. Chem*., **2005**, *44*, 4151 – 4153.

9. Choudhury, A.; Dorhout, P. K. Destruction of noncentrosymmetry through chalcogenide salt inclusion. *Inorg. Chem*., **2006**, *45*, 5245 – 5247.

10. Parkin, I. P. Solid state metathesis reaction for metal borides, silicides, pnictides and chalcogenides: ionic or elemental pathways *Chem. Soc. Rev.* **1996**, *25*, 199−207

11. Gillan, E. G.; Kaner, R. B. Synthesis of refractory ceramics via rapid metathesis reactions between solid-state precursors. *Chem. Mater*. **1996**, *8*, 333−343

12. Sheldrick, W. S.; Wachhold, M. Chalcogenidometalates of the Heavier Group 14 and 15 Elements. *Coord. Chem. Rev.* **1998**, *176* (1), 211– 322, DOI: 10.1016/S0010-8545(98)00120-9

13. Bruker- SMART. Bruker AXS Inc., Madison, Wisconsin, USA. 2002

14. Bruker-SAINT and SADABS, and SHELXTL. Bruker AXS Inc., Madison, Wisconsin, USA, 2008.

15. Sheldrick, G. M. A short history of SHELX. *Acta Crystallogr., Sect. A: Found. Crystallogr*. **2008**, 64, 112–122.

16. Hübschle, C. B.; Sheldrick, G. M.; Dittrich, B. ShelXle: A Qt Graphical User Interface for SHELXL. *J. Appl. Crystallogr.* **2011**, *44* (6), 1281–1284. https://doi.org/10.1107/S0021889811043202.

17. Kubelka, P. and Munk, F. Ein Beitrag Zur Optik Der Farbanstriche. *Z. Techn. Phys*. **1931**, *12*, 593 -601.

18. Toby, B. H.; Von Dreele, R. B. GSAS-II: the genesis of a modern open-source all-purpose crystallography software package. *J. Appl. Crystallogr*. **2013**, *46*, 544– 549, DOI: 10.1107/S0021889813003531

19. Balijapelly, S., Craig, A.J., Bin Cho, J., Jang, J.I., Ghosh, K., Aitken, J.A., Chernatynskiy, A.V., Choudhury, A. Building-block approach to the discovery of $Na_8Mn_2(Ge_2Se_6)_2$: A polar chalcogenide exhibiting promising harmonic generation signals with a high laser-induced damage threshold. *Journal of Alloys and Compounds*, **2021**, *900*, 163392. DOI: 10.1016/j.jallcom.2021.163392

20. Tachez, M.; Malugani, J.-P.; Mercier, R.; Robert, G. Ionic Conductivity of and Phase Transition in Lithium Thiophosphate Li_3PS_4. *Solid State Ionics* **1984**, *14*, 181−185

21. Balijapelly, S., Ghosh, K., Chernatynskiy, A.V., Choudhury, A. Discovery of an olivine-type lithium manganese thiophosphate, $LiMnPS_4$, Via a building block approach. *Chem. Commun.,* **2021**, *57* (97), pp. 13182-13185.DOI: 10.1039/d1cc05168g

22. Jorgens, S.; Johrendt, D.; Mewis, A. Z. Motive dichtester Kugelpackungen: Die Verbindungen $Zn_3(PS_4)_2$ und $LiZnPS_4$ *Anorg. Allg. Chem*. **2002**, 628, 1765– 1769 https://doi.org/10.1002/1521-3749(200208)628:8%3C1765::AID-ZAAC1765%3E3.0.CO;2-E

23. Hybertsen. M. S.; Louie S. G. Electron correlation in semiconductors and insulators: Band gaps and quasiparticle energies *Phys. Rev. B.* **1986,** *34*, 5390. https://doi.org/10.1103/PhysRevB.34.5390

II. TERNARY ALKALI ION THIOGALLATES, A_5GaS_4 (A = Li AND Na) WITH ISOLATED TETRAHEDRAL BUILDING UNITS AND THEIR IONIC CONDUCTIVITY

*Srikanth Balijapelly,[a] Prashanth Sandineni,[a] Amit Adhikary,[a] Nikolay N. Gerasimchuk,[b] Aleksandr V. Chernatynskiy,[c] Amitava Choudhury [a,] **

[a]*Department of Chemistry, Missouri University of Science and Technology, Rolla, MO 65409, USA.*

[b]*Department of Chemistry, Missouri State University, Springfield, MO 65897, USA*

[c]*Department of Physics, Missouri University of Science and Technology, Rolla, MO 65409, USA*

ABSTRACT

Two new ternary thiogallates in the series A_5GaS_4 (A = Li(I), Na(II)) have been synthesized for the first time employing gas passing route using oxide precursors and high temperature solid state route using stoichiometric combinations of elements, respectively. Li_5GaS_4 crystallizes in $P2_1/m$ space group and the structure is built up of layers of corner shared tetrahedra of LiS_4 and GaS_4 stacked along *a*-axis and the octahedrally coordinated Li ions residing in the interlayer space. Na_5GaS_4 crystallizes in *Pbca* space group and the structure consists of isolated $(GaS_4)^{5-}$ tetrahedra held together by charge balancing sodium ions in distorted tetrahedral and octahedral coordination geometries. Measurements of ionic conductivity of the compounds yielded the room temperature ionic conductivity of 1.8×10^{-7} and 4.0×10^{-7} S. cm^{-1} with activation energies of 0.54 and 0.28 eV, respectively, for I and II. Density functional theory calculations show close agreement in structural parameters with the measured data and predict the band gaps of 2.75 eV (I) and 2.70 eV

(II). Single point hybrid functional calculations result in band gaps of 3.95 and 3.65 eV correspondingly, in better agreement with experimental values of ~4.1 eV for both. Bond valence landscape energy maps suggest absence of any suitable diffusion path for Li in Li_5GaS_4. On the other hand, BVEL maps of Na_5GaS_4 confirm that the tetrahedrally coordinated Na ions are responsible for ionic conduction, whereas involvement of octahedrally coordinated Na ions in the conduction process could not be discerned.

1. INTRODUCTION

Alkali ion containing ternary sulfides *A/M/Q* (*A* = Li, Na, K, Rb, Cs; *M* = Main group metal, *Q* = S, Se, Te) possess wide structural and compositional varieties.[1-2] Various modes of connectivity between the chalcometallate building units lead to the formation of compounds with different dimensionality from non-van der Waal (vdW) layered, open framework type to isolated building units.[3-8] In recent years, these materials have attracted much attention because of their potential applications in solid electrolytes.[9] Highly conducting solid electrolyte would replace the flammable liquid electrolyte and impart greater safety.[9] Crystalline ternary thiophosphate, thioantimonnate and thiostannate based compounds in both lithium and sodium systems are currently extensively investigated for solid electrolyte applications.[3, 8 – 16] For example, high ionic conductivity at room temperature have been reported in some main-group metal chalcogenides as both Li- and Na-ion conductor, e.g., 6.4×10^{-4} S.cm^{-1} for $Li_{3.4}Si_{0.4}P_{0.6}S_4$,[10] and 2.2×10^{-3} S.cm^{-1} for $Li_{3.25}Ge_{0.25}P_{0.75}S_4$[11] and 1.2×10^{-2} S.cm^{-1} for $Li_{10}GeP_2S_{12}$[12]. Similarly in Na-ion conductors, ionic conductivity of 4.6×10^{-4} for Na_3PS_4,[13] 1×10^{-3} S.cm^{-1} for Na_3SbS_4[14]

4.0 × 10^{-3} S.cm^{-1} for $Na_{10}SnP_2S_{12}$[15] and 1.4× 10^{-3} S.cm^{-1} for $Na_{11}Sn_2PS_{12}$ have been reported.[16] Though some of the oxide-based materials have shown superionic conductivity in Li- and Na-ion conduction, however, they require high sintering temperature to eliminate the effect of grain boundary and achieve high conductivity.[17] In the case of chalcogenide, movement of ions is more facile because of the weak interaction of ions with the highly polarizable chalcogen lattice.[18] More importantly, these chalcogenide materials can be cold pressed to achieve high conductivity because of the higher malleability of chalcogen lattice.[9] Generally, these *A/M/Q* compounds can be synthesized by solid state reaction of elements or by employing polychalcogenide reactive flux in sealed quartz tube. Besides solid-state syntheses, these days solution-based or mechanochemical syntheses are also becoming popular because of the need to prepare large quantities of materials in a simple manner for solid electrolyte applications.[19] However, among several *A/M/Q* series of compounds, chalcogallate-based systems with simple building units are relatively less known, only a very small number of compositions exist to date.[4, 6, 20, 21] In the *A/Ga/Q* (*A* = Li, Na; *Q* = S, Se) series the reported phases are $LiGaQ_2$ (*Q* = S, Se, Te),[6] $Na_6Ga_2Q_6$ (*Q* = S, Se)[20] and $Na_4Ga_2S_5$.[21] $LiGaQ_2$ adopts $NaFeO_2$ structure type with three-dimensional structure and are well-known NLO materials.[6] $Na_6Ga_2S_6$ has unique isolated edge shared GaS_4 tetrahedra forming $Ga_2Q_6^{6-}$ dimers whereas $Na_4Ga_2S_5$ possesses one dimensional chains of corner- and edge-shared GaS_4 tetrahedra.

Hence, we have directed our focus towards finding new phases in chalcogallate based systems in presence of both lithium and sodium ions. Towards this effort we have recently reported $NaGaS_2$, a non-vdW 2D solid with supertetrahedral building units showing unusual property of water absorption.[4] There is a good reason to investigate the

formation of basic building unit of chalcogallate, such as tetrahedral, $[GaQ_4]^{5-}$ (Q = S, Se) for solid electrolyte since it will crystallize with five alkali ions. Besides favourable attributes of soft chalcogen atoms, presence of large number of ions should also play a pivotal role in facile ion conduction through the lattice. Further creation of defects in the lattice would inevitably create a good ionic conductor. However, to achieve this goal we first need to synthesize and structurally characterize the pristine and pure phase compounds made of basic building unit, A_5GaQ_4 (Q = S, Se). There are some reports of ionic conductivity measurements of Li_5GaS_4 and its solid solution with other main group elements,[22, 23] however, the crystal structure of Li_5GaS_4 is yet to be reported. To the best of our knowledge nothing is known about the Na-analogue, Na_5GaS_4. In this article, we report the synthesis, structure, and ionic conductivities of two new alkali ion containing non-isostructural thiogallates, Li_5GaS_4 (I) and Na_5GaS_4 (II), along with their theoretical band structures.

2. EXPERIMENTAL SECTION

2.1. SYNTHESIS

Li_5GaS_4 (I) was initially synthesized from a reaction of stoichiometric mixture of 2.5 mmol of Li_2S, 1 mmol of Ga shavings, 1.5 mmol of S in a sealed quartz ampoule. The heating protocol used for this reaction involved heating to 700 °C at a rate of 30 °C/h, dwelling for 18h, and cooling down to room temperature at 35 °C/h. However, this route always yielded significant amounts of $LiGaS_2$ as the secondary phase along with Li_5GaS_4 (I) as the main phase (Figure S1). Hence, we opted for gas passing route through which a

pure phase Li_5GaS_4 (I) was synthesized from 5 mmol of Li_2CO_3 and 1 mmol of Ga_2O_3 in a temperature-controlled tube furnace. The tube furnace was connected to a constant flow (20 sccm) of high purity argon carrier gas that passed through a tower of liquid carbon disulfide (CS_2) kept at room temperature. The vapours of CS_2 gas was carried over the oxide precursors for sulfidation at higher temperature. The temperature of the furnace was increased to 750 °C at a rate of 200 °C/h, after dwelling for 8 h, furnace was cooled to room temperature at a rate of 100 °C/h. Orange-red colour crystalline product was formed (Figure S2). The obtained product was ground again using a mortar pestle after transferring it inside an argon filled glovebox and subjected to a second cycle of heating in order to achieve phase pure compound. After the reaction very stable homogenous product containing orange-red colour crystals were transferred to an argon filled glove box (O2 < 0.1ppm). Na_5GaS_4 (II) was synthesized by reacting stoichiometric mixture of 2.5 mmol of Na_2S, 1 mmol of Ga shavings, 1.5 mmol of S in a sealed quartz ampoule. The sealed ampoule was heated in a temperature-controlled furnace and the temperature was ramped to 600 °C at a rate of 25 °C/h, after dwelling for 96 h, the furnace was cooled down to room temperature at 30 °C/h rate. Pale orange colour crystals were recovered after breaking the ampoule in an argon-filled glove box (Figure S2). Appropriate crystals were used for single crystal X-ray diffraction and finely ground powder samples were used for other characterizations including powder X-ray diffraction.

2.2. X-RAY DIFFRACTION

Good quality crystals were chosen for single crystal X-Ray diffraction on a Bruker smart apex diffractometer equipped with a sealed tube X-ray source of Mo–Kα radiation

(λ = 0.71073 Å). Room temperature or –53 °C diffraction data sets were collected using SMART[24] software with a step of 0.3° in ω scan and 20 s or 10 s/frame exposure time, respectively, for I and II. Programs SAINT[25] and SADABS[25] were used for the data integration and absorption correction, respectively. SHELXS-97 and difference Fourier syntheses were used to solve the structures.[26] Full-matrix least-squares refinement against $|F^2|$ was carried out using the SHELXTL-PLUS suite of programs.[25]

Table 1. Crystal data and refinement details of I and II

Compounds	I	II
Empirical formula	Li_5GaS_4	Na_5GaS_4
Formula weight	232.66	312.91
Temperature	300(2) K	220(2) K
Wavelength	0.71073 Å	0.71073 Å
Crystal system	Monoclinic	Orthorhombic
Space group	$P2_1/m$	*Pbca*
Unit cell dimensions	a = 6.2711(18) Å	a = 12.045(15) Å
	b = 7.864(2) Å	b = 7.0212(9) Å
	c = 6.8610(19) Å	c = 21.535(3) Å
	β = 90.118(4)°	
Volume	338.36(16) Å^3	1821.3(4) Å^3
Z	2	8
Density (calculated)	2.284 g/cm^3	2.282 g/cm^3
Absorption coefficient	5.166 mm^{-1}	4.089 mm^{-1}
Goodness-of-fit on F^2	1.091	1.059
R [$I > 2\sigma(I)$]	R_1 = 0.0426	R_1 = 0.0290
wR (F^2) (all data)	wR_2 = 0.1083	wR_2 = 0.0733

[a] $R_1 = \sum||F_o| - |F_c|/\sum|F_o|$

[b] $wR_2 = \{\sum[w(F_o^2 - F_c^2)^2]/\sum[w(F_0^2)^2]\}^{1/2}$, $w = 1/[\sigma^2(F_o)^2 + (aP)^2 + bP]$, where $P = [F_o^2 + 2F_c^2]/3$

Table 2. Selected bond lengths (Å) of compounds I and II.

Li_5GaS_4 (I)		Na_5GaS_4 (II)	
Ga1 – S3$^{\#1}$	2.2608(17)	Ga1 – S2$^{\#1}$	2.2758(11)
Ga1 – S1	2.2729(12)	Ga1 – S1$^{\#2}$	2.2778(11)
Ga1 – S1$^{\#2}$	2.2730(12)	Ga1 – S4	2.2834(11)
Ga1 – S2	2.2773(16)	Ga1 – S3$^{\#3}$	2.2852(11)

I: $^{\#1}$ x, -y + 1/2, z; $^{\#2}$ x, -y + 1/2, z; **II**: $^{\#1}$ x, y – 1, z; $^{\#2}$ -x + 1/2, y – 1/2, z; $^{\#3}$ -x + 1, -y + 1, -z + 1

Li_5GaS_4 crystallized in $P2_1/m$ space group while the Na-analogue, Na_5GaS_4, crystallized in *Pbca* space group. All the atoms can be easily located from the difference Fourier maps and weighted *R* factor, wR_2 converged to a low value without leaving any unaccounted electron density. Final refinements including the refinements of anisotropic thermal parameters were performed using SHELX-2018 incorporated in ShelXLe.[27] Crystal data and final refinement parameters are given in Table 1 and selected bond lengths are given in Table 2 for compounds I and II. Atomic coordinates along with their isotropic thermal parameters are given in SI (Tables S1 and S2).

2.3. POWDER X-RAY DIFFRACTION

The laboratory powder pattern was collected from a PANalytical X'Pert Pro diffractometer equipped with a Cu Kα anode and a linear array PIXcel detector over a 2θ range of 5 to 90° with an average scanning rate of 0.0472° s^{-1}. As-synthesized, hand ground

samples were loaded into an airtight cell covered with the kapton film to collect the PXRD pattern (Figure 1).

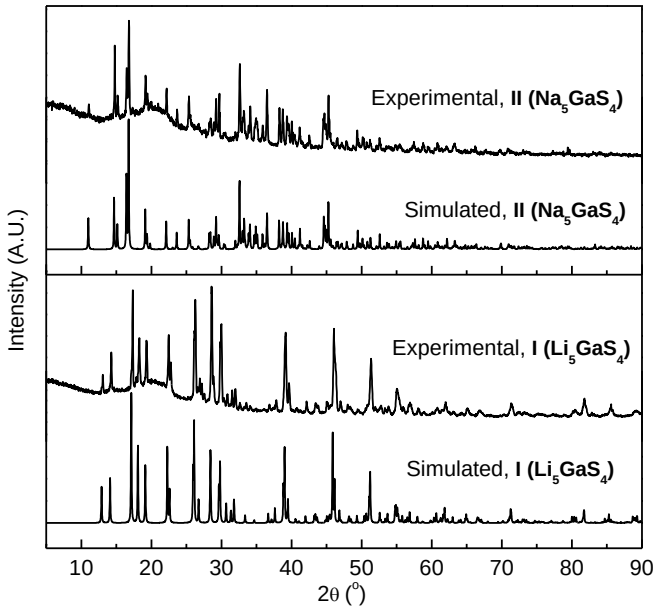

Figure 1. Comparison of simulated and experimental powder X-ray diffraction patterns for compounds, I and II. The broad hump between 2θ = 15° to 25° is due the Kapton film

2.4. DRS MEASUREMENTS

Diffuse reflectance measurements for compounds I and II were performed in Labsphere's integrating sphere (Model DRA-CA-30I) fitted on a Varian CARY 100 Bio UV-Vis spectrophotometer. A Spectralon's white standard was used as a 100% reflectance standard. The Kubelka–Munk function was used to transform the reflectance into absorption.[28] *hv vs* $(\alpha hv)^2$ plots (Figure 2) show flat region parallel to X–axis followed by a steep jump due to the electronic transition from valence band to the conduction band.

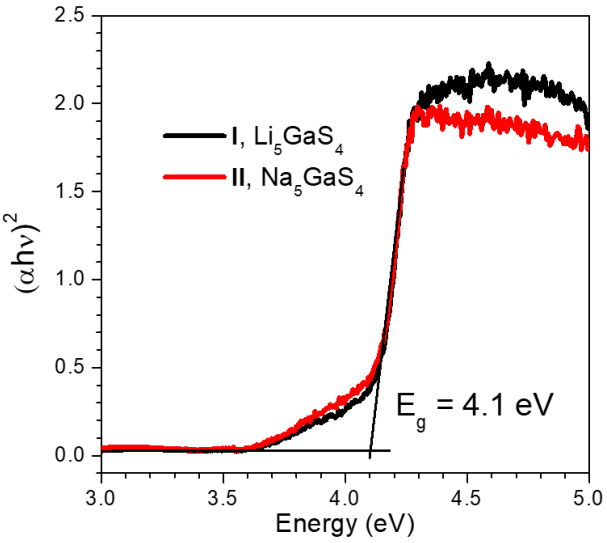

Figure 2. Diffuse reflectance plot for compounds I and II.

The band gap was determined by the intersection of the extrapolated flat and steep regions of the plot. The band gap values obtained for compounds I and II are almost similar and close to ~4.1 eV.

2.5. THERMAL ANALYSIS

Simultaneous TGA, DSC experiments were performed on TA Instruments Q50 TGA and Q600 SDT for compounds I and II from room temperature to 900 °C with a scan rate of 10 °C/min under high purity argon gas. Samples of *ca* 20 mg weight was placed into brand new calcined alumina crucible for the experiment. The plots are presented in SI (Figure S3). The TGA and DSC plots show endothermic events occurring at 837 °C for compound I and 670 °C for compound II, which could be due to melting of the compounds. However, the phase changes were not very sharp because of the weight loss of ~1.3 % after 300 °C due to reaction with oxygen impurities present in the inert gas as these TG-DSCs

were performed in unsealed open alumina cups. In fact, it is practically impossible to eliminate traces of air adsorbed on the Q600 analyzer interior surfaces of horizontal furnace even after ~20 min of the UHP-grade argon flow of 100±2 mL/min. However, it is evident that both compounds I and II are thermally stable at least up to 650 °C. Powder patterns of the remaining sample residues after TGA-DSC experiments (Figure S4) did not show any phase changes as both the samples retained the original crystal structure.

2.6. IMPEDANCE MEASUREMENTS

AC impedance measurements were performed from 1Hz to 1MHz using Biologic instruments SP-150 impedance analyzer with an AC signal amplitude of 500 or 100 mV. The hand ground samples were cold pressed applying a force of 280 MPa in a stainless-steel pressing die inside an argon filled glove box (O_2 < 0.1 ppm). Indium foil was used as the blocking electrodes. The pellets were placed in an airtight Swagelok type cell and heated in a temperature-controlled box furnace to measure the temperature dependence of the ionic conductivity. The impedance data were collected at every 10 °C increment by keeping the temperature of each measurement constant for at least an hour to reach the thermal equilibrium.

2.7. DFT CALCULATIONS

We carried out investigation of the structural and electronic properties of both compounds using Density Functional Theory (DFT) as implemented in VASP computational package.[29-32] We employed the revised Perdew-Burke-Ernzerhof generalized gradient approximation (PBESol) to the density functional[33] and used

Projected Augmented Wave (PAW) pseudopotential to describe the effect of the core electrons. Energy cut off for all calculations is 500 eV, while Brillouin zone integration used Monkhorst-Pack[34] k-point grid with dimensions of 5x5x5 for compound I and 3x3x3 for compound II**.**

3. RESULTS AND DISCUSSION

3.1. STRUCTURAL DESCRIPTION

Though compositionally both compounds I and II are similar, structurally they are different. Compound I crystallizes in a centrosymmetric monoclinic, $P2_1/m$ space group and is isostructural with Na_5InS_4,[35] Li_5AlS_4.[36] The asymmetric unit consists of three sulfur atoms, one gallium, and four lithium atoms (Figure 3a). Li1 and S1 occupy general positions on 4*f* Wyckoff site, while one gallium atom, two sulfur atoms (S2 and S3), and two lithium atoms (Li2 and Li3) are located on special positions denoted as 2*e* Wyckoff site. One remaining lithium atom (Li4) is also located on a special position, 2*a* Wyckoff site. Li1 and Li3 adopt distorted tetrahedral coordination while Li2 and Li4 adopt distorted octahedral coordination (Figure 3b and Figure S5). The structure of compound I can be described as hexagonal close packing of anions which are stacked along the *a*-axis in *ABAB* fashion. Such stacking of S creates eight tetrahedral holes and four octahedral holes of which $3/8^{th}$ of tetrahedral holes are filled with Li (Li1, Li3) and Ga cations and ½ of octahedral voids are filled with Li (Li2 and Li4). However, they differ in the manner of occupancy of tetrahedral and octahedral sites. The pair of close-packed (CP) layer (Figure 3c) in which only tetrahedral holes are occupied alternate between CP layers in which only

the octahedral holes are occupied as shown in Figure 3b. Alternatively, the structure can be viewed as a layered type with layers formed by corner shared tetrahedral network of LiS_4 (Li1 and Li3) and GaS_4 stacked along *a*-axis where the interlayer space is occupied by octahedrally coordinated Li-ions (Li2 and Li4) (Figure 3b). Li – S bond distances are in the range of 2.398(11) – 2.558(13) Å for tetrahedrally coordinated Li atoms (Li1, Li3) and 2.6562(11) – 3.040(12) Å for octahedrally coordinated Li atoms (Li2, Li4) which are in good agreements with other lithium containing main group sulfide, such as lithium thioalluminate, Li_5AlS_4.[36]

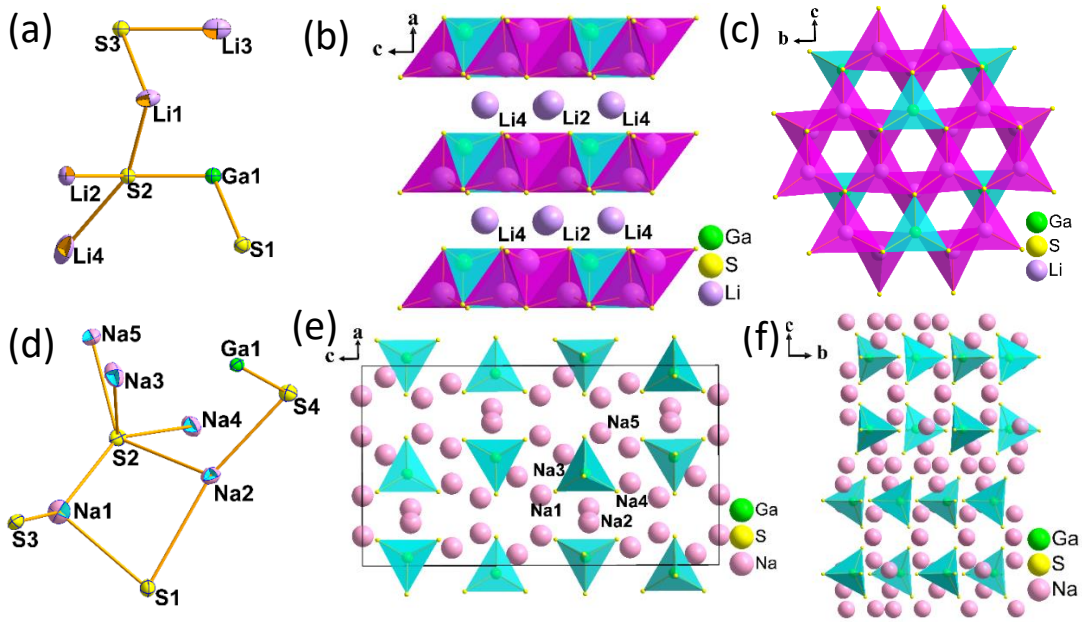

Figure 3. (a) Asymmetric unit of compound I. (b) Layers formed by GaS_4^{5-} and tetrahedrally coordinated Li stacked along *a*-axis where the interlayer space is occupied by octahedrally coordinated Li2 and Li4. (c) Polyhedral view of the layer, in which 3/8th of the tetrahedral voids are filled by Ga1, Li1 and Li3. (d) Asymmetric unit of compound II. (e) Unit cell showing the isolated GaS_4^{5-} tetrahedral units, separated by charge balancing sodium ions (f) Zig-zag arrangement of GaS_4^{5-} tetrahedral units along *b*-axis. (Thermal ellipsoids are given at 40 % probability)

Na_5GaS_4 (II) crystallizes in orthorhombic *Pbca* space group with asymmetric unit containing five sodium atoms, one gallium atom, and four sulfur atoms and all the atoms are in the general positions, 2*e* Wyckoff site (Figure 3d). Na_5GaS_4 adopts Na_5FeO_4[37] structure type and isostructural with Na_5AlS_4.[38] The structure of II composed of isolated GaS_4^{5-} tetrahedra with charge balancing sodium ions adopting distorted tetrahedral (Na1, Na3, Na4, and Na5) and distorted octahedral (Na2) coordination, respectively (Figure 3e and Figure S6). Columns of isolated GaS_4 tetrahedral building units are aligned along *b*-axis and are related by two-fold screw axis (Figure 3f). Na – S bond distances are in the range of 2.6861(19) – 2.952(2) and 2.8300(18) – 3.2360(18) Å for tetrahedrally and octahedrally coordinated Na atoms, respectively, which are in good agreement with isostructural sodium based thioalluminate Na_5AlS_4.[38] It is interesting to note here that many of the ternary compounds in the *A/M/*S series (e.g., Li_4GeS_4 or Li_4SnS_4) are moisture sensitive.[39] Though compound Na_5GaS_4 (II) is found to be reasonably stable in air for few hours, the compound Li_5GaS_4 (I) turned out to be very stable (four to five days), which could be attributed to the 2-dimensional network of LiS_4 and GaS_4.

Here, it should be noted that though the compounds with general formula A_5MQ_4 (*A* = Li, Na; *M* = Al, Ga, In; *Q* = S, Se) are compositionally similar, they adopt different structure types. This may be due to differences in sizes between the alkali ions and the main group metal ion. Among the compositions that exist in A_5MQ_4 family, for example Na_5InS_4[35] and Li_5AlS_4[36] are isostructural to I and crystallize in $P2_1/m$ space group with layered structure. Similarly, Na_5AlS_4[38] and II are isostructural and crystallize in *Pbca* space group containing isolated GaS_4 tetrahedral units. Increasing the size of alkali ion from Na to K as in K_5GaSe_4, it is still found to crystallize in *Pbca* space group similar to II

containing isolated $GaSe_4$ tetrahedra but possesses much larger unit cell volume.[40] However, recently reported K_5InSe_4 adopts a new structure type crystallizing in *C*2/*c* space group.[41]

3.2. THEORETICAL CALCULATIONS

Starting from the experimentally elucidated structures, we first performed structural relaxation until the maximum force on the atoms was less than 10^{-2} eV/Å. Relaxed structures show excellent agreement with experiment. For both compounds, the volume of the theoretical structure is slightly smaller than experimentally observed one, by 10 and 23 $Å^3$ correspondingly.

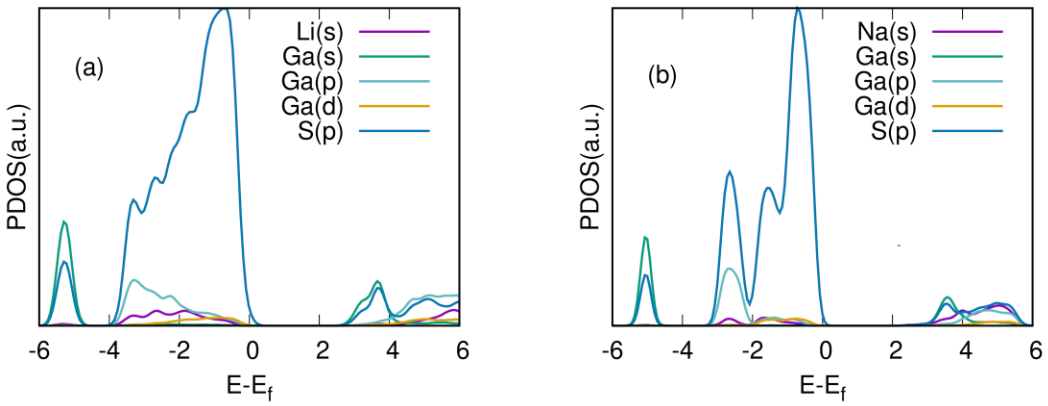

Figure 4. Projected electronic density of states in (a) Li_5GaS_4(I) and (b) Na_5GaS_4 (II).

The calculated projected density of states for Li_5GaS_4 (I) and Na_5GaS_4 (II) are shown in Figure 4 (a and b). The calculated band gaps for I and II are 2.75 and 2.69 eV, respectively. Considering the typical underestimation of band gaps by the conventional DFT, we also carried out the single point calculations with the HSE06 hybrid functional,[42] which typically improves the predictions for band gap. Due to the computational load,

lesser number of the k-points were used of the Brillouin zone integration: 2x2x2 for the compound I and gamma-point only for II. This calculation predicted band gaps of 3.95 and 3.65 eV correspondingly, in much better agreement with experiment (~4.1 eV). As illustrated in Figure 4a and 4b, projected density of states for both the compounds share some similarity in the contribution to the valence and conduction bands. The states below the Fermi level are dominated by S 3*p* states in both the compounds. The conduction band minimum (CBM) has the major contribution from S 3*p* states and Ga 4*s* states. There is no predominant contribution from alkali ion states to the valence band suggesting minimal covalent interactions with the alkali ions. It is still interesting to observe the difference in the calculated band gap of the two materials by the HSE06 functional considering both have the isolated GaS_4^{5-} unit mainly contributing to the bands around the energy gap and not the alkali ions. Therefore, the differences may come from the indirect effect of alkali ions and differences of packing of the GaS_4^{5-} units in the unit cell since I and II are not isostructural.

3.3. IONIC CONDUCTIVITY

AC impedance measurements were performed to calculate the ionic conductivity and activation energies. The Nyquist plots for the compounds I and II are shown in Figures 5 (a) and (b) consist of a high frequency semicircle and a low frequency tail corresponding to bulk resistance and charge accumulation at the blocking electrode. The equivalent circuit used, and the related fitting parameters for room temperature ionic conductivity are detailed in the SI (Figure S7). Ionic conductivity was calculated from the bulk resistance extracted from complex impedance plots. Temperature dependent ionic conductivity was measured

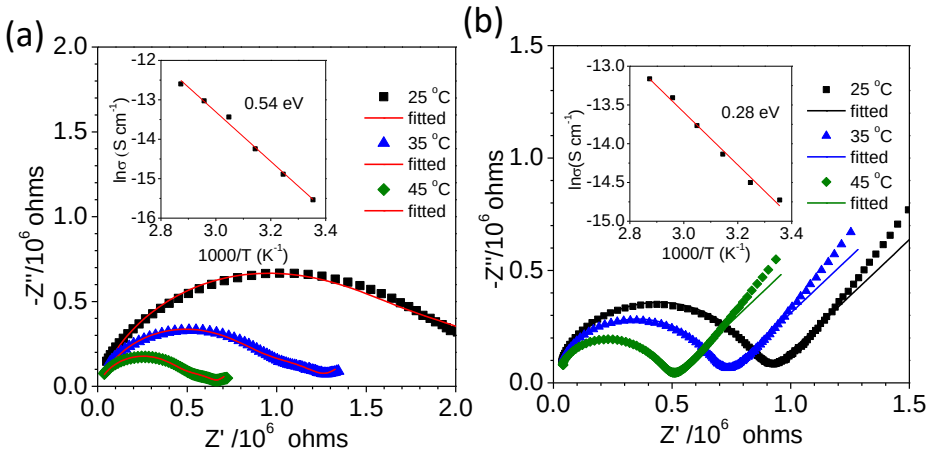

Figure 5. Nyquist plot for ionic conductivity of (a) Compound I (Li_5GaS_4) (b) Compound II (Na_5GaS_4). Inset shows the activation energy calculated from experimentally measured ionic conductivity versus temperature. Dots represents the experimental ionic conductivity and dashed line represents the Arrhenius fit to the data.

from room temperature to 75 °C at every 10 °C interval to calculate the activation energy. Within the measured range the ionic conductivities both compounds follow Arrhenius behaviour. The activation energies were calculated using $\sigma_T = \sigma_o \exp(-E_a/k_BT)$ where σ_T is the ionic conductivity, σ_o is a pre-exponential factor, T is the absolute temperature, and k_B is the Boltzmann constant. The room temperature ionic conductivities are 1.8×10^{-7} $S.cm^{-1}$ for Li_5GaS_4 (I) and 4.0×10^{-7} $S.cm^{-1}$ for Na_5GaS_4 (II). The calculated activation energies for compounds I and II are 0.54 and 0.28 eV, respectively. Despite having almost similar ionic conductivity in compounds I and II, there exist significant difference in the activation energies, which could arise due to different conduction mechanisms. Generally, a concerted type mechanism in which multiple adjacent ions simultaneously hop to neighbouring equilibrium site gives rise to low activation barriers compared to single ion hopping.[43] BVEL (Bond Valence Energy Landscapes) were calculated to find out the most

probable minimum energy trajectories for the Li and Na ions. Deviations in the Bond Valence Sum can be correlated to the possible ionic conduction path in the lattice.

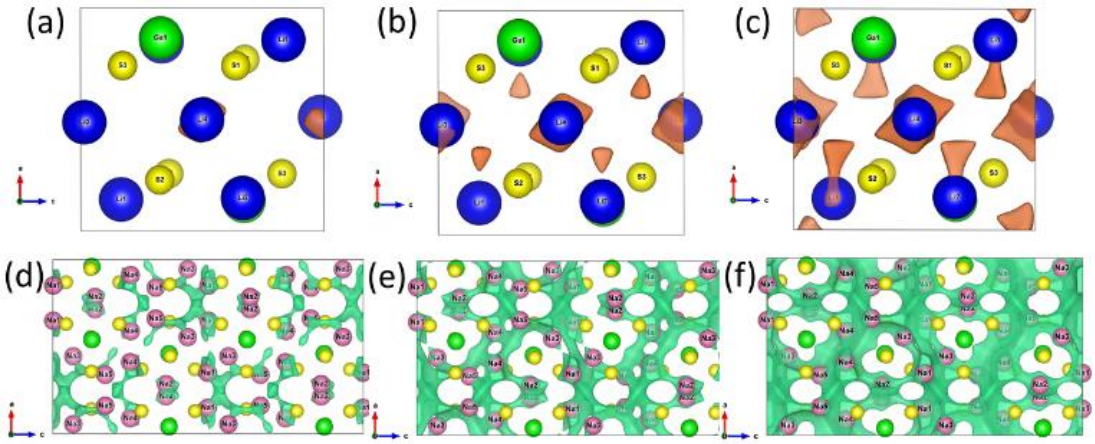

Figure 6. Bond valence sum (|ΔV|) maps of compound I at an isosurface $|\Delta V| = 0.3\ v.u.$ figure (a), $0.5\ v.u.$ figure (b) $0.7\ v.u.$ figure (c) and for compound II $|\Delta V| = 0.3\ v.u.$ figure (d), $0.5\ v.u$ figure (e), $0.7\ v.u$ figure (f).

These deviations can be plotted as an isosurface using VESTA.[44] Bond valence energy landscape maps are plotted as an isosurface energy levels $|\Delta V|$ = 0.3, 0.5, 0.7 v.u for compounds I (Figure 6 a, b, c) and II (Figure 6 d, e, f) . No suitable path for ion percolation was found for compound Li_5GaS_4 (I), which could be the reason for low ionic conductivity and high activation energy. The ionic conductivity of Li_5GaS_4 is much higher than the corresponding Al-analogue, Li_5AlS_4 (σ_{RT} = 9.73 × 10^{-9} S.cm^{-1}),[36] however, comparable to many related Li based ternary sulfide compounds, such as Li_4GeS_4 (σ_{RT} = 2.0×10^{-7} S.cm^{-1}),[22] but somewhat lower than Li_4SnS_4 (σ_{RT} = 7 × 10^{-5} S.cm^{-1})[8] and Li_2SnS_3 (σ_{RT} = 1.5 × 10^{-5} S.cm^{-1}).[3] Na_5GaS_4 has the room temperature ionic conductivity of 4.0 ×10^{-7} S.cm^{-1} which is slightly better than isostructural Al-analogue, Na_5AlS_4 (σ_{RT} =

1.64×10^{-7} S.cm^{-1}).[38] Slightly improved ionic conductivity of Na_5GaS_4 compared to Na_5AlS_4 could be due to larger ionic radii of Ga^{3+} compared to Al^{3+}. For Na_5GaS_4, a two-dimensional diffusion path was observed from BVEL calculation. BVEL map also confirms that Na2, which is in distorted octahedral coordination does not take part in the ion conduction. Similar observation has been found for isostructural Na_5AlS_4.[38]

Solid solutions with aliovalent substitutions would create Li/Na vacancies which is an important prerequisite for superionic conductors. Recently, Bernhard et al. reported that solid solutions in $Li_{4.4}M_{0.4}M'_{0.6}S_4$ (M = Al^{3+}, Ga^{3+}, and M' = Ge^{4+}, Sn^{4+}) series not only create vacancies, but also altered the arrangement of tetrahedral metal sites, with novel ordered and disordered lithium combination.[23] Harm et al. reported a solid solution series of $Na_{5-x}Al_{1-x}Si_xS_4$ ($0 \leq x \leq 1$) and emergence of double salt $Na_9(AlS_4)(SiS_4)$ in the composition range of $0.5 \leq x \leq 0.75$ with high alkali ion concentration with versatile Na-coordination.[36] However, it will be interesting to substitute some percentage of Li/Na with transition metal, in which case one can perform oxidative de-insertion of alkali ion from the host lattice to create more defects. Li_5GaS_4 would be an ideal candidate for substitution with transition metal due to its 2D layered structure. Substitution of pentavalent metal ions (P^{+5}, Sb^{+5}) in the Ga-site can also be investigated in A_5GaS_4 (A = Li, Na) to create more defects for improving the ionic conductivity. With the report of structures of pristine A_5GaS_4 (A = Li, Na) in this article, it will be much easier to investigate the structural changes as a function of dopant.

4. CONCLUSIONS

We have successfully synthesized two new ternary thiogallates containing alkali ions and determined their structures. Though both are compositionally similar but adopt different crystal structures. This work also proves that gas passing reactions would give access to new phases which may not be accessible through typical solid-state reactions from the elements. Ionic conductivity measurements along with BVEL calculations suggest no diffusion paths in Li_5GaS_4 and 2D diffusion paths in Na_5GaS_4 exists at moderate activation energies. DFT calculations show that both the compounds are wide band-gap semiconductors with optical bandgaps > 2.5 eV and no significant contribution was found from Li/Na states to the conduction and valence band indicating predominant ionic interactions with the alkali metal ions. Currently we are investigating doping of hypervalent metal ions to induce vacancies in the lattice to improve the ionic conductivity.

ACKNOWLEDGEMENTS

The authors acknowledge the funding from National Science Foundation (DMR-1809128). This work was supported in part by the National Science Foundation under Grant No. OAC-1919789.

SUPPORTING INFORMATION

Table S1. Final atomic coordinates and equivalent isotropic displacement parameters of the atoms for compounds I and II. $U_{(eq)}$ = 1/3rd of the trace of the orthogonalized U_{eq} tensor.

Atomic Parameters						
Atom	Wyckoff	Occupancy	x/a	y/b	z/c	U [Å^2]
Li_5GaS_4 (**I**)						
Ga1	2e	1	0.6335	0.25	0.1709	0.0166
S1	4f	1	0.7577	0.015	0.3271	0.0173
S2	2e	1	0.2704	0.25	0.1751	0.0159
S3	2e	1	2418	0.75	0.138	0.0167
Li1	4f	1	0.3577	0.5133	0.3341	0.0247
Li2	2e	1	0.0114	0.25	0.4846	0.0240
Li3	2e	1	0.649	0.75	0.1663	0.0280
Li4	2a	1	0	0	0	0.0420
Na_5GaS_4(**II**)						
Ga1	8c	1	0.4597	0.1673	0.3742	0.01148
S1	8c	1	0.13	0.7947	0.4575	0.0157
S2	8c	1	0.4452	0.8445	0.3782	0.0152
S3	8c	1	0.3574	0.7477	0.6238	0.0157
S4	8c	1	0.3696	0.261	0.2861	0.0163
Na1	8c	1	0.3508	0.9054	0.499	0.0261
Na2	8c	1	0.2852	0.55	0.3645	0.0197
Na3	8c	1	0.5553	0.5599	0.4342	0.0264
Na4	8c	1	0.4109	0.8763	0.2489	0.0272
Na5	8c	1	0.661	0.8877	0.3313	0.0234

Table S2. Anisotropic displacement parameters ($Å^2 x\ 10^3$) for sad. The anisotropic displacement factor exponent takes the form: $-2p^2[\ h^2 a^{*2} U^{11} + ... + 2\ h\ k\ a^*\ b^*\ U^{12}]$

Atoms	U^{11}	U^{22}	U^{33}	U^{23}	U^{13}	U^{12}
			Li_5GaS_4 (**I**)			
Ga(1)	16(1)	15(1)	18(1)	0	0(1)	0
S(1)	18(1)	16(1)	18(1)	1(1)	-1(1)	1(1)
S(2)	14(1)	14(1)	19(1)	0	1(1)	0
S(3)	18(1)	15(1)	17(1)	0	1(1)	0
Li(1)	36(5)	20(4)	18(4)	-2(3)	-2(4)	3(3)
Li(2)	16(5)	23(6)	33(7)	0	-1(4)	0
Li(4)	25(6)	55(10)	45(9)	5(6)	13(6)	13(6)
Li(3)	48(8)	27(7)	10(5)	0	-3(5)	0
			Na_5GaS_4 (**II**)			
Ga(1)	8(1)	11(1)	11(1)	0(1)	0(1)	0(1)
S(1)	15(1)	16(1)	12(1)	-2(1)	-2(1)	-1(1)
S(2)	13(1)	11(1)	17(1)	1(1)	0(1)	0(1)
S(3)	9(1)	18(1)	16(1)	-1(1)	1(1)	-2(1)
S(4)	15(1)	17(1)	12(1)	2(1)	0(1)	2(1)
Na(1)	27(1)	28(1)	19(1)	5(1)	0(1)	-3(1)
Na(2)	14(1)	17(1)	24(1)	1(1)	-2(1)	2(1)
Na(3)	34(1)	18(1)	21(1)	-3(1)	-9(1)	6(1)
Na(4)	26(1)	33(1)	18(1)	-9(1)	-5(1)	8(1)
Na(5)	13(1)	29(1)	22(1)	-8(1)	-3(1)	5(1)

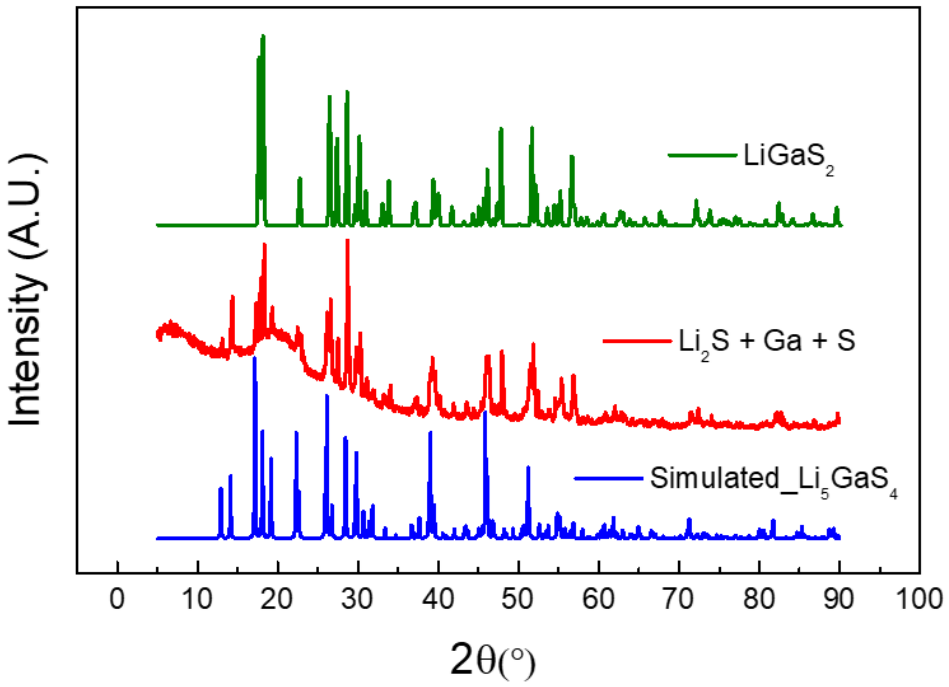

Figure S1. PXRD comparison of product from sealed tube reaction with simulated pattern of Li_5GaS_4 and the simulated pattern of the secondary phase $LiGaS_2$.

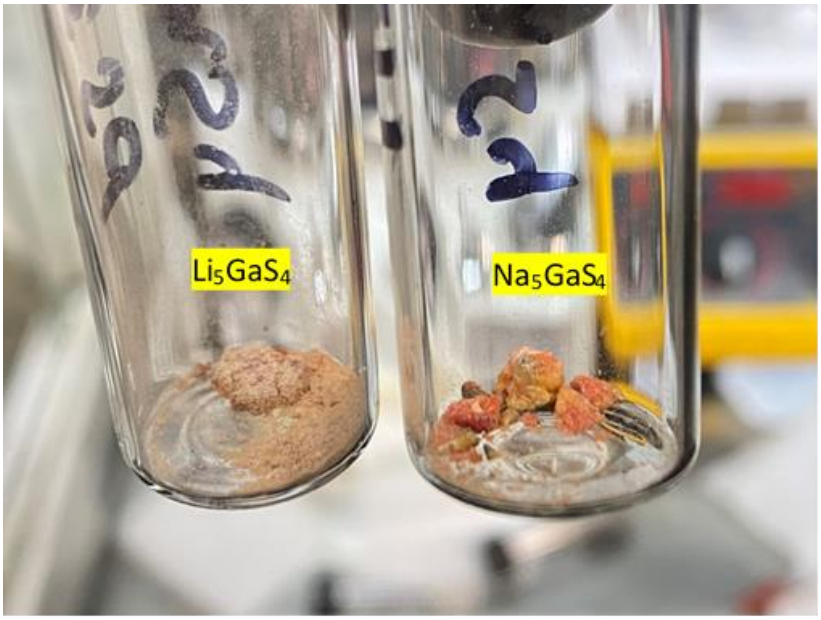

Figure S2. As synthesized crystals of compound I, Li_5GaS_4 and compound II, Na_5GaS_4

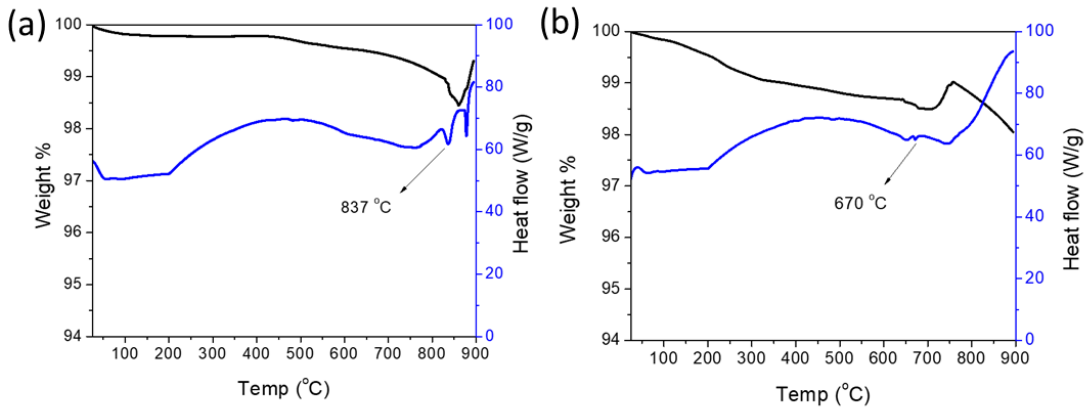

Figure S3. TGA and DSC plots of (a) compound I, Li_5GaS_4 and (b) compound II, Na_5GaS_4.

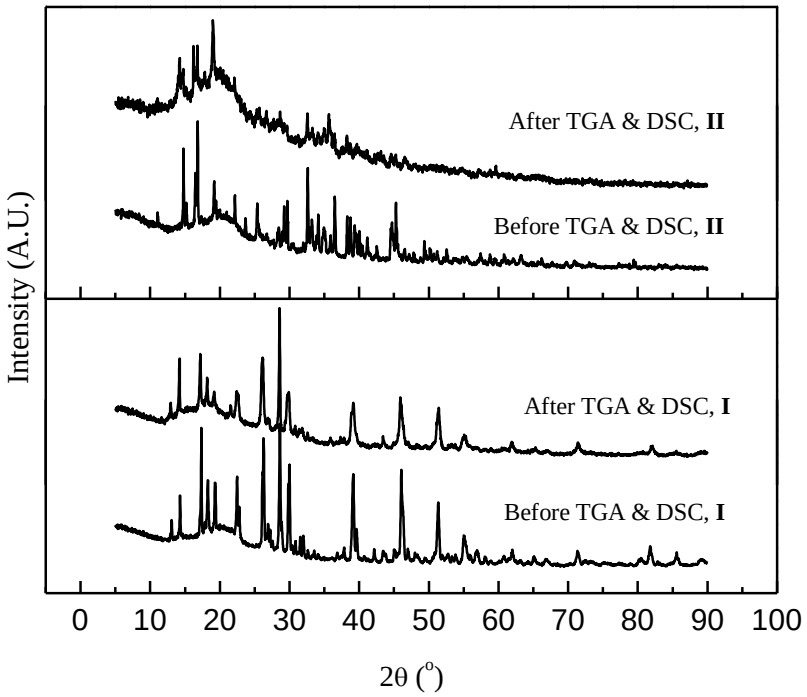

Figure S4. PXRD comparison of before and after TGA & DSC

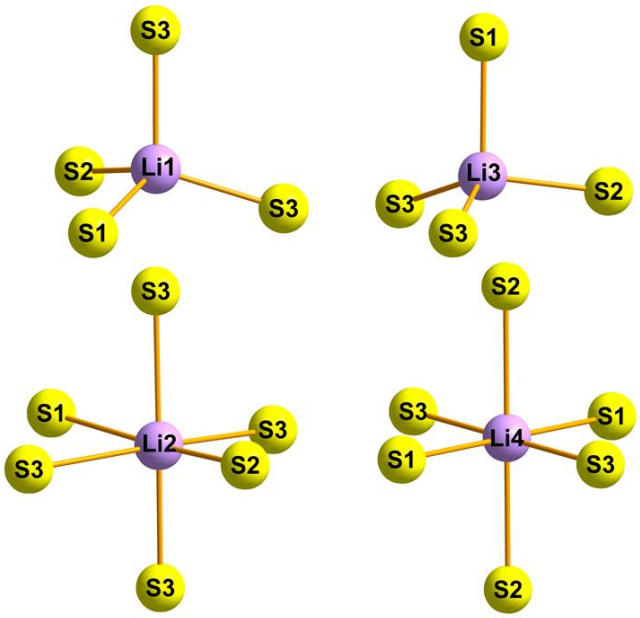

Figure S5. Coordination environment of Li atoms in Li_5GaS_4 (I).

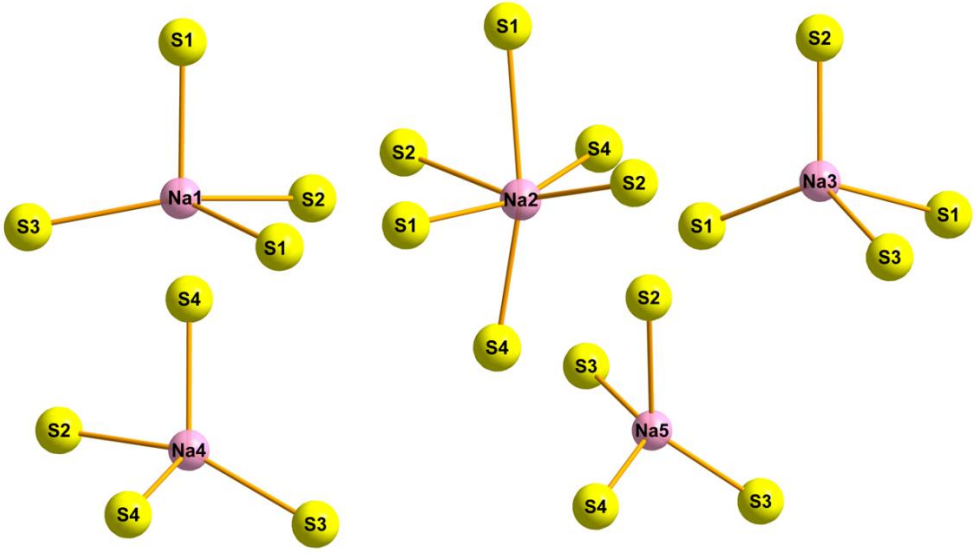

Figure S6. Coordination environment of Na atoms in Na_5GaS_4 (II).

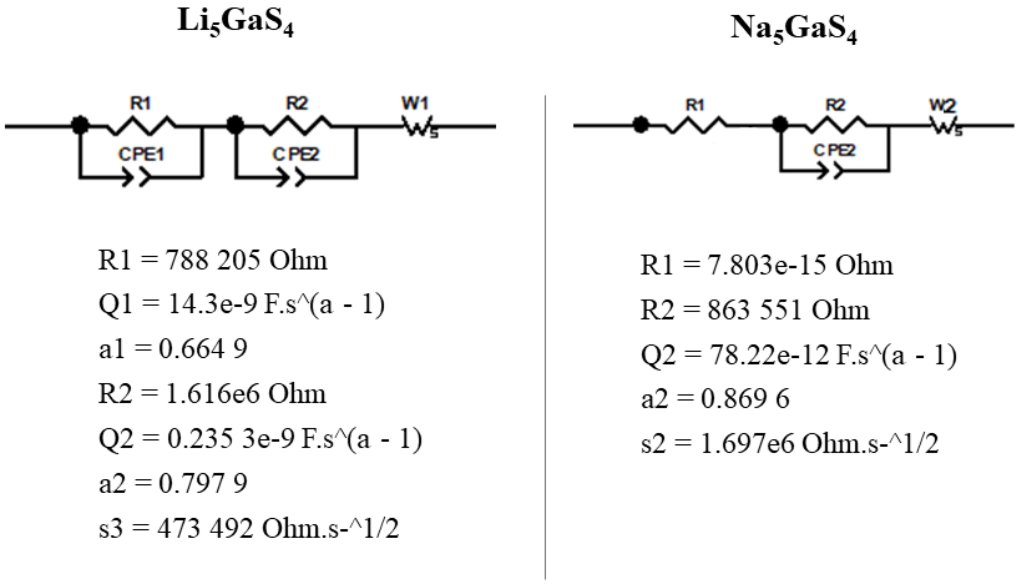

Figure S7. Equivalent circuit and the parameters used to fit the impedance data for Li_5GaS_4 (I) and Na_5GaS_4 (II).

NOTES AND REFERENCES

1. W. S. Sheldrick and M. Wachhold, *Coord. Chem. Rev.*, 1998, **176**, 211–322.

2. S. Dehnen and M. Melullis, *Coord. Chem. Rev.*, 2007, **251**, 1259–1280.

3. J. A. Brant, D. M. Massi, N. A. W. Holzwarth, J. H. Macneil, A. P. Douvalis, T. Bakas, S. W. Martin, M. D. Gross and J. A. Aitken, *Chem. Mater.*, 2015, **27**, 189–196.

4. A. Adhikary, H. Yaghoobnejad Asl, P. Sandineni, S. Balijapelly, S. Mohapatra, S. Khatua, S. Konar, N. Gerasimchuk, A. V. Chernatynskiy and A. Choudhury, *Chem. Mater.*, 2020, **32**, 5589–5603.

5. F. Alahmari, B. Davaasuren, A. H. Emwas and A. Rothenberger, *Inorg. Chem.*, 2018, **57**, 3713–3719.

6. L. Isaenko, A. Yelisseyev, S. Lobanov, A. Titov, V. Petrov, J.-J. Zondy, P. Krinitsin, A. Merkulov, V. Vedenyapin and J. Smirnova, *Cryst. Res. Technol.*, 2003, **38**, 379–387.

7. S. Huber, C. Preitschaft, R. Weihrich and A. Pfitzner, Z. Anorg. Allg. Chem., 2012, **638**, 2542–2548.

8. T. Kaib, P. Bron, S. Haddadpour, L. Mayrhofer, L. Pastewka, T. T. Jä Rvi, M. Moseler, B. Roling and S. Dehnen, Chem. Mater., 2013, 25, 2961 —2969.

9. Z. Zhang, Y. Shao, B. Lotsch, Y. S. Hu, H. Li, J. Janek, L. F. Nazar, C. W. Nan, J. Maier, M. Armand and L. Chen, *Energy Environ. Sci.*, 2018, **11**, 1945–1976.

10. M. Murayama, R. Kanno, M. Irie, S. Ito, T. Hata, N. Sonoyama and Y. Kawamoto, *J. Solid State Chem.*, 2002, **168**, 140–148.

11. R. Kanno and M. Murayama, *J. Electrochem. Soc.*, 2001, **148**, A742.

12. N. Kamaya, K. Homma, Y. Yamakawa, M. Hirayama, R. Kanno, M. Yonemura, T. Kamiyama, Y. Kato, S. Hama, K. Kawamoto and A. Mitsui, *Nat. Mater.*, 2011, **10**, 682–686.

13. A. Hayashi, K. Noi, N. Tanibata, M. Nagao and M. Tatsumisago, *J. Power Sources*, 2014, **258**, 420–423.

14. H. Wang, Y. Chen, Z. D. Hood, G. Sahu, A. S. Pandian, J. K. Keum, K. An and C. Liang, *Angew. Chemie Int. Ed.*, 2016, **55**, 8551–8555.

15. W. D. Richards, T. Tsujimura, L. J. Miara, Y. Wang, J. C. Kim, S. P. Ong, I. Uechi, N. Suzuki and G. Ceder, *Nat. Commun.*, 2016, **7**, 1–8.

16. Z. Zhang, E. Ramos, F. Lalère, A. Assoud, K. Kaup, P. Hartman and L. F. Nazar, *Energy Environ. Sci.*, 2018, **11**, 87–93.

17. K. B. Hueso, M. Armand and T. Rojo, *Energy Environ. Sci.*, 2013, **6**, 734–749.

18. A. Sakuda, A. Hayashi and M. Tatsumisago, *Sci. Rep.*, 2013, **3**, 1–5.

19. S. Boulineau, M. Courty, J. M. Tarascon and V. Viallet, *Solid State Ionics*, 2012, **221**, 1–5.

20. B. Eisenmann and A. Hofmann, *Z. Kristallogr. NCS.*, 1991, **197**, 147–148.

21. K. O. Klepp, *Z. Naturforsch.*, 1992, **47b**, 937

22. R. Kanno, T. Hata, Y. Kawamoto and M. Irie, *Solid State Ionics*, 2000, **130**, 97–104.

23. B. T. Leube, K. K. Inglis, E. J. Carrington, P. M. Sharp, J. F. Shin, A. R. Neale, T. D. Manning, M. J. Pitcher, L. J. Hardwick, M. S. Dyer, F. Blanc, J. B. Claridge and M. J. Rosseinsky, *Chem. Mater.*, 2018, **30**, 7183–7200.

24. Bruker- SMART. Bruker AXS Inc., Madison, Wisconsin, USA. 2002.

25. Bruker-SAINT and SADABS, and SHELXTL. Bruker AXS Inc., Madison, Wisconsin, USA, 2008

26. G. M. Sheldrick, Acta Crystallogr. Sect. A Found. *Crystallogr.*, 2008, **64**, 112–122.

27. C. B. Hübschle, G. M. Sheldrick and B. Dittrich, *J. Appl. Crystallogr.*, 2011, **44**, 1281–1284.

28. P. Kubelka and F. Z. Munk, *Tech. Phys.*, 1931, **12**, 593–601.

29. G. Kresse and J. Hafner, *Phys. Rev. B*, 1993, **47**, 558–561.

30. G. Kresse and J. Furthmüller, *Comput. Mater. Sci.*, 1996, **6**, 15–50.

31. G. Kresse and J. Furthmüller, *Phys. Rev. B - Condens. Matter Mater. Phys.*, 1996, **54**, 11169–11186.

32. D. Joubert, *Phys. Rev. B - Condens. Matter Mater. Phys.*, 1999, **59**, 1758–1775.

33. J. P. Perdew, A. Ruzsinszky, G. I. Csonka, O. A. Vydrov, G. E. Scuseria, L. A. Constantin, X. Zhou and K. Burke, *Phys. Rev. Lett*., 2008, **100**, 136406.

34. H. J. Monkhorst and J. D. Pack, *Phys. Rev. B*, 1976, **13**, 5188–5192.

35. B. Eisenmann and A. Hofmann, *Z. Kristallogr. NCS*., 1991, **197**, 169–170.

36. H. Lim, S. C. Kim, J. Kim, Y. Il Kim and S. J. Kim, *J. Solid State Chem*., 2018, **257**, 19–25.

37. G. Brachtel and R. Hoppe, *Z. Anorg. Allg. Chem*., 1978, **446**, 77–86.

38. S. Harm, A.-K. Hatz, C. Schneider, C. Hoefer, C. Hoch and B. V. Lotsch, *Front. Chem*., 2020, **8**, 90.

39. J. H. Macneil, D. M. Massi, J. H. Zhang, K. A. Rosmus, C. D. Brunetta, T. A. Gentile and J. A. Aitken, *J. Alloys Compd*., 2014, **586**, 736–744.

40. B. Eisenmann and A. Hofmann, *Z. Kristallogr. NCS*., 1991, **197**, 163–164.

41. M. Langenmaier, S. Wissinger and C. Röhr, Z. *Anorg. Allg. Chem.*, 2020, **646**, 1545–1554.

42. A. V. Krukau, O. A. Vydrov, A. F. Izmaylov and G. E. Scuseria, *J. Chem. Phys*., 2006, **125**, 224106.

43. X. He, Y. Zhu and Y. Mo, *Nat. Commun*., 2017, **8**, 1–7.

44. K. Momma and F. Izumi, *J. Appl. Crystallogr*., 2011, **44**, 1272–1276.

III. HIGH SODIUM-ION CONDUCTIVITY IN INTERLOCKED QUATERNARY CHALCOGENIDES BUILT WITH SUPERTETRAHEDRAL BUILDING UNITS

Srikanth Balijapelly,[a] Qi Zhang,[b] Prashanth Sandineni,[a] Amit Adhikary,[a] Sudip Mohapatra,[a] Santhoshkumar Sundaramoorthy,[a] Nikolay Gerasimchuck,[c] Aleksandr V. Chernatynskiy,[b,] Amitava Choudhury [a,] **

[a]*Department of Chemistry, Missouri University of Science and Technology, Rolla, MO 65409, USA*

[b]*Department of Physics, Missouri University of Science and Technology, Rolla, MO 65409, USA*

[c]*Department of Chemistry, Missouri State University, Springfield, MO 65897, USA*

ABSTRACT

Herein we report the syntheses, structure, Na-ion conductivity and theoretical investigation of two moisture stable quaternary compounds, Na_3ZnGaQ_4 (Q = S, Se). These compounds are synthesized using high temperature solid state synthesis routes employing polychalcogenide flux or by metathesis reactions. The crystal structure of these compounds is built up of three-dimensional (3-D) network of corner-shared supertetrahedral (T2) units, where two such 3-D networks are interlocked. The *d*-block metal and the main group metal, Ga, occupy same crystallographic site with 1:1 ratio making it a rare form of building unit. Band structure calculations show that both the compounds are wide band gap semiconductors with band gaps of 2.25 and 1.61 eV, respectively, for Na_3ZnGaS_4(I) and $Na_3ZnGaSe_4$(II**)**, which are slightly underestimated compared to experimentally determined band gaps of 3.0 and 1.90 eV, respectively. I and II possess ionic conductivity of 3.74×10^{-4} and 0.12 mS/cm with activation energies of 0.42 and 0.38 eV, respectively,

at 30 °C. Interestingly, I shows significantly high ionic conductivity of 0.13 mS/cm at 30 °C upon exposure to air which could be due to water adsorption on the surface or occlusion in the grain boundaries. Assuming the vacancy assisted diffusion mechanism for ionic conductance, this difference is consistent with the difference on vacancy formation energies in these compounds, as predicted by DFT calculations. The bond valence sum map indicates that in both structures, the lowest energy diffusion path is one dimensional and it is along *c*-axis of the unit cell.

1. INTRODUCTION

Multinary chalcogenides are one of the most diverse class of compounds currently being explored in many cutting edge research.[1] Among the various applications chalcogenides are extensively investigated as solid electrolytes and as cathode materials for lithium and sodium ion batteries.[2-4] Sodium ion batteries are considered to be the best alternative energy storage technologies for next generation energy storage systems due to its low cost, more abundance, and equal distribution throughout the world.[5] Therefore, current research is focused on finding a high voltage-high capacity cathodes and a highly conducting sodium-ion conductor as solid electrolyte for all-solid-state batteries. Solid state batteries have advantages over liquid electrolyte batteries in terms of safety, high energy density, ease of fabrication and a large window of operating voltages.[6,7] A lot of progress has been made in the discovery of solid sodium-ion electrolytes.[8] In this regard chalcogenide based solid electrolytes have attracted much attention because of their high ionic conductivity and low activation barriers[3, 7, 9] compared to classical oxide based solid

electrolytes such as Na beta-alumina and NASICON type structures which require high sintering temperatures to achieve the high conductivity.[10,11]

After the report of high ionic conductivity in Na_3PS_4 by Hayashi *et al*.,[12] other chalcogenide-based solid electrolytes such as selenophosphates, thioantimonates and selenoantimonates with high ionic conductivity (> 0.1 mS/cm) were reported.[13-16] Ceder group reported a high ionic conductivity of 0.4 mS/cm in a quaternary chalcogenide compound, $Na_{10}SnP_2S_{12}$, which was computationally designed and synthesized.[17] Nazar *et al.* later reported another superionic conductor $Na_{11}Sn_2PS_{12}$ which showed an ionic conductivity of 3.7 mS/cm.[18] This high ionic conductivity was due to partial occupancy of Na sites in the structure which facilitates Na migration in three dimensions. More recently, highest ionic conductivity of 32 mS/cm with good moisture stability has been achieved in Na_3SbS_4 by doping W at Sb sites, $Na_{2.88}Sb_{0.88}W_{0.12}S_4$.[15] Na vacancies, existence of defects and short diffusion pathways with low energy barriers in the lattice play very important role in the migration of ions through the lattice.

One of the advantages of chalcogenide-based solid electrolytes is that a cold pressing results in very low grain boundary resistances because of the lower elastic moduli of the chalcogenide lattices.[3, 16, 19] This also facilitates good contact with the electrodes due to the soft and deformable nature of the S/Se anions.[16,19, 20] Note that most of these chalcogenide-based sodium solid electrolytes also suffer from poor moisture stability.[21] According to Pearson HSAB theory, hard acids preferentially reacts with hard bases and soft acid preferentially reacts with soft bases.[22] Generally thiophosphate based solid electrolytes are moisture sensitive because the hard base O-donor preferentially reacts with hard acid P^{5+}. Taking advantage of HSAB theory, relatively softer ions compared to P^{+5}

and Sb^{+5}, for example, Ga^{3+} and Zn^{2+} can be chosen to build a moisture stable framework by connecting GaS_4 and ZnS_4 polyhedra. This hypothesis lead us to consider our recently reported Na_3MGaS_4 (M = Mn, Fe, and Co) structure-type built with super tetrahedral T2 (adamantane type) units which has large tunnel filled with Na-ions.[23] Our investigation in the Ga-chalcogenide system also resulted in several new ternary thiogallates in both Li and Na systems.[24,25] Therefore, we extended Na_3MgaS_4 structure type to Zn and into selenide analogues to create moisture stable quaternary compounds, Na_3MgaQ_4 (Q = S/Se, M = Zn). Herein, we report their synthesis, structure, and Na-ion conductivity of two Zn analogues. First principle calculations were employed to calculate the band structure and vacancy formation energies for compounds I and II. Additionally, the compounds were also characterized by diffuse reflectance spectroscopy and thermal analysis.

2. EXPERIMENTAL SECTION

2.1. SYNTHESIS OF COMPOUNDS, Na_3ZnGaS_4 (I) AND $Na_3ZnGaSe_4$ (II)

Compound I was prepared by heating a stoichiometric combination of reactants, 1.5 mmol of Na_2S, 1 mmol of Zn powder, 1 mmol of Ga, and 2.5 mmol of S in a sealed quartz tube. Similarly, for compound II, 1 mmol of Zn, 1 mmol of Ga, 2.5 mmol of Se and 3 mmol of Na_2Se_2 were heated in sealed quartz ampoule. Compound I was also synthesized via a metathesis route by reaction between Na_5GaS_4 and $ZnCl_2$ ($Na_5GaS_4 + ZnCl_2 \rightarrow Na_3ZnGaS_4 + 2NaCl$) with a yield of 90-95%. Na_5GaS_4 was prepared by our own reported method[25] and Na_2Se_2, which acted as a flux was prepared by combining the elements in liquid ammonia[26] and all the remaining reactants used in the syntheses were purchased

from Alfa Aesar. All the precursors including powdered elements (Ga shavings) and alkali chalcogenides were weighed accordingly and loaded into carbon coated quartz ampoules inside an argon filled glove box. The ampoules were then taken out of glove-box with the help of adaptors to prevent exposure to air and flame-sealed under vacuum. The sealed ampoules were placed in temperature-controlled furnace and the temperature was ramped up at a rate of 20 °C/h to 750 °C and dwelled for 120 h before cooling down to room temperature at a rate of 35 °C/h. Pale brown, shiny orange-red crystals of compounds I and II, respectively, were recovered after breaking the ampoules in air followed by washing with N, N dimethylformamide (DMF) to remove the excess flux. In all cases crystals were found to be air and moisture stable.

SEM images taken with Hitachi TM1000 Tabletop Scanning Electron Microscope on as-synthesized Na_3ZnGaS_4 crystals from both solid state and metathesis route. Though the average sizes of the crystallites are different, 15-20 μm for solid-state product and 8-10 μm for the metathesis product, the dodecahedron shape of the crystals is consistent in products from both synthetic routes (Figure S1). Appropriate crystals from the DMF-washed products were used for single-crystal X-ray diffraction and well-ground powder samples were used for other characterizations.

2.2. X-RAY CRYSTALLOGRAPHY

Good quality crystals were chosen for single crystal X-Ray diffraction on Bruker smart apex equipped with a sealed tube X-ray source with Mo–Kα radiation (λ = 0.71073 Å). Room temperature or –33 °C diffraction data sets were collected using SMART[27] software with a step of 0.3° in ω scan and 20 s/frame exposure time. Programs SAINT[28]

and SADABS[28] were used for the data integration and absorption correction, respectively. SHELXS-97 and difference Fourier syntheses were used to solve the structures.[29] Full-matrix least-squares refinement against $|F^2|$ was carried out using the SHELXTL-PLUS suite of programs.[28] All the compounds crystallize in $I4_1/acd$ space group (No. 142) with two sodium, three chalcogen (S or Se), and one gallium atom present in the asymmetric unit, which can be easily located from the difference Fourier map. However, in the absence of any remaining unaccounted-for e-density, the weighted *R* factor wR_2 did not converge to a low value though the isotropic thermal parameters were reasonably good. Similar situation was encountered while solving isostructural compounds involving transition metals (Na_3MgaS_4, *M* = Mn, Fe, and Co) for which a Ga/*M* mixed occupancy was found.[23] By similar analogy Ga and Zn occupancies were refined freely, yielding 50 % occupancy for both Ga and Zn and the weighted *R* factor (wR_2) reduced significantly. Based on the occupancies, a charge balanced formula was attained with a composition of Na_3ZnGaQ_4 (*Q* = S/Se). Final refinements including the refinements of anisotropic thermal parameters were performed using SHELX-2014/2018 embedded in ShelXLe.[30] Crystal data and final refinement parameters are given in Table 1 and selected bond lengths are given in Table 2 for compounds, I, and II. Atomic coordinates along with their isotropic thermal parameters are given in SI (Tables S1 and S2).

2.3. POWDER X-RAY DIFFRACTION

The laboratory powder X-ray diffraction (PXRD) pattern was obtained from a PANalytical X'Pert Pro diffractometer equipped with a Cu Kα anode and a linear array PIXcel detector over a 2θ range of 5 to 90° with an average scanning rate of 0.0472° s^{-1}.

Hand ground samples were loaded into an air-tight cell with the Kapton film to collect the PXRD pattern (Figure 1). PXRD of the metathesis-route reaction product of I is provided in SI (Figure S2). To evaluate the air sensitivity of the samples, finely ground (in air) samples were left outside for few days. The PXRD patterns of the air-exposed samples did not show any change for I up to seven days and some line broadening for II after one day (Figure S3). Comparison of SEM images of the as-synthesized product of II after minimum exposure (few minutes for sample preparation) and two days of exposure clearly show signs of reaction with moisture/oxygen on the surface of the crystal as evident by the appearance of ridges and cracks. On the other hand, the crystal surfaces of I appeared same after five days of air exposure (Figure S4). Prolonged exposure (more than two days) of II in air turns the color of the sample red and decomposition to Se, Na_2SeO_3 and Na_2O became evident in the PXRD taken after five days (Figure S5).

2.4. OPTICAL BAND GAP MEASUREMENTS

Optical band gap measurements were performed on compounds I and II on a Varian Cary 5000 UV-Vis-NIR spectrophotometer equipped with a praying mantis set up. $BaSO_4$ powder (Fisher, 99.2%) was used as a ~100 % reflectance standard and the Kubelka-Munk function[31] was employed to transform the reflectance into absorption data to find out the band gap.

2.5. THERMAL ANALYSIS

Powder samples of compounds I and II were used to collect simultaneous TGA-DSC data on TA Instruments Q600 SDT from room temperature to 1000 °C with a scan

rate of 10 °C min^{-1} under argon atmosphere. The DSC and TGA plots are provided in the SI (Figure S6). Compounds I and II possess high thermal stabilities and melts at 846 and 741.5 °C, respectively.

Table 1. Crystal data and refinement details of I and II.

	I	**II**
Empirical formula	Na_3ZnGaS_4	$Na_3ZnGaSe_4$
Formula weight	332.3	519.9
Temperature	293(2) K	240(2) K
Wavelength	0.71073 Å	0.71073 Å
Crystal system	Tetragonal	Tetragonal
Space group	$I4_1/acd$	$I4_1/acd$
Unit cell dimensions	a = 12.925(2) Å	a = 13.43(3) Å
	b = 12.925(2) Å	b = 13.43(3) Å
	c = 18.623(3) Å	c = 19.15(5) Å
Volume	3111.0(12) Å3	3453(18) Å3
Z	16	16
Density (calculated)	2.838 Mgm^{-3}	4.000 Mgm^{-3}
Absorption coefficient	7.682 mm^{-1}	22.817 mm^{-1}
Goodness-of-fit on F2	1.091	1.057
R [$I > 2\sigma(I)$]	R1 = 0.0243	R1 = 0.0229
wR ($F2$) (all data)	wR2 = 0.0612	wR2 = 0.0545

[a] $R_1 = \sum||F_o| - |F_c|/\sum|F_o|$.
[b] $wR_2 = \{\sum[w(F_o^2 - F_c^2)^2]/\sum[w(F_0^2)^2]\}^{1/2}$, $w = 1/[\sigma^2(F_o)^2 + (aP)^2 + bP]$, where $P = [F_o^2 + 2F_c^2]/3$

Table 2. Selected bond lengths (Å) of compounds I and II.

	I	**II**
Ga1/Zn1 – *Q*1	2.284(4)	2.385(5)
Ga1/Zn1 – *Q*1$^{\#1}$	2.301(4)	2.405(4)
Ga1/Zn1 – *Q*2	2.314(4)	2.424(5)
Ga1/Zn1 – *Q*3	2.358(4)	2.458(4)

#1 -y+3/4, x-1/4, -z+1/4

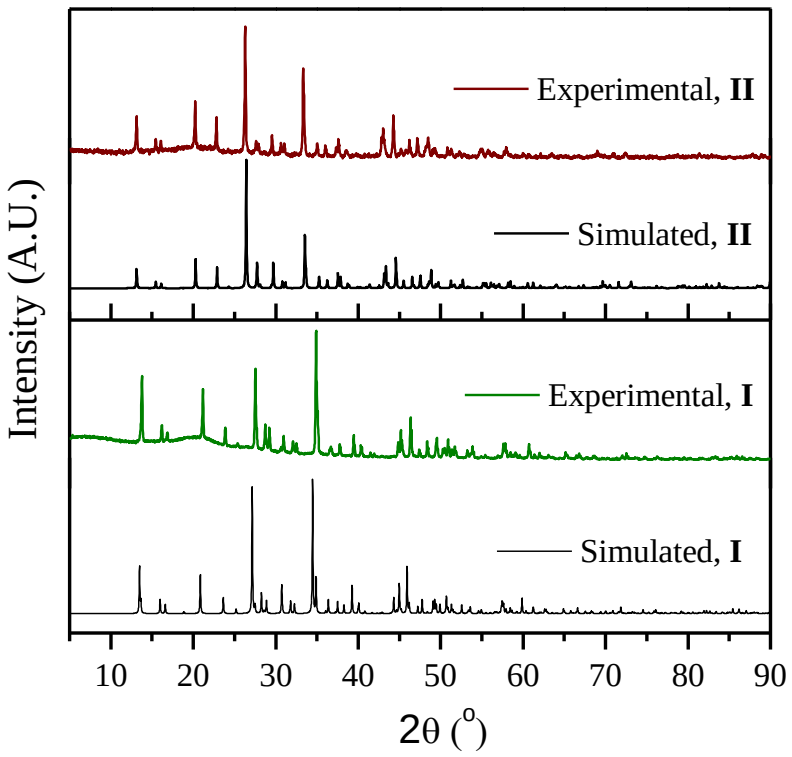

Figure 1. Comparison of simulated and experimental powder X-ray diffraction patterns for compounds, Na_3ZnGaS_4, I and $Na_3ZnGaSe_4$, II.

2.6. IMPEDANCE MEASUREMENTS

AC Impedance measurements were performed from 1Hz to 1MHz using Ivumstat Impedance Analyzer with an AC signal amplitude of 50 mV. The hand ground samples were cold pressed applying a force of 280 MPa in a stainless steel pressing die inside an argon filled glove box (O_2< 0.1 ppm). Indium foil for compound I and silver powder for compound II were used as the blocking electrodes. The pellets were placed in an airtight Swagelok type cell and heated in a temperature controlled furnace to measure the temperature dependence of the ionic conductivity. The impedance data were collected for every 10 °C increment by keeping the temperature of each measurement constant for at least an hour to reach the thermal equilibrium. No reactions were observed between the electrolyte pellet and the blocking electrode after the measurements.

2.7. THEORETICAL CALCULATIONS

We carried out band structure calculations using density functional theory as implemented in Vienna Ab-initio computational Package (VASP).[32-35] Core electrons were treated by Projector Augmented Wave (PAW)[36-39] approach, with the following states treated as valence states: 4*s* and 4*p* for Ga, 3*s* for Na, 3*d* and 4*s* for Zn, 3*s* and 3*p* for S, 4*s* and 4*p* for Se. Plane wave basis sets were used with a cutoff energy 520eV. For structural relaxation, Brillouin zone integration employed 2×2×2 mesh in the reciprocal space and Gaussian smearing of the electronic states around Fermi energy. For accurate band structure calculation, the tetrahedron method with Blochl corrections was used. The global break condition for the electronic self-consistency loop was set to $2x10^{-4}$.

3. RESULTS AND DISCUSSION

3.1. STRUCTURAL DESCRIPTION

The asymmetric unit of compounds I and II contains two Na atoms, two chalcogenide (S/Se) atoms and a 1:1 mixed occupied Zn/Ga site. Zn/Ga, one chalcogen (*Q1* = S1 or Se1) and one Na (Na2) atoms are located on 32*g* Wyckoff site while two *Q* (*Q*2 and *Q*3) and one Na (Na1) are located in 16*e*, 16*b* and 16*c* sites, respectively. Considering their occupancies, a formula of Na_3ZnGaQ_4 (*Q* = S/Se) (Figure 2a) can be derived with 16 such units present in the unit cell. Selected bond lengths for the compounds are given in Table 2. The detailed structural description can be found in our previous publication and here we will only briefly describe the salient features.[23] Ga/Zn – *Q* tetrahedral units form a super tetrahedral (T2) building units through corner sharing (Figures 2b -2d). These T2 building units are further joined through their vertices and form three dimensional (3-D) anionic network (Figure 3a). Two such identical anionic lattices of Ga/ZnQ_4^{3-} are fused together through interpenetration and create a huge void space which accommodate Na ions to balance the charge of the anionic network (Figure 3b). The Na atoms coordinate with the corner *Q* (S, Se) atoms of the supertetrahedra to form octahedral geometry (Figure S7a). Both Na1 and Na2-centered octahedra are connected to each other through corner-, edge-, and face-sharing to form a complex polyhedral network of Na-ions (Figure S7b). Na – *Q* bond distances are in the range 2.65(8) – 3.27(3) and 2.732(7) – 3.50(5) Å, respectively, for Na – S and Na – Se, which are in good agreement with the isostructural Na_3MGaS_4 (*M* = Mn, Fe, Co) [23] phases for the sulfide compound and

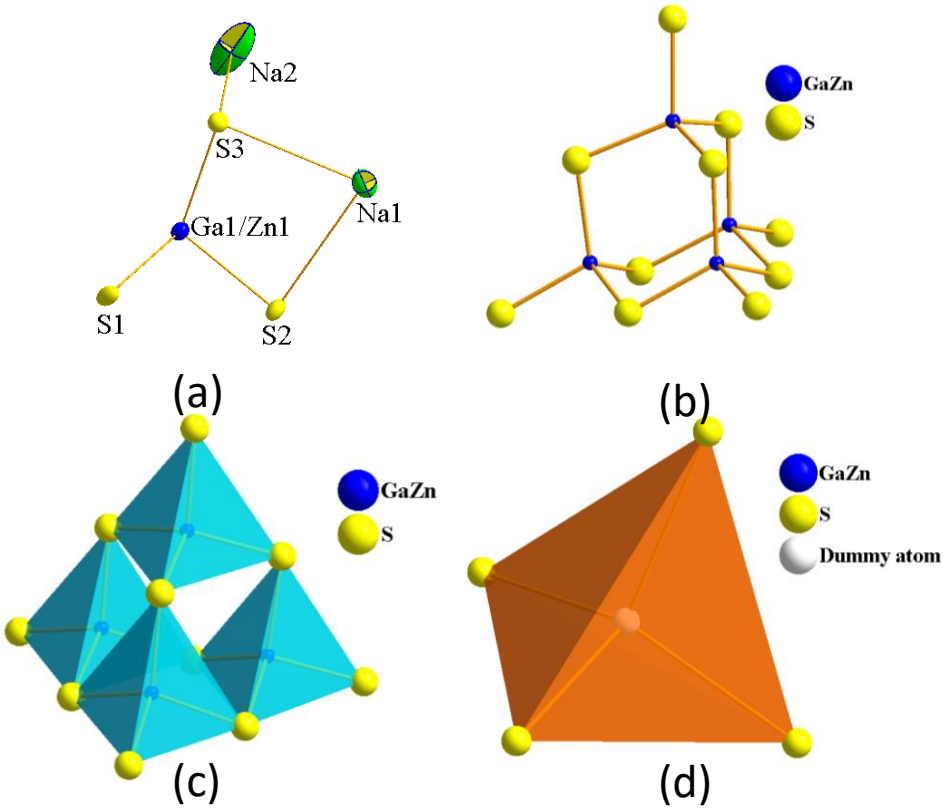

Figure 2. (a) Asymmetric unit of compounds I and II, shown here for compound I at 40 % probability for thermal ellipsoids. (b) Skeleton structure of T2-Supertetrahedral building unit. (c) Polyhedral view of T2 supertetrahedral building unit. (d) Tetrahedra created by connecting corner S atoms of super tetrahedra and a dummy atom at the center of gravity of the T2 supertetrahedral building unit.

$NaLnGa_4Se_8$ (*Ln* = La, Ce, Nd)[40] for selenide, respectively. When each of these individual non-interpenetrating lattices are viewed along [1 1 1] direction, they form six membered ring channels resembling zinc blende lattice but made of supertethedral units. If the centers of the super tetrahedral units are connected to each other, the overall framework structure resembles interpenetrated zinc blende lattice as shown in Figure 4. In our earlier publication on isostructural compounds we have adequately discussed the role of interpenetration in filling large voids.[23] Interpenetrating diamond lattices have been

frequently observed in multinary chalcogenide chemistry specially with Ga and In with various supertetrahedral units ranging from T2 to T5.[41 - 43] Interestingly, besides the current structure type, interpenetration in T2 building unit was not observed, however, non-interpenetrating cubic ZnS structure type with T2 cluster has been reported.[43]

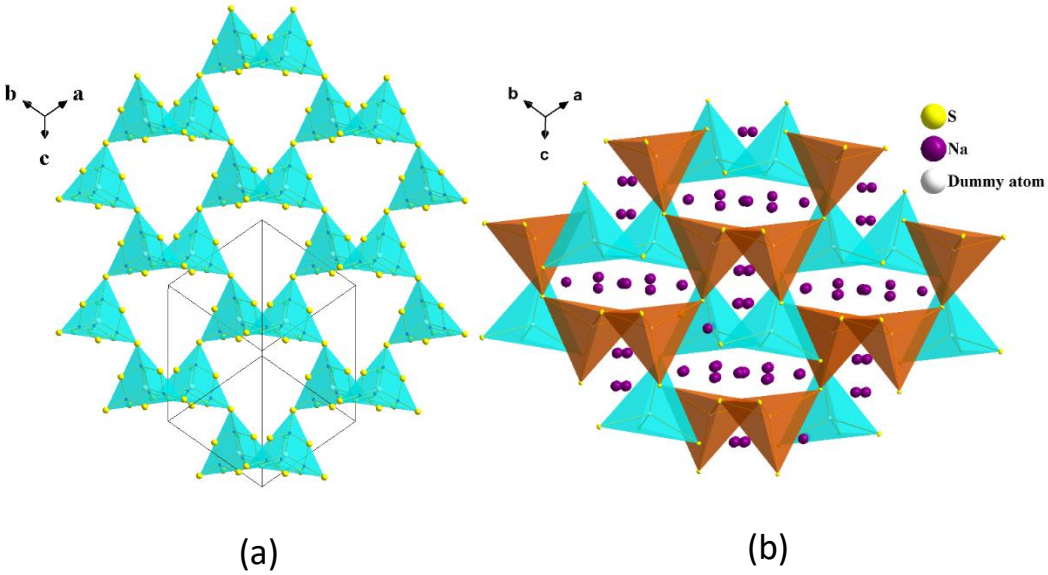

Figure 3. (a) T2 supertrahedral building units connected to each other via corner sharing to form a 3D network. (b) Interpenetrated view of the T2 superterahedral building units creating channels for the Na^+ ions.

Most of these interpenetrating lattices are formed in hydro/solvothermal synthesis and void space was often filled by organoammonium cations or hydrated alkali ions. Negatively charged interpenetrated chalcogenide lattices filled with alkali ions can exhibit fast ionic conductivity through the channel made by soft chalcogen anions.

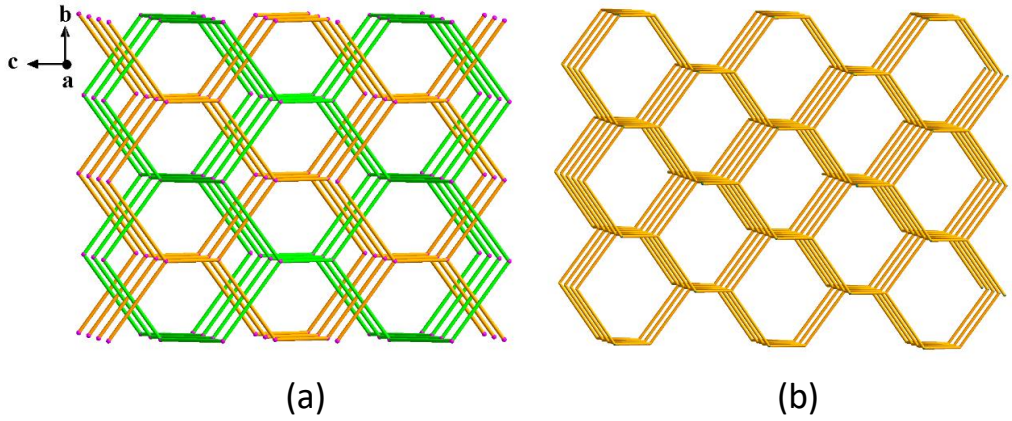

Figure 4. Zinc blende type arrangement of super tetrahedral building units. a) Center of super tetrahedra are connected to each other. Green and yellow color bonds represent interpenetration of two different lattices. Pink balls represent the center of gravity of the super tetrahedra. b) Zinc and S atoms are connected (Zinc blende structure type).

It is to be noted here that we also noticed an article with similar composition of Na_3ZnGaQ_4, however, the authors of the article did not interpret them as interpenetrating.[44] Recently, an isostructural Na_3MnInS_4 has been reported in which In and Mn occupy same site with 50:50 % occupancies.[45]

3.2. DIFFUSE REFLECTANCE SPECTROSCOPY AND BAND STRUCTURE CALCULATION

Diffuse reflectance measurements were performed on compounds I and II from 200 – 2500 nm range. $h\nu$ *vs* $(\alpha h\nu)^2$ plots (Figure 5) show flat linear region parallel to X- axis followed by a steep absorption due the movement of electron from valence to the conduction band, in other words due to the band gap of the material.

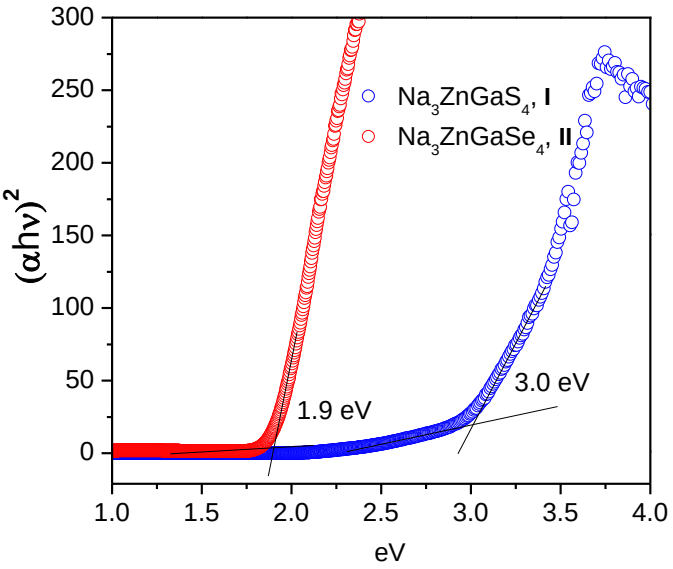

Figure 5. The diffuse reflectance plots for compounds Na_3ZnGaS_4, I and $Na_3ZnGaSe_4$, II.

The band gap is determined by the intersection of the extrapolated flat and steep regions of the plot, which revealed the band gaps of 3.0 and 1.90 eV for the compounds I and II, respectively. Compounds I and II are direct band gap semiconductors with the theoretical band gaps of 2.25 and 1.61 eV, respectively, which are lower than the experimental band gaps in accord with the well-known underestimation the band gaps by the DFT.[46]

The band gap of Se analogue is lower than the sulfide analogue due to the increased covalence of Zn/Ga – *Q* bond from S to Se. We present the projected density of states of both compounds in Figure 6. They clearly show very similar features, with direct band gaps of 2.25 eV and 1.61 eV showing typical underestimation by the DFT. At the same time, simulation correctly reproduces sulfur compound as having a larger band gap.

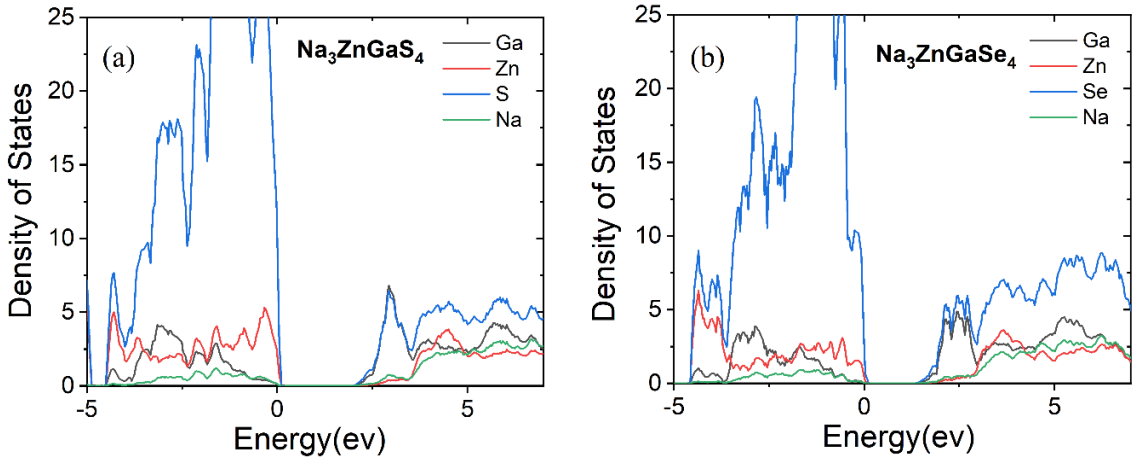

Figure 6. Projected electronic density of states of each element and individual orbital in (a) Na_3ZnGaS_4 (I) and (b) $Na_3ZnGaSe_4$ (II).

In compound I, significant weight of valence band near the top is from the *p*-orbital of sulfur, most of the weight at the bottom of the conduction band comes from *p*-orbitals of sulfur with some admixture of *s*-orbital of gallium. The construction of the valence and conduction bands in the case of Se-analogue (II) is essentially same except that valence band now involves 4*p* orbitals of Se. Larger size of the 4*p* orbitals compared 3*p* and slightly lower electronegativity of Se allows greater overlap and pushes the valence band up and decreases the band gap in the Se-analogue.

3.3. Na-ION CONDUCTIVITY AND AIR STABILITY

AC impedance measurements were performed on the cold pressed pellets with the density close to 90% of the theoretical density. The Nyquist plots of compounds I and II are shown in Figure 7 (a and b). Generally, chalcogenide based ionic conductors show one semicircle because often bulk and grain boundary resistances could not be discerned.

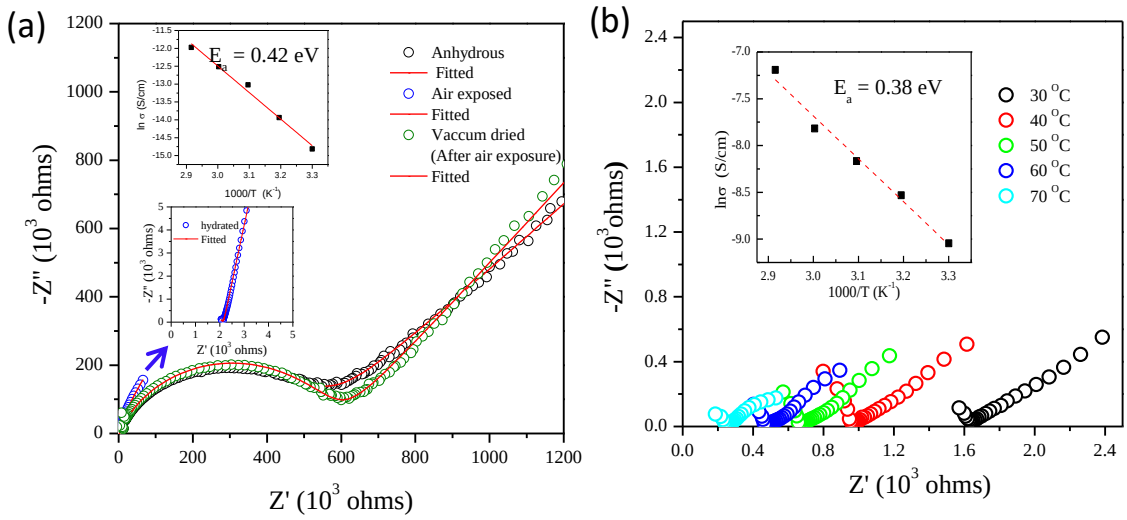

Figure 7. Nyquist plot for room temperature ionic conductivity of (a) Compound I (b) Compound II. Inset shows the activation energy calculated from experimentally measured ionic conductivity verses temperature plot. Dots represents the experimental ionic conductivity and dashed line represents the Arrhenius fit to the data. A second inset in (a) shows the 30 °C impedance of I from the air-exposed sample.

Accordingly, the Nyquist plot at room temperature showed one semicircle and a spike, in which semicircle represents the total resistance, spike represents the building up of the charge at the blocking electrodes indicating that the investigated materials are ionically conducting. The equivalent circuit used, and the fitting parameters are detailed in the SI (Figure S8). The capacitance values of the semicircle fall in the range of 10^{-10} to 10^{-11} F, characteristic of the grain boundary capacitance in chalcogenide based solid electrolytes. As a result, the room temperature ionic conductivities calculated for compounds I and II are 3.74×10^{-4} and 0.12 mS/cm, respectively. In order to calculate the activation energies, the ionic conductivity of compounds I and II were measured as a function of temperature for every 10 °C interval in the range of 30 to 70 °C with the help

of a temperature-controlled furnace. By employing the Arrhenius equation (Eqn. 1) the activation energies calculated for compounds I and II are ~0.42 and 0.38 eV, respectively.

$$\sigma_T = \sigma_o \exp(-Ea/k_B T) \quad (1)$$

Though the ionic conductivity of the compound I is not very impressive, the ionic conductivity of compound II is comparable to many well-known chalcogenide based Na-ion conductors (Table 3). The reason for the higher ionic conductivity of compound II compared to compound I could be due to increased ionic radii, easily polarizable and therefore, much softer nature of selenium atom. In order to evaluate the effect of moisture on ionic conductivity, the impedance data were collected on I upon air exposure. Interestingly, ionic conductivity of air-exposed sample of I jumped manifold and a conductivity value of 0.13 mS/cm at 30 °C was observed. Since there was no structural transformation upon air exposure as evident from the PXRD pattern (Figure S3), drastic change in the ionic conductivity could be due to adsorption of water on the surface or in the grain boundaries. The IR spectrum of the air-exposed sample of I confirmed the presence of H_2O in the sample (Figure S9). To evaluate the reversibility of surface water adsorption, the air exposed sample was vacuum dried at 80 °C for 12 hours to remove the adsorbed water. The PXRD pattern collected on vacuum dried sample indicated retention of crystal structure (Figure S10). The impedance collected on the vacuum dried sample showed almost similar ionic conductivity as the pristine anhydrous phase (never exposed). The increased ionic conductivity upon air/humid air exposure has been found in some Li and Na-ionic conductors and the reason has been attributed to the hydroxylation of oxide-sites or formation of hydroxyl radical.[47, 48] It will require further in-depth studies to ascertain the actual cause of increased conductivity in I due to water adsorption. However,

no such enhancement in the ionic conductivity was observed for II upon air exposure (Figure S11). Instead, one order of magnitude decrease has been observed in ionic conductivity (0.01mS/cm) upon air-exposure which can be attributed to the reaction taking place on the surface, though not apparent in PXRD pattern after one day but on prolonged exposure presence of selenium became evident (Figure S5). Solid electrolyte, in general, should be considered as mixed conductor as they display electronic conductivity though often very low. Electronic conductivities were measured by performing Hebb–Wagner polarization techniques using sodium as the reference electrode and indium foil as the sodium ion-blocking electrode, (–)Na/Na_3ZnGaQ_4/In(+) cell at 30 °C.[49] As the sodium ions were blocked, the resulting steady state current was due to electrons and holes at the irreversible In-Na_3ZnGaQ_4 interface. The electronic conductivities were calculated by linear fitting in the voltage range 2 – 4 V. The resultant steady state electronic current was in the order of 10^{-7}A and the exponential increase in current was not seen up to 4.5 V (Figure S12). As expected, the selenide analogue having smaller band gap showed electronic conductivity of 4.7×10^{-6} mS/cm, which was slightly higher than the sulfide analogue, 4.74×10^{-7} mS/cm at 30 °C. The measured electronic conductivities were three to four orders of magnitude lower than the ionic conductivity values, suggesting that both compounds are predominantly ionic conductors at moderate temperatures.

3.4. BOND VALENCE SUM (BVS) MAP

Bond valence Sum (BVS) difference maps were analyzed using soft BV parameters through Bondstr incorporated in FullProf suite of programs provided by Adams.[50] These maps provide hypothetical diffusion paths that are available for the mobile ion at modest

activation energies. Volume fraction for ion mobility in the unit cell found to be larger for the compound II than for compound I which could also be a reason for the higher ionic conductivity of compound II.

Table 3. Comparison of ionic conductivity of some sulfide and selenide-based sodium superionic conductors.

Solid electrolyte	σ_{RT} (mS/cm)	E_a (eV)
$Na_{11}Sn_2PS_{12}$[18]	1.4	0.25
Na_3PSe_4[57]	1.2	0.21
Na_3SbS_4[a]	1	0.22
Na_3SbSe_4[13]	0.85	0.19
Na_3PS_4[12]	0.46	0.2
$Na_{10}SnP_2S_{12}$[17]	0.4	0.36
$Na_{3.1}Sn_{0.1}P_{0.9}S_4$[b]	0.25	0.18
$Na_{4-x}Sn_{1-x}Sb_xS_4$ (at 30°C)[c]	0.2-0.5	0.39
$Na_{4-x}[Sn_{0.67}M_{0.33}]_{1-x}Sb_xS_4$[d]	0.17	0.31
$Na_3ZnGaSe_4$ (compound **II**)	0.12	0.38
Na_3PS_4 (tetragonal)[e]	0.01	0.36

[a] Wang et al, *Angew. Chemie Int. Ed.* **2016**, *55* (30), 8551–8555; [b] Rao et. al. *J. Mater. Chem. A* **2017**, *5*, 3377– 3388, [c] Heo, et al. *Adv. Energy Mater*. **2018**, *8*, 1702716; [d] Jia et al. *J. Energy Chem.* **2020**, *48*, 102-106; [e] Huang et al. *Phys. Chem. Chem. Phys.* **2018**, *20*, 20525– 20533.

The plots of iso-surfaces using VESTA[51] at an energy level $|\Delta V| = 0.5\ v.u$ are given in Figure S13. No suitable diffusion path was found for compound I based on the bond valence sum calculations, however, for compound II, a clear diffusion path exists along the *c*-axis, and diffusion along *b*-axis could also be achieved at slightly higher

activation barrier (Figure 8). Interestingly, between two crystallographically different Na ions only Na2 (32*g* Wyckoff site) was found to be more mobile than Na1 (16*f* Wyckoff site). Na1 forms polyhedral connectivity with sharing edges and corners (Figure 8e). However, BVS maps could not show diffusion along this connectivity. Na2, on the other hand, forms two distinct polyhedral connectivities designated as A and B along *b*-axis (Figure 8 a and b). The BVS mapping shows that the Na2 can percolate through these polyhedral networks (Figure 8 c and d). Polyhedral networks A and B are further connected through the sharing of common edges (Figure 8a) which allow the diffusion along *c*-axis. Note that among several modes of connections between the Na polyhedra, face shared and edge shared connections show feasible diffusion paths whereas diffusion path could not be discerned along the corner shared polyhedral units.

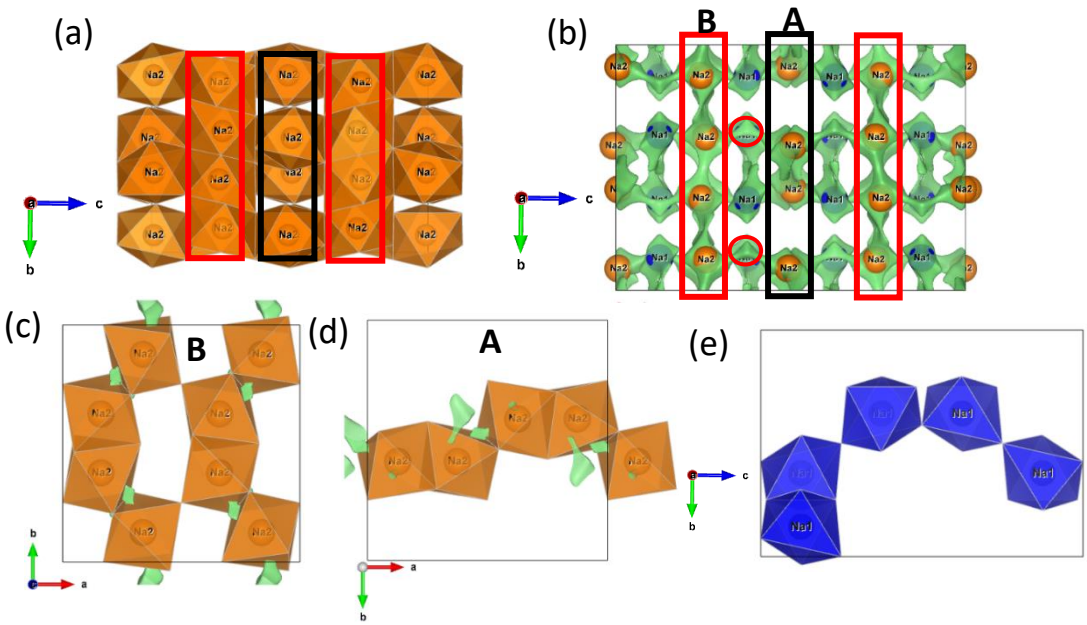

Figure 8. Na ion polyhedral network (a) Na2 polyhedral connectivity forming two distinct connectivity designated as A and B; (b) BVS maps showing the Na2 percolation along channels A and B (c) BVS map showing Na2 hopping through channel path B (c) BVS map showing Na2 hopping through path A (e) Na1 polyhedral

3.5. VACANCY FORMATION ENERGY BY DFT

The simplest ionic diffusion mechanism is a defect-assisted migration either by vacancy[52] or interstitials,[53] with the former being more common. We thus assume vacancy

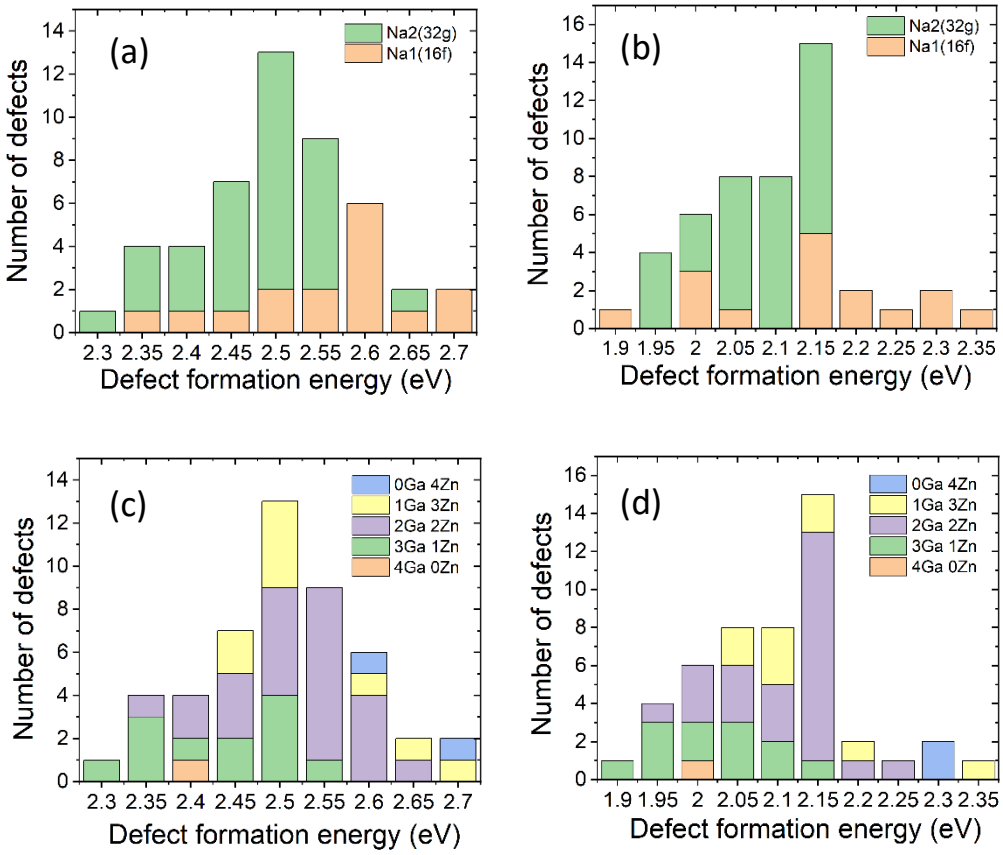

Figure 9. Defect formation energy with respect to different sodium type (a) compound I (b) compound II, Different Zn and Ga next-neighbors (c) compound I (d) compound II.

assisted migration in this work. Elucidating the diffusion pathways then requires the calculation of the transition state along the possible defect migrations paths. There are two crystallographically inequivalent sodium atoms in the structure, Na1(16*f*) and Na2(32*g*),

however, due to the random distribution of the Ga and Zn atoms in the second coordination sphere of sodium atoms each has distinct chemical environment, local structure, and vacancy formation energy. This in turn leads to a large number of the distinct diffusion pathways. Determination of the rate limiting transition in this situation is not possible. *Ab initio* simulation could in principle provide additional insight through the molecular dynamics simulations,[54] however, such investigations are computationally costly for the system of interest.

Despite this difficulty, DFT calculations can be used to provide some insight into the observed differences in the ionic conductivity. Here, we considered a particular realization of the Ga/Zn random distribution in the primitive cell in the compounds I and II and carried out the calculation of the vacancy formation energies for all 48 sodium atoms in the structure (Figure S14). The volume of the primitive cell was kept constant while relaxing the atomic configuration, thus we consider the limit of the small concentrations of vacancies. Only the neutral vacancies were considered here. The defect formations energies ΔE were calculated using the formula:

$$\Delta E = E_{vac} + E_{Na} - E_{ideal} \quad (2)$$

where E_{vac} is the energy of the structure with the sodium vacancy, E_{ideal} is the energy of the ideal structure and E_{Na} is the energy of the sodium atom in the bulk BCC structure. Figure 9 presents the resultant distribution of the defect energies in compounds **I** (Figure 9a) and II (Figure 9b). These figures show the number of the sodium sites that have the vacancy formation energy in the given energy interval. The average defect formation energy is 2.5 and 2.1 eV, with the standard deviation of 0.09 and 0.1eV for compounds I

and II, respectively. One observes that distribution for the Na1 sites is skewed to the higher energies in comparison with the Na2 sites for both compounds, i.e. on average, the sodium atom in the Wycoff position 16*f* has slightly higher vacancy formation energy than those in 32g. This is consistent with the experimental finding that 32*g* site (U_{11} = 45(1), U_{22} = 82(2), and U_{33} = 142(2) Å^2 X 10^3 for I) display higher thermal parameters than 16*f* (U_{11} = 42(1), U_{22} = 42(1), and U_{33} = 28(1) Å^2 X 10^3 for I) in both sulfide and selenide analogues (very similar values for II, see Table S2). Further, the vacancy formation energy correlates with the increase in the number of the Ga next neighbors for a given Na site: the larger the number of the Ga atoms, the lower the vacancy formation energy (See Figures 9c and 9d). The average value of the defect formation energy indicates a very small concentration of the intrinsic defects at normal conditions. Nevertheless, in selenide-analogue (II) we predict the lower vacancy formation energy than in sulfide compound. Thus, the concentration of the vacancies is expected to be higher in selenide, and possibly explains the larger ionic conductivity between the two compounds. The lowering of vacancy formation energy in the randomized Na-sites, where S/Se atoms coordinated to Na are attached to higher number of Ga^{3+} than Zn^{2+} atoms has implication on further improvement of ionic conduction. This finding can be used as a design tool to dope even higher valent cations such as Sn^{4+} and P^{5+} in the Zn^{2+} site to create more defect and reduce vacancy formation energy.

The chalcogenide-based sodium ion conductors reported so far have emerged from the most common structure types that are already known. For example, tetragonal Na_3PS_4[55] and Na_3SbS_4[14] belongs to $P\bar{4}2_1c$ space group and for the same compositions there exist cubic phases that belongs to $I\bar{4}3m$ space group.[56] Selenide analogues of the cubic phases

also found to be superionic conductors.[57] In all of these structures MQ_4^{3-} anionic building unit adopts bcc type arrangement and Na ion occupies tetrahedral holes. But in case of $Na_{11}Sn_2PS_{12}$,[19] the structure consists of ordered SnS_4, PS_4 tetrahedra and the Na ions occupy octahedral holes. Hence, the arrangement of anion sub lattice and the coordination of mobile ion plays vital role in determining the plausible diffusion pathways. Synthesizing new structure types, creating disorder with suitable dopants could provide much deeper understanding of the structure property relationships. In this respect the present open framework structure can provide valuable scope to design and synthesize new structure types with desired properties which has remained as a big challenge. This work is the result of a hypothesis that new structure types can be rationally synthesized by choosing appropriate main group/transition metal polyhedral units, which ultimately results in stable structures with huge channels and void spaces. Modification with suitable substitutions and creation of defects may further improve the properties, especially ionic conductivities. Also note that the design strategy can be extended to other redox active transition metal and building units, in which case the resulting structure can also be a good cathode material for Na ion batteries. This type of materials can be considered as chalcometallate analogue of polyanion-based cathode.

4. CONCLUSIONS

New quaternary chalcogenide-based sodium-ion solid electrolytes have been synthesized by solid-state polychalcogenide flux-based techniques. The room temperature Na-ion conductivity is at least one order of magnitude higher for the selenide analogue

compared to sulfide due to more polarizable softer Se ligand (3.3×10^{-4} in Na_3ZnGaS_4 *vs* 0.12 mS/cm in $Na_3ZnGaSe_4$), which in turn produces lower vacancy formation energy. Both compounds show reasonable moisture stability, resulting from the 3D interwoven structure built by interconnected T2 building unit. DRS measurements reveal that both compounds are wide band gap semiconductors, as further confirmed by first principle calculations. This work also emphasizes that with appropriate selection of building units, one can employ basic design principles to achieve new phases with interesting functional properties. We believe that this type of 3D open framework chalcogenide can be outstanding high rate capability host for Na-ion batteries especially it can enable all-chalcogenide sodium-ion solid state battery. The solid-state metathesis route can be employed to gain access to such phases. Future design should also pay attention to electrochemical potential window along with achieving higher ionic conductivities.

ACKNOWLEDGEMENT

The authors are grateful for the funding of this work from National Science Foundation (NSF) under the grant No. DMR- 1809128.

SUPPLEMENTARY INFORMATION

Table S1. Final atomic coordinates and equivalent isotropic displacement parameters of the atoms for compounds I and II. U(eq) = 1/3 of the trace of the orthogonalized Ueq tensor.

Atomic parameters						
Atom	Wyckoff	Occupancy	x/a	y/b	z/c	U(Å^2)
Na_3ZnGaS_4, I						
Ga1	32g	0.5	0.4212(4)	0.3728(3)	0.1882(2)	0.010(1)
Zn1	32g	0.5	0.4219(4)	0.3721(4)	0.1880(2)	0.024(2)
S1	32g	1	0.5462(1)	0.4600(1)	0.1262(1)	0.024(1)
S2	16e	1	0.3321(1)	0.5000	0.2500	0.019(1)
S3	16d	1	0.5000	0.2500	0.2642(1)	0.021(1)
Na1	16f	1	0.3833(1)	0.3667(1)	0.3750	0.037(1)
Na2	32g	1	0.3400(2)	0.1214(2)	0.2636(2)	0.090(1)
$Na_3ZnGaSe_4$, II						
Ga1	32g	0.5	0.4216(1)	0.3721(1)	0.1881(1)	0.012(1)
Zn1	32g	0.5	0.4216(1)	0.3721(1)	0.1881(1)	0.012(1)
Se1	32g	1	0.5466(1)	0.4623(1)	0.1263(1)	0.016(1)
Se2	16e	1	0.3297(1)	0.5000	0.2500	0.013(1)
Se3	16d	1	0.5000	0.2500	0.2664(1)	0.015(1)
Na1	16f	1	0.3817(2)	0.3683(2)	0.3750	0.029(1)
Na2	32g	1	0.3388(2)	0.1243(2)	0.2568(2)	0.085(1)

Table S2. Anisotropic displacement parameters ($Å^2 x\ 10^3$) for compounds I and II. The anisotropic displacement factor exponent takes the form: $-2p^2[h^2a^{*2}U^{11} + ... + 2\ h\ k\ a^*\ b^*\ U^{12}]$

Atoms	U^{11}	U^{22}	U^{33}	U^{23}	U^{13}	U^{12}
Na_3ZnGaS_4, I						
Ga(1)	14(2)	8(2)	9(2)	-2(1)	2(1)	-1(2)
Zn(1)	18(3)	24(3)	30(3)	-3(2)	1(2)	2(2)
S(1)	24(1)	16(1)	33(1)	-1(1)	14(1)	-1(1)
S(2)	14(1)	19(1)	23(1)	-8(1)	0	0
S(3)	22(1)	20(1)	21(1)	0	0	0(1)
Na(1)	42(1)	42(1)	28(1)	4(1)	4(1)	1(1)
Na(2)	45(1)	82(2)	142(2)	-62(2)	41(1)	-40(1)
$Na_3ZnGaSe_4$, II						
Ga(1)	11(1)	10(1)	14(1)	-2(1)	2(1)	0(1)
Zn(1)	11(1)	10(1)	14(1)	-2(1)	2(1)	0(1)
Se(1)	16(1)	10(1)	23(1)	-1(1)	9(1)	0(1)
Se(2)	8(1)	12(1)	19(1)	-8(1)	0	0
Se(3)	15(1)	13(1)	17(1)	0	0	-1(1)
Na(1)	33(1)	33(1)	22(1)	2(1)	2(1)	3(1)
Na(2)	42(2)	81(2)	132(3)	-70(2)	47(2)	-45(2)

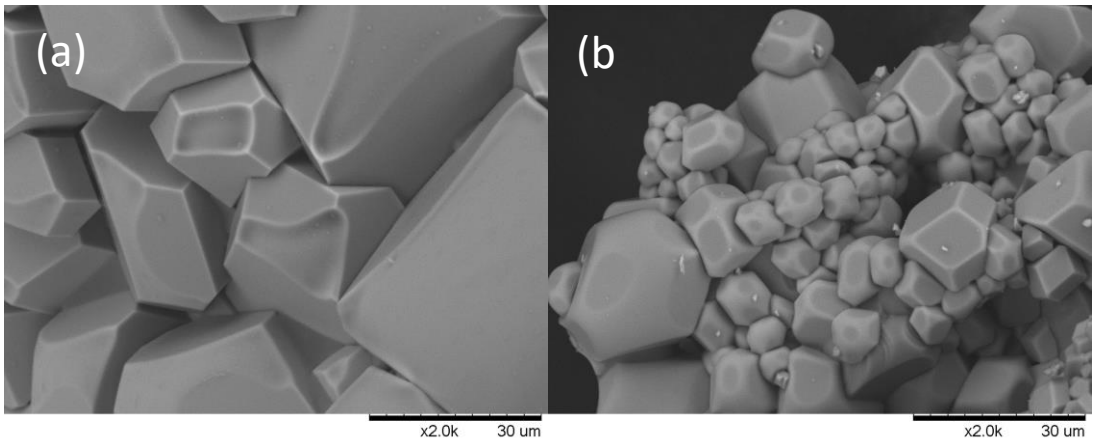

Figure S1. SEM images showing the particle sizes and shapes for Na_3ZnGaS_4 synthesized using (a) Solid state route; (b) Metathesis route.

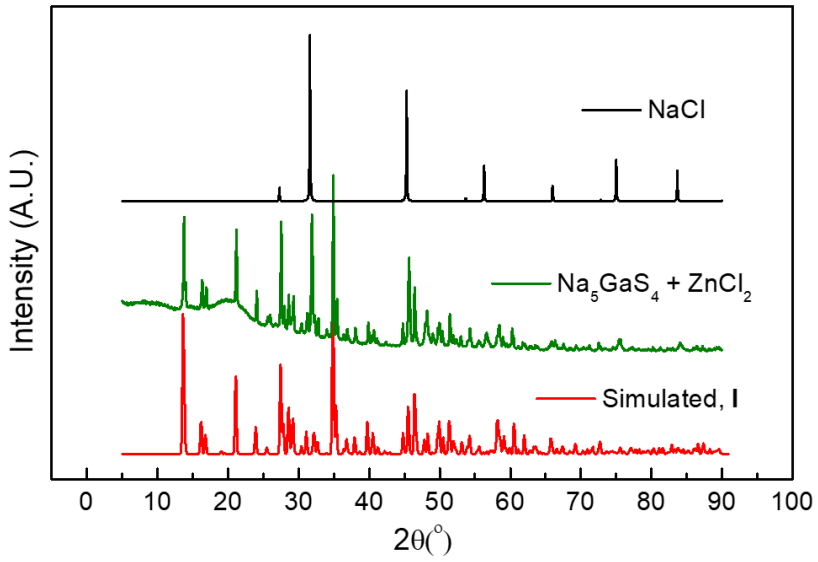

Figure S2. Comparing simulated PXRD pattern of Na_3ZnGaS_4 (I) with metathesis reaction products. Note the presence of NaCl as by-product from the metathesis reaction.

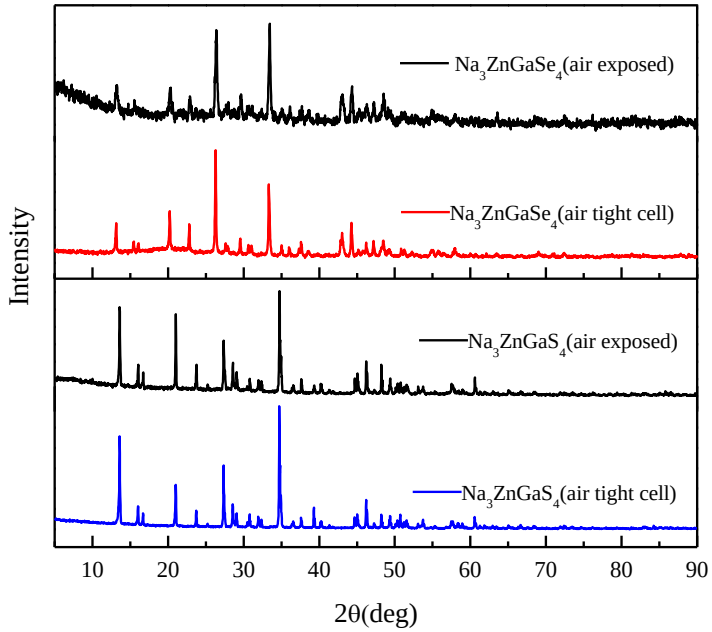

Figure S3. Comparing PXRD patterns of compound I (Na_3ZnGaS_4) and compound II ($Na_3ZnGaSe_4$) after exposing the powder samples to air for five and one days, respectively.

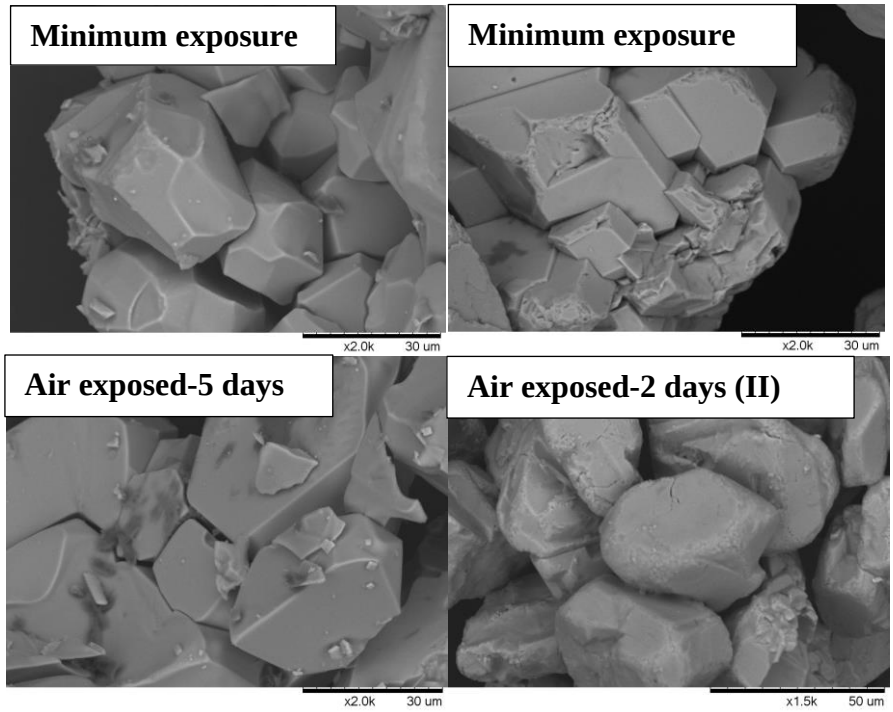

Figure S4. Comparing SEM images of compounds, I (Na_3ZnGaS_4) and II ($Na_3ZnGaSe_4$) after exposing the powder samples to air for five and two days, respectively.

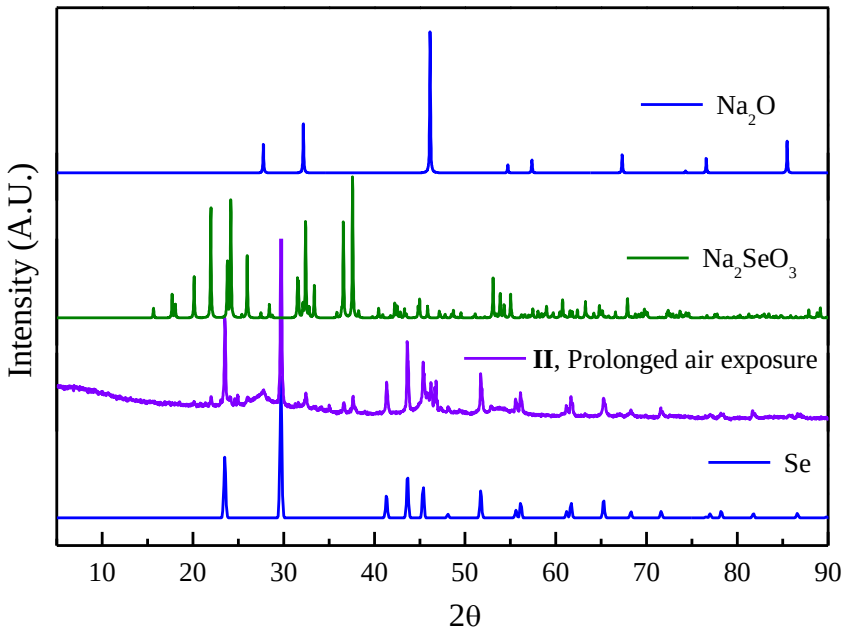

Figure S5. Air-exposed PXRD of II showing the peaks for Se, Na_2SeO_3 and Na_2O.

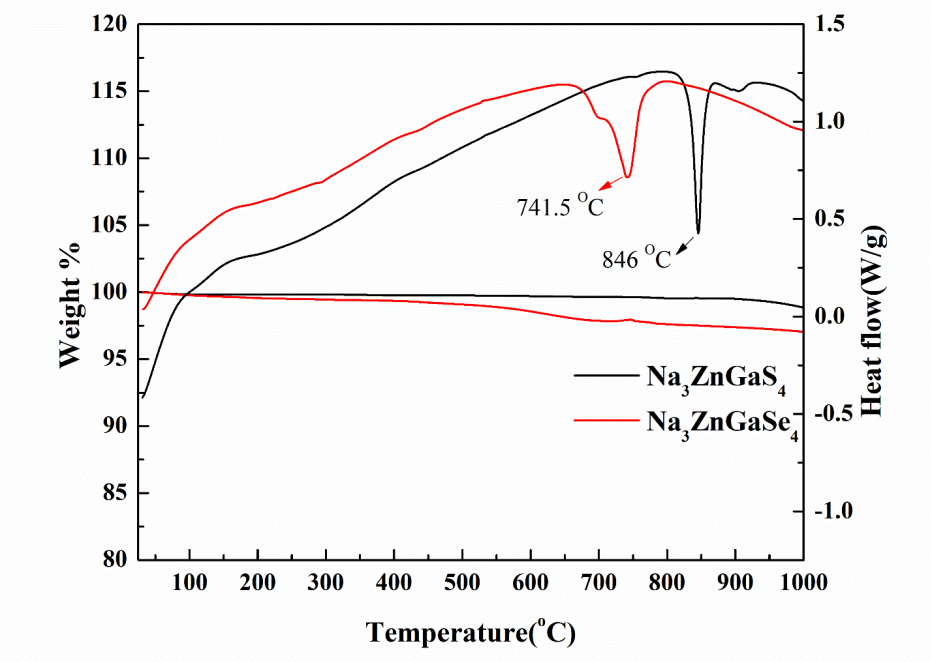

Figure S6. DSC & TGA plots for compound I (Na_3ZnGaS_4) and compound II ($Na_3ZnGaSe_4$).

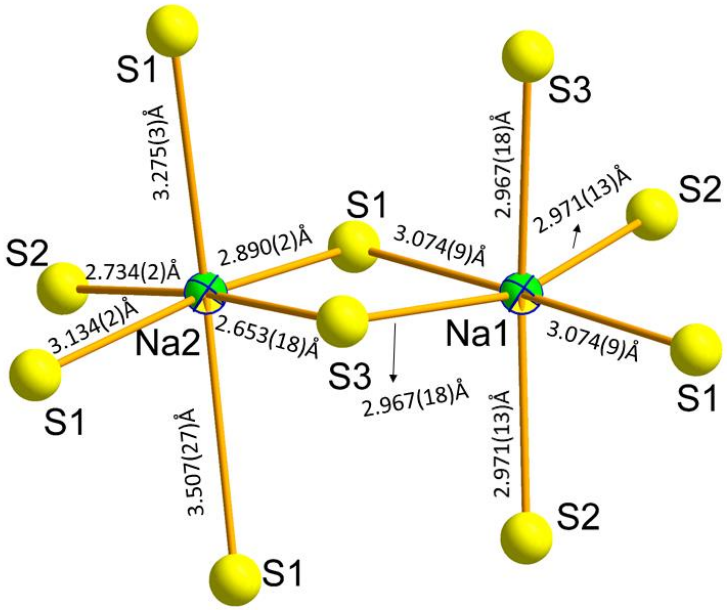

(b)

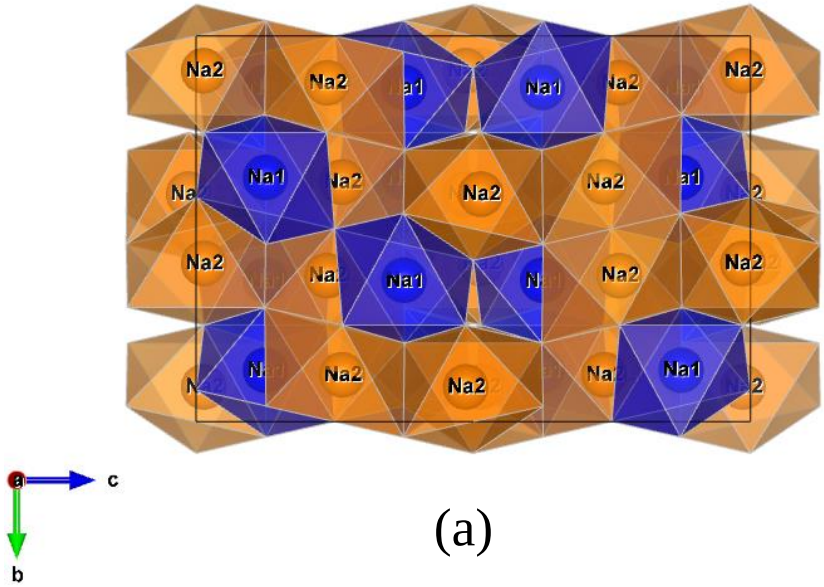

(a)

Figure S7. (a) Polyhedral connectivity of $Na1S_6$ and $Na2S_6$ (I). (b). Distorted octahedral coordination of Na1 and Na2 in Na_3ZnGaS_4

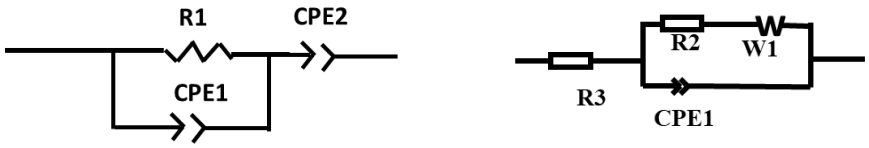

Element	Na_3ZnGaS_4	Element	$Na_3ZnGaSe_4$
R1	507 008 Ω	R3	1.23E-06 Ω
Q1	0.800 9e-9 F.s^(a - 1)	R2	1590 Ω
a1	0.762 5	W1-R	3601 Ω
Q2	0.205 5e-6 F.s^(a - 1)	W1-T	3.83
a2	0.488 8	W1-P	3.62E-01
		CPE1-T	1.54E-10 F
		CPE1-P	9.95E-01

Figure S8. Equivalent circuit used and fitting parameters for room temperature ionic conductivity.

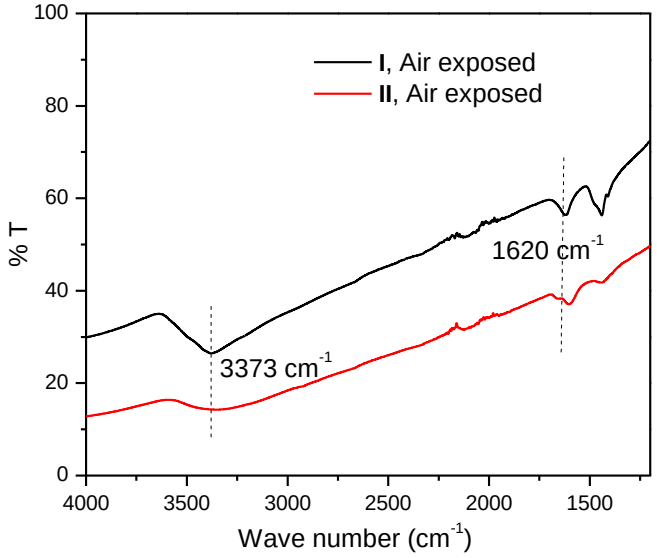

Figure S9. FT-IR spectra of air exposed samples of for compound I (Na_3ZnGaS_4) and compound II ($Na_3ZnGaSe_4$). The broad vibration bands due to symmetric (ν_1) and antisymmetric (ν_3) stretching of H_2O can be seen at ~ 3373 cm^{-1} along with the bending modes at 1620 cm^{-1}.

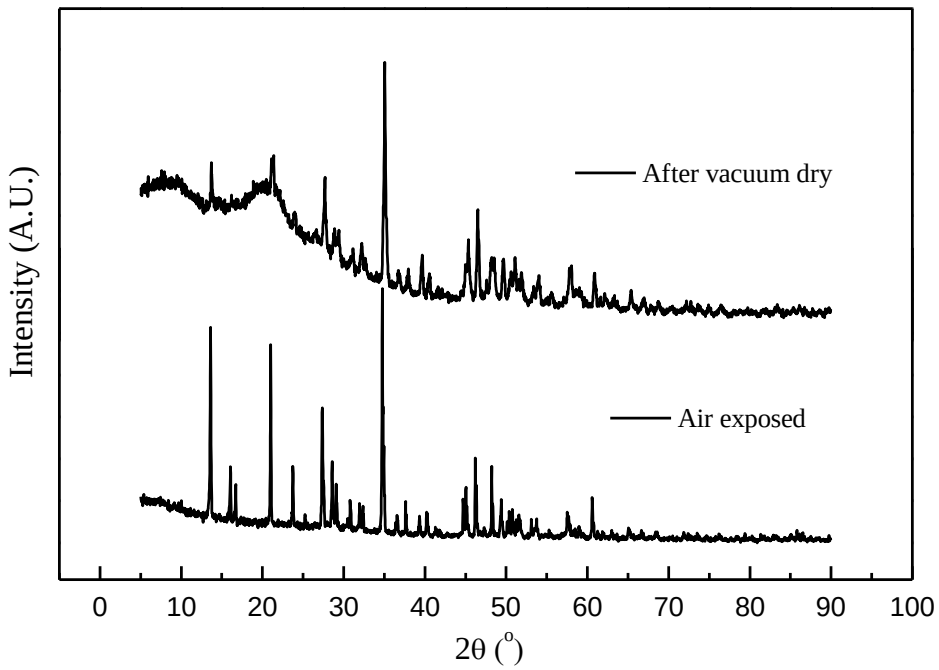

Figure S10. Comparison of PXRD patterns of I after air-exposure and vacuum-dried overnight. PXRD of vacuum-dried sample was taken in air-tight cell. The broad background comes from the Kapton film.

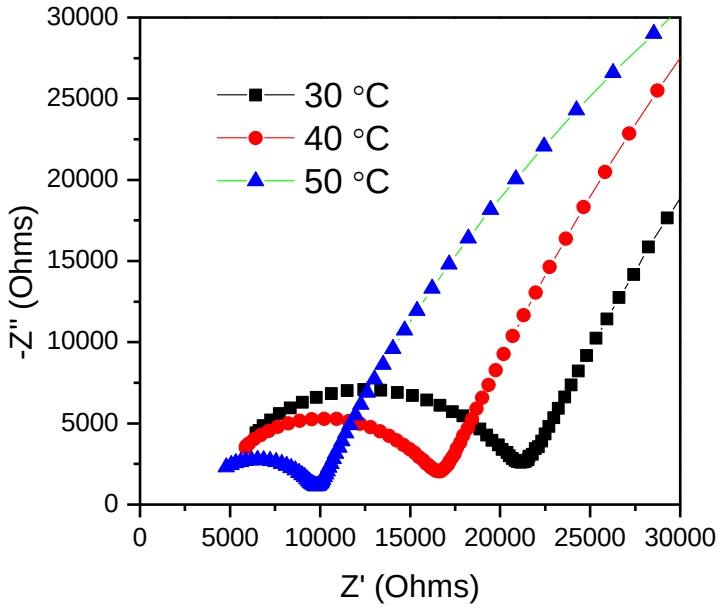

Figure S11. Nyquist plot for room temperature ionic conductivity of $Na_3ZnGaSe_4$ (II) after air exposure for two hours. The ionic conductivity at 30 °C is ~ 0.01mS/cm.

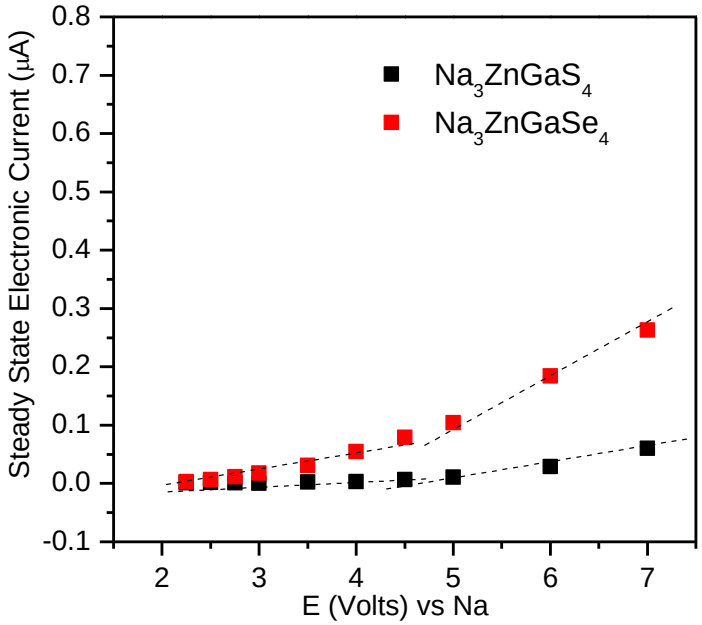

Figure S12. Steady-state electronic current as a function of applied voltage for compound I and II at 30 °C by Hebb-Wagner polarization measurements with elemental sodium as the reference electrode and indium as the ion blocking electrode.

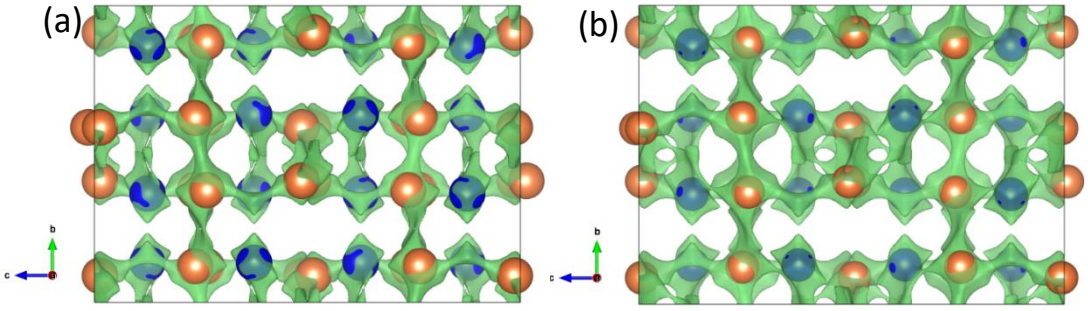

Figure S13. Bond valence sum (|ΔV|) maps of compound I Figure (a) and compound II Figure (b) at an isosurface $|\Delta V| = 0.5\ v.u.$ Blue color indicates Na1 and orange color indicates Na2.

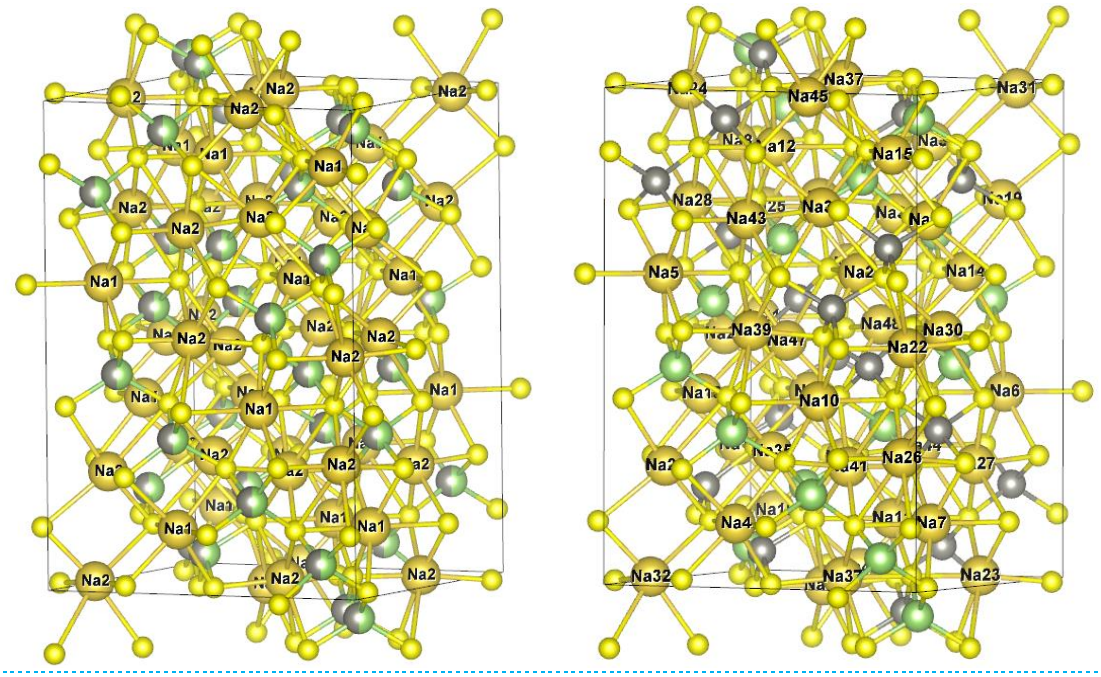

(a) (b)

Figure S14. (a) shows the random distrubution of Ga and Zn atoms. (b) is the structure we used to calculate Na defect formation energy with Ga and Zn atoms randomly assigned on their shared sites.

REFERENCES

1. Kanatzidis, M. G. Discovery-Synthesis, Design, and Prediction of Chalcogenide Phases. *Inorg. Chem.* **2017**, *56* (6), 3158–3173. https://doi.org/10.1021/acs.inorgchem.7b00188.

2. Kamaya, N.; Homma, K.; Yamakawa, Y.; Hirayama, M.; Kanno, R.; Yonemura, M.; Kamiyama, T.; Kato, Y.; Hama, S.; Kawamoto, K.; Mitsui, A. A Lithium Superionic Conductor. *Nat. Mater.* **2011**, *10* (9), 682–686. https://doi.org/10.1038/nmat3066.

3. Hayashi, A.; Noi, K.; Sakuda, A.; Tatsumisago, M. Superionic Glass-Ceramic Electrolytes for Room-Temperature Rechargeable Sodium Batteries. *Nat. Commun.* **2012**, *3* (1), 1–5. https://doi.org/10.1038/ncomms1843.

4. Saha, S.; Assat, G.; Sougrati, M. T.; Foix, D.; Li, H.; Vergnet, J.; Turi, S.; Ha, Y.; Yang, W.; Cabana, J.; Rousse, G.; Abakumov, A. M.; Tarascon, J. M. Exploring the Bottlenecks of Anionic Redox in Li-Rich Layered Sulfides. *Nat. Energy*. **2019**, *4* (11), 977–987. https://doi.org/10.1038/s41560-019-0493-0.

5. Larcher D.; Tarascon J.-M. Towards greener and more sustainable batteries for electrical energy storage. *Nat. Chem*. **2015**, *7*, 19–29. 10.1038/nchem.2085.

6. Knauth, P. Inorganic solid Li ion conductors: An overview. *Solid State Ionics* **2009**, *180* (14–16), 911– 916, DOI: 10.1016/j.ssi.2009.03.022.

7. Janek, J., Zeier, W. A solid future for battery development. *Na.t Energy* **2016**, *1***,** 16141. https://doi.org/10.1038/nenergy.2016.141.

8. Goodenough, J. B.; Singh, P. Review—Solid Electrolytes in Rechargeable Electrochemical Cells. *J. Electrochem. Soc.* **2015**, *162* (14), A2387–A2392. https://doi.org/10.1149/2.0021514jes.

9. Zhou, C.; Bag, S.; Thangadurai, V. Engineering materials for progressive all-solid-state Na batteries. *ACS Energy Lett.* **2018**, *3*, 2181– 2198, DOI: 10.1021/acsenergylett.8b00948.

10. Hueso, K. B.; Armand, M.; Rojo, T. High Temperature Sodium Batteries: Status, Challenges and Future Trends. *Energy Environ. Sci.* **2013**, *6*, 734– 749, DOI: 10.1039/c3ee24086j.

11. Kummer, J. T. β-Alumina Electrolytes. *Prog. Solid State Chem.* **1972**, *7*, 141, DOI: 10.1016/0079-6786(72)90007-6.

12. Hayashi, A.; Noi, K.; Tanibata, N.; Nagao, M.; Tatsumisago, M. High Sodium Ion Conductivity of Glass-Ceramic Electrolytes with Cubic Na_3PS4. *J. Power Sources* **2014**, *258*, 420–423. https://doi.org/10.1016/j.jpowsour.2014.02.054.

13. Xiong, S.; Liu, Z.; Rong, H.; Wang, H.; McDaniel, M.; Chen, H. Na3SbSe4-x S x as Sodium Superionic Conductors. *Sci. Rep.* **2018**, *8* (1). https://doi.org/10.1038/s41598-018-27301-8.

14. Banerjee, A.; Park, K. H.; Heo, J. W.; Nam, Y. J.; Moon, C. K.; Oh, S. M.; Hong, S.-T.; Jung, Y. S. Na_3SbS_4 : A Solution Processable Sodium Superionic Conductor for All-Solid-State Sodium-Ion Batteries. *Angew. Chemie Int. Ed.* **2016**, *55* (33), 9634–9638. https://doi.org/10.1002/anie.201604158.

15. Hayashi, A.; Masuzawa, N.; Yubuchi, S.; Tsuji, F.; Hotehama, C.; Sakuda, A.; Tatsumisago, M. A Sodium-Ion Sulfide Solid Electrolyte with Unprecedented Conductivity at Room Temperature. *Nat. Commun.* **2019**, *10* (1), 1–6. https://doi.org/10.1038/s41467-019-13178-2.

16. Zhang, Z.; Shao, Y.; Lotsch, B.; Hu, Y. S.; Li, H.; Janek, J.; Nazar, L. F.; Nan, C. W.; Maier, J.; Armand, M.; Chen, L. New Horizons for Inorganic Solid State Ion Conductors. *Energy Environ. Sci.* **2018**, *11*, 1945– 1976, DOI: 10.1039/C8EE01053F.

17. Richards, W. D.; Tsujimura, T.; Miara, L. J.; Wang, Y.; Kim, J. C.; Ong, S. P.; Uechi, I.; Suzuki, N.; Ceder, G. Design and Synthesis of the Superionic Conductor $Na_{10}SnP_2S_{12}$. *Nat. Commun.* **2016**, *7* (1), 1–8. https://doi.org/10.1038/ncomms11009.

18. Zhang, Z.; Ramos, E.; Lalère, F.; Assoud, A.; Kaup, K.; Hartman, P.; Nazar, L. F. $Na_{11}Sn_2PS_{12}$: A New Solid State Sodium Superionic Conductor. *Energy Environ. Sci.* **2018**, *11* (1), 87–93. https://doi.org/10.1039/c7ee03083e.

19. Sakuda, A.; Hayashi, A.; Tatsumisago, M. Sulfide Solid Electrolyte with Favorable Mechanical Property for All-Solid-State Lithium Battery. *Sci. Rep.* **2013**, *3* (1), 1–5. https://doi.org/10.1038/srep02261.

20. Banerjee, A.; Wang, X.; Fang, C.; Wu, E. A.; Meng, Y. S. Interfaces and Interphases in All-Solid-State Batteries with Inorganic Solid Electrolytes. *Chem. Rev*. **2020**, *120*, 6878–6933. https://doi.org/10.1021/acs.chemrev.0c00101.

21. Zhu, Y., Mo, Y. Materials Design Principles for Air-Stable Lithium/Sodium Solid Electrolytes, *Angew. Chem. Int. Ed.*, **2020**, *59 (40)*, 17472 – 17476. https://doi.org/10.1002/anie.202007621.

22. Pearson, R. G. Absolute Electronegativity and Absolute Hardness of Lewis Acids and Bases. *J. Am. Chem. Soc*. **1985**, *107*, 6801-6806.

23. Mohapatra, S.; Adhikary, A.; Ghosh, K.; Choudhury, A. Magnetically Frustrated Quaternary Chalcogenides with Interpenetrating Diamond Lattices. *Inorg. Chem.* **2017**, *56* (14), 7650–7656. https://doi.org/10.1021/acs.inorgchem.7b00121.

24. Adhikary, A.; Yaghoobnejad Asl, H.; Sandineni, P.; Balijapelly, S.; Mohapatra, S.; Khatua, S.; Konar, S.; Gerasimchuk, N.; Chernatynskiy, A. V.; Choudhury, A. Unusual Atmospheric Water Trapping and Water Induced Reversible Restacking of 2D Gallium Sulfide Layers in $NaGaS_2$ Formed by Supertetrahedral Building Unit . *Chem. Mater.* **2020**, *32*, 5589–5603. https://doi.org/10.1021/acs.chemmater.0c00836.

25. Balijapelly, S; Sandineni, P.; Adhikary, A.; Gerasimchuk, N.; Chernatynskiy, A. V; Choudhury, A. Ternary Alkali Ion Thiogallates, A_5GaS_4 (A = Li and Na) with Isolated Tetrahedral Building Units and Their Ionic Conductivity. *Dalton Trans.* **2021**. https://doi.org/10.1039/D1DT00766A.

26. Schewe-Miller, I. Metallreiche Hauptgruppenmetall-Chalkogenverbindungen: Synthese, Strukturen Und Eigenschaften. **1990**.

27. Bruker- SMART. Bruker AXS Inc., Madison, Wisconsin, USA. 2002.

28. Bruker-SAINT and SADABS, and SHELXTL. Bruker AXS Inc., Madison, Wisconsin, USA, 2008.

29. Sheldrick, G. M. A short history of SHELX. *Acta Crystallogr., Sect. A: Found. Crystallogr.* **2008**, 64, 112–122.

30. Hübschle, C. B.; Sheldrick, G. M.; Dittrich, B. ShelXle: A Qt Graphical User Interface for SHELXL. *J. Appl. Crystallogr.* **2011**, *44* (6), 1281–1284. https://doi.org/10.1107/S0021889811043202.

31. Kubelka, P. and Munk, F. Ein Beitrag Zur Optik Der Farbanstriche. *Z. Techn. Phys*. **1931**, *12*, 593 -601.

32. Kresse, G.; Hafner, J. Ab Initio Molecular Dynamics for Liquid Metals. *Phys. Rev. B* **1993**, *47* (1), 558–561. https://doi.org/10.1103/PhysRevB.47.558.

33. Kresse, G.; Hafner, J. Ab Initio Molecular-Dynamics Simulation of the Liquid-Metalamorphous- Semiconductor Transition in Germanium. *Phys. Rev. B* **1994**, *49* (20), 14251–14269. https://doi.org/10.1103/PhysRevB.49.14251.

34. Kresse, G.; Furthmüller, J. Efficient Iterative Schemes for Ab Initio Total-Energy Calculations Using a Plane-Wave Basis Set. *Phys. Rev. B - Condens. Matter Mater. Phys.* **1996**, *54* (16), 11169–11186. https://doi.org/10.1103/PhysRevB.54.11169.

35. Kresse, G.; Furthmüller, J. Efficiency of Ab-Initio Total Energy Calculations for Metals and Semiconductors Using a Plane-Wave Basis Set. *Comput. Mater. Sci.* **1996**, *6* (1), 15–50. https://doi.org/10.1016/0927-0256(96)00008-0.

36. Perdew, J. P.; Burke, K.; Ernzerhof, M. Generalized Gradient Approximation Made Simple. *Phys. Rev. Lett.* **1996**, *77* (18), 3865–3868. https://doi.org/10.1103/PhysRevLett.77.3865.

37. Perdew, J. P.; Burke, K.; Ernzerhof, M. Erratum: Generalized Gradient Approximation Made Simple (Physical Review Letters (1996) 77 (3865)). *Phys. Rev. Lett.* **1997**, *78* (8), 1396. https://doi.org/10.1103/PhysRevLett.78.1396.

38. Blöchl, P. E. Projector Augmented-Wave Method. *Phys. Rev. B* **1994**, *50* (24), 17953–17979. https://doi.org/10.1103/PhysRevB.50.17953.

39. Joubert, D. From Ultrasoft Pseudopotentials to the Projector Augmented-Wave Method. *Phys. Rev. B - Condens. Matter Mater. Phys.* **1999**, *59* (3), 1758–1775. https://doi.org/10.1103/PhysRevB.59.1758.

40. Choudhury, A.; Dorhout, P. K. Synthesis, Structure, and Optical Properties of the Quaternary Seleno-Gallates $NaLnGa_4Se_8$ (Ln = La, Ce, Nd) and Their Comparison with the Isostructural Thio-Gallates. *Inorg. Chem.* **2008**, *47* (9), 3603–3609. https://doi.org/10.1021/ic701986j.

41. Zheng, N.; Bu, X.; Feng, P. Synthetic design of crystalline inorganic chalcogenides exhibiting fast-ion conductivity. *Nature* **2003**, *426*, 428– 432. https://doi.org/10.1038/nature02159.

42. Wu, T.; Bu, X.; Zhao, X.; Khazhakyan, R.; Feng, P. Phase Selection and Site-Selective Distribution by Tin and Sulfur in Supertetrahedral Zinc Gallium Selenides. *J. Am. Chem. Soc.* **2011**, *133*, 9616 – 9625. https://doi.org/10.1021/ja203143q.

43. Zheng, N.; Bu, X.; Feng, P. Synthetic design of crystalline inorganic chalcogenides exhibiting fast-ion conductivity. *Nature* **2003**, *426*, 428– 432. https://doi.org/10.1038/nature02159.

44. Chen, R.; Wu, X.; Su, Z. Structural Insights into T2-Cluster-Containing Chalcogenides with Vertex-, Edge- and Face-Sharing Connection Modes of NaQ_6 Ligands: $Na_3ZnM^{III}Q_4$ (M^{III} = In, Ga; Q = S, Se). *Dalton Trans.* **2018**, *47*, 15538. https://doi.org/10.1039/c8dt03281e.

45. Langenmaier, M.; Brantl, J.; Röhr, C. Mixed Mn/In Chalcogenides $A_3(Mn^{II}In^{III})_3Q_4$ (A = Na, K, Rb, Cs; Q = S, Se, Te). *J. Solid State Chem*. **2021**, 294, 121455. https://doi.org/10.1016/j.jssc.2020.121455.

46. Hai, X.; Tahir-Kheli, J.; Goddard, W. A. Accurate band gaps for semiconductors from density functional theory. *J. Phys. Chem. Lett.* **2011**, *2(3)*, 212 – 217. https://doi.org/10.1021/jz101565j.

47. Song, A. -Y.; Xiao, Y.; Turcheniuk, K.; Upadhya, P.; Ramanujapuram, A.; Benson, J.; Magasinski, A.; Olguin, M.; Meda, L.; Borodin, O.; Yushin, G. Protons Enhance Conductivities in Lithium Halide Hydroxide/Lithium Oxyhalide Solid Electrolytes by Forming Rotating Hydroxy Groups. *Adv. Energy Mater.* **2018**, *8 (3)*, art. no. 1700971. https://doi.org/10.1002/aenm.201700971

48. Sun, J.; Sun, Q.; Plewa, A.; Wang, Y.; He, L.; Zheng, F.; Chen, C.; Zajac, W.; Molenda, J.; Zeng, K.; Lu, L. Abnormal Ionic Conductivities in Halide $NaBi_3O_4Cl_2$ Induced by Absorbing Water and a Derived Oxhydryl Group. *Angew. Chem., Int. Ed.*, **2020**, *59 (23)*, 8991 – 8997. https://doi.org/10.1002/anie.201912145

49. Neudecker, B. J.; Weppner, W. Li_9SiAlO_8: A lithium ion electrolyte for voltages above 5.4 V. *J. Electrochem. Soc.* **1996**, *143*, 2198 – 2203. https://doi.org/10.1149/1.1836980

50. Adams, S. Relationship between Bond Valence and Bond Softness of Alkali Halides and Chalcogenides. *Acta Crystallogr. Sect. B Struct. Sci.* **2001**, *57* (3), 278–287. https://doi.org/10.1107/S0108768101003068.

51. Momma, K.; Izumi, F. VESTA 3 for Three-Dimensional Visualization of Crystal, Volumetric and Morphology Data. *J. Appl. Crystallogr.* **2011**, *44* (6), 1272–1276. https://doi.org/10.1107/S0021889811038970.

52. Zeier, W. G.; Schlem, R.; Banik, A.; Eckardt, M.; Zobel, M. $Na_{3-x}Er_{1-x}Zr_xCl_{6-A}$ Halide-Based Fast Sodium-Ion Conductor with Vacancy-Driven Ionic Transport. *ACS Appl. Energy Mater.* **2020**, *3* (10), 10164–10173. https://doi.org/10.1021/acsaem.0c01870.

53. Zhu, Z.; Chu, I. H.; Deng, Z.; Ong, S. P. Role of Na+ Interstitials and Dopants in Enhancing the Na+ Conductivity of the Cubic Na_3PS_4 Superionic Conductor. *Chem. Mater.* **2015**, *27* (24), 8318–8325. https://doi.org/10.1021/acs.chemmater.5b03656.

54. Zhu, Z.; Deng, Z.; Chu, I. H.; Radhakrishnan, B.; Ong, S. P. Ab Initio Molecular Dynamics Studies of Fast Ion Conductors. In *Computational Materials System Design*; Springer International Publishing, 2017; pp 147–168. https://doi.org/10.1007/978-3-319-68280-8_7.

55. Jansen, M.; Henseler, U. Synthesis, Structure Determination, and Ionic Conductivity of Sodium Tetrathiophosphate. *J. Solid State Chem.* **1992**, *99*, 110– 119, DOI: 10.1016/0022-4596(92)90295-7.

56. Nishimura, S. I.; Tanibata, N.; Hayashi, A.; Tatsumisago, M.; Yamada, A. The Crystal Structure and Sodium Disorder of High-Temperature Polymorph β-Na_3PS_4. *J. Mater. Chem. A* **2017**, *5* (47), 25025–25030. https://doi.org/10.1039/c7ta08391b.

57. Zhang, L.; Yang, K.; Mi, J.; Lu, L.; Zhao, L.; Wang, L.; Li, Y.; Zeng, H. Na_3PSe_4: A Novel Chalcogenide Solid Electrolyte with High Ionic Conductivity. *Adv. Energy Mater.* **2015**, *5* (24).

IV. SODIUM STUFFED OPEN FRAMEWORK QUATERNARY CHALCOGENIDE BUILT WITH $(Cu_2Ga_6S_{18})^{16-}$ RIBBONS CROSS-LINKED BY UNUSUAL LINEAR Cu (I) PILLARS

*Srikanth Balijapelly,[a] Amit Adhikary,[a] Sudip Mohapatra,[a] Aleksandr V. Chernatynskiy,[b] Amitava Choudhury[a, *]*

[a]Department of Chemistry, Missouri University of Science and Technology, Rolla, MO 65409, USA

[b]Department of Physics, Missouri University of Science and Technology, Rolla, MO 65409, USA

ABSTRACT

A quaternary compound, $Na_{15}Cu_3Ga_6S_{18}$, first member in the series *A*–Cu–Ga–S (*A* = Alkali metal) has been synthesized from a solid-state metathesis reaction between $Na_6Ga_2S_6$ and CuCl as well as from a combination of Na_2S, Ga, Cu, and S. The compound crystallizes in monoclinic crystal system, C2/c space group, and represents a unique open-framework structure with channels filled with eight crystallographically distinct Na-ions. The anionic framework is built up of infinite chains of corner-shared GaS_4 tetrahedra fused together by edge shared dimer of CuS_4 tetrahedra forming one dimensional ribbons of $(Cu_2Ga_6S_{18})^{16-}$, which are cross-linked by linearly coordinated S – Cu – S linkages resulting in a three dimensional network with tunnels filled with Na atoms. Optical band gap measurements show that the compound has direct band gap of 3.00 eV which is in good agreement with the theoretical band gap derived from DFT calculations. Band structure calculations further indicate that the states near the Fermi level are dominated by tetrahedral Cu^+ (*d*) and S(*p*) states resulting from the antibonding interactions, while *s-d*

hybridization is prevalent in linear Cu^{+} coordination. Ionic conductivity measurements show that the compound has room temperature Na-ion conductivity of 2.72×10^{-5} mS/cm with an activation energy of 0.68 eV, which corroborates well with the NEB calculations.

1. INTRODUCTION

Quaternary systems in chalcogenides offer greater degrees of freedom in tuning chemical compositions and enable structural modifications compared to binary and ternary compositions .[1-4] The ability of the main group chalcometallate anions to form a myriad of building units offer a tremendous opportunity to design structures with desired properties.[5] These building units can be simple tetrahedral to complex supertetrahedral units as well as various modes of connectivity between the tetrahedral units can give rise to edge- or corner-shared finite and infinite chains and ribbons.[6] Interconnections between these building units *via* a main group or transition metals would give access to various 2-D and 3-D structures, often open framework with varied sizes of pores and channels because of the availability of a range of supertetrahedral and other complex units of different shapes and dimensions.[7-13] The rich structural chemistry also endow fascinating physicochemical properties. For examples, the negatively charged frameworks often host alkali ions which are highly mobile by virtue of the weak interactions with soft chalcogen ligands leading to super-ionic conductors.[14] Due to the same reason the framework possesses excellent ion exchange capacity which find promising applications in radioactive ion removal from nuclear waste or as hazardous heavy metal capture material.[15] The natural tendency to form non-centrosymmetric structures makes them good candidate for nonlinear optics.[16] On the

other hand, their semiconducting properties make them useful in photo-catalysis, photovoltaics,[17, 18] and thermoelectric[19] applications. Presence of transition metals also generate interesting magnetic properties such as magnetically frustrated lattice or a redox active lattice useful in solid-state electrochemistry.[20] All these attributes make perfect playground for solid state chemists to investigate chalcometallates in combination with transition metals. Among the transition metals Cu and Ag possess unique characteristics in chalcogenide solid state chemistry ascribed to their ability to adopt different coordination environment.[21,22] A large number of open-framework chalcogenides with copper has been synthesized hydro/solvothermally where the role of copper has been pivotal in forming certain building units e.g, icosahedron, super tetrahedra or in linking the building units/clusters and so on.[9, 23-32] More importantly Cu also modulates the band structure of the compound, where Cu-*d* states contributes close to the Fermi level and tunes the band gap of chalcometallates. However, under purely solid-state synthetic conditions at moderately high temperatures, the role of copper in building specific structural component has not been explored extensively. Towards this goal, we sought to synthesize quaternary composition in *A*–*Cu*–Ga–*Q* series (*A* = Alkali metal, *Q* = Chalcogen). In this effort we have employed solid-state metathesis reaction between $Na_6Ga_2S_6$ and CuCl to replace part of the Na-ions with Cu^+ and form a 3-dimensionally connected network. Our investigation has resulted in a unique quaternary compound, $Na_{15}Cu_3Ga_6S_{18}$, with open-framework structure where ribbons of Cu – Ga – Sulfide are cross-linked by unique linear Cu coordination. The pores are filled with eight crystallographically distinct Na-ions. In this article we present the ionic conductivity properties of this interesting material along with

the theoretical investigation of ion conduction path and the role of linearly coordinated Cu^{+} in bonding and over all band structure analysis.

2. EXPERIMENTAL

2.1. SYNTHESIS, CHARACTERIZATION, AND PROPERTY MEASUREMENTS

The compound, $Na_{15}Cu_3Ga_6S_{18}$, was synthesized in a sealed quartz tube by solid state metathesis route using $Na_6Ga_2S_6$ and CuCl in 1:1 ratio at 700 °C. A direct stoichiometric combination of elements and binary alkali sulfide, Cu, Ga, S and Na_2S, respectively, were employed to synthesize the compound **I** in bulk quantities (See *SI* for details). Pale yellow crystal suitable for single-crystal X-ray diffraction was used to collect the diffraction data sets and the structure was solved by using direct methods (see *SI* for details). Details of the crystal data, refinement, selected bond-lengths, isotropic and anisotropic thermal parameters are given in Table 1 and Tables S1- S3 (*SI*).

Hand ground powder samples from the as-synthesized batch show good agreement with the experimental powder X-ray diffraction pattern with very little impurity ($NaCu_2S_2$) (Figure S2 and S3 in *SI*). and this powder was used for other characterization and property studies. Details of the powder X-ray diffraction, diffuse reflectance spectra, impedance spectroscopy and DFT calculations are given in *SI*.

3. RESULTS AND DISCUSSION

3.1. STRUCTURE DESCRIPTION

The asymmetric unit of $Na_{15}Cu_3Ga_6S_{18}$ contains twenty two crystallographically distinct sites of which eight sites are occupied by Na atoms, nine by S atoms, two by Cu

Table 1. Crystal data and refinement details for compound, $Na_{15}Cu_3Ga_6S_{18}$, I.

Empirical formula	$Na_{15}Cu_3Ga_6S_{18}$
Formula weight	1530.87
Temperature	293(2) K
Wavelength	0.71073 Å
Crystal system	Monoclinic
Space group	*C*2/*c*
Unit cell dimensions	a = 14.222(3) Å
	b = 15.199(3) Å
	c = 17.239(3) Å
	β = 107.624(2)°
Volume	3551.6(12) Å^3
Z	4
Density (calculated)	2.863 Mg/m^3
Absorption coefficient	7.485 mm^{-1}
Goodness-of-fit on F^2	1.024
R [$I > 2\sigma(I)$]a	R_1 = 0.0368
wR ($F2$) (all data)[b]	wR_2 = 0.0915

[a] $R_1 = \sum||F_o| - |F_c|/\sum|F_o|$.
[b] $wR_2 = \{\sum[w(F_o^2 - F_c^2)^2]/\sum[w(F_0^2)^2]\}^{1/2}$, $w = 1/[\sigma^2(F_o)^2 + (aP)^2 + bP]$, where $P = [F_o^2 + 2F_c^2]/3$

atoms and three by Ga atoms yielding a charge balanced formula of $Na_{7.5}Cu_{1.5}Ga_3S_9$ (Figure 1a) assuming +1 oxidation state of Cu and other elements in their standard oxidation state. Eight such units are present in the unit cell; however, we preferred a formula of $Na_{15}Cu_3Ga_6S_{18}$ with Z = 4. Cu2 and Na8 atoms occupy special positions with two-fold symmetry and all remaining atoms are in general positions. All three Ga sites adopt distorted tetrahedral geometry. A unique feature of this compound is the presence of Cu^+ in two different coordination geometries, Cu1 adopts distorted tetrahedral coordination while Cu2 adopts a perfect linear coordination with S atoms. Among eight crystallographically distinct Na atoms, six Na atoms adopt distorted octahedral coordination. The remaining two Na sites adopt distorted trigonal bipyramidal (Na5) and distorted tetrahedral coordination (Na7) with S atoms, respectively. The overall structure resembles open framework architecture built up of intricate connectivity of infinite chains of corner-shared GaS_4 tetrahedra, cross-linked by Cu-tetrahedra and linear Cu-coordination (Figures 1a and 1b). It is also important to note that though the compound can be synthesized by metathetic reaction between $Na_6Ga_2S_6$ and CuCl, the reaction is not topotactic. The structural signature of the precursor, $Na_6Ga_2S_6$, which contains an edge-shared dimer is not retained in the product $Na_{15}Cu_3Ga_6S_{18}$.The isolated edge-shared dimer, $(Ga_2S_6)^{6-}$ transforms into infinite chains of corner shared GaS_4 tetrahedral units in $Na_{15}Cu_3Ga_6S_{18}$. Two infinite GaS_4 tetrahedral chains are stitched by edge shared dimers of $Cu1S_4$ to form anionic ribbons of $(Cu_2Ga_6S_{18})^{16-}$ running through [102] direction (Figure 1c).

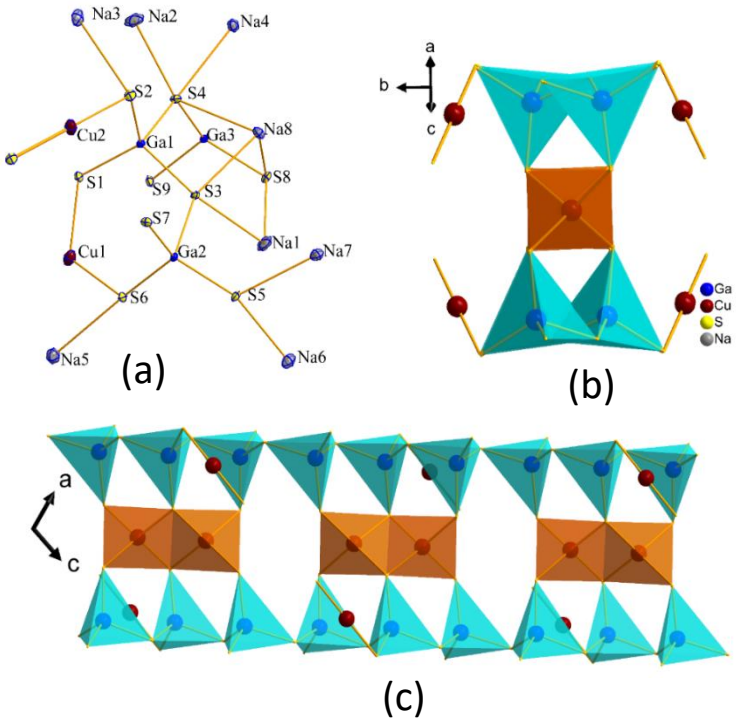

Figure 1. (a) Asymmetric unit of I, thermal ellipsoids are given at 40% probability. (b) $(Cu_2Ga_6S_{18})^{16-}$ building block showed along [102] direction. (c) The figure shows the connections between $(Cu_2Ga_6S_{18})^{16-}$ building blocks to form the ribbon.

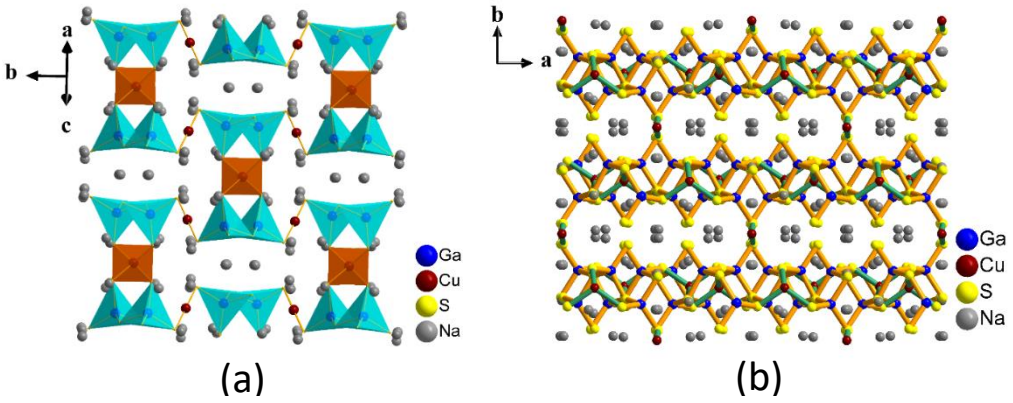

Figure 2. (a) Open framework structure I shown along [102] direction formed by the inter connection of $(Cu_2Ga_6S_{18})^{16-}$ ribbons through linearly coordinated Cu2, with Na^+ occupying the tunnels. (b) Ball-and-Stick representation of structure of I along [001] direction with Na^+ occupying the tunnels.

These ribbons made of $(Cu_2Ga_6S_{18})^{16-}$ building blocks are further connected to other such ribbons *via* linearly coordinated S – Cu2 – S linkages to create a three-dimensional network (Figure 2a). All Na atoms occupy the tunnels resulted from interconnection of these anionic $(Cu_2Ga_6S_{18})^{16-}$ ribbons with Na – S distances in the range, 2.729(2) – 3.337(3) Å (Figure 2b). All Ga – S and Cu1 – S bond distances are in the range, 2.2304(11) – 2.3315(11) and 2.3587(12) – 2.4398(12) Å, respectively, which are in agreement with Ga – S (2.261(2) – 2.304(2) Å) and Cu – S distances (2.383(2) – 2.400(2) Å) found in $Ba_4CuGa_5S_{12}$.[16] The bond distance for linearly coordinated Cu, Cu2 – S = 2.1597(11) Å is close to Cu – S distances found in several linearly coordinated Cu-sulfide-based compounds.[32-36] S–Ga–S and S–Cu1–S bond angles are in the range of 99.11(4) – 118.69(4)° and 104.02(4) – 116.61(4)°, suggesting highly distorted tetrahedral geometry for GaS_4 and $Cu1S_4$, respectively, whereas a bond angle of 180° for S–Cu2–S reflects perfectly linear coordination.

3.2. A DISCUSSION ON THE ROLE OF Cu^+

In chalcogenide chemistry, Cu is present mostly as Cu^+, which is a soft acid and show unique flexibility in coordination with the soft chalcogen anions. The most prevalent coordination of Cu^+ in complex chalcogenides and in open-framework materials is planar trigonal and tetrahedral. The planar trigonal coordination often leads to an icosahedral cluster of Cu – S in many open framework materials.[9, 25, 26, 28, 35] Whereas a tetrahedral coordination of Cu^+ can be an integral part of the supertetrahedral building unit.[29, 30, 32] There are only a handful of examples in open framework materials where Cu^+ is in linear coordination as seen in organically templated $CuGe_2S_5{\cdot}(C_2H_5)_4N$,[34] where Ge_4S_{10}-T2 super

tetrahedral units are exclusively connected by linear S – Cu – S linkages. In another example, Cu^{+} is both part of super tetrahedra and linear coordination connecting the supertetrahedra.[30] However, there are some examples of linear coordination of Cu^{+} in relatively dense ternary compounds which are listed in (Table 2 and Figure S4 in the *SI*) along with their Cu–S bond distances and S–Cu–S bond angles. Each of these linear coordination plays unique role in framework building. For example, in $Na_4Cu_2S_3$,[38] the anionic framework is built-up of unique V shaped $(Cu_2S_3)^{4-}$ type building units, while in KCuS[36] there exists infinite zig-zag chains of linear Cu–S linkages. There are two types of Cu^{+} in $NaCu_5S_3$,[37] Cu1 adopts linear coordination, Cu2 has a trigonal pyramid coordination. Similarly, structure of $CsCu_3S_2$[35] consists of zig-zag chains of Cu–S linked by linearly coordinated Cu–S bonds. In general, it is expected that due to the increase in covalency of the M–S bond, there will be lowering of coordination numbers.[39]

Table 2. List of sulfide-based compounds with linear coordination of Cu^{+}.

Compound	Space group	S-Cu-S(bond angle)	Cu-S (Å)
KCuS[34]	*P*na2_1	178.86°	2.162
$Na_4Cu_2S_3$[36]	*I* 4_1/aZ	176.26°(3) & 174.33°(3)	2.16(9)
$NaCu_5S_3$[35]	*P* 6_3 2 2	171.319°(31)	2.186
$CsCu_3S_2$[33]	*P* $\bar{3}$m 1	179.98°	2.162
$Na_{15}Cu_3Ga_6S_{18}$	*C*2/c	180°	2.1593(10)

However, in contrary, in moving from oxides to tellurides in a series of compounds where covalency is increasing, the coordination of Cu jumps from 2 in KCuO[40] and KCuS[36] to 3 in KCuSe[41] and KCuTe,[41] similarly in Cu_2O, Cu is linearly coordinated whereas it is tri coordinated in more covalent Cu_2S.[42,43] To identify a better indicator for the stabilization of low coordination of Cu^+, investigation by Gaudin *et al*[44] revealed that a strong Cu (*s*-*d* (d_z^2)) hybridization and subsequent strong bonding interactions of this hybrid orbitals with ligand (O or S) *p* orbital is responsible for the linear coordination as it was also observed in the band structure calculations of $Na_{15}Cu_3Ga_6S_{18}$ (Figure 4a, discussed later). Another important factor that governs the low coordination of Cu^+ and Ag^+ is their high polarization due to poor screening of the *d*-electrons. This cation polarization is reduced as we move from oxide to sulfide to selenide and cation's coordination increases. To stabilize low coordination in sulfides, the polarization of the cation needs to be raised. The cation polarization can be increased by the charge transfer through the alkali ions present in the system and that successfully explains the low coordination for compounds listed in Table 2.[36] In our present case high ratio of Na:Cu (>5) in $Na_{15}Cu_3Ga_6S_{18}$ could also be a factor for the stabilization of the linearly coordinated Cu2. However, in $Na_{15}Cu_3Ga_6S_{18}$ there is also present a tetrahedral Cu^+ (Cu1) and therefore, to understand the role of these two copper sites we performed band structure calculations and Crystal Orbital Hamiltonian Population (COHP) to evaluate their contribution in bonding.

3.3. OPTICAL BAND GAP AND BAND STRUCTURE

The room temperature optical band gap of I was obtained from diffuse reflectance spectrum (DRS). The spectrum was further analyzed by

equation, $\alpha h\nu = A(h\nu - E_g)^m$ (equation 1) to derive the band gap, E_g, where α = absorption coefficient/Kubelka-Munk function ($\alpha/S = (1-R)^2/2R$), $h\nu$ = photon energy, and A = constant.[45] A steep linear rise of the absorption edge was obtained by plotting $(h\nu\alpha)^2$ vs $h\nu$ (m = 2) indicative of a direct band gap material and from the extrapolation of the linear region a band gap of 3.00 eV can be derived (Figure 3). The density functional theory (DFT) derived band gap, however, severely underestimates the value, producing a band gap of 1.65 eV. This is a well-known observation for the local approximations to the density functional, such as currently employed PBESol functional, a revised version for solids of Perdew, Burke and Ernzerhof (PBE) exchange correlation functional (details in *SI*). Hybrid functionals are known to predict energy gap with higher accuracy than LDA/GGA functionals, albeit at much higher computational cost. We thus carried out a single point calculation with HSE06[46] functional using the PBESol-relaxed atomic structure and using only the gamma-point for the Brillouin zone integration.

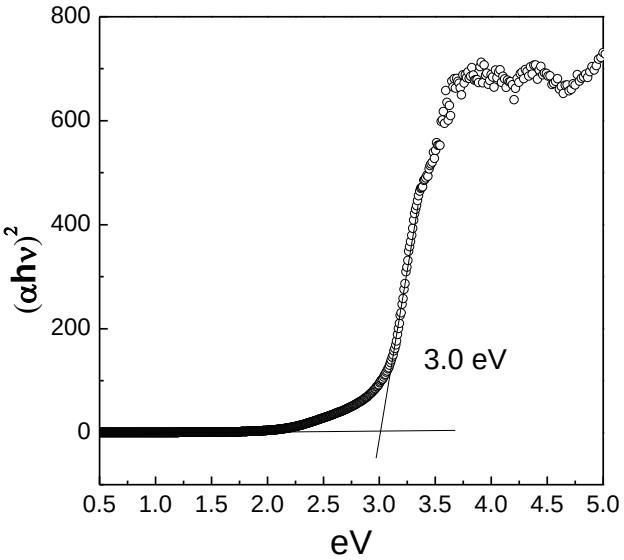

Figure 3. Tauc plot $(\alpha h\nu)^2$ vs $h\nu$ calculated using the diffuse reflectance data.

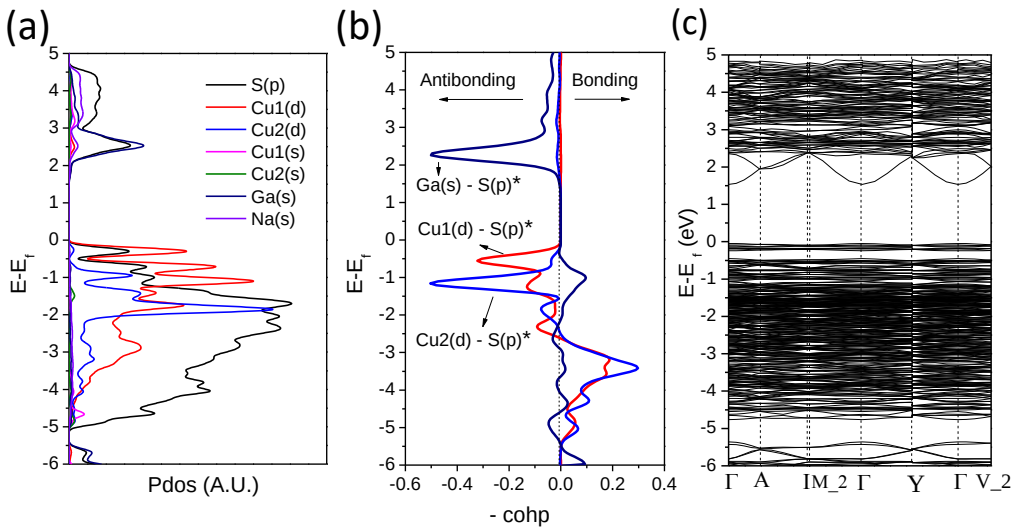

Figure 4. (a) Projected density of states, (b) COHP curves for Cu1–S, Cu2–S and Ga–S contacts (c) Electronic band structure of I.

The band structure from this calculation shows similar features as that with the PBESol functional, but the band gap of 3.5 eV is in much better agreement with the experimental value of 3.0 eV. PDOS shows that the Cu1(*d*) levels are close to the Fermi level and almost overlapping with the S(*p*) states, while Cu2(*d*) states are shifted towards the lower energy side (Figure 4a). The PDOS indicates that there are significant Cu(*s*) states coinciding with the Cu2(*d*) states, which signifies the extent of *s*-*d* hybridization involved in stabilization of Cu2 linear coordination as observed by Gaudin et al.[44] The conduction band has major contribution from Ga(*s*) and S(*p*). COHP analysis was performed to derive bond weighted density of states between pair of adjacent atoms (details in *SI*). COHP curves for Cu1–S, Cu2–S and Ga–S pairs shows that the density of state near the Fermi level are the result of antibonding interactions of Cu1(*d*) – S(*p*) , whereas the antibonding states of Cu2(*d*) – S(*p*) were lying below the Cu1(*d*) – S(*p*) states (Figure 4b). The conduction bands are strongly Ga–S antibonding. This corroborates well with the atom

projected density of states (Figure 4a). Band structure calculations (Figure 4c) indicate that $Na_{15}Cu_3Ga_6S_{18}$ belongs to a direct band gap material with conduction band minimum and valence band maximum positioned at Γ point of the Brillouin zone, which is in good agreement with the experimental optical band gap determination (Figures 3).

3.4. IONIC CONDUCTION AND THEORETICAL INVESTIGATION

Owing to its high abundance of alkali ions present in the framework, a high sodium ion conductivity is anticipated. AC Impedance measurements were performed to evaluate the room temperature ionic conductivity and to estimate activation energy from the variable temperature data using Arrhenius equation (see *SI* for details).

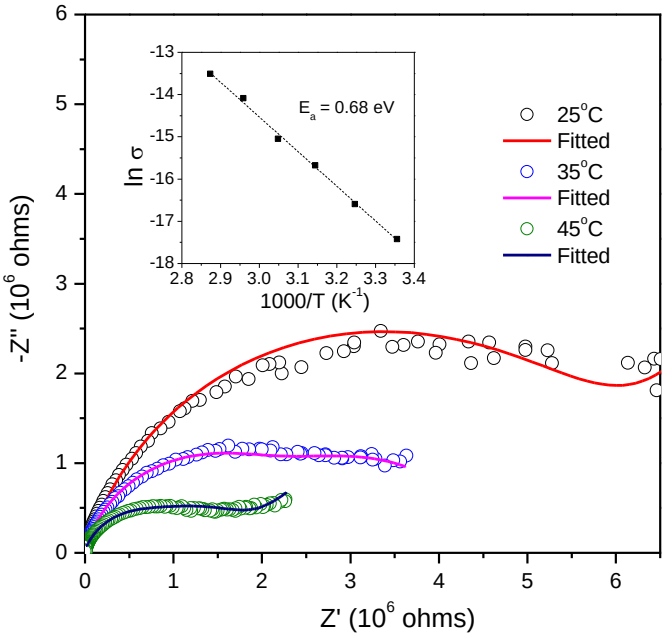

Figure 5. Activation energy calculated form experimentally measured ionic conductivity verses temperature. Dots represents the experimental ionic conductivity and dashed line represents the Arrhenius fit to the data. Inset shows the Nyquist plot for room temperature ionic conductivity

Room temperature ionic conductivity is found to be 2.72 $\times 10^{-5}$ mS/cm with an activation energy of 0.68 eV (Figure 5) indicating sluggish nature of the alkali ion diffusion within the lattice. Sodium ion conductivity in this range has been found in some chalcogenide glass-ceramics.[47, 48] Bond valence sum energy landscapes were constructed to understand the probable diffusion pathways within the unit cell at moderate activation energies. BVEL algorithm could not find any continuous diffusion pathways at $|\Delta V| = 0.5\, v.u$ (see Figure S6a and other details in *SI*). However, BVEL could find that the migration between Na1–Na7 (Figure S6b) could occur without much deviation in the bond valence sum. This finding corroborates well with the Nudged Elastic Band results. To further support the experimental results, Nudged Elastic Band (NEB)[49] calculations were performed based on the DFT energy landscape. Since this structure does not feature sites partially occupied with sodium atoms, we assume that ionic conductivity is assisted by the defects of the crystalline lattice, specifically by the sodium vacancies. Due to the lack of the open space in the structure we consider interstitial-assisted diffusion to be unlikely mechanism. Experimentally, there are intrinsic finite concentration of vacancies that can be further increased by doping, while in simulations we add a vacancy (remove sodium atom) to the simulation cell. We then compute the activation barrier using NEB for a migration of the vacancy to the neighboring sodium sites, which correspond to the ion migration in the opposite direction. The activation barrier can be directly compared to the experimentally measured activation energy. First, we assessed the energetics of the sodium vacancy formations.

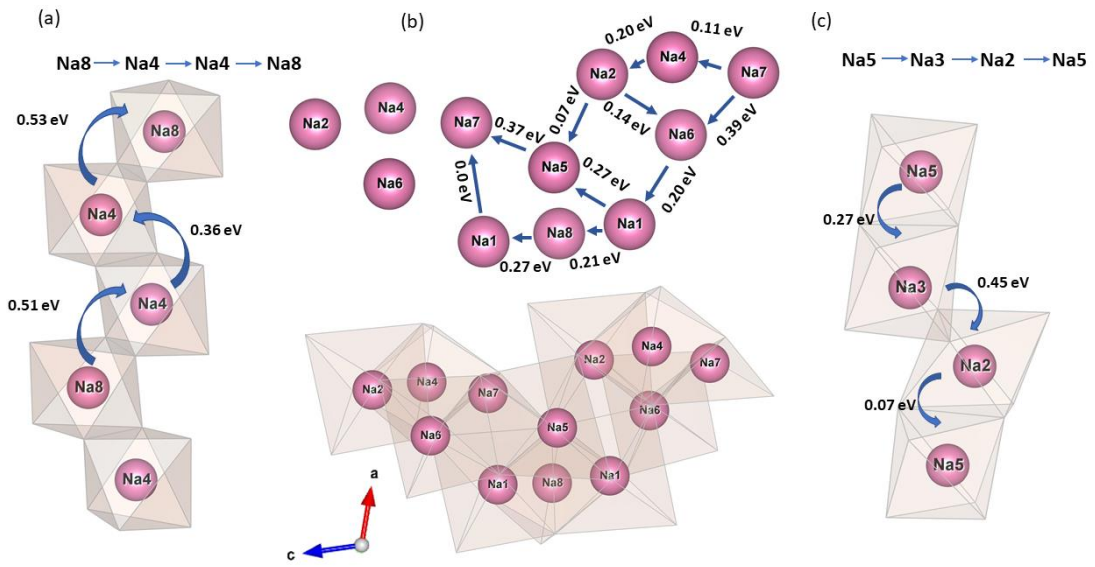

Figure 6. Vacancy migration activation barriers along different diffusion paths in $Na_{15}Cu_3Ga_6S_{18}$. (a) Activation barrier along Na4–Na8–Na4–Na4–Na8 is 0.53 eV (b) Lowest energy path is along [001] direction with a barrier of 0.27 eV (c) Activation barrier along Na5–Na3–Na2–Na5 is 0.45 eV.

There are 8 crystallographically distinct sodium atoms, and thus there are 8 possible vacancy sites. All sodium vacancy formation energies are calculated in the small concentration limit, thus the volume of the simulation cell was kept fixed at the ideal structure volume.

Formation energies for all the sites are within 0.25 eV from each-other (listed in Table 3), with the smallest being that for Na6 (2.14 eV) and the largest is that for the Na3 (2.38 eV). Sodium vacancies in the sites that occupy positions in the possible conduction channel, Na4 and Na8, have very similar formation energies of 2.23 and 2.24 eV. In the table (Table 3) we have also listed the bond valence sum values of each of these Na-ions, however, apparently there seems to be no direct correlation between the defect formation energies with BVS values. Further, we carried out the NEB calculations of the activation

energy for the vacancy assisted diffusion for the pathway along the channel. Due to the staggered arrangement of the sodium ions in the channel, the preferred path for the vacancy migration is by alternating between the rows of the atoms, which corresponds to migration from Na8 to Na4 and between Na4 and Na4 sites (see Figure 6a). The second transition corresponds to the return into the original row.

Table 3. Defect formation energies and bond valence sum values of eight crystallographically distinct Na^+ ions.

Site	Na1	Na2	Na3	Na4	Na5	Na6	Na7	Na8
Formation energy (eV)	2.30	2.36	2.38	2.22	2.23	2.14	2.28	2.24
Bond Valence Sum	0.958	0.989	0.991	1.109	0.847	0.985	1.004	1.219

The DFT prediction for the activation energy along this path is 0.53 eV. In addition to migration along the channels, we investigated a possibility of other migration paths. In particular, sodium ions form a possible diffusion path along the [001] direction of the cell. Sites occupied by the sodium atoms form rather complex interlocking arrangement with the key block being (almost) flat quadrilateral shape consisting of Na2-Na4-Na7-Na6 sites (Figure 6b). This shape is connected to the next tilted identical shape either via Na5 site, or by a Na6-Na1-Na8-Na1-Na7 chain of transitions (Figure 6b). The latter has the lowest barrier with the magnitude of 0.27 eV for the transport in the [001] direction. Another set of diffusion routes exist in [100] and [010] crystallographic directions (Figure 6c). These routes are crystallographically identical, include atoms -Na2-Na3-Na5-, and there are 2 routes in each direction per primitive cell. The highest activation barrier along this route as

predicted by DFT is for the vacancy migration between sites Na2 and Na3, with the magnitude of 0.45 eV. The pathway with the lowest activation energy is along [001] direction in the lattice with the activation energy of 0.27 eV. This activation energy is significantly lower than experimental value, that of 0.68 eV. This kind of discrepancies between the experimental and theory can be attributed to the presence of little impurity phase, specially impurities in the grain boundaries can create substantial impedance to ion-conduction. Unfortunately, all our attempts to form 100% pure sample have failed.

4. CONCLUSIONS

Three-dimensional open architecture built by unusual linearly coordinated S–Cu–S (180°) along with tetrahedrally coordinated Cu1 polyhedra within the same framework makes this compound distinct from other chalcogenide-based open framework structures. To the best of our knowledge, $Na_{15}Cu_3Ga_6S_{18}$ is the first compound in the quaternary series of *A*–Cu–Ga–S (*A* = alkali metal) system. This has been achieved by our strategy to replace part of the sodium ion from $Na_6Ga_2S_6$ by Cu^+ via metathesis route (Figure S7). Despite having a sea of sodium ions in the channels, the compound did not show a high Na-ion conduction and emphasizes the need to create defect in the structure. The coordination stability of the linearly coordinated Cu^+ can be attributed to higher cation polarization due to high amount of alkali ion substitution and strong *s*-*d* hybridization of Cu^+. However, it requires more fundamental study in solid state chemistry of Cu^+, especially in chalcogenide matrix, if understood clearly, this can unravel the limit of maximum number of alkali-ions substitution into the framework when there is presence of linear S – Cu – S bonds.

ACKNOWLEDGEMENTS

The authors are grateful for the funding of this work from National Science Foundation (NSF) under the grant No. DMR- 1809128.

SUPPLEMENTARY INFORMATION

SYNTHESIS

$Na_{15}Cu_3Ga_6S_{18}$ was synthesized by solid state metathesis route using 0.6 mmol of $Na_6Ga_2S_6$ and 0.6 mmol of CuCl in s sealed quartz tube of 12 cm length and 1.1 cm diameter. $Na_6Ga_2S_6$ was prepared by stoichiometric mixture of 3.5 mmol of Na_2S, 2.3 mmol of Ga and 3.5 mmol of S. Bulk quantities of $Na_{15}Cu_3Ga_6S_{18}$ was also synthesized by 2 mmol of Cu, 4 mmol of Ga, 5 mmol of Na_2S and 7 mmol of S in a sealed quartz tube of 12 cm length and 1.1 cm diameter. All the reactants used in the synthesis were purchased from Alfa Aesar. The compound was prepared in a scale of 1.5 g. All the powder precursors along with Ga shavings were weighed accordingly and loaded into pre-heated graphitized quartz ampoule inside an argon filled glovebox (O2 < 1ppm). To prevent exposure from air, the ampoules were taken out with the help of an adapter and flame sealed under vacuum. The sealed ampoules were heated to 700 °C at a rate of 20 °C /h, dwelled for five days, and subsequently cooled to room temperature at a rate 35 °C/h. There was no sign of any compound deposition in the cold zone. After breaking the ampoule in an argon-filled glove box, nice pale-yellow crystals (Figure S1 a) were obtained. Single crystals from the

as synthesized compound were used to collect the single-crystal X-ray diffraction data and the hand ground powder samples were used for other characterization.

X-RAY CRYSTALLOGRAPHY

Good quality crystal was mounted on a thin glass fiber with epoxy glue. Diffraction data was collected on Bruker smart apex diffractometer equipped with a sealed tube X-ray source with Mo–Kα radiation (λ = 0.71073 Å). SMART software[1] was used to collect the diffraction data with a scan rate of 0.3° in ω scan and 20 s/frame exposure time. Data integration and absorption correction was done by using programs SAINT and SADABS.[2] SHELXS-97 and difference Fourier syntheses were used to solve the structure.[3] Full-matrix least-squares refinement against $|F^2|$ was carried out using the SHELXTL-PLUS suite of programs.[2] Centrosymmetric space group C2/c (No. 15) was assigned based on the systematic absences of reflections. The positions of Ga, Cu and S were easily located from the difference Fourier maps. Isotropic refinement resulted in a good thermal parameters for Ga, Cu and S atoms. After the first cycle of refinement all the Na positions were assigned leaving no unaccounted residual electron density. Further isotropic refinements resulted reasonably good thermal parameters for all the Na atoms. All the occupancies were refined freely, and no Na-vacancies were observed. Final refinements including the refinements of anisotropic thermal parameters were performed using SHELX-2018 incorporated in ShelXLe.[4]After the final anisotropic refinement and application of the weight convergence scheme, the weighted *R*-factor (wR_2) reduced significantly. Crystal data and final structure refinement parameters are given in Table 1, and selected bond lengths are provided

in Table S1. The atomic coordinates along with their thermal displacement parameters are provided in Tables S2 and S3.

POWDER X-RAY DIFFRACTION

Powder X-ray diffraction pattern was collected from PANalytical X'Pert Pro diffractometer equipped with a Cu Kα anode and a linear array PIXcel detector. Finely ground sample (Figure S1b) of $Na_{15}Cu_3Ga_6S_{18}$ was loaded into an airtight cell covered with kapton film to prevent the sample from exposing to air. PXRD pattern was collected over a 2θ range of 5 to 90° with an average scanning rate of $0.0472°s^{-1}$.

OPTICAL BAND GAP MEASUREMENTS

Optical band gap measurements were performed on Varian Cary 5000 UV-Vis-NIR spectrophotometer equipped with praying mantis set up. Powder samples ground inside the glove box from as-synthesized batch of $Na_{15}Cu_3Ga_6S_{18}$ was used to collect the DRS spectrum. $BaSO_4$ powder (Fisher, 99.2%) was used as a ~100 % reflectance standard. Kubelka - Munk function was applied to calculate the band gap.

IONIC CONDUCTIVITY MEASUREMENTS

AC impedance measurements were performed on biologic instruments SP-150 in the frequency range of 1.00 Hz to 1MHz with a voltage amplitude of 500mV. The as synthesized powder samples were cold pressed using 280 MPa force in a stainless steel pressing die having inner diameter of 0.635 mm to make the pellet. Indium foil of thickness 0.05mm was pressed onto both sides of the pellet which acts as blocking electrode. The

pellet was placed in an air-tight Swagelok cell to prevent it from air exposure. The whole set up was loaded into a box furnace with temperature controller to measure the temperature dependence of ionic conductivity. Impedance data were collected from room temperature (25 °C) to 75 °C for every 10 °C interval. Before taking measurements, the temperature was held constant at least for an hour to reach the thermal equilibrium. No reaction was found after the measurements between the solid electrolyte and the blocking electrode. The equivalent circuit used, and the fitting parameters for room temperature ionic conductivity has been detailed in Figure S5. The activation energies were calculated using $\sigma_T = \sigma_o \exp(-E_a/k_B T)$ where σ_T is the ionic conductivity, σ_o is a pre-exponential factor, T is the absolute temperature, and k_B is the Boltzmann constant.

BVEL MAPS

Bondstr incorporated in FullProf suite of programs is used to construct the BVEL (Bond valence energy landscapes). Hypothetical diffusion paths for the mobile ion can be mapped based on the bond valence mismatch as defined by Adams.[5] Figures S6 a and b were plotted as an isosurface using VESTA[6] at an energy level $|\Delta V| = 0.5$ *v.u.*

DFT CALCULATIONS

Electronic structure calculations were performed in the framework of density functional theory as implemented in VASP computational package[7-10]. Calculations were performed using projector augmented-wave (PAW) with generalized gradient approximation (GGA) exchange-correlation (XC) functionals parametrized according to PBEsol[11] which is a revised version of Perdew–Burke–Ernzerhof (PBE).[12] Relaxation of

atomic coordinates and the unit-cell parameters were performed until the maximum force on the atoms was less than 10^{-2} eV/Å, using energy cutoff for the plane wave expansion of the electronic wave function was 500 eV and 4x3x3 Monkhorst-Pack[13] k-point grid. Total energy convergence criteria was set to 10^{-6} eV/atom. Hybrid functional calculations employed HSE06[14] functional, with the energy cutoff of 500 eV and Γ-point only k-mesh for the Brillouin zone integration. Relaxed atomic structure by the standard DFT was used for Defect formation energies and NEB calculations. Defect formation energies where calculated by the structural atomic relaxation and keeping the volume constant. We chose sodium metal as a reference state for all defect energy calculations. NEB calculations used 5 images to resolve the transition state and calculate the activation barrier. Chemical bonding analysis of plane-wave data by Crystal Orbital Hamiltonian Population (COHP) were performed using LOBSTER[15-17].

Table S1. Selected bond lengths (Å) in $Na_{15}Cu_3Ga_6S_{18}$.

atom-atom	***d*(Å)**	**atom-atom**	***d*(Å)**	**atom-atom**	***d*(Å)**
Ga1 – S1	2.2528(10)	Ga3 – S8	2.2492(10)	Cu1 – S6	2.3583(10)
Ga1 – S2	2.2782(10)	Ga3 – S9	2.2550(10)	Cu1 – S1$^{\#2}$	2.3710(11)
Ga1 – S3	2.2972(10)	Ga3 – S4	2.3036(10)	Cu1 – S9$^{\#2}$	2.4190(12)
Ga1 – S4	2.3055(10)	Ga3 – S7$^{\#1}$	2.3315(10)	Cu1 – S1	2.4394(11)
Ga2 – S5	2.2359(10)			Cu2 – S2	2.1593(10)
Ga2 – S6	2.2470(10)				
Ga2 – S3	2.3077(10)				
Ga2 – S7	2.3169(10)				

Symmetry transformations used to generate equivalent atoms:

#1 x-1/2,-y+1/2,z-1/2 #2 -x+1/2,-y+1/2,-z+1

Table S2. Final atomic coordinates and equivalent isotropic displacement parameters for $Na_{15}Cu_3Ga_6S_{18}$. $U_{(eq)}$ = 1/3 of the trace of the orthogonalized U_{eq} tensor.

Atom	Wyckoff	Occupancy	x/a	y/b	z/c	U(Å^2)
Ga(1)	8*f*	1	0.4148(1)	0.3295(1)	0.3859(1)	0.008(1)
Ga(2)	8*f*	1	0.5818(1)	0.1758(1)	0.5505(1)	0.008(1)
Ga(3)	8*f*	1	0.2575(1)	0.1732(1)	0.2227(1)	0.008(1)
Cu(1)	8*f*	1	0.3274(1)	0.2458(1)	0.5797(1)	0.024(1)
Cu(2)	4*a*	1	0.5	0.5	0.5	0.023(1)
S(1)	8*f*	1	0.3154(1)	0.3438(1)	0.4650(1)	0.013(1)
S(2)	8*f*	1	0.5061(1)	0.4522(1)	0.3837(1)	0.015(1)
S(3)	8*f*	1	0.5057(1)	0.2021(1)	0.4140(1)	0.009(1)
S(4)	8*f*	1	0.3364(1)	0.3072(1)	0.2493(1)	0.010(1)
S(5)	8*f*	1	0.6716(1)	0.545(1)	0.5530(1)	0.014(1)
S(6)	8*f*	1	0.4717(1)	0.1592(1)	0.6192(1)	0.012(1)
S(7)	8*f*	1	0.6696(1)	0.3057(1)	0.5860(1)	0.010(1)
S(8)	8*f*	1	0.3483(1)	0.517(1)	0.2241(1)	0.013(1)
S(9)	8*f*	1	0.1593(1)	0.1617(1)	0.3033(1)	0.012(1)
Na(1)	8*f*	1	0.5085(2)	0.205(1)	0.3777(1)	0.033(1)
Na(2)	8*f*	1	0.3236(2)	0.4836(1)	0.2064(1)	0.038(1)
Na(3)	8*f*	1	0.4933(1)	0.6446(1)	0.3570(1)	0.026(1)
Na(4)	8*f*	1	0.3320(1)	0.3189(1)	0.0811(1)	0.019(1)
Na(5)	8*f*	1	0.3604(1)	0.1437(1)	0.7341(1)	0.026(1)
Na(6)	8*f*	1	0.6658(1)	0.-1272(1)	0.5556(1)	0.024(1)
Na(7)	8*f*	1	0.7705(2)	0.0212(1)	0.4375(1)	0.027(1)
Na(8)	4*e*	1	0.5	0.1871(2)	0.25	0.017(1)

Table S3. Anisotropic displacement parameters ($Å^2 x\ 10^3$) for $Na_{15}Cu_3Ga_6S_{18.}$ The anisotropic displacement factor exponent takes the form: $-2p^2[\ h^2a^{*2}U^{11} + ... + 2\ h\ k\ a^*\ b^*\ U^{12}]$

Atoms	U_{11}	U_{22}	U_{33}	U_{23}	U_{13}	U_{12}
Ga(1)	8(1)	7(1)	8(1)	0(1)	2(1)	0(1)
Ga(2)	7(1)	7(1)	8(1)	0(1)	2(1)	0(1)
Ga(3)	8(1)	7(1)	8(1)	0(1)	2(1)	1(1)
Cu(1)	20(1)	22(1)	26(1)	-2(1)	3(1)	4(1)
Cu(2)	24(1)	25(1)	19(1)	-6(1)	5(1)	1(1)
S(1)	14(1)	12(1)	15(1)	1(1)	9(1)	2(1)
S(2)	20(1)	9(1)	19(1)	-2(1)	8(1)	-6(1)
S(3)	11(1)	8(1)	7(1)	0(1)	1(1)	2(1)
S(4)	13(1)	8(1)	8(1)	1(1)	0(1)	-2(1)
S(5)	15(1)	8(1)	19(1)	1(1)	5(1)	5(1)
S(6)	12(1)	13(1)	15(1)	3(1)	8(1)	3(1)
S(7)	12(1)	9(1)	8(1)	0(1)	1(1)	-4(1)
S(8)	13(1)	9(1)	16(1)	0(1)	4(1)	3(1)
S(9)	14(1)	12(1)	14(1)	-2(1)	9(1)	-1(1)
Na(1)	50(1)	13(1)	33(1)	-1(1)	9(1)	6(1)
Na(2)	63(2)	13(1)	33(1)	2(1)	7(1)	-4(1)
Na(3)	19(1)	24(1)	38(1)	-2(1)	15(1)	-2(1)
Na(4)	17(1)	24(1)	18(1)	0(1)	7(1)	3(1)
Na(5)	24(1)	28(1)	28(1)	-1(1)	9(1)	3(1)
Na(6)	19(1)	20(1)	33(1)	3(1)	8(1)	1(1)
Na(7)	42(1)	15(1)	25(1)	3(1)	14(1)	1(1)
Na(8)	16(1)	23(1)	14(1)	0	8(1)	0

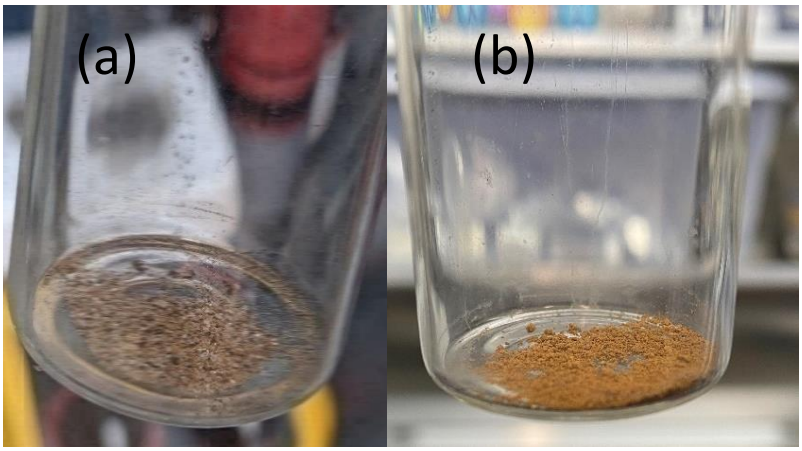

Figure S1. (a) As-synthesized DMF washed crystals; (b) Finely ground sample of $Na_{15}Cu_3Ga_6S_{18}$.

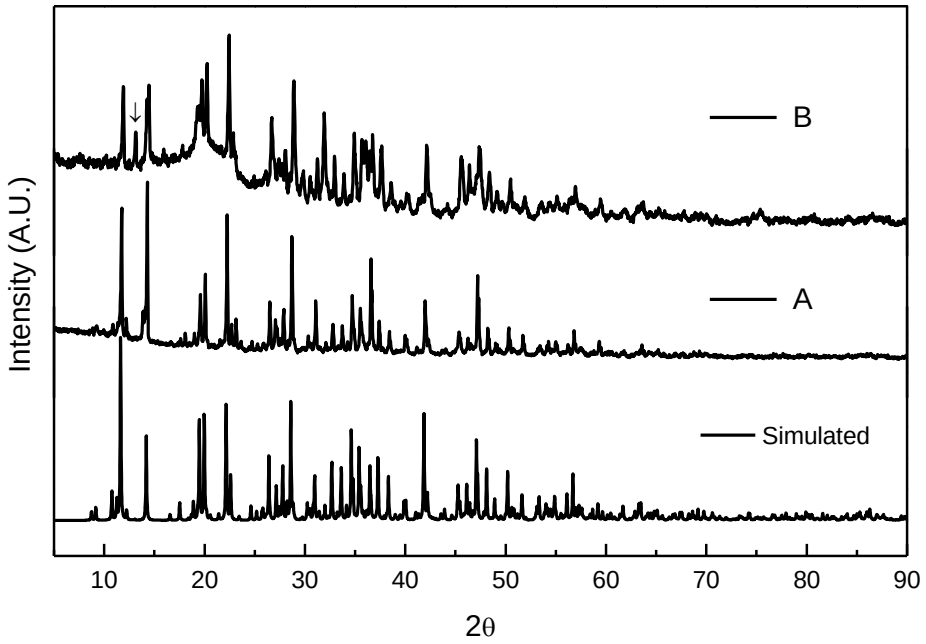

Figure S2. PXRD patterns collected on powder samples from as-synthesized batches, A: Stoichiometric reaction of Na_2S, Cu, Ga, S; B: reaction of $Na_6Ga_2S_6$ + CuCl, arrow indicate an impurity phase. Sample A is the PXRD of manually separated yellowish crystals carefully avoiding the dark crystals. This sample was used for impedance measurements.

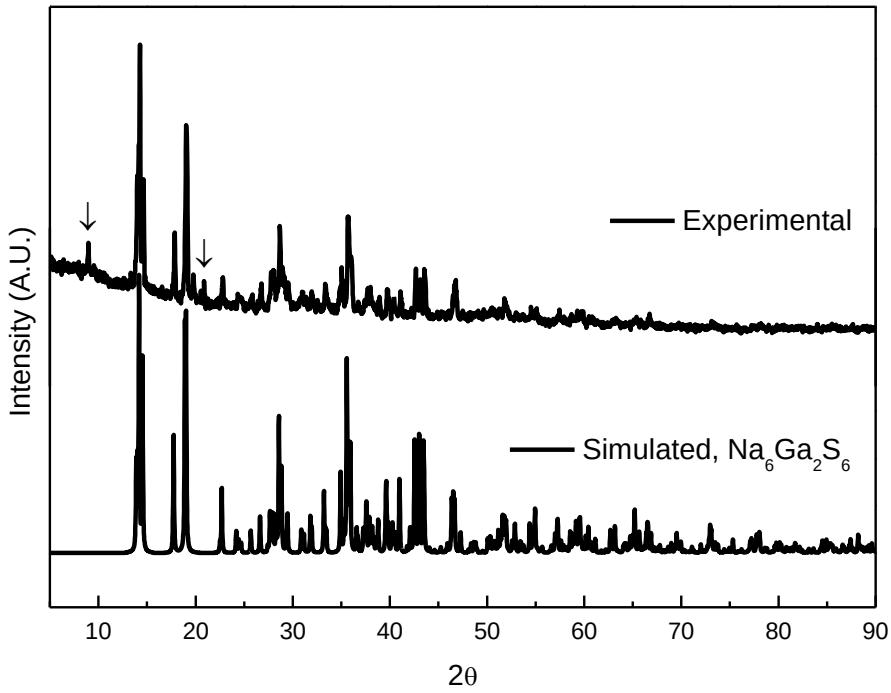

Figure S3. PXRD pattern of as synthesized $Na_6Ga_2S_6$ with the simulated pattern. The arrows indicate the presence of impurity phase, $Na_4Ga_2S_5$ (Eisenmann, B.; Hofmann, A. Crystal structure of hexasodium di-mu-thiobis(dithiogallate) – I. Z. Kristallogr. 1991, 197, 143– 144).

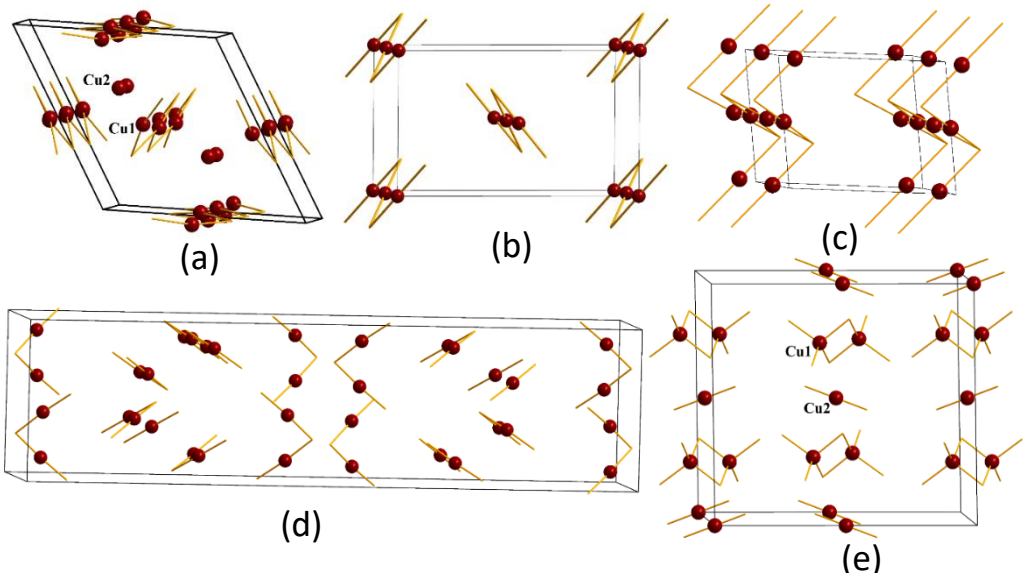

Figure S4. Cu coordination in compounds having linear coordination of Cu (a) $NaCu_5S_3$; (b) KCuS; (c) $CsCu_3S_2$; (d). $Na_4Cu_2S_3$; (e) Current compound (Cu2 in $Na_{15}Cu_3Ga_6S_{18}$).

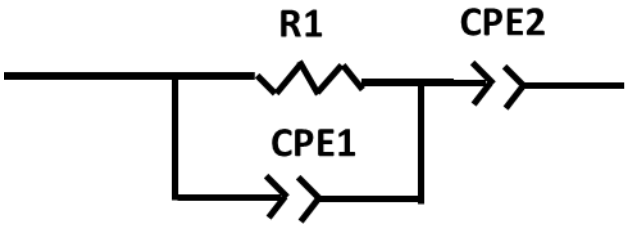

R1	5.801e6 Ohm
Q1	217.5e-12 F.s^(a - 1)
a1	0.8247
Q2	18.49e-9 F.s^(a - 1)
a2	0.6391

Figure S5. Equivalent circuit and the parameters used to fit the impedance data for $Na_{15}Cu_3Ga_6S_{18}$ for the room temperature data.

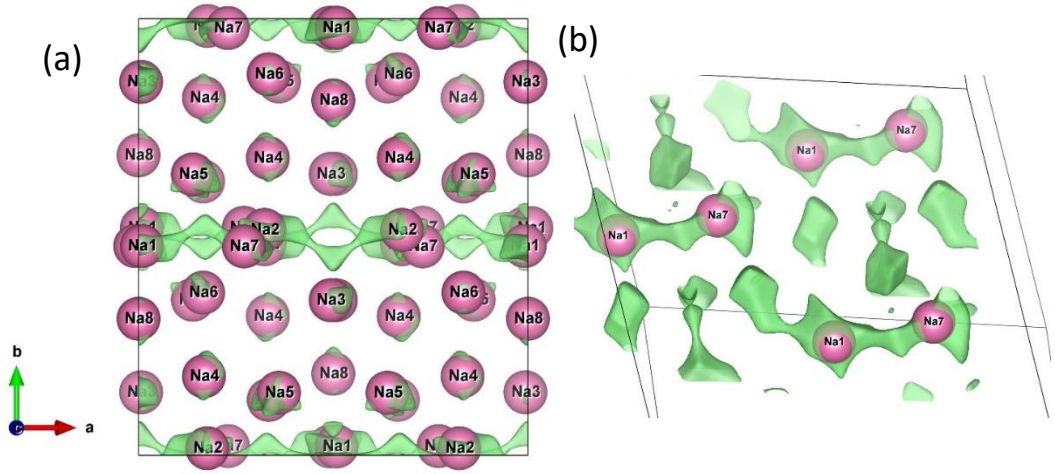

Figure S6. BVEL map for $Na_{15}Cu_3Ga_6S_{18}$ (a) At an isosurface level $|\Delta V| = 0.5\ v.u$ (b) Path between Na1 and Na7, which is found be the lowest vacancy migration from DFT.

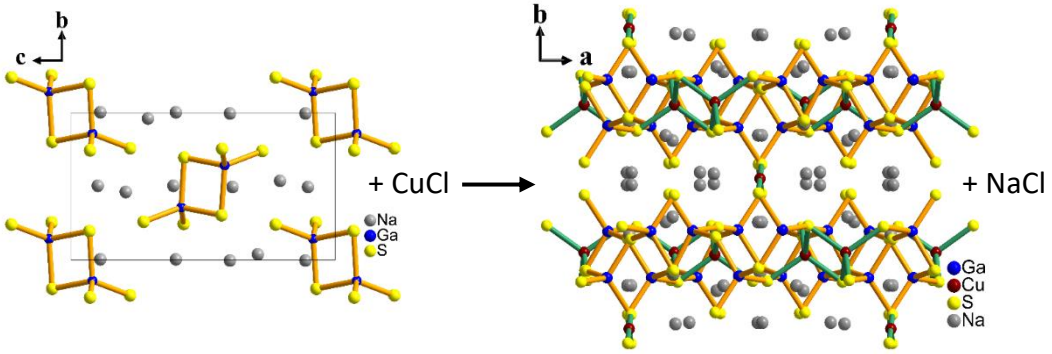

Figure S7. Solid state metathesis reaction between $Na_6Ga_2S_6$ and CuCl (3:3) to synthesize $Na_{15}Cu_3Ga_6S_{18}$.

REFERENCES

1. Bruker- SMART. Bruker AXS Inc., Madison, Wisconsin, USA. 2002.

2. Bruker- SAINT, SADABS and SHELXTL. Bruker AXS Inc., Madison, Wisconsin, USA, 2008.

3. Sheldrick, G. M. A short history of SHELX. Acta Cryst. 2008, A64, 112

4. Hübschle, C. B.; Sheldrick, G. M.; Dittrich, B. ShelXle: A Qt Graphical User Interface for SHELXL. *J. Appl. Crystallogr.* **2011**, *44* (6), 1281–1284. https://doi.org/10.1107/S0021889811043202.

5. Adams, S. Relationship between Bond Valence and Bond Softness of Alkali Halides and Chalcogenides. *Acta Crystallogr. Sect. B Struct. Sci.* **2001**, *57* (3), 278–287. https://doi.org/10.1107/S0108768101003068.

6. Momma, K.; Izumi, F. VESTA 3 for Three-Dimensional Visualization of Crystal, Volumetric and Morphology Data. *J. Appl. Crystallogr.* **2011**, *44* (6), 1272–1276. https://doi.org/10.1107/S0021889811038970.

7. Kresse, G.; Hafner, J. Ab Initio Molecular Dynamics for Liquid Metals. *Phys. Rev. B* **1993**, *47* (1), 558–561. https://doi.org/10.1103/PhysRevB.47.558.

8. Kresse, G.; Furthmüller, J. Efficiency of Ab-Initio Total Energy Calculations for Metals and Semiconductors Using a Plane-Wave Basis Set. *Comput. Mater. Sci.* **1996**, *6* (1), 15–50. https://doi.org/10.1016/0927-0256(96)00008-0.

9. Kresse, G.; Furthmüller, J. Efficient Iterative Schemes for Ab Initio Total-Energy Calculations Using a Plane-Wave Basis Set. *Phys. Rev. B - Condens. Matter Mater. Phys.* **1996**, *54* (16), 11169–11186. https://doi.org/10.1103/PhysRevB.54.11169.

10. Joubert, D. From Ultrasoft Pseudopotentials to the Projector Augmented-Wave Method. *Phys. Rev. B - Condens. Matter Mater. Phys.* **1999**, *59* (3), 1758–1775. https://doi.org/10.1103/PhysRevB.59.1758

11. Perdew, J. P.; Ruzsinszky, A.; Csonka, G. I.; Vydrov, O. A.; Scuseria, G. E.; Constantin, L. A.; Zhou, X.; Burke, K. Restoring the Density-Gradient Expansion for Exchange in Solids and Surfaces. *Phys. Rev. Lett.* **2008**, *100* (13), 136406. https://doi.org/10.1103/PhysRevLett.100.136406.

12. Perdew, J. P.; Burke, K.; Ernzerhof, M. Generalized Gradient Approximation Made Simple. *Phys. Rev. Lett.* **1996**, *77* (18), 3865– 3868, DOI: 10.1103/PhysRevLett.77.3865

13. Monkhorst, H. J.; Pack, J. D. *Special Points for Brillonin-Zone Integrations**; 1976; Vol. 13.

14. Krukau, A. V.; Vydrov, O. A.; Izmaylov, A. F.; Scuseria, G. E. Influence of the Exchange Screening Parameter on the Performance of Screened Hybrid Functionals. *J. Chem. Phys.* **2006**, *125* (22), 224106. https://doi.org/10.1063/1.2404663.

15. Deringer, V. L.; Tchougreeff, A. L.; Dronskowski, R. Crystal Orbital Hamilton Population (COHP) Analysis as Projected from Plane-wave Basis Sets. *J. Phys. Chem. A* **2011**, *115*, 5461– 5466, DOI: 10.1021/jp202489s

16. Maintz, S.; Deringer, V. L.; Tchougréeff, A. L.; Dronskowski, R. Analytic Projection from Plane-Wave and PAW Wavefunctions and Application to Chemical-Bonding Analysis in Solids. *J. Comput. Chem.* **2013**, *34*, 2557– 2567, DOI: 10.1002/jcc.23424

17. Maintz, S.; Deringer, V. L.; Tchougréeff, A. L.; Dronskowski, R. LOBSTER: A tool to extract chemical bonding from plane-wave based DFT. *J. Comput. Chem.* **2016**, *37*, 1030– 1035, DOI: 10.1002/jcc.24300

REFERENCES

1. Aitken, J. A.; Kanatzidis, M. G. Interwoven Pair of Open Frameworks in the Thiosphosphate $K_6Yb_3(PS_4)_5$. *J. Am. Chem. Soc.* **2004**, *126*, 11780–11781. https://doi.org/10.1021/ja0474648.

2. Choudhury, A.; Dorhout, P. K. An Ordered Assembly of Filled Nanoscale Tubules of Europium Seleno-Silicate in the Crystal Structure of a Quaternary Compound. *J. Am. Chem. Soc.* **2007**, *129* (30), 9270–9271. https://doi.org/10.1021/ja073335q.

3. Lin, Y. M.; Massa, W.; Dehnen, S. ″Zeoball″ $[Sn_{36}Ge_{24}Se_{132}]^{24-}$: a molecular anion with zeolite-related composition and spherical shape. *J. Am. Chem. Soc.* **2012**, *134*, 4497– 4500, DOI: 10.1021/ja2115635

4. Zhang, J.; Bu, X.; Feng, P.; Wu, T. Metal chalcogenide supertetrahedral clusters: synthetic control over assembly, dispersibility, and their functional applications. *Acc. Chem. Res.* **2020**, *53* (10), 2261– 2272, DOI: 10.1021/acs.accounts.0c00381

5. Kanatzidis, M. G. Discovery-Synthesis, Design, and Prediction of Chalcogenide Phases. *Inorg. Chem.* **2017**, *56* (6), 3158–3173. https://doi.org/10.1021/acs.inorgchem.7b00188.

6. Sheldrick, W. S.; Wachhold, M. Chalcogenidometalates of the Heavier Group 14 and 15 Elements. *Coord. Chem. Rev.* **1998**, *176* (1), 211–322. https://doi.org/10.1016/S0010-8545(98)00120-9.

7. Zheng, N.; Bu, X.; Wang, B.; Feng, P. Microporous and Photoluminescent Chalcogenide Zeolite Analogs. *Science* **2002**, *298* (5602), 2366–2369. https://doi.org/10.1126/science.1078663.

8. Choudhury, A.; Dorhout, P. K. Synthesis, Structure, and Optical Properties of the Quaternary Seleno-Gallates $NaLnGa_4Se_8$ (Ln = La, Ce, Nd) and Their Comparison with the Isostructural Thio-Gallates. *Inorg. Chem.* **2008**, *47* (9), 3603–3609. https://doi.org/10.1021/ic701986j.

9. Zhang, Z.; Zhang, J.; Wu, T.; Bu, X.; Feng, P. Three-Dimensional Open Framework Built from Cu-S Icosahedral Clusters and Its Photocatalytic Property. *J. Am. Chem. Soc.* **2008**, *130* (46), 15238–15239. https://doi.org/10.1021/ja805449p.

10. Choudhury, A.; Grandjean, F.; Long, G. J.; Dorhout, P. K. $Na_{1.515}EuGeS_4$, A Three-Dimensional Crystalline Assembly of Empty Nanotubules Constructed with Europium(II/III) Mixed Valence Ions. *Inorg. Chem.* **2012**, *51* (21), 11779–11786. https://doi.org/10.1021/ic301724v.

11. Choudhury, A.; Dorhout, P. K. Alkali-Metal Thiogermanates: Sodium Channels and Variations on the La_3CuSiS_7 Structure Type. *Inorg. Chem.* **2015**, *54* (3), 1055–1065. https://doi.org/10.1021/ic502418s.

12. Adhikary, A.; Yaghoobnejad Asl, H.; Sandineni, P.; Balijapelly, S.; Mohapatra, S.; Khatua, S.; Konar, S.; Gerasimchuk, N.; Chernatynskiy, A. V.; Choudhury, A. Unusual Atmospheric Water Trapping and Water Induced Reversible Restacking of 2D Gallium Sulfide Layers in $NaGaS_2$ Formed by Supertetrahedral Building Unit. *Chem. Mater.* **2020**, *32* (13), 5589–5603. https://doi.org/10.1021/acs.chemmater.0c00836.

13. Chica, D. G.; Iyer, A. K.; Cheng, M.; Ryan, K. M.; Krantz, P.; Laing, C.; dos Reis, R.; Chandrasekhar, V.; Dravid, V. P.; Kanatzidis, M. G. P_2S_5 Reactive Flux Method for the Rapid Synthesis of Mono- and Bimetallic 2D Thiophosphates $M_{2-x}M'_xP_2S_6$. *Inorg. Chem.* **2021**, *60* (6), 3502–3513. https://doi.org/10.1021/acs.inorgchem.0c03577.

14. Kraft, M. A.; Culver, S. P.; Calderon, M.; Böcher, F.; Krauskopf, T.; Senyshyn, A.; Dietrich, C.; Zevalkink, A.; Janek, J.; Zeier, W. G. Influence of Lattice Polarizability on the Ionic Conductivity in the Lithium Superionic Argyrodites Li_6PS_5X (X = Cl, Br, I). *J. Am. Chem. Soc.* **2017**, *139* (31), 10909–10918. https://doi.org/10.1021/jacs.7b06327.

15. Manos, M. J.; Kanatzidis, M. G. Metal Sulfide Ion Exchangers: Superior Sorbents for the Capture of Toxic and Nuclear Waste-Related Metal Ions. *Chem. Sci.* 2016, *7*, 4804–4824. https://doi.org/10.1039/c6sc01039c.

16. Kuo, S. M.; Chang, Y. M.; Chung, I.; Jang, J. I.; Her, B. H.; Yang, S. H.; Ketterson, J. B.; Kanatzidis, M. G.; Hsu, K. F. New Metal Chalcogenides $Ba_4CuGa_5Q_{12}$ (Q = S, Se) Displaying Strong Infrared Nonlinear Optical Response. *Chem. Mater.* **2013**, *25* (12), 2427–2433. https://doi.org/10.1021/cm400311v.

17. Shin, D.; Ngaboyamahina, E.; Zhou, Y.; Glass, J. T.; Mitzi, D. B. Synthesis and Characterization of an Earth-Abundant $Cu_2BaSn(S,Se)_4$ Chalcogenide for Photoelectrochemical Cell Application. *J. Phys. Chem. Lett.* **2016**, *7* (22), 4554–4561. https://doi.org/10.1021/acs.jpclett.6b02010.

18. Shin, D.; Saparov, B.; Mitzi, D. B. Defect Engineering in Multinary Earth-Abundant Chalcogenide Photovoltaic Materials. *Adv. Energy Mater.* **2017**, *7* (11), 1602366. https://doi.org/10.1002/aenm.201602366.

19. Zeier, W. G.; Zevalkink, A.; Gibbs, Z. M.; Hautier, G.; Kanatzidis, M. G.; Snyder, G. J. Thinking Like a Chemist: Intuition in Thermoelectric Materials. *Angew. Chemie Int. Ed.* **2016**, *55* (24), 6826–6841. https://doi.org/10.1002/anie.201508381.

20. Mohapatra, S.; Adhikary, A.; Ghosh, K.; Choudhury, A. Magnetically Frustrated Quaternary Chalcogenides with Interpenetrating Diamond Lattices. *Inorg. Chem.* **2017**, *56* (14), 7650–7656. https://doi.org/10.1021/acs.inorgchem.7b00121.

21. Greenwood, N. N.; Earnshaw, A. “Chemistry of the Elements”, 2nd edition, Butterworth-Heinemann, Linacre House, Jordan Hill, Oxford OX2 8DP. **1998**, Chapter 28, Pages 1173-1199.

22. Goble, R. J. Relationship Between Crystal Structure, Bonding and Cell Dimensions in the Copper Sulfides *Can. Mineral.* **1985**, 23, 61– 76

23. Wang, Y.; Xujie, L.; Zheng, C.; Liu, X.; Chen, Z.; Yang, W.; Lin, J.; Huang, F. Chemistry Design Towards a Stable Sulfide-Based Superionic Conductor $Li_4Cu_8Ge_3S_{12}$. *Angew. Chemie - Int. Ed.* **2019**, *58* (23), 7673–7677. https://doi.org/10.1002/anie.201901739.

24. Zhang, X.; Wang, Q.; Ma, Z.; He, J.; Wang, Z.; Zheng, C.; Lin, J.; Huang, F. Synthesis, Structure, Multiband Optical, and Electrical Conductive Properties of a 3D Open Cubic Framework Based on $[Cu_8Sn_6S_{24}]z$- Clusters. *Inorg. Chem.* **2015**, *54* (11), 5301–5308. https://doi.org/10.1021/acs.inorgchem.5b00317.

25. Wang, L.; Wu, T.; Zuo, F.; Zhao, X.; Bu, X.; Wu, J.; Feng, P. Assembly of Supertetrahedral T5 Copper-Indium Sulfide Clusters into a Super-Supertetrahedron of Infinite Order. *J. Am. Chem. Soc.* **2010**, *132* (10), 3283–3285. https://doi.org/10.1021/ja9100672.

26. Zhang, R. C.; Zhang, J. C.; Cao, Z.; Wang, J. J.; Liang, S. S.; Cong, H. J.; Wang, H. J.; Zhang, D. J.; An, Y. L. Unusual Flexibility of Microporous Sulfides during Ion Exchange. *Inorg. Chem.* **2018**, *57* (21), 13128–13136. https://doi.org/10.1021/acs.inorgchem.8b01238.

27. Lv, J.; Zhang, J.; Xue, C.; Hu, D.; Wang, X.; Li, D. S.; Wu, T. Two Penta-Supertetrahedral Cluster-Based Chalcogenide Open Frameworks: Effect of the Cluster Spatial Connectivity on the Electron-Transport Efficiency. *Inorg. Chem.* **2019**, *58* (6), 3582–3585. https://doi.org/10.1021/acs.inorgchem.8b03503.

28. Zhang, J.; Wang, X.; Lv, J.; Li, D. S.; Wu, T. A Multivalent Mixed-Metal Strategy for Single-Cu+-Ion-Bridged Cluster-Based Chalcogenide Open Frameworks for Sensitive Nonenzymatic Detection of Glucose. *Chem. Commun.* **2019**, *55* (45), 6357–6360. https://doi.org/10.1039/c9cc02905b.

29. Zhang, R. C.; Yao, H. G.; Ji, S. H.; Liu, M. C.; Ji, M.; An, Y. L. $(H_2en)_2Cu_8Sn_3S_{12}$: A Trigonal CuS_3-Based Open-Framework Sulfide with Interesting Ion-Exchange Properties. *Chem. Commun.* **2010**, *46* (25), 4550–4552. https://doi.org/10.1039/b924581b.

30. Zhang, R.-C.; Yao, H.-G.; Ji, S.-H.; Liu, M.-C.; Ji, M.; An, Y.-L. Copper-Rich Framework Sulfides: $A_4Cu_8Ge_3S_{12}$ (A = K, Rb) with Cubic Perovskite Structure Two Copper-Rich Open-Framework Sulfides, K_4Cu_8Ge. *J. Chem. Soc., Chem. Commun* **2010**, *49* (4), 1556–1558. https://doi.org/10.1021/ic100690q.

31. Behrens, M.; Ordolff, M. E.; Näther, C.; Bensch, W.; Becker, K. D.; Guillot-Deudon, C.; Lafond, A.; Cody, J. A. New Three-Dimensional Thiostannates Composed of Linked Cu8S 12 Clusters and the First Example of a Mixed-Metal Cu_7SnS_{12} Cluster. *Inorg. Chem.* **2010**, *49* (18), 8305–8309. https://doi.org/10.1021/ic100688z.

32. Tan, K.; Parise, J. B.; Darovsky, A. Synthesis of a Novel Open-Framework Sulfide, $CuGe_2S_5 \cdot (C_2H_5)_4N$, and Its Structure Solution Using Synchrotron Imaging Plate Data. *J. Am. Chem. Soc.* **1995**, *117* (26), 7039–7040. https://doi.org/10.1021/ja00131a042.

33. Burschka, C. H. $CsCu_4S_3$ Und $CsCu_3S_2$: Sulfide Mit Tetraedrisch Und Linear Koordiniertem Kupfer. *Z. Anorg. Allg. Chem*. **1980**, *463* (1), 65–71. https://doi.org/10.1002/zaac.19804630108.

34. Savelsberg, G.; Schäfer, H. Darstellung Und Kristallstruktur von Na_2AgAs Und KCuS. *Zeitschrift fur Naturforsch. - Sect. B J. Chem. Sci.* **1978**, *33* (7), 711–713. https://doi.org/10.1515/znb-1978-0705.

35. Effenberger, H.; Pertlik, F. Crystal Structure of NaCu5S3. *Monatsh. Chem.*, **1985**, *116* (8–9), 921–926. https://doi.org/10.1007/BF00809185.

36. Klepp, K. O.; Sing, M.; Boller, H. Preparation and Crystal Structure of $Na_4Cu_2S_3$, a Thiocuprate with Discrete Anions. *J. Alloys Compd.* **1992**, *184* (2), 265–273. https://doi.org/10.1016/0925-8388(92)90500-9.

37. Mooser, E.; Pearson, W. B. On the Crystal Chemistry of Normal Valence Compounds. *Acta Crystallogr.* **1959**, *12* (12), 1015–1022. https://doi.org/10.1107/s0365110x59002857.

38. Hestermann, K.; Hoppe, R. Notiz über KCuO. *Z. Anorg. Allg. Chem.*, **1968**, *360* (3–4), 113–116. https://doi.org/10.1002/zaac.19683600302.

39. Savelsberg, G.; Schäfer, H. Ternäre Pnictide Und Chalkogenide von Alkalimetallen Und IB- Bzw.IIB-Elementen. *Zeitschrift fur Naturforsch. - Sect. B J. Chem. Sci.* **1978**, *33* (4), 370–373. https://doi.org/10.1515/znb-1978-0404.

40. Kirfel, A.; Eichhorn, K. Accurate Structure Analysis with Synchrotron Radiation. The Electron Density in Al_2O_3 and Cu_2O. *Acta Crystallogr. Sect. A* **1990**, *46* (4), 271–284. https://doi.org/10.1107/S0108767389012596.

41. Cava, R. J.; Reidinger, F.; Wuensch, B. J. Mobile Ion Distribution and Anharmonic Thermal Motion in Fast Ion Conducting Cu_2S. *Solid State Ionics* **1981**, *5* (C), 501–504. https://doi.org/10.1016/0167-2738(81)90302-7.

42. Gaudin, E.; Boucher, F.; Evain, M. Some Factors Governing Ag+ and Cu+ Low Coordination in Chalcogenide Environments. *J. Solid State Chem.* **2001**, *160* (1), 212–221. https://doi.org/10.1006/jssc.2001.9225.

43. P. Kubelka, and F. Munk, Ein Beitrag Zur Optik Der Farbanstriche. *Z. Techn. Phys*. **1931**, *12*, 593 -601.

44. Krukau, A. V.; Vydrov, O. A.; Izmaylov, A. F.; Scuseria, G. E. Influence of the Exchange Screening Parameter on the Performance of Screened Hybrid Functionals. *J. Chem. Phys.* **2006**, *125* (22), 224106. https://doi.org/10.1063/1.2404663.

45. Kim, S. K.; Mao, A.; Sen, S.; Kim, S. Fast Na-Ion Conduction in a Chalcogenide Glass-Ceramic in the Ternary System Na_2Se-Ga_2Se_3-$GeSe_2$. *Chem. Mater.* **2014**, *26* (19), 5695–5699. https://doi.org/10.1021/cm502542p.

46. Zhai, S.; Li, L.; Chen, F.; Jiao, Q.; Rüssel, C.; Lin, C. Glass Formation and Ionic Conduction Behavior in $GeSe_2$-Ga_2Se_3-NaI Chalcogenide System. *J. Am. Ceram. Soc.* **2015**, *98* (12), 3770–3774. https://doi.org/10.1111/jace.13815.

47. Mills, G.; Jónsson, H.; Schenter, G. K. Reversible Work Transition State Theory: Application to Dissociative Adsorption of Hydrogen. *Surf. Sci.* **1995**, *324*, 305– 337, DOI: 10.1016/0039-6028(94)00731-4

V. DISCOVERY OF AN OLIVINE-TYPE LITHIUM MANGANESE THIOPHOSPHATE, $LiMnPS_4$, VIA BUILDING BLOCK APPROACH

Srikanth Balijapelly,[a] Kartik Ghosh,[b] Aleksandr V. Chernatynskiy,[c] Amitava Choudhury[a,]*

[a]Department of Chemistry, Missouri University of Science and Technology, Rolla, MO 65409, USA. E-mail: choudhurya@mst.edu

[b]Department of Physics, Astronomy and Materials Sci, Missouri State University, 901 S. National Ave., Springfield, MO 65897, USA

[c]Department of Physics, Missouri University of Science and Technology, Rolla, MO 65409, USA

ABSTRACT

An olivine-type orthothiophospate $LiMnPS_4$ has been synthesized for the first time through building block approach by reacting preformed ternary lithium thiophospate with $MnCl_2$. Diffuse reflectance measurements show an optical band gap of 2.36 eV which is further confirmed by DFT calculations. Irreversible weak ferromagnetic ordering and metamagnetism are verified through priliminary magnetic measurements.

1. INTRODUCTION

Transition metal oxy-phosphates are ubiquitous as they are found in mineral kingdom and easily made in the laboratory.[1, 2] A large number of oxy-phosphates especially ortho-phosphates of transition metals have been synthesized in the last couple of decades as these materials became potential candidates for electrodes and solid-electrolytes in Li-

and Na-ion batteries.[3-5] On the other hand, as of now there is no report of any chalcophosphate mineral;[6] as they can only be accessed through laboratory synthesis.[7-21] Synthetic chalco-phosphates can form a myriad of chalcophosphate anions, $[P_xQ_y]^{z-}$ (Q = S, Se) which includes $[PQ_4]^{3-}$,[8,9, 11, 13, 14] $[P_2Q_6]^{4-}$,[7, 12, 17, 18] $[P_2Q_7]^{4-}$,[10] $[P_2Q_9]^{4-}$,[16] $[P_5Q_{12}]^{5-}$,[19] $[P_6Q_{12}]^{4-}$,[19, 20] and many others. In most of these chalco-phosphate building blocks P is formally in +5 oxidation state except when P – P bond is present, where it is +4 as in $[P_2Q_6]^{4-}$. These $[P_xQ_y]^{z-}$ units can be stabilized with alkali ions or with metals; transition or main-group metals. Several groups, namely Kanatzidis,[10, 13, 18-20] Dorhout,[12, 16] Schleid,[14] Bensch,[15] Lotsch[17] and others,[7, 8, 9, 11] have extensively investigated synthesis of new ternary and quaternary chalco-phosphates either from elements or using binaries often in presence of polychalcogenide or poly-chalcophosphate flux. These reactions involving rare-earth metals mainly led to ortho-chalcophosphates[12, 13, 14, 15] or hexachalcohypodiphosphates[12, 17] often incorporating alkali ions. However, with 1st row transition series it has rarely formed ortho-chalcophosphates because of the high prevalence of $[P_2Q_6]^{4-}$ unit. To our knowledge there are only a few examples of ortho-thiophosphate structure in 1st row transition metal, $KNiPS_4$,[8] $NaTi_2(PS_4)_3$,[9] $Na_3Cr_2(PS_4)_3$,[11] and Cu_3PS_4.[21] There is a renewed interest in the synthesis and crystal growth of chalco-phosphates especially in layered two-dimensional (2D) materials with van der Waals gap ($M_2P_2Q_6$, M = 1st row transition metals) and non-vdW 2D materials with intercalated alkali ions ($A_2MP_2S_6$, A = Li, K) for their magnetism and other exotic phenomena in low dimensions.[22-26] 2D $M_2P_2Q_6$ compositions are well-known cathode material[27] and there is a growing interest in chalco-phosphates as electrode materials.[28-30] In this connection we asked ourselves why it is difficult to synthesize ortho-thiophosphates of transition metals

analogous to well-known structure types in ortho-(oxy)phosphates for example, olivine[3] and NASICON;[5] phases that have defined new direction in electrode materials.[4] Strong covalent bonding of chalco-phosphate moiety with transition metals can lead to semiconducting solid with intermediate range band gap useful for photovoltaics and presence of unfilled 3*d* electrons can give rise to magnetic and redox (batteries) properties, while a combination of both can have applications in spintronics and magnetoelectrics.[22-24] Hence, if the rich structural diversity of ortho-oxy phosphates is accessed in transition metal chalco-phosphates, a plethora of new properties can be expected.

Therefore, we have directed our efforts to synthesize ortho-thiophosphate of transition metals. We have employed an innovative building block approach in which lithium thiophosphate Li_3PS_4 consisting a preformed PS_4^{3-} tetrahedral building unit is reacted with $MnCl_2$ in so-called solid state metathesis reaction to create first ever olivine-type ortho-thiophosphate with transition metal, $LiMnPS_4$.

In this communication, we report the synthesis, crystal structure, optical, and preliminary magnetic properties along with theoretical calculations within DFT framework eluciding the electronic band structure.

$$\gamma\text{-}Li_3PS_4 + MnCl_2 \rightarrow LiMnPS_4 + 2LiCl$$

$LiMnPS_4$ has been synthesized from solid-state metathesis route using γ-Li_3PS_4 and $MnCl_2$ in sealed evacuated quartz tube at 500 °C (for details, see ESI). Pale yellow color crystals (Figure S1, ESI) were obtained after breaking the ampoule inside an argon-filled glove box. Crystal structure was determined from single-crystal X-ray diffraction. Crystal data and final refinement parameters are summarized in Table 1 and other crystallographic details are given in ESI (Tables S1 - S3). The laboratory powder X-ray diffraction (PXRD)

pattern confirmed the phase purity of the bulk sample (Figure S2, ESI). The PXRD of γ–Li_3PS_4 and the air exposed (>24 hours) sample of $LiMnPS_4$ are provided in ESI (Figures S3 and S4, ESI). The PXRD of $LiMnPS_4$ after air exposure did not show any change indicating good air stability. EDS elemental analysis (Figure S5, ESI) performed on as-synthesized crystals is in good agreement with the crystallographic composition ($Mn_{1.04}P_{1.02}S_4$). $LiMnPS_4$ crystallizes in olivine structure type in *Pnma* space group. The asymmetric unit of $LiMnPS_4$ consists of one Mn (4*b*, Wyckoff site), one P (4*c*), one Li (4*c*) and three S (S1 in 8*a*, S2 and S3 in 4*c*) sites yielding a composition of $Li_{0.5}Mn_{0.5}P_{0.5}S_2$ (Figure 1a). If an empirical formula of $LiMnPS_4$ is used, then four such units (Z = 4) will be present in the unit cell.

Table 1. Crystal data and refinement parameters for $LiMnPS_4$.

Empirical formula	$LiMnPS_4$
Temperature	300(2) K
Crystal system	Orthorhombic
Space group	*Pnma*
Unit cell dimensions	a = 12.540(3) Å
	b = 7.654(2) Å
	c = 5.834(2) Å
Volume	560.0(2) $Å^3$
Z	4
Goodness-of-fit on F^2	1.112
Final *R* indices [I>2σ(I)]	R_1 = 0.0330
R indices (all data)	wR_2 = 0.0852

The structure of $LiMnPS_4$ can be described as hcp array of S atoms in which half of the octahedral sites in alternate layers are filled with Mn and Li atoms, respectively, while one-eighth of the tetrahedral holes are filled with P atoms. Such filling up of holes by Mn and P creates a situation where edge-shared MnS_6 octahedra form infinite chains parallel to the *b*-axis, which are further stitched together by PS_4 tetrahedral units forming layers perpendicular to *a*-axis. The interlayer space is filled by Li ions (Figure 1b).

The structure of $LiMnPS_4$ belongs to olivine-Mg_2SiO_4 structure type,[31] where Li and Mn replaces two crystallographically distinct Mg ions in 4*a* and 4*c* sites, respectively, and SiO_4 unit is replaced by PS_4 unit. However, there is a slight difference in the atomic positions when compared with the ortho-(oxy)phosphate analogue, olivine-$LiMnPO_4$ or in general, olivine-Li*M*PO_4 (*M* = Mn, Fe, Co, and Ni), all of which are well-known cathode materials for Li-ion batteries.[3, 4] In the thiophosphate analogue, the position of transition metal and lithium ion are interchanged when compared to $LiMnPO_4$ i.e. in oxy-phosphate 4*c* Wyckoff site is occupied by Mn ion whereas the same site is occupied by Li ion in the thiophosphate. Such switching of Li and Mn positions makes $LiMnPS_4$ a layered material meaning covalent connectivity between PS_4 and MnS_6 extends only in 2-dimensions and such layers are held together *via* predominantly ionic forces by intervening Li-ions. On the other hand, $LiMnPO_4$ has three-dimensional structure with one- dimensional channels filled with Li-ions. Hence, $LiMnPS_4$ can be considered as the first example of chalco-phosphate olivine analogue of the well investigated $LiMnPO_4$.

Considering our implemented metathesis synthesis method, it is worth comparing the structure of starting material, γ-Li_3PS_4 or its polymorph, β-Li_3PS_4 with $LiMnPS_4$. γ-Li_3PS_4 is the room temperature polymorph, which on heating undergoes phase transition

to superionic phase β-Li_3PS_4.[32] It is to be noted here that β-Li_3PS_4 is very close to olivine, out of the three Li-sites one of the Li occupies an octahedral site (4*b*), the same as Li in $LiMnPO_4$. However, it has two additional Li-sites which are tetrahedral and those are not filled in olivine.

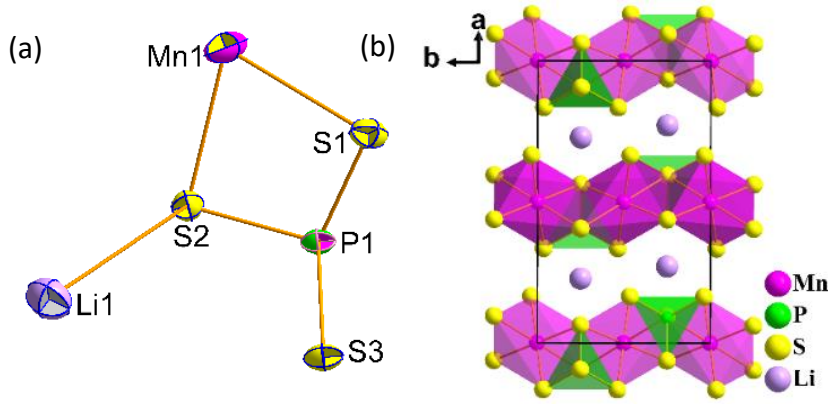

Figure 1. (a) Asymmetric unit of $LiMnPS_4$; (b) Layers formed by parallel chains of MnS_6 edge sharing octahedra connected by PS_4 tetrahedra separated by interlayer octahedrally coordinated Li ions.

On close inspection it is found that $LiMnPS_4$ can be topotactically generated from the high temperature polymorph β-Li_3PS_4. The Figure 2 shows the structural comparison of β-Li_3PS_4, $LiMnPS_4$, and $LiMnPO_4$. During the solid-state metathetic reaction with $MnCl_2$, the starting reaction precursor, γ-Li_3PS_4, transforms to β-Li_3PS_4 above 200 °C and octahedral Li(Li2) is substituted by Mn followed by a change in coordination of Li1 from tetrahedral to octahedral coordination leading to the formation of $LiMnPS_4$ with the elimination of tetrahedral Li(Li3) site as one Mn^{2+} will compensate charges for two Li^+ ions. This is the innovativeness of our building block approach which enabled retention of the building block, ortho-thiophosphate unit, and led to the discovery of olivine phase, $LiMnPS_4$.

The traditional solid-state synthesis using elements in chalco-phosphate flux is perceived as the most viable way to synthesize transition metal thiophosphates.[10, 26] Metathesis reactions have also been employed in some cases, for example, reaction between $Li_4P_2S_6$ and Ni^{2+} salt in aqueous medium yielded poorly crystalline $Ni_2P_2S_6$;[33] a mixed metal seleno-phosphate, $M^{+1}M^{+3}P_2Se_6$ has been synthesized by reacting $M^{+1}Cl$ and $M^{+3}Cl_3$ with $Mg_2P_2S_6$.[34, 35] Metathesis reactions offer advantage over typical solid state reactions using elements or flux in terms of lower reaction temperatures, better control over the product formation and often allows rational design when the reaction is topotactic.[36] The formation enthalpy of the salt byproduct in metathesis reactions drive the reaction in forward direction. This is the first report of metathesis reaction with a preformed PS_4^{3-} building unit with transition metal chloride salt.

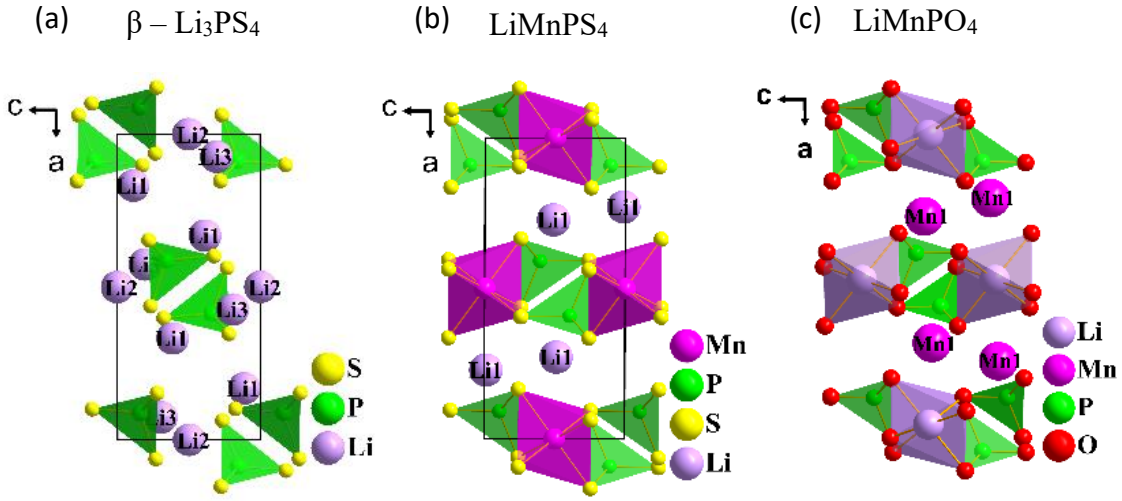

Figure 2. Comparing the crystal structures of (a) β – Li_3PS_4; (b) $LiMnPS_4$;(c) $LiMnPO_4$.

This novel synthetic route can give access to new materials which otherwise may not have been discovered through traditional solid-state elemental or flux-based reactions. From the charge neutral formula, $LiMnPS_4$, it can be expected to have semiconductor-like band gap. Accordingly, the optical band gap is found to be 2.36 eV from the diffuse reflectance spectra as shown in Fig 3a (details in ESI). The optical band gap of γ-Li_3PS_4 is found to be 3.8 eV (Figure S6, ESI), therefore, the topotactic insertion of Mn for Li ion in Li_3PS_4 reduces the band gap by ~1.5 eV. Weak spin-forbidden *d-d* transitions due to high spin Mn(II) can be seen before the steep jump due to band gap (Figure 3b).

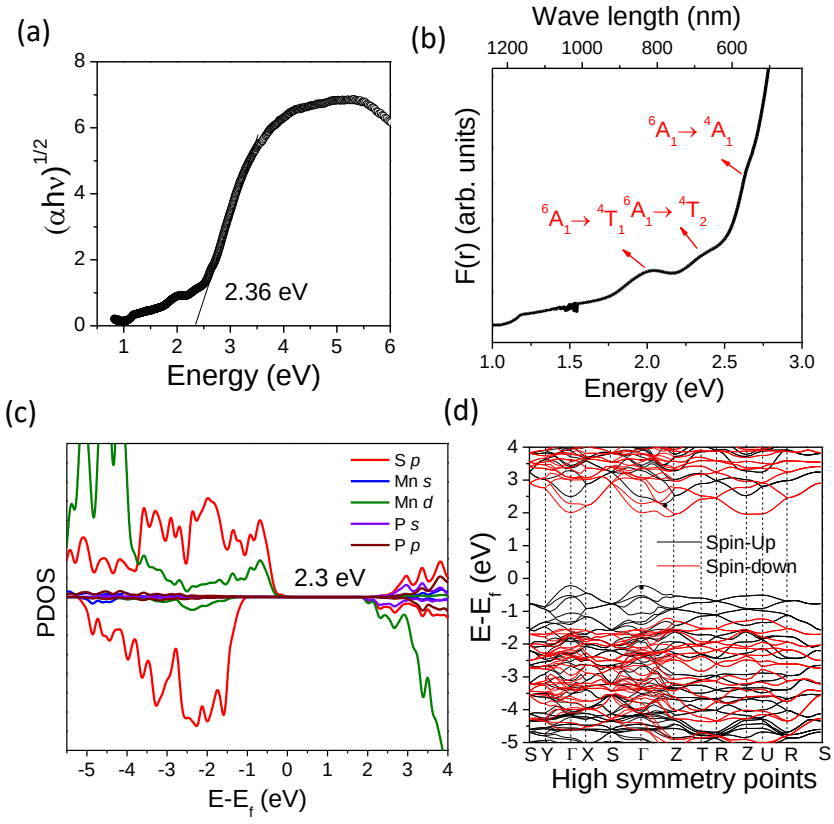

Figure 3. (a) Diffuse reflectance plot of $LiMnPS_4$; (b) Spin forbidden weak $d - d$ transitions; (c) Partial density of states of $LiMnPS_4$; (d) Band structure of $LiMnPS_4$.

To understand the origin of this band gap narrowing, we performed spin polarized band structure calculations on experimentally determined structure using density functional theory (DFT) as implemented in VASP. Further details of DFT calculations are given in ESI. The calculated band gap of 2.3 eV using HSE06 hybrid functional (Figure 3c) is in very good agreement with the experimentally obtained band gap of 2.36 eV. The projected density of states for $LiMnPS_4$ calculated using HSE06 hybrid functional is shown in Figure 3c (Figure S7, ESI). The top of the valence band has the contribution mainly from S *p* states and Mn *d* states, whereas the bottom of the conduction band has major contribution from S *p* and P *s* states.

Contribution of Li ions is almost negligible near the Fermi level. Figure 3d shows the electronic band structure along the high symmetry points in the Brillouin zone of orthorhombic lattice. The valence band maximum occurs at Γ point and the conduction band minimum occurs close to Z point of the Brillouin zone confirming that $LiMnPS_4$ is an indirect band gap material. The indirect nature of the band gap agrees well with the experimental DRS measurements.

2. MAGNETIC PROPERTIES

Temperature dependence of magnetic susceptibility and inverse susceptibility of $LiMnPS_4$ measured at an applied field of 1T from 3.2K to room temperature are given in Figure 4a. The molar magnetic susceptibility (χ_M) increases asymptotically and reaches a maximum at 28 K and after that there is a sharp fall of χ_M indicating onset of antiferromagnetic ordering below 28K. The temperature dependence of the inverse

magnetic susceptibility, χ_M^{-1}(T), shows linear behavior between 150-300K which can be fitted with Curie-Weiss law yielding a Curie constant of 4.045 emu.K.mol^{-1} and a Weiss constant (θ_p) of –52.29 K, respectively. Large negative, θ_p, value indicates strong antiferromagnetic interactions between adjacent Mn(II) ions. The experimental magnetic moment per Mn derived from Curie constant is 5.69 μ_B, which is close to the spin only magnetic moment 5.92 μ_B for high spin Mn^{2+} with five unpaired electrons.

To understand the nature of antiferromagnetic transition, dc magnetization measurements were performed under field cooled (FC) and zero field cooled (ZFC) conditions under low applied field of 0.01T (Figure 4b). The FC and ZFC magnetic susceptibilities show an obvious divergence below 24 K, which could be due to irreversible weak ferromagnetic transition resulting from spin canting. The presence of weak ferromagnetic transition at lower applied fields and disappearance at higher applied field indicates field-induced metamagnetic transition. Variable field isothermal magnetization measured at 300K shows sluggish increase in the magnetization to 0.11Nβ whereas at 3K magnetization gradually increases to 0.25 Nβ, after that a steep rise from 0.25 to 0.38 Nβ between 3.75 and 5T, respectively (Figure 4c), indicating a field-induced metamagnetic transition from antiferromagnetic to ferromagnetic state. A small but detectable hysteresis loop (inset, Figure 4d) was also observed. Metamagnetism has been observed in many compounds containing Mn(II) chains with various bridging networks.[37-39] Because of the presence of the inversion centers between the adjacent Mn(II) ions, rules out the occurrence of antisymmetric interactions, however, at much lower temperatures, slight distortion in the crystal structure could cause spins to be tilted away from the antiparallel arrangement causing weak ferromagnetic ordering.

In summary, we reported a new quaternary sulfide, $LiMnPS_4$, with olivine structure synthesized for the first time through solid-state metathesis route using preformed Li_3PS_4 and $MnCl_2$. Parallel chains of edge shared MnS_6 connected by PS_4 tetrahedral units form 2D layers, where the interlayer space is occupied by Li ions. $LiMnPS_4$ possess an indirect band gap of 2.36 eV which is further confirmed by HSE06 calculations.

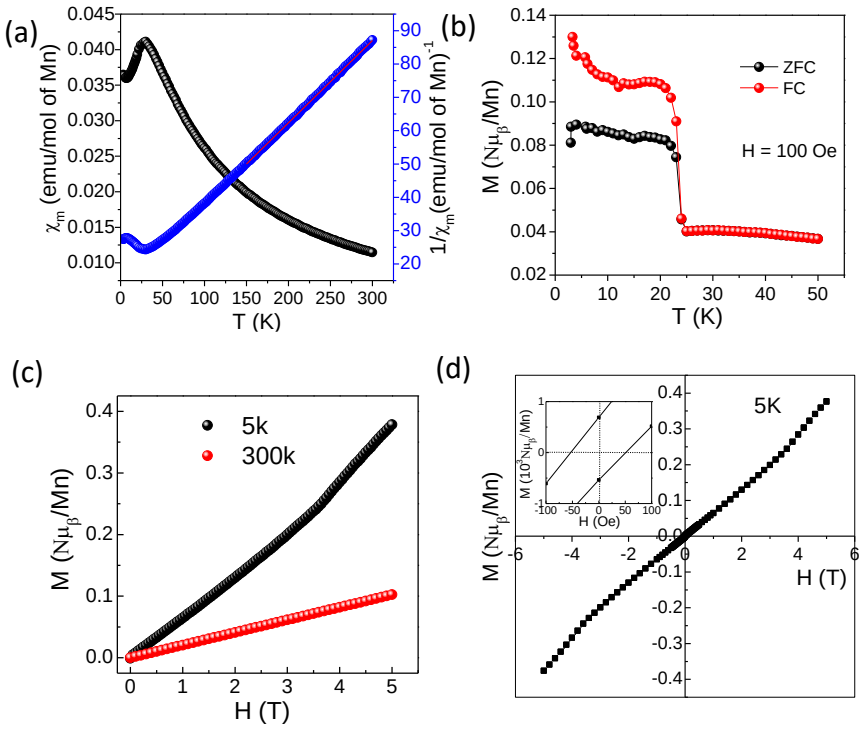

Figure 4. (a) Temperature dependent molar and inverse molar magnetic susceptibility of $LiMnPS_4$ acquired at an applied field of 1T; (b) ZFC–FC curves at 100 Oe; (c) Isothermal *M–H* scans at 5 and 300 K; (d) Magnetization *vs.* field variation hysteresis loop. Inset shows an enlargement view of the remanent magnetization around the zero-field strength.

Preliminary magnetic measurements confirm the field induced metamagnetic transition resulting from spin canting. This work emphasizes that chalco-analogues of oxy-

(ortho)phosphate structures can be accessed through solid-state metathesis route by employing building block approach.

ACKNOWLEDGEMENTS

The authors thank NSF (grant No. DMR- 1809128) for funding and Dr. O'Malley for EDS analysis.

SUPPLEMENTARY INFORMATION

SYNTHESIS

$LiMnPS_4$ has been synthesized from solid-state metathesis route using γ-Li_3PS_4 and $MnCl_2$. First Li_3PS_4 was synthesized from stoichiometric mixture of Li_2S (4.5 mmol) and P_2S_5 (1.5 mmol) ($1.5Li_2S + 0.5P_2S_5 = Li_3PS_4$). Li_2S and P_2S_5 were ground together inside argon-filled glove box (O_2 < 0.1ppm) and loaded into a carbon coated quartz ampule. The flame sealed quartz ampoule was heated to 700 °C at a rate of 30 °C /h, dwelled for 12 h and subsequently cooled to room temperature at a cooling rate of 35 °C /h. White crystalline powder sample was obtained after breaking the ampoule inside argon filled glove box. Phase pure Li_3PS_4 (1 mmol) and $MnCl_2$ (1 mmol) were ground together in 1:1 ratio in an agate mortar and loaded in carbon coated quartz ampoule. The quartz tube was flame sealed and heated to 500 °C for 48 h, the heating and cooling rates were 25 and 30 °C /h, respectively. A schematic of the reaction is shown in scheme S1. Shiny single chunk containing pale yellow color crystals were obtained after breaking the ampoule inside an

argon-filled glove box. To remove the salt (LiCl) byproduct ($Li_3PS_4 + MnCl_2 = LiMnPS_4 + 2LiCl$), the as synthesized single chunk was sonicated in *N*,*N* dimethylformamide (DMF). The crystals were found to be stable in air for several days. Appropriate crystal was chosen for single crystal X-ray diffraction and the as synthesized crystals/hand ground powder was used for further characterization. A digital photograph showing the as-synthesized $LiMnPS_4$ was provided in ESI (Figure S1).

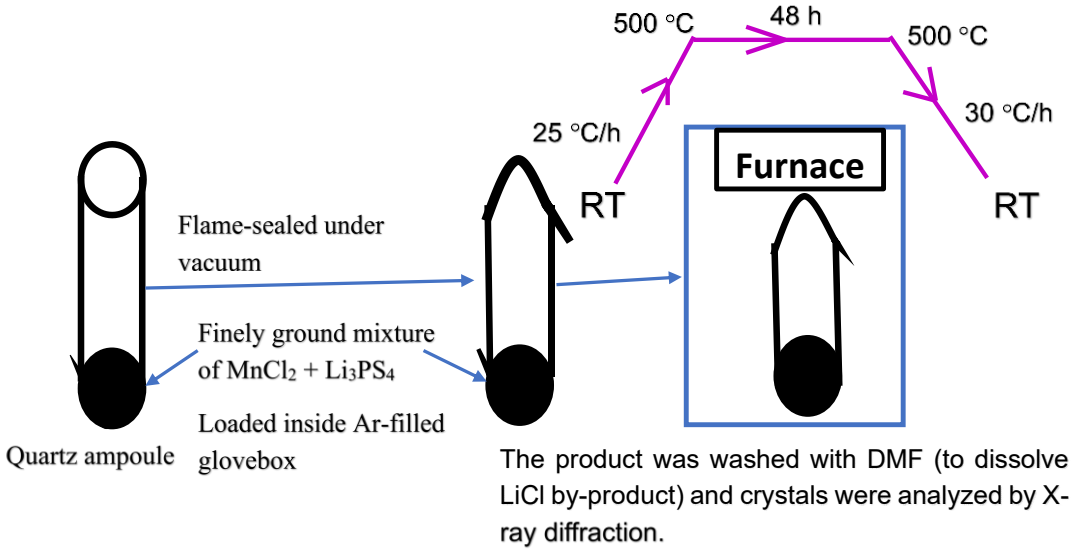

Scheme S1. A schematic showing how the reactions are carried out in sealed ampoules.

X-RAY CRYSTALLOGRAPHY

Good quality crystal was chosen for single-crystal X-Ray diffraction on a Bruker smart apex equipped with a sealed tube X-ray source with Mo−Kα radiation (λ = 0.71073 Å). Room temperature diffraction data sets were collected using SMART[1] software with a step of 0.3° in the ω scan and 10 s/ frame exposure time. Program SAINT[2] was used for data integration and SADABS[2] was used for the absorption correction, respectively.

SHELXS-97 and difference Fourier syntheses were used to solve the structure.[3] Full-matrix least-square refinement against $|F^2|$ was carried out using the SHELXTL-PLUS suite of programs.[2] The compound crystallizes in orthorhombic crystal system with *Pnma* (No.62) space group. The asymmetric unit consists of three sulfur, one manganese, one phosphorous and one lithium which can be easily located from the difference Fourier map. Absence of unaccounted e-density and reasonably good thermal displacement parameters with low weighted *R* factor wR_2, the charge balanced formula $LiMnPS_4$ was derived based on the 100% occupancies of the atoms. Final refinements including the refinement of anisotropic thermal parameters were performed using SHELX-2018 embedded in ShelXLe.[4] Selected bond lengths, atomic coordinates along with their isotropic thermal parameters are given in the ESI (Tables S1-S3).

POWDER X-RAY DIFFRACTION

Hand ground powder sample in an argon filled glove box was used to collect the laboratory powder X-ray diffraction (PXRD) pattern from a PANalytical X'Pert Pro diffractometer equipped with a Cu Kα anode and a linear array PIXcel detector over a 2θ range of 5−90° with an average scanning rate of 0.0472° s^{-1}. Air-tight cell holder with Kapton film window was used to minimize the air exposure. The PXRD patterns of the as-synthesized and air exposed $LiMnPS_4$ are provided in Figures S2 and S4. The PXRD of the as-synthesized γ–Li_3PS_4 is provided in Figure S3. The PXRD of the $LiMnPS_4$ after air exposure didn't show any change indicating good air and moisture stability.

EDS ANALYSIS

Elemental analysis is studied by Scanning electron microscope (SEM) using an TESCAN-ASCAT system equipped with Bruker energy dispersive spectroscopy (EDX). The elemental mapping (Figure S5) shows uniform distribution of Mn, P, and S with ratio's 1.04:1.02:4 which is in very good agreement with the crystallographically-derived composition.

OPTICAL BAND GAP MEASUREMENTS

Optical band gap measurements were performed on a Varian Cary 5000 UV−vis−NIR spectrophotometer equipped with a praying mantis set up. $BaSO_4$ powder (Fisher, 99.2%) was used as an ∼100% reflectance standard, and the Kubelka-Munk[5] function was employed to transform the reflectance into absorption data to find out the band gap. Tauc plot $\alpha h\nu = A(h\nu - E_g)^m$ was employed to estimate the nature of optical band gap, where α is absorption coefficient (Kubelka-Munk function), $h\nu$ is the photon energy, and m = 2 or ½ depending on whether the transition is direct or indirect. $LiMnPS_4$ exhibit linearity in $h\nu$ *vs* $(\alpha h\nu)^{1/2}$ plot, suggesting that the sample possess indirect band gap of 2.36 eV. Diffuse reflectance spectra of γ-Li_3PS_4 shows an indirect band gap of 3.8 eV (Figure S6).

THEORETICAL CALCULATIONS

Spin polarized band structure calculations were performed on experimentally determined structure using density functional theory as implemented in Vienna *Ab-intio* Simulations Package (VASP).[6-9] Hybrid functional (HSE06) calculations were employed

to describe accurate band structure and estimate the band gap.[10] Kinetic energy cut off was set to 520 eV and Γ centered *k*-point grid size of 2×3×4 was used for Brillouin zone integration. Relaxed atomic structure by the standard DFT with convergence threshold of 10^{-6} eV for total energy and 10^{-3} eV/Å for the maximum force was used for the hybrid functional calculations. All the calculations were performed in ferromagnetic (FM) configuration. The density of states is calculated using gaussian smearing of 0.05 eV.

MAGNETIC MEASUREMENTS

The DC magnetic susceptibility was measured at 1 Tesla (1 Tesla = 10000 Oe) magnetic field after zero-field cooling over the temperature range 3.2-300 K in a Quantum Design SQUID magnetometer. Isothermal magnetization at 5 and 300 K was measured in an applied field range of 0 – 5 Tesla. Zero field cooled (ZFC) and field cooled (FC) magnetization data were collected from 3 – 50 K at an applied field of 100 Oe. Variable field magnetization was measured at 5K under ZFC condition in an applied field range of +5 to -5 Tesla. A $\chi_m T$ versus T plot is given Figure S8.

Table S1. Final atomic coordinates and equivalent isotropic displacement parameters for $LiMnPS_4$. U(eq) is defined as 1/3rd of the trace of the orthogonalized U^{ij} tensor.

Atom	Wyckoff	Occupancy	x/a	y/b	z/c	U(Å^2)
Mn(1)	4b	1	0	0	0.5	0.025(1)
P(1)	4c	1	0.0911(1)	0.25	0.1064(2)	0.013(1)
S(1)	8d	1	0.1649(1)	0.0357(1)	0.2428(1)	0.018(1)
S(2)	4c	1	-0.0625(1)	0.25	0.2409(2)	0.016(1)
S(3)	4c	1	0.0947(1)	0.25	-0.2420(1)	0.017(1)
Li(1)	4c	1	-0.2281(7)	0.25	-0.0109(12)	0.030(2)

Table S2. Selected bond lengths for $LiMnPS_4$

Bonds	Distance (Å)	Bonds	Distance (Å)
Mn1 – S2	2.5613(7)	P1 – S3	2.0333(13)
Mn1 – S2$^{\#1}$	2.5613(7)	P1 – S1$^{\#4}$	2.0451(10)
Mn1 – S1$^{\#1}$	2.5696(8)	P1 – S1	2.0451(10)
Mn1 – S1	2.5696(8)	P1 – S2	2.0791(14)
Mn1 – S3$^{\#2}$	2.7087(7)		
Mn1 – S3$^{\#3}$	2.7087(7)		

Symmetry transformations used to generate equivalent atoms:
#1 -x, -y, -z + 1 #2 -x, -y, -z #3 x, y, z+1 #4 x, -y+1/2, z

Table S3. Anisotropic displacement parameters ($Å^2 x\ 10^3$) for LiMnPS4. The anisotropic displacement factor exponent takes the form: $-2p^2[\ h^2 a^{*2} U^{11} + ... + 2\ h\ k\ a^*\ b^*\ U^{12}]$

Atoms	U^{11}	U^{22}	U^{33}	U^{23}	U^{13}	U^{12}
Mn(1)	30(1)	24(1)	21(1)	8(1)	7(1)	1(1)
P(1)	17(1)	16(1)	7(1)	0	0(1)	0
S(1)	21(1)	21(1)	13(1)	1(1)	1(1)	5(1)
S(2)	15(1)	20(1)	13(1)	0	1(1)	0
S(3)	23(1)	21(1)	7(1)	0	1(1)	0
Li(1)	30(4)	36(4)	25(4)	0	-6(3)	0

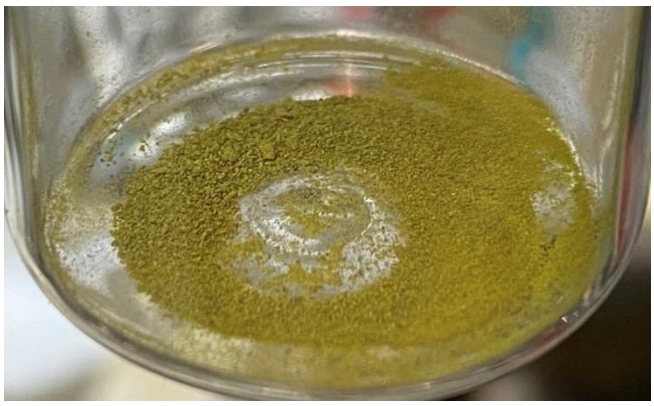

Figure S1. (a) As-synthesized DMF washed crystals of $LiMnPS_4$ synthesized from metathesis route ($Li_3PS_4 + MnCl_2$).

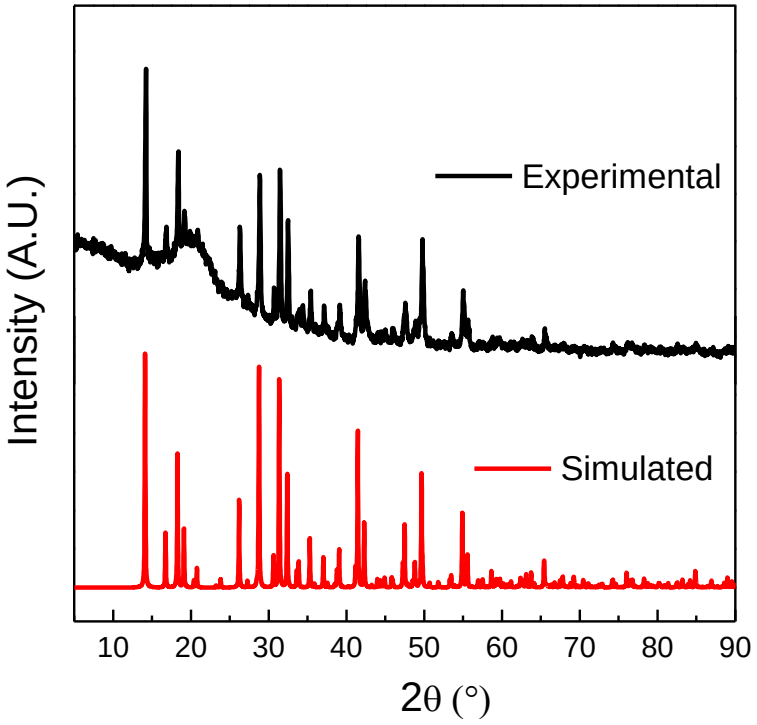

Figure S2. Comparison of simulated and experimental powder X-ray diffraction pattern for $LiMnPS_4$ synthesized from metathesis route (Li_3PS_4 + $MnCl_2$).

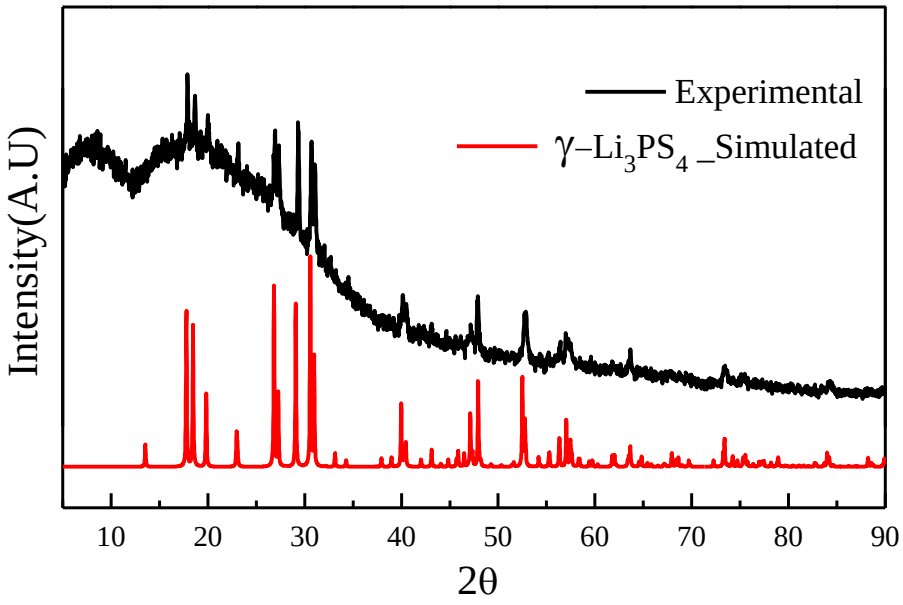

Figure S3. PXRD patterns showing the comparison of experimental Li_3PS_4 with the simulated patterns of γ – Li_3PS_4.

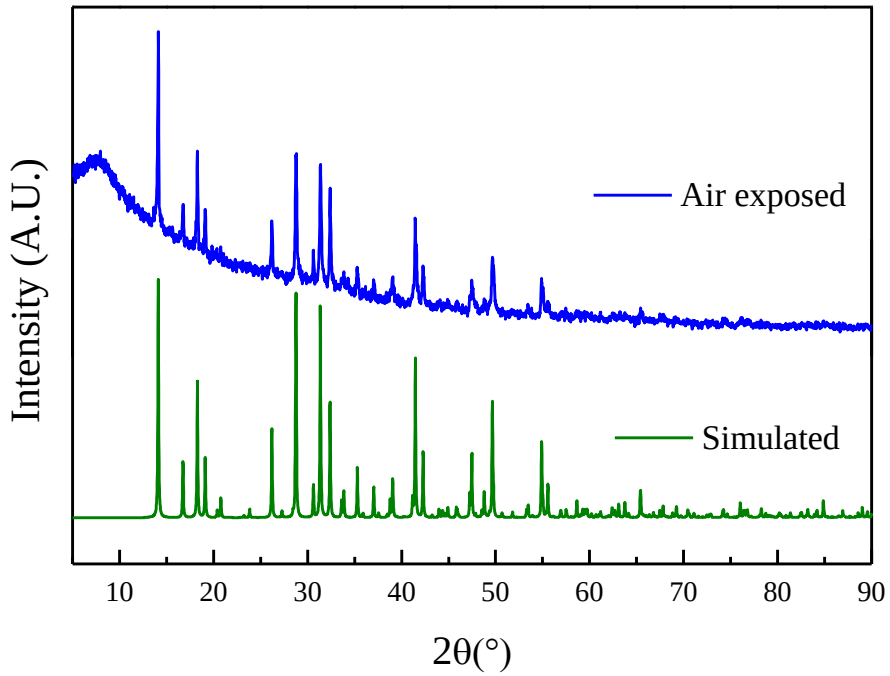

Figure S4. PXRD patterns showing the comparison of air exposed $LiMnPS_4$ with the simulated pattern of $LiMnPS_4$.

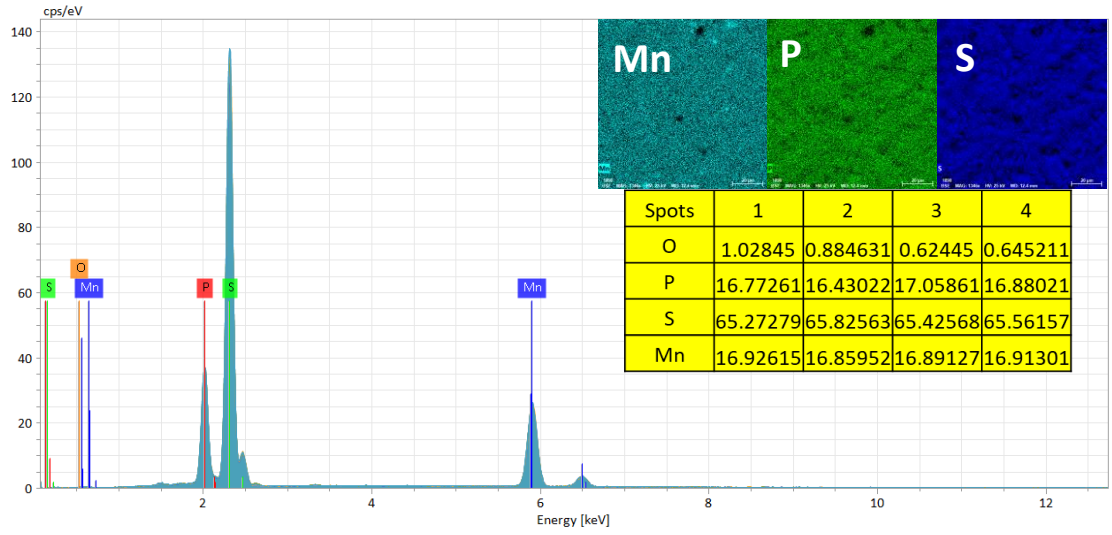

Spots	1	2	3	4
O	1.02845	0.884631	0.62445	0.645211
P	16.77261	16.43022	17.05861	16.88021
S	65.27279	65.82563	65.42568	65.56157
Mn	16.92615	16.85952	16.89127	16.91301

Figure S5. EDS analysis of the as synthesized $LiMnPS_4$. The table indicates the atomic percentage of the elements at different spots. A small percentage of oxygen is not avoidable as sulfides are known to undergo some surface oxidation.

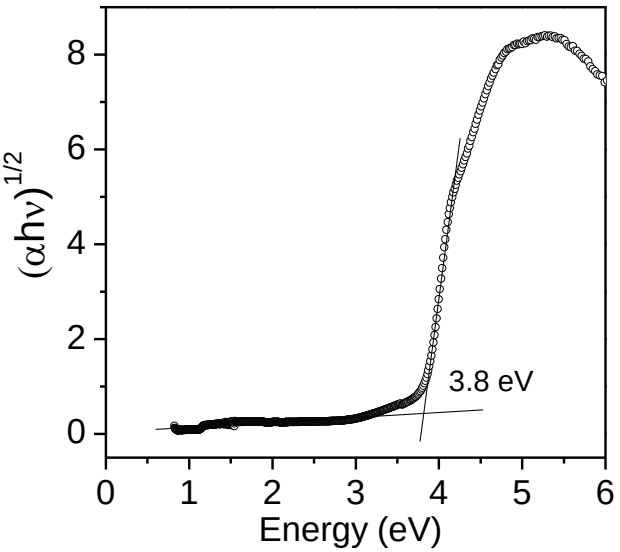

Figure S6. Diffuse reflectance plot for γ-Li_3PS_4.

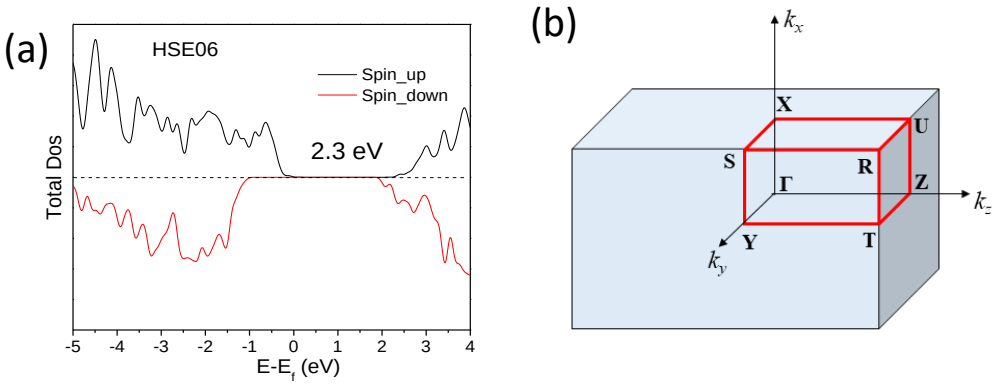

Figure S7. (a) Total density of states calculated using HSE06 hybrid functionals; (b) Brillouin zone of primitive orthorhombic lattice with high symmetry points.

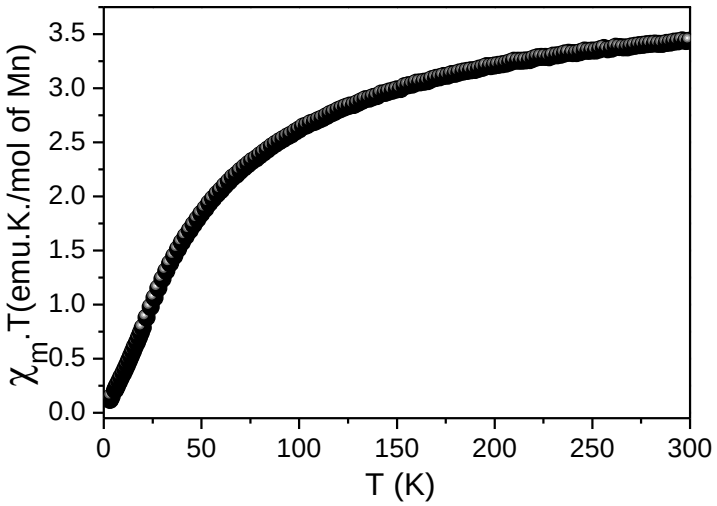

Figure S8. $\chi_m T$ versus T plot indicating the antiferromagnetic behavior of $LiMnPS_4$ phase at low temperatures.

REFERENCES

1. Bruker- SMART, Bruker AXS Inc., Madison, Wisconsin, USA, 2002.

2. Bruker-SAINT and SADABS, and SHELXTL, Bruker AXS Inc., Madison, Wisconsin, USA, 2008.

3. G. M. Sheldrick *Acta Crystallogr., Sect. A: Found. Crystallogr.*, 2008, **64** , 112 – 122

4. C. B. Hübschle , G. M. Sheldrick and B. Dittrich , *J. Appl. Crystallogr.*, 2011, **44** , 1281 – 1284.

5. P. Kubelka and F. Z. Munk , *Tech. Phys.*, 1931, **12** , 593 – 601.

6. G. Kresse and J. Hafner , *Phys. Rev. B: Condens. Matter Mater. Phys.*, 1993, **47** , 558 – 561.

7. G. Kresse and J. Furthmüller , *Comput. Mater. Sci.*, 1996, **6** , 15 – 50.

8. G. Kresse and J. Furthmüller , *Phys. Rev. B: Condens. Matter Mater. Phys.*, 1996, **54** , 11169 – 11186.

9. D. Joubert *Phys. Rev. B: Condens. Matter Mater. Phys.*, 1999, **59** , 1758 – 1775.

10. A. V. Krukau, O. A. Vydrov, A. F. Izmaylov and G. E. Scuseria, *J. Chem. Phys.*, 2006, **125**, 224106.

NOTES AND REFERENCES

1. Nriagu, J.O. Phosphate Minerals: Their Properties and General Modes of Occurrence. In: *Phosphate Minerals* (J.O. Nriagu and P.B. Moore, Eds.), Springer-Verlag, Heidelberg, 1984; pp. 1–136.

2. R. Murugavel, A. Choudhury, M. G. Walawalkar, R. Pothiraja and C. N. R. Rao, *Chem. Rev.*, 2008, **108**, 3549–3655.

3. K. Padhi, K. S. Nanjundaswamy and J. B. Goodenough, *J. Electrochem. Soc.*, 1997, **144**, 1188.

4. C. Masquelier and L. Croguennec, *Chem. Rev.*, 2013, **113**, 6552–6591.

5. K. Arbi, W. Bucheli, R. Jiménez and J. Sanz, *J. Eur. Ceram. Soc.*, 2015, **35**, 1477–1484.

6. Y. Moëlo, E. Makovicky, N. N. Mozgova, J. L. Jambor, N. Cook, A. Pring, W. Paar, E. H. Nickel, S. Graeser, S. Karup-Møller, T. Balic-Žunic, W. G. Mumme, F. Vurro, D. Topa, L. Bindi, K. Bente and M. Shimizu, *Eur. J. Mineral.*, 2008, **20**, 7–46.

7. G. Ouvrard, R. Brec and J. Rouxel, *Mater. Res. Bull.*, 1985, **20**, 1181–1189.

8. S. H. Elder, A. Van der Lee, R. Brec and E. Canadell, *J. Solid State Chem.*, 1995, **116**, 107–112.

9. X. Cieren, J. Angenault, J. C. Couturier, S. Jaulmes, M. Quarton and F. Robert, *J. Solid State Chem.*, 1996, **121**, 230–235.

10. Jason A. Hanko, Julien Sayettat, Stéphane Jobic, and Raymond Brec and Mercouri G. Kanatzidis, *Chem. Mater.*, 1998, **10**, 3040–3049.

11. S. Coste, E. Kopnin, M. Evain, S. Jobic, C. Payen and R. Brec, *J. Solid State Chem.*, 2001, **162**, 195–203.

12. C. R. Evenson and P. K. Dorhout, *Inorg. Chem.*, 2001, **40**, 2884–2891.

13. J. A. Aitken and M. G. Kanatzidis, *J. Am. Chem. Soc.*, 2004, **126**, 11780–11781.

14. P. L. Lange and T. Schleid, *Eur. J. Inorg. Chem.*, 2021, (32) 3247-3254

15. Y. Klawitter, W. Bensch and C. Wickleder, *Chem. Mater.*, 2005, **18**, 187–197.

16. J. M. Knaust and P. K. Dorhout, *J. Chem. Crystallogr.* 2006, **36**, 217–223.

17. L. M. Schoop, R. Eger, R. K. Kremer, A. Kuhn, J. Nuss and B. V. Lotsch, *Inorg. Chem.*, 2017, **56**, 1121–1131.

18. S. Haynes, C. C. Stoumpos, H. Chen, D. Chica and M. G. Kanatzidis, *J. Am. Chem. Soc.*, 2017, **139**, 10814–10821.

19. Chung, J. I. Jang, M. A. Gave, D. P. Weliky and M. G. Kanatzidis, *Chem. Commun.*, 2007, 4998–5000.

20. Chung, A. L. Karst, D. P. Weliky and M. G. Kanatzidis, *Inorg. Chem.*, 2006, **45**, 2785–2787.

21. Garin, and E. Parthe, *Acta Cryst.*, 1972, **B28**, 3672-3674.

22. M. A. Susner, M. Chyasnavichyus and M. A. Mcguire, *Adv. Mater.*, 2017, **29**, 1602852.

23. C. C. Mayorga-Martinez, Z. Sofer, D. Sedmidubský, Š. Huber, A. Y. S. Eng and M. Pumera, *ACS Appl. Mater. Interfaces*, 2017, **9**, 12563–12573.

24. Y. Zhang, T. Fan, S. Yang, F. Wang, S. Yang, S. Wang, J. Su, M. Zhao, X. Hu, H. Zhang and T. Zhai, *Small Methods*, 2021, **5**, 2001068.

25. T. J. Diethrich, P. Y. Zavalij, S. Gnewuch and E. E. Rodriguez, *Inorg. Chem.*, 2021, **60**, 10280–10290.

26. D. G. Chica, A. K. Iyer, M. Cheng, K. M. Ryan, P. Krantz, C. Laing, R. dos Reis, V. Chandrasekhar, V. P. Dravid and M. G. Kanatzidis, *Inorg. Chem.*, 2021, **60**, 3502–3513.

27. R. Brec, *Solid State Ionics*, 1986, **22**, 3.

28. Y. Kim, N. Arumugam and J. B. Goodenough, *Chem. Mater.*, 2007, **20**, 470–474.

29. P. Bron, S. Johansson, K. Zick, J. S. auf der Günne, S. Dehnen and B. Roling, *J. Am. Chem. Soc.*, 2013, **135**, 15694–15697.

30. M. Ghidiu, J. Ruhl, S. P. Culver and W. G. Zeier, *J. Mater. Chem. A*, 2019, **7**, 17735–17753.

31. W. L. Bragg and G. B. Brown, *Z. Krist.*, 1926, **63**, 538–556.

32. M. Tachez, J. P. Malugani, R. Mercier and G. Robert, *Solid State Ionics*, 1984, **14**, 181–185.

33. P. Fragnaud, E. Prouzet, G. Ouvrard, J. L. Mansot, C. Payen, R. Brec and H. Dexpert, *J. Non. Cryst. Solids*, 1993, **160**, 1–17.

34. R. Pfeiff and R. Kniep, *Z. Naturforsch. B*, 1993, **48**, 1270–1274.

35. Z. Le Huang, J. T. Zhao, J. X. Mi, S. Y. Mao and L. S. Zheng, *J. Solid State Chem.*, 1999, **144**, 388–391.

36. E. G. Gillan and R. B. Kaner, *Chem. Mater.*, 1996, **8**, 333–343.

37. E. -Q. Gao, Z. -M. Wang, and C. -H. Yan, *Chem. Commun.*, 2003, 1748–1749.

38. X. -N. Cheng, W. Xue, J. -H. Huang, and X.-M. Chen, *Dalton Trans.*, 2009, 5701–5707.

39. Cheng, W. -X. Zhang, B. -H. Ye, J. -B. Lin, and X. -M. Chen, *Eur. J. Inorg. Chem.* 2007, 2668–2676.

VI. BUILDING BLOCK APPROACH TO THE DISCOVERY OF $Na_8Mn_2(Ge_2Se_6)_2$: A POLAR CHALCOGENIDE EXHIBITING PROMISING HARMONIC GENERATION SIGNALS WITH A HIGH LASER-INDUCED DAMAGE THRESHOLD

Srikanth Balijapelly,[a] Andrew J. Craig,[b] Jeong Bin Cho,[c] Joon I. Jang,[c,] Kartik Ghosh,[d] Jennifer A. Aitken,[b] Aleksandr V. Chernatynskiy,[e] and Amitava Choudhury[a,] **

[a]Department of Chemistry, Missouri University of Science and Technology, Rolla, MO 65409, USA

[b]Department of Chemistry and Biochemistry, Duquesne University, Pittsburgh, PA 15282, USA

[c]Department of Physics, Sogang University, 35 Baekbeom-ro, Mapo-gu, Seoul, 04107 South Korea

[d]Department of Physics, Astronomy and Materials Sci, Missouri State University, 901 S. National Ave., Springfield, MO 65897, USA

[e]Department of Physics, Missouri University of Science and Technology, Rolla, MO 65409, USA*

ABSTRACT

A new polar quaternary chalcogenide, $Na_8Mn_2(Ge_2Se_6)_2$, has been synthesized using the building-block approach by reacting preformed $Na_6Ge_2Se_6$ and $MnCl_2$ at 750 °C. The structure consists of layers of $[Na(1)\ Mn(Ge_2Se_6)]^{3-}$ stacked perpendicular to the *c*-axis and sodium ions occupying the interlayer space. An indirect bandgap of 1.52 eV has been calculated using density functional theory, which is expectedly underestimated compared to the observed optical bandgap of 1.95 eV derived from diffuse reflectance spectroscopic measurements in the UV/Vis/NIR region. Magnetic measurements confirm the paramagnetic nature of $Na_8Mn_2(Ge_2Se_6)_2$ with an experimental magnetic moment of $5.8\mu_B$ in good agreement with the theoretical spin only moment of $5.92\mu_B$ for high spin

Mn^{2+}. $Na_8Mn_2(Ge_2Se_6)_2$ exhibits a potentially wide region of transparency in the measured range of 2.5 to 25 microns. $Na_8Mn_2(Ge_2Se_6)_2$ shows a modest second-harmonic generation (SHG) response but with a high laser-induced damage threshold (LIDT) of ~9x $AgGaSe_2$. Third harmonic generation (THG) measurements indicate that $Na_8Mn_2(Ge_2Se_6)_2$ displays a high THG coefficient (1.9x $AgGaSe_2$) at λ = 1800 nm.

1. INTRODUCTION

Second-order nonlinear optical (NLO) materials that produce a coherent beam in the infrared (IR) region find many applications in telecommunications, IR remote sensing, and minimally-invasive medical surgery [1 – 4]. On the other hand, third-order NLO materials that exhibit third harmonic generation (THG), the frequency tripling process, are less explored compared to second-order NLO materials. THG materials can be used in several optoelectronic applications [5 – 7]. While a noncentrosymmetric (NCS) structure is a prerequisite to show second harmonic generation (SHG), it is not necessary for achieving THG. Noncentrosymmetric quaternary chalcogenides with wide bandgaps are perceived as promising NLO materials in the IR region of the electromagnetic spectrum due to their exceptional transparency and optimum bandgap compared to oxides [1 – 3]. A better understanding and control of the synthetic methodology of chalcogenides has unlocked several promising NLO candidates in the past decade for example, $LiGaGe_2Q_6$ [8], $A_2In_2MQ_6$(*M* = Si, Ge; *Q* = S, Se) [9], Li_2CdGeS_4 [10, 11], Li_2MnGeS_4 [12], $Na_4MgM_2Se_6$ [13], Na_2BaMQ_4 [14], $AgZnPS_4$ and $LiZnPS_4$ [15], α-Li_2ZnGeS_4 [16], and $Li_4MgGe_2S_7$ [17]. Among several main-group chalcometallate compositions,

chalcogermanates are unique because of their ability to form various building blocks such as isolated ($[GeQ_4]^{4-}$) [18], corner-shared ($[Ge_2Q_7]^{6-}$) [19], and edge-shared ($[Ge_2Q_6]^{4-}$) [20] tetrahedral units where Ge is formally in +4 oxidation state. On the other hand, there exist Ge–Ge bond containing building units where Ge is formally in +3 oxidation state as in the ethane-like building units, $[Ge_2Q_6]^{6-}$ [21, 22] and $[Ge_4Q_{10}]^{8-}$ [22]. Depending on the mode of connectivity between these building units and the other metal ions, M^{n+}, where M can be a rare earth, main group, and transition metal, different structure types can be formed [12], [13], [16], [23 – 28]. Though several compounds exist containing ethane-like chalcogermanate building units [13, 23, 24, 28, 29], only $Na_4MgGe_2Se_6$ crystallizes in a NCS space group [13]. To the best of our knowledge, no transition metal analogue of $Na_4MgGe_2Se_6$ structure-type has been reported thus far, especially with the first row M^{2+} transition metals (M = Mn, Fe, Co, Ni). Hence, we sought to synthesize new NCS compounds containing ethane-like building units and a transition metal. Towards this approach, we have employed the solid-state metathesis route by reacting preformed $Na_6Ge_2Se_6$, which contains ethane-like building units, and $MnCl_2$. This strategy proved successful, as we have isolated $Na_8Mn_2(Ge_2Se_6)_2$, which crystallizes in the polar, NCS space group $C2$. In this article, we report the synthesis, crystal structure, calculated electronic structure, and magnetic properties of $Na_8Mn_2(Ge_2Se_6)_2$ along with its linear and nonlinear optical properties, which make it an attractive new NLO candidate material.

2. MATERIALS AND METHODS

2.1. SYNTHESIS

$Na_8Mn_2(Ge_2Se_6)_2$ was synthesized using the metathesis route by reacting $Na_6Ge_2Se_6$ and $MnCl_2$. First, $Na_6Ge_2Se_6$ was prepared by combining a stoichiometric combination of elements; 3 mmol of Na (Sigma, 99.9%), 1 mmol of Ge (Acros Organics, 99.9%) and 3 mmol of Se (Acros Organics, 99.5%) were heated in a sealed carbon-coated quartz ampoule. The sealed tubes were heated to 800 °C at a rate of 45 °C/h, held at that temperature for 2 h and subsequently cooled to room temperature at a rate of 45 °C/h. Greenish-yellow-colored chunks of $Na_6Ge_2Se_6$ were recovered after breaking the ampoule inside an argon-filled glove box. The crystals were found to be air and moisture sensitive. The bulk purity of $Na_6Ge_2Se_6$ was confirmed from laboratory-grade powder X-ray diffraction. $Na_6Ge_2Se_6$ and $MnCl_2$ (1:1) were hand ground together for 15 min and the mixture was loaded into a carbon-coated quartz ampoule. The sealed quartz ampoule was heated to 750 °C at a rate of 25 °C/h and held for 96 h followed by cooling to room temperature at a rate of 35 °C/h. Orange color crystals were recovered after breaking the ampoule in air followed by washing with 10% water in *N*, *N* dimethylformamide (DMF) solution to remove the NaCl byproduct and to loosen the crystals. A representative digital photograph showing DMF-washed crystals is provided in Figure S1 (supplementary material). The crystals were found to be reasonably stable for several hours under ambient conditions. $Na_8Mn_2(Ge_2Se_6)_2$ was also prepared by reacting a stoichiometric combination of elements; 4 mmol of Na, 1 mmol of Mn, 2 mmol of Ge and 6 mmol of Se were heated in a sealed quartz tube. The temperature of the furnace was raised to 600 °C at a rate of 20

°C/h and held for 96 h followed by cooling to room temperature at a rate of 30 °C/h. An appropriate crystal from the DMF-washed product obtained from metathesis reaction was used for single crystal X-ray diffraction.

2.2. X-RAY CRYSTALLOGRAPHY

A good-quality crystal was chosen for single crystal X-ray diffraction data collection on a Bruker Smart Apex CCD X-ray diffractometer equipped with a sealed tube X-ray source with Mo – Kα radiation (λ = 0.71073 Å). Low-temperature data sets were collected at –53 °C with a step size of 0.3° in the ω scan and 20 s/frame exposure time using SMART [30] software. Data integration and absorption correction were done using the programs SAINT [31] and SADABS [31], respectively. SHELXS-97 [32] and difference Fourier syntheses were used to solve the crystal structures. Full-matrix least-squares refinement against $|F^2|$ was carried out using the SHELXTL-PLUS [32] suite of programs. Final refinements including the anisotropic thermal parameters were carried out using SHELX-2018 with the ShelXle graphical user interface [33]. The compound crystallizes in polar, NCS space group *C*2 (No. 5). Four sodium, three selenium, one germanium and one manganese were easily located from a difference Fourier map and refined isotropically with acceptable thermal displacement parameters. Taking into account the occupancies of each element, a charge balanced formula of $Na_8Mn_2(Ge_2Se_6)_2$ was obtained (Z = 1). It should be noted that in order to be consistent with the previously reported compounds of the general formula $Na_{12-nx}M'_x{}^{n+}(M_2Q_6)_2$ (*M* = Si, Ge; *M′* = Eu^{2+}, La^{3+}, Sm^{3+}, Pb^{2+}, Sn^{2+}; *Q* = S, Se), [23], [24], [28], [29] a formula of $Na_8Mn_2(Ge_2Se_6)_2$ (Z = 1) has been used here instead of $Na_4MnGe_2Se_6$ (Z = 2). Selected crystallographic data

and structure refinement details are provided in Table 1. Selected bond lengths are listed in Table 2.

Table 1. Selected crystallographic data and refinement details for $Na_8Mn_2(Ge_2Se_6)_2$.

Empirical formula	$Na_8Mn_2Ge_4Se_{12}$
Formula weight	1531.68 g/mol
Temperature	220(2) K
Wavelength	0.71073 Å
Crystal system	Monoclinic
Space group	*C*2
Unit cell dimensions	a = 7.727(4) Å
	b = 11.943(7) Å
	c = 7.085(4) Å
	β = 106.682(6)°
Volume	626.4(6) Å^3
Z	1
Density (calculated)	4.061 Mgm^{-3}
Absorption coefficient	23.278 mm^{-1}
Goodness-of-fit on F2	1.059
R_1 [$I > 2\sigma(I)$][a]	0.0339
wR_2 (F^2) (all data)[b]	0.0790
Absolute structure parameter	0.48(6)
Largest diff. peak and hole	2.021 and -1.234 e.Å^{-3}

[a] $R_1 = \sum||F_o| - |F_c|/\sum|F_o|$.
[b] $wR_2 = \{\sum[w(F_o^2 - F_c^2)^2]/\sum[w(F_0^2)^2]\}^{1/2}$, $w = 1/[\sigma^2(F_o)^2 + (aP)^2 + bP]$, where $P = [F_o^2 + 2F_c^2]/3$

Fractional atomic coordinates along with the corresponding isotropic and anisotropic displacement parameters are provided in Tables S1 and S2, respectively

(Supplementary Materials). The CIF file has been submitted to CCDC (CSD 2126428) and can be obtained free of charge from The Cambridge Crystallographic Data Centre via www.**ccdc**.cam.ac.uk/data_request/**cif**.

Table 2. Selected bond lengths of $Na_8Mn_2(Ge_2Se_6)_2$.

Bond	*d* (Å)	Bond	*d* (Å)
Mn1 – Se1$^{\#1}$	2.767(3)	Na2 – Se2$^{\#6}$	3.032(6)
Mn1 – Se1$^{\#2}$	2.767(3)	Na2 – Se1$^{\#7}$	3.106(6)
Mn1 – Se2$^{\#3}$	2.826(3)	Na2 – Se1$^{\#5}$	3.106(6)
Mn1 – Se2	2.826(3)	Na2 – Se3	3.120(3)
Mn1 – Se3$^{\#5}$	2.837(2)	Na2 – Se3$^{\#8}$	3.120(3)
Mn1 – Se3	2.837(2)	Na3 – Se1	2.960(2)
Ge1 – Se3	2.345(2)	Na3 – Se1$^{\#8}$	2.960(2)
Ge1 – Se2	2.344(3)	Na3 – Se2$^{\#6}$	3.089(5)
Ge1 – Se1	2.364(3)	Na3 – Se2$^{\#4}$	3.089(5)
Ge1 – Ge1$^{\#4}$	2.402(2)	Na3 – Se3$^{\#9}$	3.127(6)
Na1 – Se3	2.990(5)	Na3 – Se3$^{\#10}$	3.127(6)
Na1 – Se3$^{\#4}$	2.990(5)	Na4 – Se3$^{\#11}$	2.932(6)
Na1 – Se1$^{\#2}$	3.006(2)	Na4 – Se3	2.932(6)
Na1 – Se1$^{\#5}$	3.006(2)	Na4 – Se1	3.006(6)
Na1 – Se2$^{\#2}$	3.064(6)	Na4 – Se1$^{\#11}$	3.006(6)
Na1 – Se2$^{\#5}$	3.064(6)	Na4 – Se2$^{\#3}$	3.023(2)
Na2 – Se2$^{\#4}$	3.032(6)	Na4 – Se2$^{\#6}$	3.023(2)

Symmetry transformations used to generate equivalent atoms:

$^{\#1}$ x, y, z-1; $^{\#2}$ x+1/2, y+1/2, z; $^{\#3}$ -x, y, -z; $^{\#4}$ x-1/2, y-1/2, z; $^{\#5}$ x-1/2, y+1/2, z; $^{\#6}$ -x+1/2, y+1/2, -z; $^{\#7}$ -x+1, y, -z; $^{\#8}$ x, y, z+1; $^{\#9}$ -x+1/2, y+1/2, -z+1; $^{\#10}$ -x, y, -z+1; $^{\#11}$ -x+1, y, -z+1.

2.3. POWDER X-RAY DIFFRACTION

The laboratory-grade powder X-ray diffraction (PXRD) pattern was obtained using a PANalytical X'Pert Pro diffractometer equipped with a Cu – Kα anode and a linear array

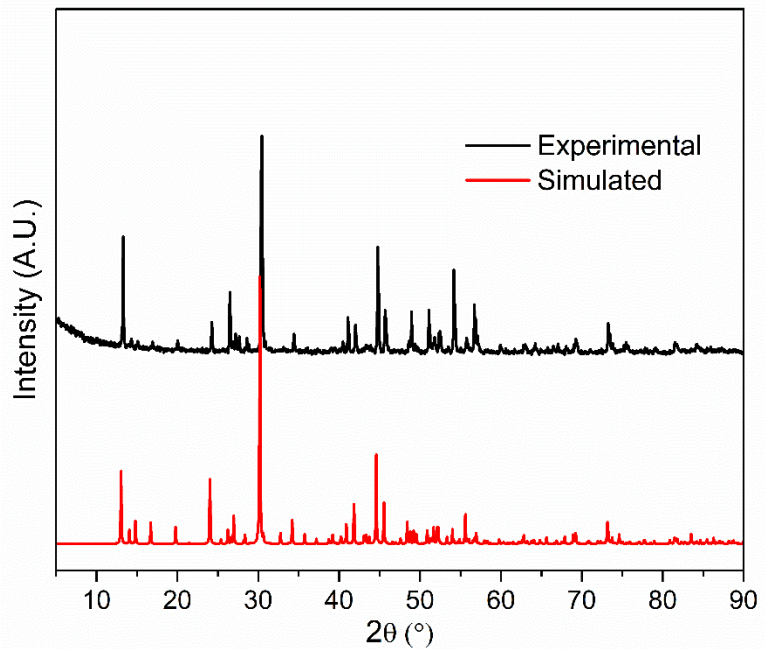

Figure 1. Comparison of simulated and experimental PXRD pattern of DMF washed $Na_8Mn_2(Ge_2Se_6)_2$ synthesized from solid-state metathesis reaction ($Na_6Ge_2Se_6$ + $MnCl_2$).

PIXcel detector over a 2θ range of 5–90° with an average scanning rate of 0.0472° s^{-1}. Hand-ground samples were loaded into an air-tight cell covered with the Kapton film to collect the PXRD pattern. The PXRD pattern of the DMF-washed metathesis route synthesis product is provided in Figure 1. The experimental PXRD pattern matched very well with the simulated pattern derived from the atomic coordinates of single-crystal structure solution, indicating phase purity. The finely-ground DMF-washed samples derived from metathesis reactions were used for further characterization and property

studies. PXRD of the elemental-route synthesis product is provided in Figure S2 (supplementary materials), which shows presence of a small amount of an unknown impurity. This sample was not used for any property measurement or characterization.

2.4. DIFFERENTIAL THERMAL ANALYSIS

Approximately 30 mg of sample was used to collect simultaneous TGA-DSC data on a TA Instruments Q600 SDT from room temperature to 800 °C with a scan rate of 10 °C min^{-1} under an argon atmosphere. The DSC and TGA plots are provided in the Supplementary Materials. The title compound was found to be thermally stable up to 700 °C, after which it shows a melting behavior followed by weight loss, which could be due to selenium loss (Figure S3).

2.5. MAGNETIC MEASUREMENTS

The molar magnetic susceptibility measurements of $Na_8Mn_2(Ge_2Se_6)_2$ were carried out with a Quantum Design MPMS SQUID magnetometer while warming in a 2 T applied field from 2 to 300 K under zero-field-cooled and field-cooled (ZFC and FC) conditions. The isothermal magnetization was subsequently measured at 5 and 300 K in varying applied magnetic field of −5 to +5 T.

2.6. DIFFUSE REFLECTANCE UV/VIS/NIR SPECTROSCOPY

The optical bandgap was determined from the diffuse reflectance data obtained from a Varian Cary 5000 UV-Vis-NIR spectrophotometer. The specimen was quickly ground, pressed on top of the 100% reflectance standard, $BaSO_4$ (Fisher Scientific,

99.92%), and loaded into the Harrick Praying Mantis accessory. Scans were collected between 2500 and 200 nm at a rate of 600 nm min^{-1}. Wavelength values were converted to energy in electron volts and reflectance data were converted to absorption through the Kubelka-Munk equation [34].

2.7. ATTENUATED TOTAL REFLECTANCE (ATR) FOURIER TRANSFORM INFRARED (FT-IR) SPECTROSCOPY

A Thermo Nicolet 380 FT-IR spectrometer outfitted with an attenuated total reflectance (ATR) accessory was used to collect optical transparency data in the IR region. This setup allows a diamond crystal to be in optical contact with the sample, in this case a microcrystalline powder, resulting in a depth of penetration into the sample that approaches the lower limit of the powder sample particle size, ~2 μm. As a result, the effect of thickness dependence on the intensity of the obtained spectrum is rendered negligible [35]. The spectrum, collected and analyzed with the OMNIC software, consists of 32 scans from 400 cm^{-1} to 4000 cm^{-1}.

2.8. NONLINEAR OPTICAL (NLO) CHARACTERIZATION

Polycrystalline powder of $Na_8Mn_2(Ge_2Se_6)_2$ was provided for NLO characterization. Samples were sieved with size ranges of 20–45 μm, 45–75 μm, 75–90 μm, 90–125 μm, 125–150 μm, and >150 μm to examine the phase-matching behavior of SHG and THG, laser-induced damage threshold (LIDT) and two-photon absorption (2PA) coefficient β of the sample. Each sample was sealed in a glass capillary tube and mounted on a homemade sample holder. The SHG and THG efficiencies of the sample were compared with an optical-quality reference material, $AgGaSe_2$, obtained from G&H,

Cleveland, that was ground to a powder and prepared in the same fashion as the sample under investigation. Note here that the particle size ranges for the reference are slightly different from those for the sample, but this does not affect our determination of the NLO properties.

The series of NLO measurements were carried out at room temperature using the input wavelength (λ = 1800 nm) and intensity (0.67 GW/cm^2). We confirmed that sample damage at this intensity is insignificant. Coherent light with a wavelength of 1064 nm was initially produced using an EKSPLA PL-2250 series diode-pumped Nd:YAG laser with a pulse width, τ, of 30 ps and a repetition rate of 50 Hz to generate tunable pulses. The Nd:YAG laser pumped an EKSPLA Harmonics Unit (HU) H400, in which the input beam was frequency tripled by successive NLO processes of SHG and sum frequency generation (SFG). The beam then entered an EKSPLA PG403-SH-DFG Optical Parametric Oscillator (OPO) composed of four main parts: (i) a double-pass parametric generator, (ii) a single pass parametric amplifier, (iii) a second-harmonic generator (SH), and (iv) a difference frequency generation (DFG) scheme. The output wavelength from the OPO used in our experiments was 1800 nm. This wavelength was deliberately selected in order to ensure that SHG (900 nm) occurs below the bandgap of both the test sample and the reference. This implies that bandgap absorption of SHG can be neglected in the $\chi^{(2)}$ measurement. However, the corresponding THG wavelength is 600 nm, which is above the bandgaps for the title compound and the reference. On the other hand, the LIDT experiment was performed at λ = 1064 nm, which is a typical wavelength for DFG to generate mid-IR radiation. Since both the sample and the reference are optically transparent at 1064 nm, two-photon absorption (2PA) is the major mechanism for laser-induced damage. The SHG

and THG signal was collected using a reflection geometry and a fiber-optic bundle coupled to a spectrometer equipped with a CCD camera. The data collection time was 30 seconds for SHG and 300 seconds for THG. A detailed description of our laser and detection setup can be found elsewhere [12].

2.9. ELECTRONIC STRUCTURE CALCULATIONS

Spin polarized electronic band structure calculations were performed using DFT as implemented in the Vienna ab initio simulation package (VASP) [36 – 39]. We employed the revised Perdew–Burke–Ernzerhof generalized gradient approximation (PBESol) [39] to the density functional and used Projected Augmented Wave (PAW) pseudopotential to describe the effect of the core electrons with the following states treated as valence states: 4*s* and 4*p* for Se, 4*s* and 4*p* for Ge, 3*p*, 4*s* and 3*d* for Mn, and 3*s* for Na. The kinetic energy cutoff was set to 520 eV and Monkhorst-pack *k*-point grid size of 7×4×7 was used for Brillouin zone integration [41]. Total energy convergence criterion was set to 10^{-6} eV. The rotationally invariant Hubbard-U type (U = 3 eV) [42] was used to correct the strong correlation of *d* electrons in Mn^{2+} ion. The structure was fully relaxed until the force on each atom was below 0.001 eV/Å.

3. RESULTS AND DISCUSSION

3.1. SYNTHESIS AND CRYSTAL STRUCTURE

Solid-state metathesis stands unique compared to traditional elemental or polychalcogenide flux synthesis in terms of precise product control. Our hypothesis was to

replace two sodium ions with a divalent transition metal ion, Mn^{2+}, in $Na_6Ge_2Se_6$ expecting a product in which transition metal ions will covalently connect the preformed ethane-like building units, $[Ge_2Se_6]^{6-}$, to form a layer while the charge balancing Na^+ ions will fill the interlayer space. In this way, one could avoid the formation of several thermodynamically stable binary or ternary phases and form a quaternary phase in which the transition metal preserves its original oxidation state, and the building unit remains intact during the reaction. Figure 2 shows the solid-state metathesis scheme adopted here with the product retaining the starting building unit and illustrates the mode of connectivity between ethane-like building units $[Ge_2Se_6]^{6-}$ and the Mn^{2+} to generate a more predictable composition and structural features. $Na_8Mn_2(Ge_2Se_6)_2$ crystallizes in polar, NCS space group *C*2, and it is isostructural to $Na_4MgGe_2Se_6$ [13]. The asymmetric unit of $Na_8Mn_2(Ge_2Se_6)_2$ consists of four sodium atoms located on 2*b* and 2*a* Wyckoff sites, one germanium atom and three selenium atoms located on the 4*c* Wyckoff site and one manganese on the 2*a* Wyckoff site (Figure 3a).

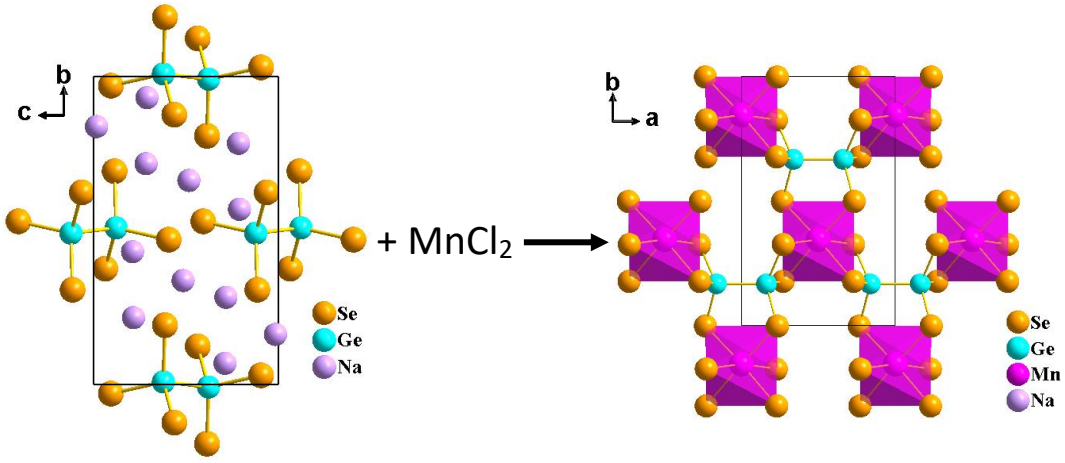

Figure 2. Schematic representation of the solid-state metathesis reaction, showing the mode of connectivity between ethane-like $[Ge_2Se_6]^{6-}$ units and transition metal Mn^{2+}, leading to the formation of layers in the *ab* plane.

The structure of $Na_8Mn_2(Ge_2Se_6)_2$ can be explained in terms of close packing (CP), where the anions form a hexagonal close packing (*hcp*) array in which 5/6th of the octahedral holes are filled by Na and Mn atoms, and the remaining octahedral holes are filled by the Ge–Ge dimer placed parallel to the anion layer (Figure 3b). Such placement of the Ge–Ge dimer forces Ge to coordinate with the two opposite trigonal faces of the octahedron forming an ethane-like dimer. Considering the standard oxidation state of Na, Mn and Se as +1, +2 and –2, respectively, a formal charge of +6 can be assigned to the [Ge–Ge] unit.

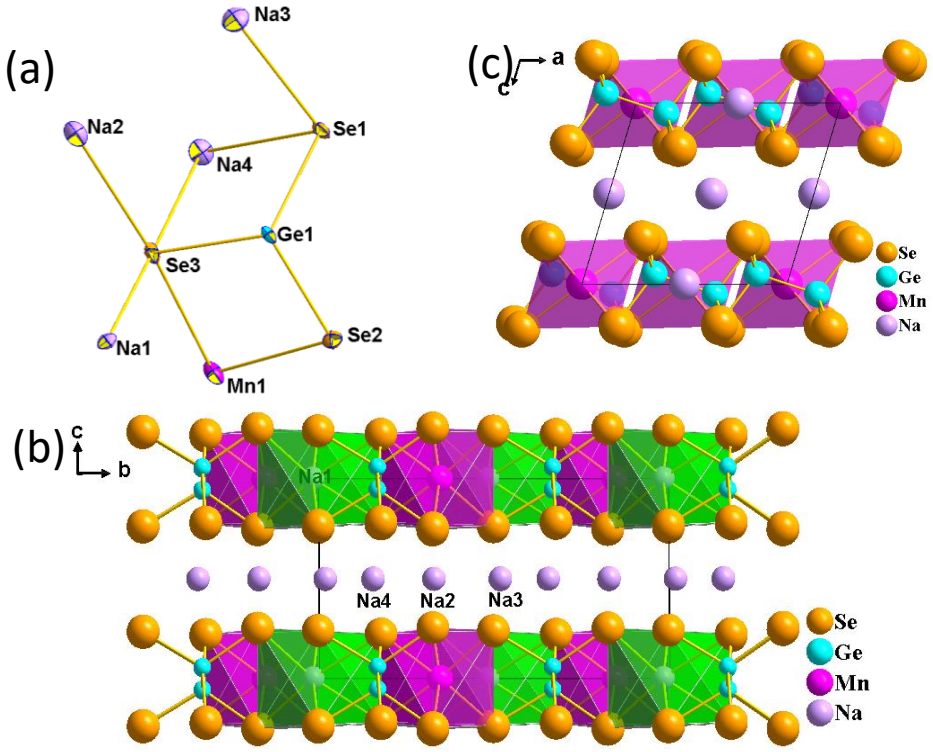

Figure 3. (a) Asymmetric unit of $Na_8Mn_2(Ge_2Se_6)_2$; (b) View along the *a*-axis showing an *ABAB*-type close packing of anion layers with cations filling octahedral holes; (c) View along the *b*-axis showing the orientation of Ge–Ge bond with respect to the layer plane

In other words, the structure contains ethane-like building units, $[Ge_2Se_6]^{6-}$, connecting the transition metal ions and Na ion forming layers of $[Na(1)Mn(Ge_2Se_6)]^{3-}$. The center of the Ge–Ge bonds is located in octahedral interstitials in the $[Na(1)Mn(Ge_2Se_6)]^{3-}$ layers (Figure 3c). The $[Na(1)Mn(Ge_2Se_6)]^{3-}$ layers are separated by sodium atoms along the *c*-axis of the unit cell. Manganese and sodium ions adopt distorted octahedral coordination with Mn–Se and Na–Se bond distances in the range of 2.767(3) – 2.837(2) and 2.932(6) – 3.127(6) Å, respectively. Coordination environments of the four sodium atoms are provided in Figure S4 (Supplementary Materials). The orientation of Ge–Ge bond (2.402(2) Å) makes an angle of 18.43°(6) with the layer plane, similar to the isostructural $Na_4MgM_2Se_6$ (*M* = Si, Ge). Though several compounds with the general formula $Na_{12-nx}M_x^{n+}(Ge_2Q_6)_2$ (Q = S, Se) have been reported, there exist subtle structural differences among them. Compounds containing trivalent metal ions (M^{3+}) with general formula $Na_9M(Ge_2Q_6)_2$ (*M* = La^{3+}, Sm^{3+}; Q = S, Se) [24, 29] crystallize in a centrosymmetric space group in which rare earth metal (M^{3+}) and sodium ion occupy the same crystallographic site (25:75), with Ge–Ge bond making an angle of 19.2° with the layer plane. Compounds containing divalent metal ions with general formula $Na_8M_2(Ge_2Q_6)_2$ (*M* = Eu^{2+}, Pb^{2+}, Sn^{2+}; Q = S, Se) [23], [28] also crystallize in a centrosymmetric space group in which M^{2+} and sodium ion occupy the same crystallographic site (50:50) with Ge–Ge bond perpendicular to the layer plane. However, recently reported $Na_4MgGe_2Se_6$ adopts an NCS structure in which the Mg^{2+} ion occupies an independent crystallographic site with the Ge–Ge bond making an angle of 18.54°(3) with the anion layer unlike other M^{2+} compositions. The reported compound $Na_8Mn_2(Ge_2Se_6)_2$ is thus isostructural to the Mg analogue. These subtle structural

differences between the similar compositions could be due to the different ionic radii of the metal cations.

3.2. MAGNETIC PROPERTIES

Figure 4a shows the temperature dependence of magnetic susceptibility and corresponding inverse molar magnetic susceptibility of $Na_8Mn_2(Ge_2Se_6)_2$ in an applied field of 2T from 2-300 K. The asymptotic nature of χ_M vs T plot within the measured temperature range indicates a paramagnetic behavior without any ordering.

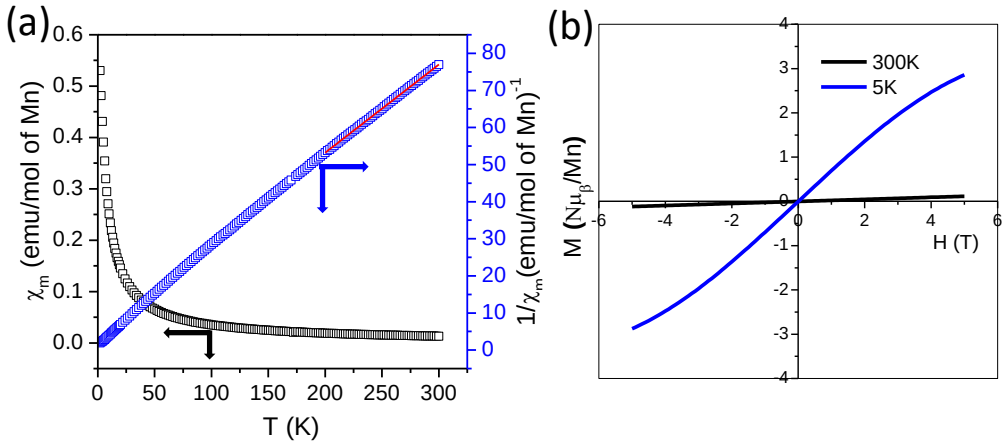

Figure 4. (a) Temperature-dependent molar and inverse molar magnetic susceptibility of $Na_8Mn_2(Ge_2Se_6)_2$ acquired at an applied field of 2 T. The red line indicates linear fitting of the data. (b) Isothermal *M–H* scans at 5 and 300 K.

The temperature dependence of the inverse magnetic susceptibility χ_M^{-1} (T) shows a linear behavior and fitting of the Curie-Weiss law between 200 -300K yields a Curie constant of 4.206 emu.K.mol^{-1} and a Curie-Weiss constant of (θ_p) of –23.88 K, respectively. A Curie-Weiss constant (θ_p) with a negative value indicates overall

antiferromagnetic (AF) interactions between Mn(II) ions albeit no sign of any AF ordering up to the lowest temperature measured. The experimental magnetic moment per manganese derived from the Curie constant is 5.8 μ_B, which is very close to the spin-only magnetic moment of 5.92 μ_B for high spin Mn^{2+} with five unpaired *d* electrons. The variable field isothermal magnetization measured at 300K shows a sluggish increase in the magnetization to a value of 0.11 $N\mu_B$ at 5 T, whereas at 3K, the magnetization gradually increases up to 2.86 $N\mu_B$, giving ~60% of the theoretical saturation moment (5 $N\mu_B$) for high spin Mn^{2+} (Figure 4b).

3.3. OPTICAL BANDGAP AND BAND STRUCTURE ANALYSIS

Diffuse reflectance measurements were performed on an as-synthesized, powder sample of $Na_8Mn_2(Ge_2Se_6)_2$. The equation $\alpha h\nu = A(h\nu - E_g)^m$ was employed to estimate the optical bandgap, where α is the absorption coefficient (Kubelka–Munk function), $h\nu$ is the photon energy, and m = 2 and 1/2 depending on whether the transition is direct or indirect, respectively. $Na_8Mn_2(Ge_2Se_6)_2$ exhibits linearity in the $h\nu$ *vs.* $(\alpha h\nu)^{1/2}$ plot suggesting an indirect nature of the bandgap with a value of 1.95 eV (Figure 5a).In order to understand the origin of bandgap and the contribution of orbitals to the Fermi level, spin polarized electronic band structure calculations at the DFT level were carried out. Because of the presence of localized *d* electrons, an additional Hubbard-like term with simplified Dudarev approach $U_{eff} = U - J = 3$ eV, was used for Mn 3*d* orbitals. Figure 5b displays the partial density of states (pDOS) with a bandgap of 1.52 eV. This value is in reasonable agreement, i.e. expectedly underestimated, with the experimental bandgap of 1.95 eV obtained through diffuse reflectance spectroscopy (DRS) measurements.

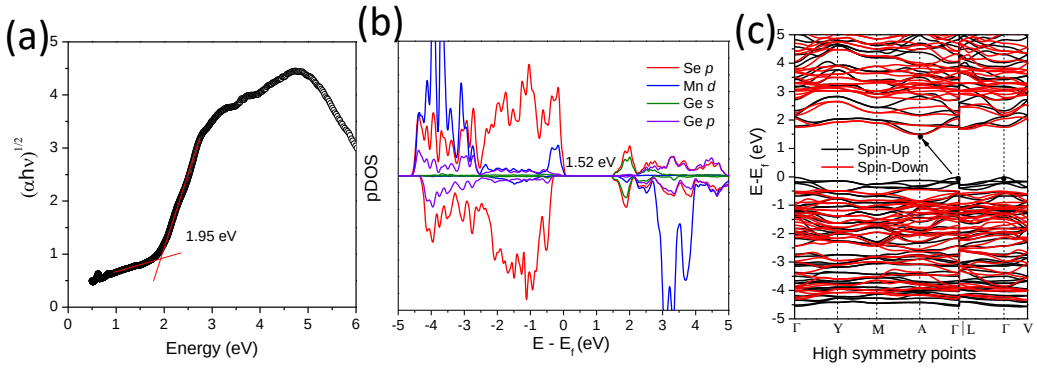

Figure 5. (a) Absorption vs photon energy constructed from the diffuse reflectance UV-Vis-NIR data of $Na_8Mn_2(Ge_2Se_6)_2$; (b) Partial density of states of $Na_8Mn_2(Ge_2Se_6)_2$ calculated using DFT + U by applying U = 3 eV; (c) Electronic band structure of $Na_8Mn_2(Ge_2Se_6)_2$.

The pDOS shows that the states at the top of the valence band have major contributions from Se *p* orbitals and Mn *d* orbitals, whereas the bottom of the conduction band has major contributions from Se *p* orbitals and Ge *s* orbitals. Band dispersion along the high symmetry points in the Brillouin zone is provided in Figure 5c. The band dispersion shows the indirect nature of the bandgap, which agrees well with the experimental DRS measurements. The top of the valence band occurs at the Γ point and the bottom of the conduction band occurs at the A point of the Brillouin zone. Note that in the isostructural $Na_4MgGe_2Se_6$, the contribution from Mg to the top of the valence band is not very significant. This suggests predominant ionic interactions between Mg and Se, thus resulting in a wider bandgap of 2.53 eV compared to $Na_8Mn_2(Ge_2Se_6)_2$ which has the bandgap of 1.95 eV as the Mn *d* orbitals have significant overlap with the Se *p* orbitals and that raises the Fermi level [13]. Therefore, substitution with other M^{+2} metals for Mn could further tune the bandgap of this compound.

3.4. OPTICAL TRANSPARENCY

ATR FT-IR spectroscopy of a microcrystalline specimen of the title compound was used to gain a preliminary assessment of the window of optical clarity. $Na_8Mn_2(Ge_2Se_6)_2$ exhibits a potentially wide region of optical transparency throughout the measured range of 2.5 to 25 microns (Figure 6). A more accurate assessment of the transparency can only be determined on a high-quality, sizeable single crystal specimen. As generally expected for chalcogenides, the IR transparency is theoretically high and extremely attractive.

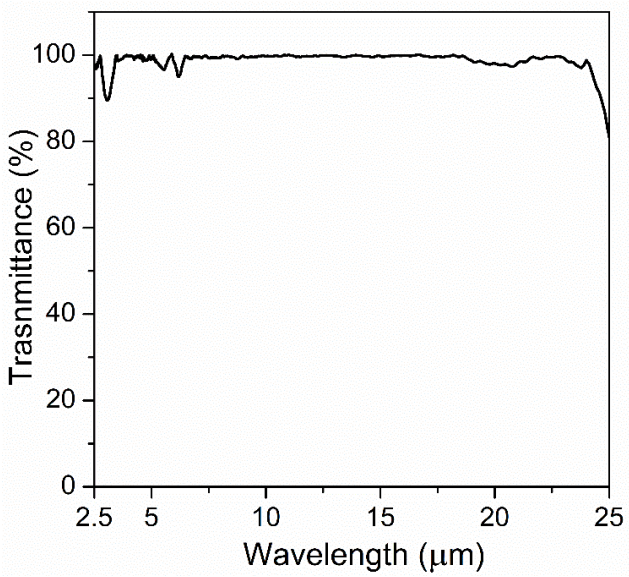

Figure 6. Transmittance (%) from 2.5 – 25μm for $Na_8Mn_2(Ge_2Se_6)_2$.

3.5. SECOND AND THIRD HARMONIC GENERATION (SHG AND THG)

A plot of the SHG counts of the sample (red) and the reference (black) as a function of particle size range for $\lambda = 1800$ nm is shown in Figure 7a. The compound is non-phase matchable, as the measured SHG counts decrease with increasing particle size, although there are some oscillatory behaviors in the middle sizes due to the phase-matching factor

of a sinc function squared [43]. The second-order susceptibility of the sample, $\chi_S^{(2)}$, was compared with that of $AgGaSe_2$ using the Kurtz powder method [12][43] for the non-phase-matching case;

$$\chi_S^{(2)} = \chi_R^{(2)} \frac{l_R}{l_S} \left(\frac{I_S^{SHG}}{I_R^{SHG}}\right)^{1/2}, \quad (1)$$

where I_S^{SHG} and I_R^{SHG} are the measured SHG counts from the sample and the reference and l_S and l_R are the experimentally estimated SHG coherence lengths of the sample and reference, which are 60 and 32.5 μm, respectively. Using $\chi_R^{(2)} \sim 66$ pm/V for $AgGaSe_2$ [16], our calculation yields $\chi_S^{(2)}(Na_8Mn_2(Ge_2Se_6)_2) \sim 3.2 \pm 0.3$ pm/V at 1800 nm.

In order to assess the LIDT, the SHG counts of $AgGaSe_2$ and $Na_8Mn_2(Ge_2Se_6)_2$ of the powder diameter d = 106 – 125 μm were measured as a function of input laser intensity at 1064 nm (Figure 7 b and c). $AgGaSe_2$ and $Na_8Mn_2(Ge_2Se_6)_2$ are both 2PA active at this excitation wavelength. Note here that a lower β value corresponds to a higher LIDT. The SHG counts, measured as a function of input intensity, are expected to increase according to the square power law as given by

$$I_{SHG} = a\left(\frac{I}{1+\beta dI}\right)^2 \quad (2)$$

where I is the fundamental intensity, I_{SHG} is the SHG intensity, β is the 2PA coefficient, d is the particle size of the microcrystalline powder, and a is a proportionality constant that incorporates $\chi^{(2)}$. We estimated the LIDT as the intensity in which the data (dots) deviate from the black dashed line in Figure 7 b and c. Accordingly, the LIDT and β of $AgGaSe_2$ are 0.2 GW/cm^2 and 48.9 cm/GW and those of $Na_8Mn_2(Ge_2Se_6)_2$ are 1.8 GW/cm^2 and 4.8

cm/GW, respectively. Although the second-order nonlinearity of the sample is small, it is notable that the title compound is less prone to optical damage, which may be due to its wider bandgap compared with that of the reference.

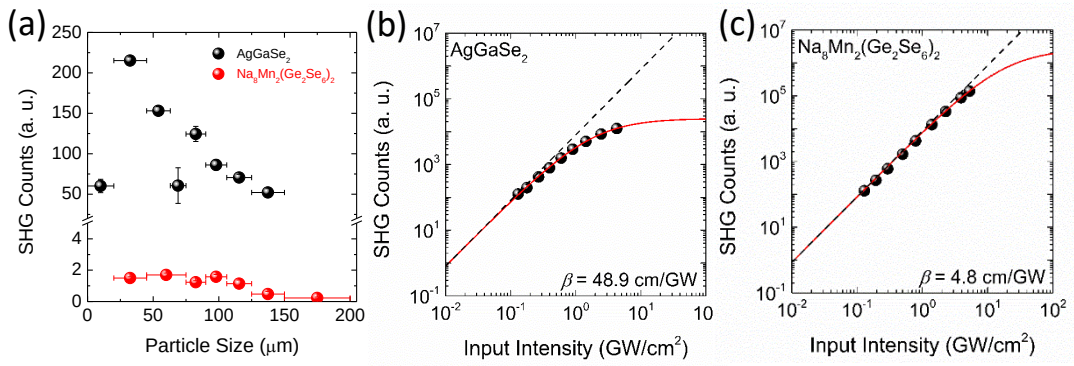

Figure 7. (a) Particle size dependence of SHG for $AgGaSe_2$ (black) and $Na_8Mn_2(Ge_2Se_6)_2$ (red) at λ = 1800 nm. Logarithmic plots of the SHG counts versus input laser intensity for (b) $AgGaSe_2$ and (c) $Na_8Mn_2(Ge_2Se_6)_2$ for I = 0.1–10 GW/cm^2 at λ = 1064 nm and τ=30 ps. The red curve in each case indicates the best fit using equation 2. The black dashed line corresponds to the case for no optical damage, ie. when $\beta = 0$.

The figure of merit (FOM) for the SHG performance can be defined by $\left|\chi^{(2)}\right|^2/\beta$. The corresponding values, including $\chi^{(2)}$, β, LIDT and FOM for the sample and reference are listed in Table 3. Lastly, the THG responses of $Na_8Mn_2(Ge_2Se_6)_2$ and $AgGaSe_2$ were examined using the smallest particle size with an incident wavelength of λ = 1800 nm (Figure 8), because it is quite certain that both sample and reference would exhibit non-phase-matching THG with a larger phase mismatch between the fundamental frequency and the THG frequency, compared with the case for SHG. Note here that THG radiation

would be efficiently absorbed by both sample and reference because the corresponding THG photon energy is about 2.07 eV (600 nm in wavelength) that is above their bandgaps.

Table 3. Comparison of NLO properties of the sample and the reference.

	$AgGaSe_2$	$Na_8Mn_2(Ge_2Se_6)_2$
$\chi^{(2)}$ (pm/V) (λ=1800 nm)	66	3.2±0.3
β (cm/GW) (λ=1064 nm)	48.9	4.8
LIDT(GW/cm^2) (λ=1064 nm; τ=30 ps)	0.2	1.8
FOM	89.1	2.1±1.0

Typically, a good SHG material also exhibits a good THG response. Therefore, it is rather surprising that the THG counts from the sample are about 3.8 times larger than those from the reference, although this could arise partly from more severe THG absorption by the reference having a smaller bandgap of 1.80 eV.

The $\chi_S^{(3)}$ value for $Na_8Mn_2(Ge_2Se_6)_2$ was calculated from the experimentally measured THG counts from the sample (I_S^{THG}) and the reference (I_R^{THG}) by using

$$\chi_S^{(3)} = \chi_R^{(3)}\left(\frac{I_S^{THG}}{I_R^{THG}}\right)^{1/2} \quad (3)$$

where $\chi_R^{(3)}$ is about 1.6×10^5 pm^2/V^2 [7] and the THG coherence lengths, being much smaller than our smallest sieve size, are assumed to be same for simplicity. Equation 3 yields $\chi_S^{(3)}$ ~ 3.0×10^5 pm^2/V^2 at 1800 nm for our sample. This value could be somewhat

overestimated, but our initial assessment clearly indicates that $Na_8Mn_2(Ge_2Se_6)_2$ is a good candidate material for various applications utilizing the third-order nonlinearity.

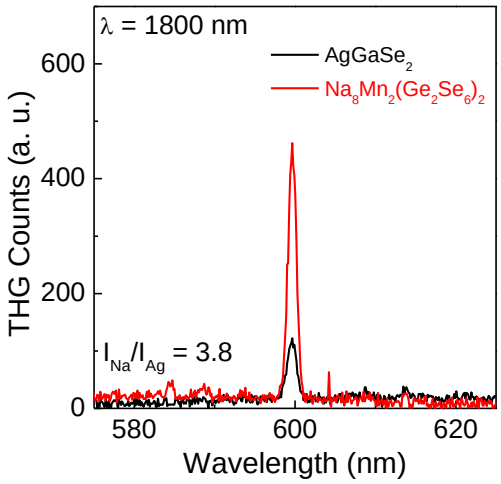

Figure 8. THG measurements of $AgGaSe_2$ (black) and $Na_8Mn_2(Ge_2Se_6)_2$ (red).

4. CONCLUSIONS

A new polar, paramagnetic semiconductor compound, $Na_8Mn_2(Ge_2Se_6)_2$, was synthesized. $Na_8Mn_2(Ge_2Se_6)_2$ shows high LIDT (9x $AgGaSe_2$) and modest SHG response. More importantly, THG measurements indicate that $Na_8Mn_2(Ge_2Se_6)_2$ shows strong THG response at 1800 nm. The observed NLO properties of the title compound is rather unusual exhibiting the modest $\chi^{(2)}$ and the excellent $\chi^{(3)}$, which needs more investigation in the future. Although $Na_8Mn_2(Ge_2Se_6)_2$ is less attractive in terms of SHG efficiency at this moment, it is believed that there are avenues to improve the NLO properties by systematic derivatization of the constituent elements to induce larger dipole moments. High LIDT,

modest SHG, and strong THG response along with potentially wide IR transmission range make the title compound a promising candidate for various IR NLO applications.

ACKNOWLEDGEMENTS

The authors, AC, AVC and SB, thank NSF (grant No. DMR- 1809128) for the funding of this project. The authors JAA and AJC acknowledge the support of the United States National Science Foundation, Division of Materials Research, under grant number DMR-1611198.

SUPPLEMENTARY INFORMATION

Table S1. Fractional atomic coordinates and equivalent isotropic displacement parameters for $Na_8Mn_2(Ge_2Se_6)_2$. U(eq) is defined as 1/3rd of the trace of the orthogonalized U^{ij} tensor.

	x	y	z	U(eq) ($Å^2$)
Se(1)	0.2335(2)	-0.0025(1)	0.2356(2)	0.011(1)
Se(2)	0.2712(2)	0.1766(1)	-0.2201(2)	0.011(1)
Se(3)	0.2724(2)	0.3245(1)	0.2492(2)	0.012(1)
Ge(1)	0.1622(1)	0.1664(2)	0.0560(1)	0.007(1)
Mn(1)	0.5000	0.3444(3)	0	0.013(1)
Na(1)	0	0.4818(6)	0	0.011(1)
Na(2)	0	0.3277(8)	0.5000	0.020(2)
Na(3)	0	0.0176(7)	0.5000	0.020(2)
Na(4)	0.5000	0.1542(7)	0.5000	0.016(2)

Table S2. Anisotropic displacement parameters ($Å^2 x\ 10^3$) for $Na_8Mn_2(Ge_2Se_6)_2$. The anisotropic displacement factor exponent takes the form: $-2p^2[\ h^2a^{*2}U^{11} + ... + 2\ h\ k\ a^*\ b^*\ U^{12}]$

	U^{11}	U^{22}	U^{33}	U^{23}	U^{13}	U^{12}
Se(1)	13(1)	5(1)	14(1)	2(1)	4(1)	1(1)
Se(2)	10(1)	12(1)	12(1)	0(1)	5(1)	-1(1)
Se(3)	13(1)	7(1)	15(1)	-3(1)	4(1)	-3(1)
Ge(1)	7(1)	4(1)	12(1)	0(1)	3(1)	0(1)
Mn(1)	11(1)	8(1)	21(1)	0	5(1)	0
Na(1)	10(3)	13(4)	11(3)	0	7(3)	0
Na(2)	24(4)	13(3)	22(4)	0	7(3)	0
Na(3)	16(4)	23(5)	23(4)	0	10(3)	0
Na(4)	12(3)	17(4)	18(3)	0	1(3)	0

Figure S1. As-synthesized, DMF-washed crystals of $Na_8Mn_2(Ge_2Se_6)_2$.

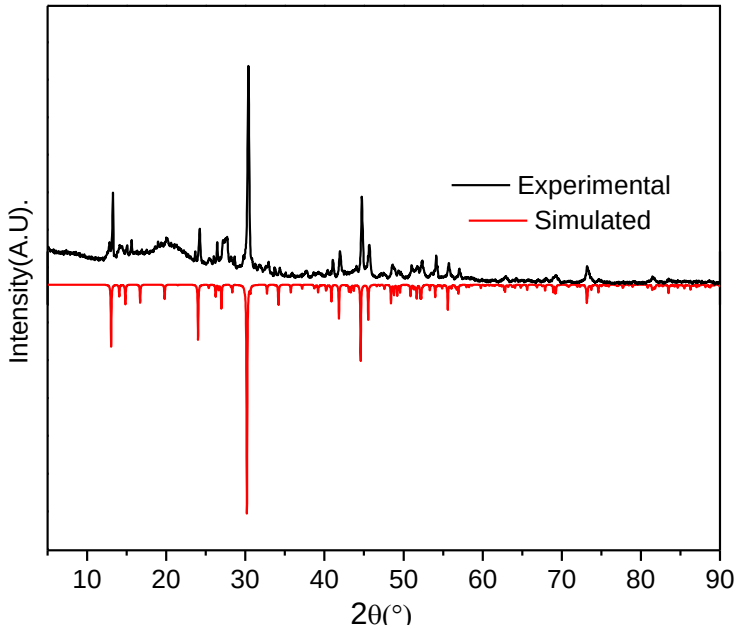

Figure S2. Comparison of simulated and experimental PXRD patterns of $Na_8Mn_2(Ge_2Se_6)_2$ synthesized from elemental route.

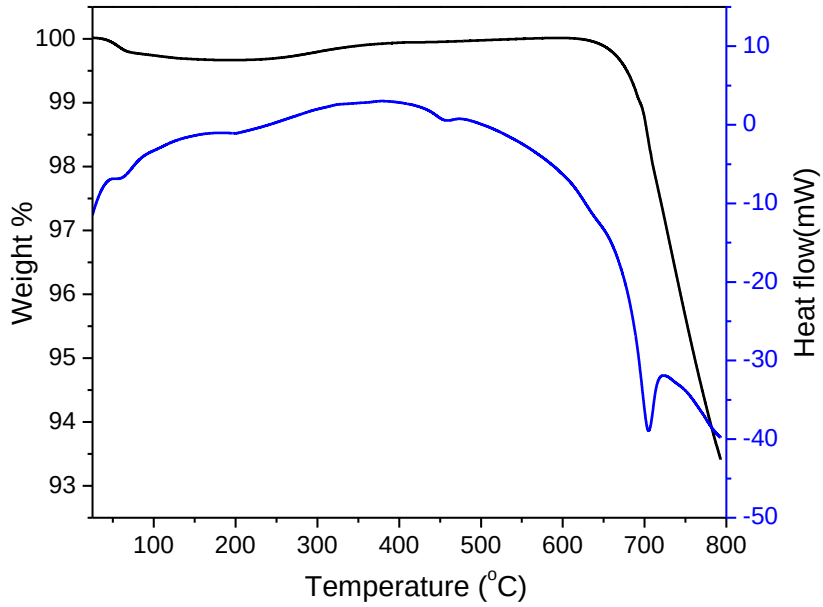

Figure S3. TG-DSC of $Na_8Mn_2(Ge_2Se_6)_2$.

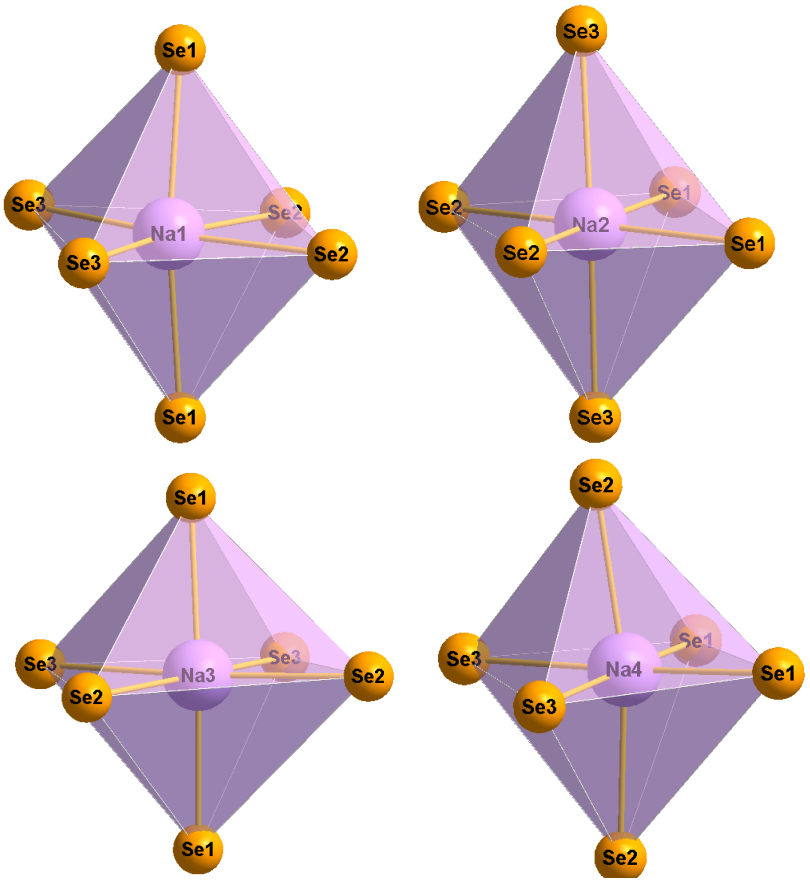

Figure S4. Coordination environments of Na atoms in $Na_8Mn_2(Ge_2Se_6)_2$.

REFERENCES

[1] B.J. Eggleton, B. Luther-Davies, K. Richardson, Chalcogenide photonics, Nat. Photon. 5 (2011) 141-148. https://doi.org/10.1038/nphoton.2011.309.

[2] I. Chung, M.G. Kanatzidis, Metal Chalcogenides: A rich source of nonlinear optical materials, Chem. Mater. 26 (2013) 849–869. https://doi.org/10.1021/CM401737S

[3] X. Luo, Z. Li, Y. Guo, J. Yao, Y. Wu Recent progress on new infrared nonlinear optical materials with application prospect, J. Solid State Chem. 270 (2019) 674-687. https://doi.org/10.1016/j.jssc.2018.12.036.

[4] V. A. Serebryakov, É. V. Boĭko, N. N. Petrishchev, and A. V. Yan, Medical applications of mid-IR lasers. Problems and prospects, J. Opt. Technol. 77 (2010) 6–17. https://doi.org/10.1364/JOT.77.000006.

[5] A.S. Haynes, F.O. Saouma, C.O. Otieno, D.J. Clark, D.P. Shoemaker, J.I. Jang, M .G. Kanatzidis, Phase-change behavior and nonlinear optical second and third harmonic generation of the one-dimensional $K_{(1-x)}Cs_xPSe_6$ and metastable β-$CsPSe_6$, Chem. Mater. 27 (2015) 1837– 1846. https://doi.org/10.1021/acs.chemmater.5b00065.

[6] A. S. Haynes, A. Banerjee, F. O. Saouma, C. O. Otieno, J. I. Jang and M. G. Kanatzidis, Phase transition, conformational exchange, and nonlinear optical third harmonic generation of $ACsP_2Se_8$ (A = K, Rb, Cs), Chem. Mater. 28 (2016) 2374– 2383. https://doi.org/10.1021/acs.chemmater.6b00551.

[7] D. Friedrich, H.R. Byun, S. Hao, S. Patel, C. Wolverton, J.I. Jang, M.G. Kanatzidis, Layered and cubic semiconductors $AGaM'Q4$ ($A^+ = K^+, Rb^+, Cs^+, Tl^+$; $M'^{4+} = Ge^{4+}, Sn^{4+}$; $Q^{2-} = S^{2-}, Se^{2-}$) and high third-harmonic generation, J. Am. Chem. soc. 142 (2020) 17730–17742. https://doi.org/10.1021/jacs.0c08638.

[8] Y. Kim, I. Seo, S.W. Martin, J. Baek, P. Shiv Halasyamani, N. Arumugam, H. Steinfink, Characterization of new infrared nonlinear optical material with high laser damage threshold, $Li_2Ga_2GeS_6$, Chem. Mater. 20 (2008) 6048– 6052. https://doi.org/10.1021/cm8007304.

[9] W. Yin, K. Feng, W. Hao, J. Yao, Y. Wu, Synthesis, structure, and properties of $Li_2In_2MQ_6$ (M = Si, Ge; Q = S, Se): A new series of ir nonlinear optical materials, Inorg. Chem. 51 (2012) 5839–5843. https://doi.org/10.1021/ic300373z.

[10] J.A. Brant, D.J. Clark, Y.S. Kim, J.I. Jang, J.-H. Zhang, J.A. Aitken, $Li_2CdGeS4$, A diamond-like semiconductor with strong second order optical nonlinearity in the infrared and exceptional laser damage threshold, Chem. Mater. 26 (2014) 3045-3048. https://doi.org/10.1021/cm501029s.

[11] J.I. Jang, D.J. Clark, J.A. Brant, J.A. Aitken, Y.S. Kim, Highly efficient infrared optical nonlinearity of a wide-bandgap chalcogenide Li_2CdGeS_4, Opt. Lett. 39 (2014) 4579-4582. https://doi.org/10.1364/OL.39.004579.

[12] J.A. Brant, D.J. Clark, Y.S. Kim, J.I. Jang, A. Weiland, J.A. Aitken, Outstanding laser damage threshold in Li_2MnGeS_4 and tunable optical nonlinearity in diamond-like semiconductors, Inorg. Chem. 54 (2015) 2809–2819. https://doi.org/10.1021/IC502981R.

[13] K. Wu, Z. Yang, S. Pan, $Na_4MgM_2Se_6$ (M = Si, Ge): The first noncentrosymmetric compounds with special ethane-like $[M_2Se_6]^{6-}$ units exhibiting large laser-damage thresholds, Inorg. Chem. 54 (2015) 10108–10110. https://doi.org/10.1021/acs.inorgchem.5b01859.

[14] K. Wu, Z. Yang, S. Pan, Na_2BaMQ_4 (M = Ge, Sn; Q = S, Se): Infrared nonlinear optical materials with excellent performances and that undergo structural transformations, Angew. Chem., Int. Ed. 55 (2016**)** 6713– 6715. https://doi.org/10.1002/anie.201602317.

[15] M.L. Zhou, L. Kang, J.Y. Yao, Z.S. Lin, Y.C. Wu, C.T. Chen. Midinfrared nonlinear optical thiophosphates from $LiZnPS_4$ to $AgZnPS_4$: A combined experimental and theoretical study, Inorg. Chem., 55 (2016) 3724-3726. https://doi.org/10.1021/acs.inorgchem.6b00517.

[16] J.-H. Zhang, D.J. Clark, J.A. Brant, K.A. Rosmus, P. Grima, J.W. Lekse, J.I. Jang, J.A. Aitken, α-Li_2ZnGeS_4: A wide-bandgap diamond-like semiconductor with excellent balance between laser-induced damage threshold and second harmonic generation response, Chem. Mater. 32 (2020) 8947–8955. https://doi.org/10.1021/acs.chemmater.0c02929.

[17] A. Abudurusuli, J.B. Huang, P. Wang, Z.H. Yang, S.L. Pan, J.J. Li, $Li_4MgGe_2S_7$: The first alkali and alkaline-earth diamond-like infrared nonlinear optical material with exceptional large band gap, Angew. Chem., Int. Ed. 60 (2021) 24131–24136. https://doi.org/10.1002/anie.202107613.

[18] K.O. Klepp, Darstellung und Kristallstruktur von Na_4GeSe_4: Ein neues ortho-Selenogermanat(IV), Z. Naturforsch., B. 40 (1985) 878–882. https://doi.org/10.1515/ZNB-1985-0705.

[19] B. Eisenmann, J. Hansa, H. Schaefer, $Na_6Ge_2Se_7$, das erste Selenidosorogermanat(IV), Revue Chim. Minar. 23 (1986) 8-13.

[20] B. Eisenmann, J. Hansa Z. Crystal structure of tetrapotassium hexaselenodigermanate, $K_4Ge_2Se_6$, Z. Kristallogr. - Cryst. Mater. 203 (1993) 301-302. https://doi.org/10.1524/zkri.1993.203.12.301.

[21] B. Eisenmann, E. Kieselbach, H. Schäfer, H. Schrod, Über Thio-, Selenido- und Telluridogermanate (III): Zur Kenntnis von $K_6Ge_2S_6$, $K_6Ge_2Se_6$ und $Na_6Ge_2Te_6$, Z. Anorg. Allg. Chem. 516 (1984) 49–54. https://doi.org/10.1002/ZAAC.19845160908.

[22] B. Eisenmann, J. Hansa, u. H. Schäfer, Oligoselenidogermanate (III): Zur kenntnis von $Na_6Ge_2Se_6$ und $Na_8Ge_4Se_{10}$, Mater. Res. Bull. 20 (1985) 1339–1346. https://doi.org/10.1016/0025-5408(85)90127-8.

[23] G.A. Marking, M.G. Kanatzidis, The ethane-like $[Ge_2S_6]$ metals in $Na_8Pb_2[Ge_2S_6]_2$, $Na_8Sn_2[Ge_2S_6]_2$, and $Na_8Pb_2[Si_2Se_6]_2$, J. Alloys Compd. 259 (1997) 122–128. https://doi.org/10.1016/S0925-8388(97)00038-8.

[24] B.R. Martin, L.A. Polyakova, P.K. Dorhout, Synthesis and characterization of a family of two related quaternary selenides: $Na_8Eu_2(Si_2Se_6)$ 2 and $Na_9Sm(Ge_2Se_6)_2$, J. Alloys Compd. 408-412 (2006), 490-495. https://doi.org/10.1016/j.jallcom.2004.12.091.

[25] A. Choudhury, L.A. Polyakova, I. Hartenbach, T. Schleid, P.K. Dorhout, Synthesis, structures, and properties of layered quaternary chalcogenides of the general formula $ALnEQ_4$ (A = K, Rb; Ln = Ce, Pr, Eu; E = Si, Ge; Q = S, Se), Z. Anorg. Allg. Chem. 632 (2006) 2395–2401. https://doi.org/10.1002/ZAAC.200600226.

[26] A. Choudhury, L.A. Polyakova, S. Strobel, P.K. Dorhout, Two non-centrosymmetric cubic seleno-germanates related to CsCl-type structure: Synthesis, structure, magnetic and optical properties, J. Solid State Chem. 180 (2007) 1381-1389. https://doi.org/10.1016/j.jssc.2007.02.002.

[27] A. Choudhury, S. Strobel, B.R. Martin, A.L. Karst, P.K. Dorhout, Synthesis of a family of solids through the building-block approach: A case study with Ag+ substitution in the ternary Na-Ge-Se system, Inorg. Chem. 46 (2007) 2017-2027. https://doi.org/10.1021/ic061064z.

[28] A. Choudhury, K. Ghosh, F. Grandjean, G.J. Long, P.K. Dorhout, Structural, optical, and magnetic properties of $Na_8Eu_2(Si_2S_6)_2$ and $Na_8Eu_2(Ge_2S_6)_2$: Europium(II) quaternary chalcogenides that contain an ethane-like $(Si_2S_6)^{6-}$ or $(Ge_2S_6)^{6-}$ moiety, J. Solid State Chem. 226 (2015) 74–80. https://doi.org/10.1016/j.jssc.2015.02.006.

[29] B.R. Martin, J.M. Knaust, P.K. Dorhout, Crystal structure of nonasodium lanthanum(III) bis[hexaselenodigermanate], $Na_9La[Ge_2Se_6]_2$, Z. Krist. - New Cryst. Struct. 220 (2005) 294–294. https://doi.org/10.1524/ncrs.2005.220.3.294.

[30] Bruker- SMART. Bruker AXS Inc., Madison, Wisconsin, USA. 2002.

[31] Bruker-SAINT and SADABS, and SHELXTL. Bruker AXS Inc., Madison, Wisconsin, USA, 2008.

[32] G. M. Sheldrick, A short history of SHELX. Acta Crystallogr., Sect. A: Found. Crystallogr. 64 (2008) 112–122. https://doi.org/10.1107/S0108767307043930.

[33] C.B. Hübschle, G.M. Sheldrick, B. Dittrich, ShelXle: A Qt Graphical user interface for SHELXL. J. Appl. Crystallogr. 44 (2011) 1281–1284. https://doi.org/10.1107/s0021889811043202.

[34] P. Kubelka, F. Munk, Ein Beitrag Zur Optik Der Farbanstriche, Z. Techn. Phys. 12 (1931) 593 - 601.

[35] R.J. McGowan, Attenuated total reflectance vs. Transmission infrared spectrometry in the quantitative evaluation of paint vehicles, Anal. Chem. 35 (1963) 1664-1665. https://doi.org/10.1021/ac60204a037.

[36] G. Kresse, J. Hafner, Ab initio molecular dynamics for liquid metals. Phys. Rev. B 47 (1993) 558–561. https://doi.org/10.1103/PhysRevB.47.558.

[37] G. Kresse, J. Furthmüller, Efficiency of ab-initio total energy calculations for metals and semiconductors using a plane-wave basis set, Comput. Mater. Sci. 6 (1996) 15–50. https://doi.org/10.1016/0927-0256(96)00008-0.

[38] G. Kresse, J. Furthmüller, Efficient iterative schemes for ab initio total-energy calculations using a plane-wave basis set, Phys. Rev. B 54 (1996) 11169–11186. https://doi.org/10.1103/PhysRevB.54.11169

[39] D. Joubert, From ultrasoft pseudopotentials to the projector augmented-wave method, Phys. Rev. B 59 (1999) 1758–1775. https://doi.org/10.1103/PhysRevB.59.1758.

[40] J.P. Perdew, A. Ruzsinszky, G.I. Csonka, O.A. Vydrov, G.E. Scuseria, L.A. Constantin, X. Zhou, K. Burke, Restoring the density-gradient expansion for exchange in solids and surfaces, Phys. Rev. Lett. 100 (2008) 136406. https://doi.org/10.1103/PhysRevLett.100.136406.

[41] H.J. Monkhorst, J.D. Pack, Special points for brillonin-zone integrations, Phys. Rev. B. 13 (1976) 5188. https://doi.org/10.1103/PhysRevB.13.5188.

[42] A.I. Liechtenstein, V.I. Anisimov, J. Zaanen, Density-functional theory and strong interactions: orbital ordering in mott-hubbard insulators, Phys. Rev. B. 52(1995) R5467. https://doi.org/10.1103/PhysRevB.52.R5467.

[43] S.K. Kurtz, T.T. Perry, A powder technique for the evaluation of nonlinear optical materials, J. Appl. Phy. 39 (2003) 3798. https://doi.org/10.1063/1.1656857.

VII. ULTRALOW THERMAL CONDUCTIVITY THROUGH THE INTERPLAY OF COMPOSITION AND DISORDER BETWEEN THICK AND THIN LAYERS OF MAKOVICKYITE STRUCTURE

*Srikanth Balijapelly,[a] Ashlee Hauble,[b] Mathew Pollard,[c] Morgane Poupon,[d] Václav Petříček,[d] Jeremy Lee Watts,[e] Yew San Hor,[c] Susan M. Kauzlarich,[b] and Amitava Choudhury[a,] **

[a]Department of Chemistry, Missouri University of Science and Technology, Rolla, MO 65409, USA

[b]Department of Chemistry, One Shields Avenue, University of California, Davis, California 95616, United States

[c]Department of Physics, Missouri University of Science and Technology, Rolla, MO 65409, USA

[d]Institute of Physics, Czech Academy of Sciences, Na Slovance 2, 182 21 Prague, Czech Republic

[e]Department of Materials Science and Engineering, Missouri University of Science and Technology, Rolla, MO 65409, USA*

ABSTRACT

Here we report the synthesis and characterization of three quaternary complex chalcogenides, $Ag_{0.72}Bi_{5.48}Cu_{0.88}S_9$ (I), $Ag_{0.70}Bi_{5.30}Cu_{1.3}S_9$ (II), $Ag_{0.34}Bi_{4.54}Cu_{1.98}PbS_9$ (III). All the compounds in this homologous series crystallize in the *C2/m* space group and can be described as Pavonite structures. This structure type consists of alternating NaCl-like layers with varied thickness (^nP), separated by a pair of square pyramids. All the compounds reported here are synthetic analogues of the n = 4 pavonite family and are known as makovickyite minerals. Compounds I – III possess complex crystal structures, consisting of mixed occupancies of Bi/Ag/Pb sites, as well as partially occupied Cu sites.

These intrinsic assets lead to ultra-low lattice thermal conductivities, in the range of 0.75 – 0.42 $Wm^{-1}K^{-1}$ from 300 – 500 K, and make these materials promising candidates for thermoelectric applications. All three structures exhibit very narrow indirect band gaps of less than 0.5 eV as confirmed by DRS measurements. Charge transport properties are consistent with *n*-type semiconducting behavior with moderate electrical conductivities and large Seebeck coefficients. Low temperature electrical resistivity and Seebeck coefficient measurements are also performed on II. A promising figure of merit, *zT*, of 0.09 for I and II, 0.11 for III can be achieved at 475 K.

1. INTRODUCTION

Complex crystal structure and intrinsic structural disorder in ternary and quaternary chalcogenides have been demonstrated to have strong influences on thermoelectric properties, especially on lattice thermal conductivity.[1,2] Minimization of total thermal conductivity is one of the key factors in developing high-performance thermoelectric materials, since the efficiency of thermoelectric materials is defined by the figure of merit, $zT = \frac{S^2\sigma T}{\kappa_{total}}$, where S is Seebeck coefficient, σ is electrical conductivity, κ_{total} is total thermal conductivity and T is the absolute temperature. All these properties are interrelated via carrier concentration, making it difficult to isolate and improve one without negatively impacting another. For example, higher electrical conductivity is associated with lowering of the Seebeck coefficient and increasing the electronic component of the thermal conductivity.[1,3-5] Given the correlated nature of these properties, one strategy to increase *zT* is to focus on lattice thermal conductivity, which does not depend on carrier

concentration. Synthesizing new compounds is in the hands of solid state chemists where lattice thermal conductivity can be minimized without adversely affecting S or σ. Strategies to reduce lattice thermal conductivity often rely on approaches that scatter phonons without affecting electrical conductivity and include defect engineering, such as point defect creation, grain boundaries, nano structuring, disorder and structural complexity. Additionally, compounds with lattice anharmonicity originating from stereo-active lone pairs located on heavy elements such as Bi, Sb, and Pb make ideal candidates to achieve ultra-low thermal conductivity.[6,7] All of these strategies to minimize thermal conductivity can be implemented in complex chalcogenides, which highlights the fact that identifying an appropriate family of crystal structures is crucial to discovering a high efficiency thermoelectric material.

Among several complex chalcogenide structures, the pavonite mineral family exhibits a high degree of structural and compositional diversity.[8-10] The Pavonite family of compounds possesses three-dimensional (3-D) structure with layer-like modules stacked through bridging S atoms. The thin slab, called the 'a' layer, consists of paired square pyramids of BiS_5 and the thick slab, called an incremental slab, is comprised of BiS_6 octahedra which can have varied number of octahedra '*n*' (in ^{n}P series) along the diagonal direction. The idealized unsubstituted homologues of the pavonite family can be described by the general formula $Ag^{ab}{}_{n-1}Bi^{a}{}_{4}Bi^{ab}Bi^{b}{}_{n+2}S_{2n+10}$ (for $Z = 1$, formula unit), where $n = 2 – 11$.[9] Because of their high tolerance of specific crystallographic sites for cations of different radii, a wide range of compositions can be derived and synthesized by incorporating transition as well as main group metals, Cu, Mn, Pb, In, Sb and Sn and so on.[11-24] Recently, several pavonite compounds were investigated and displayed promising thermoelectric

properties.[11-16,19,25] For example, the Kanatzidis group has investigated $AgBi_3S_5$ which belongs to the ^{5}P pavonite family and features remarkably low lattice thermal conductivity (0.6 $Wm^{-1}K^{-1}$) at room temperature due to double rattling phonon modes of Bi and Ag atoms.[17] Cd*M*Bi_4Se_8 (*M* = Pb/Sn) belongs to the *n* = 3 pavonite family with ultralow thermal conductivity of 0.58 $Wm^{-1}K^{-1}$ at 320 K and a peak *zT* of 0.63 for $CdPbBi_4Se_8$ at 850 K.[18] Pavonites containing alkali ions (^{5}*P*) *A*$Sn_2Bi_5S_{10}$ (*A* = Li/Na) show low thermal conductivities in the range of 0.6 – 0.8 $Wm^{-1}K^{-1}$.[15] Intrinsic high frequency thermal vibration of interstitial Cu atoms in the lattice were proven to scatter phonons effectively in the $Cu_{x+y}Bi_{5-y}Q_8$ (*Q* = S, Se) series.[26,27,28] All these attributes make pavonite compounds an interesting class of materials for further investigation. However, several compositions have yet to be studied and the origin of the low thermal conductivity understood.

In this work, we have identified a ^{4}*P* pavonite series also known as makovickyite family which has an idealized formula of $Ag_{1.5}Bi_{5.5}S_9$ (Z = 2, formula), in which Ag occupies an octahedral site in the thin layer as well as substituting on the Bi site in the thick layer.[9] However, when Ag is replaced by Cu^+, the Cu^+ can occupy both tetrahedral and interstitial sites in the thin layer (*a)*, along with heterotopic substitution in the thick layer.[29,30] When both Cu and Ag are present in the structure, Ag may or may not be present in the thin layer[8,9,31-33] and if the amount of Cu is more (1.5 to 2 per formula unit, Z = 2), Cu atoms can substitute with statistical disorder and partial occupancy on crystallographic sites in the thin layer.[33] Substitution of excess Pb and Cu for Bi adds additional complexity, as one of the cell axes doubles resulting in a Cu-ordered structure similar to cupromakovickyite minerals.[31,32] Taking cue from these observations we sought to synthesize analogues of makovickyite/cupromakovickyites with varying amounts of Cu

while keeping the content of Ag relatively constant to study the effect of disorder in the lattice on thermal conductivity. We also substitute Pb in one of the compositions to evaluate the effect of lattice anharmonicity on the lattice thermal conductivity. Thus, in this manuscript we are reporting the synthesis, structural characterization, and thermoelectric properties of compositions $Ag_{0.72}Bi_{5.48}Cu_{0.88}S_9$ (I), $Ag_{0.70}Bi_{5.30}Cu_{1.3}S_9$ (II), $Ag_{0.34}Bi_{4.54}Cu_{1.98}PbS_9$ (III) with Cu/Ag ratio of 1.22 (I), 1.85(II), and 5.82(III), respectively. Measurements of physical properties exhibited ultra-low thermal conductivities (<0.8 $Wm^{-1}K^{-1}$), high Seebeck coefficient values, and moderate electrical conductivities, which give rise to reasonably good thermoelectric figures of merit for compounds, I – III, at moderately low temperatures.

2. EXPERIMENTAL SECTION

2.1. SYNTHESIS

Compounds, I – III, are the synthetic analogues of naturally occurring minerals.[31-33] In our target stoichiometry we have closely followed the reported nominal compositions, $Ag_{0.68}Bi_{5.60}Cu_{1.06}S_9$ for I,[32] $Ag_{0.62}Bi_{5.38}Cu_{1.56}S_9$ for II,[33] and $Ag_{0.52}Bi_{4.48}Cu_2PbS_9$ for III.[31, 32] Compounds, I – III, were synthesized by melting stoichiometric combinations of high purity Cu (Aldrich 99%), Ag (Alfa Aesar 99.9%), Bi (Cominco electronic materials), Pb (Alfa Aesar 99.9%), and S (Alfa Aesar 99.99%) powders. All the powder precursors were weighed accordingly and loaded into 12 mm diameter quartz ampoule (total weight of 3 g) and flame sealed under vacuum. The sealed ampoules were heated to 700 °C at a rate of 20 °C/h and dwelled for four days before cooling to room temperature at a rate of 35 °C/h.

A silvery single ingot was obtained in all cases. Appropriate crystals were picked from crushed large ingots and used for single-crystal X-ray diffraction. Well-ground powder samples were used for further characterizations.

2.2. SINGLE CRYSTAL X-RAY DIFFRACTION

High quality single-crystals from I, II, and III were mounted on a Bruker smart apex diffractometer equipped with a sealed tube X-ray source with Mo–Kα radiation (λ = 0.71073 Å) using a glass fiber. Room temperature diffraction data were collected using SMART[34] software with a step of 0.3° in ω scan and 20 s/frame exposure time. SADABS[35], respectively. SHELXS-97 and difference Fourier syntheses were used to solve the structures.[36] Full-matrix least-squares refinement against $|F^2|$ was carried out using the SHELXTL-PLUS suite of programs.[35] For all compounds final refinements were carried out by SHELX-2018 incorporated in SHELXLe.[37] Our crystal structure solutions match very well with the reported ones for I and II. However, for III we did not get the doubled *c*-axis cell as the mineral structure,[32] which could be due to the high temperature synthesis procedure adopted in the laboratory compared to natural crystal growth or due to slight deviation in our composition compared to the reported mineral. This was clear when all the reflections were projected on the reciprocal lattice, except for few spurious reflections all reflections fit into the normal cell. There were no systematic unaccounted reflections that would suggest a doubling of cell (Figure S1). All the compounds crystallize in *C*2/*m* space group (No.12). There are five well-behaved S sites, out of which four are located on 4*i* and one on 2*c* and Bi can be located on three 4*i* site either fully or jointly occupied with Ag/Pb. Out of three Bi sites, Bi1 and Bi2 are located in the thick layer and Bi3 is located

in the thin layer. In compound I, two 4*i* sites are fully occupied by Bi and the other by Bi/Ag (Bi1 and Ag1) jointly occupied with 74:26 ratio. Besides mixed occupancy with Bi, Ag is present in an octahedral 2*a* site (Ag2) in thin layer with 20% site occupancy.

Table 1. Crystal data and refinement details for I, II and III.

	I	**II**	**III**
Empirical formula	$Ag_{0.72}Bi_{5.48}Cu_{0.88}S_9$	$Ag_{0.70}Bi_{5.30}Cu_{1.3}S_9$	$Ag_{0.34}Bi_{4.54}Cu_{1.98}PbS_9$
Formula weight	1567.33	1554.24	1606.98
Temperature	295(2) K	295(2) K	295(2) K
Wavelength	0.71073 Å	0.71073 Å	0.71073 Å
Crystal system	Monoclinic	Monoclinic	Monoclinic
Space group	*C* 2/*m*	*C* 2/*m*	*C* 2/*m*
Unit cell dimensions	a = 13.1938(15) Å	a = 13.227(2) Å	a = 13.356(2) Å
	b = 4.0566(5) Å	b = 4.0511(6) Å	b = 4.0339(6) Å
	c = 14.6417(17) Å	c = 14.637(2) Å	c = 14.841(2) Å
	b= 99.5290(10)°	b= 99.496(3)°	b= 99.915(2)°
Volume	772.84(16) $Å^3$	773.6(2) $Å^3$	787.6(2) $Å^3$
Z	2	2	2
Density (calculated)	6.735 g/cm^3	6.673 g/cm^3	6.776 g/cm^3
Absorption coefficient	65.420 mm^{-1}	63.858 mm^{-1}	65.366 mm^{-1}
Goodness-of-fit on F2	1.034	1.011	1.094
R [$I > 2\sigma(I)$][a]	R1 = 0.0283	R1 = 0.0299	R1 = 0.0318
wR ($F2$) (all data)[b]	wR2 = 0.0676	wR2 = 0.0696	wR2 = 0.0706

[a] $R_1 = \sum||F_o| - |F_c|/\sum|F_o|$.

[b] $wR_2 = \{\sum[w(F_o^2 - F_c^2)^2]/\sum[w(F_0^2)^2]\}^{1/2}$, $w = 1/[\sigma^2(F_o)^2 + (aP)^2 + bP]$, where $P = [F_o^2 + 2F_c^2]/3$

Table 2. Selected bond lengths (Å) for $Ag_{0.72}Bi_{5.48}Cu_{0.88}S_9$ (I), $Ag_{0.70}Bi_{5.30}Cu_{1.3}S_9$ (II), $Ag_{0.34}Bi_{4.54}Cu_{1.98}PbS_9$ (III).

I		**II**		**III**	
Moiety	Distances (Å)	Moiety	Distances (Å)	Moiety	Distances (Å)
Bi1 – S2	2.651(3)	Bi1 – S2	2.653(3)	Bi1 – S2	2.675(3)
Bi1 – S4$^{\#1}$	2.805(2)	Bi1 – S4$^{\#1}$	2.806(2)	Bi1 – S4$^{\#1}$	2.809(2)
Bi1 – S1$^{\#3}$	2.8860(4)	Bi1 – S1$^{\#3}$	2.8912(4)	Bi1 – S1$^{\#3}$	2.8998(4)
Bi1 – S4	3.003(4)	Bi1 – S4	2.983(4)	Bi1 – S4	3.070(4)
Bi2 – S5	2.657(3)	Bi2 – S5	2.663(3)	Bi2 – S5	2.661(3)
Bi2 – S2$^{\#5}$	2.761(2)	Bi2 – S2$^{\#5}$	2.761(2)	Bi2 – S2$^{\#5}$	2.766(2)
Bi2 – S4$^{\#2}$	2.927(2)	Bi2 – S4$^{\#2}$	2.928(2)	Bi2 – S4$^{\#2}$	2.929(2)
Bi2 – S1	3.0131(6)	Bi2 – S1	2.9943(6)	Bi2 – S1	3.0294(7)
Bi3 – S3$^{\#7}$	2.590(3)	Bi3 – S3$^{\#7}$	2.595(3)	Bi3 – S3$^{\#7}$	2.546(4)
Bi3 – S5$^{\#4}$	2.840(2)	Bi3 – S5$^{\#3}$	2.839(2)	Bi3 – S3$^{\#3}$	2.785(3)
Bi3 – S3$^{\#3}$	2.858(2)	Bi3 – S3$^{\#3}$	2.8562(19)	Bi3 – S5$^{\#4}$	2.976(4)
Ag2 – S5	2.233(3)			Pb1 – S3$^{\#7}$	2.769(5)
Ag2 – S3$^{\#8}$	2.902(2)			Pb1 – S5$^{\#4}$	2.809(4)
				Pb1 – S3$^{\#3}$	3.042(4)

Symmetry transformations used to generate equivalent atoms:

I #1 -x+1/2,-y-1/2,-z+1 #2 -x+1/2,-y+1/2,-z+1 #3 x+1/2,y+1/2,z #4 x+1/2,y-1/2,z #5 x-1/2,y-1/2,z #7 -x+1,-y,-z #8 -x,-y,-z II #1 -x+1/2,-y-1/2,-z+1 #2 -x+1/2,-y+1/2,-z+1 #3 x+1/2,y+1/2,z #5 x-1/2,y-1/2,z #7 -x+1,-y,-z III #1 -x+1/2,-y-1/2,-z+1 #2 -x+1/2,-y+1/2,-z+1 #3 x+1/2,y+1/2,z #4 x+1/2,y-1/2,z #5 x-1/2,y-1/2,z #7 -x+1,-y,-z

Additionally, there are three partially occupied Cu sites with 35% (Cu1, 4g), 7% (Cu2, 4*i*) and 2%(Cu3, 4*i*) occupancy in the thin layer yielding a final charge balanced formula of $Ag_{0.72}Bi_{5.48}Cu_{0.88}S_9$ (I). For the refinement of II, three 4*i* sites have been assigned to Bi, among which two 4*i* sites in the thick layer contain Ag with 28% and 7%

site occupancies, respectively. Further refinements resulted in partial occupancy for Cu in four crystallographically unique positions in the thin layer, yielding a low *R* factor of 3.0% with a final charge balanced formula of $Ag_{0.70}Bi_{5.30}Cu_{1.3}S_9$ (II). A different situation was observed in compound III, with one 4*i* site (Bi2) having almost full occupancy of Bi (94%) with small amount of Cu (Cu3) substitution (6%) taking place at slightly off from Bi site. The other two sites are mixed occupied by Bi/Ag (Bi1/Ag1) and Bi/Pb (Bi3/Pb1), respectively. Due to the similar X-ray scattering power of Bi (Z = 83) and Pb (Z = 82), free refinement of their occupancies was not reasonable, therefore, relative proportions according to stoichiometry used for the reaction were considered for further refinements. However, the position of Bi and Pb found to be split between Pb1 and Bi3 positions. By freely refining the Bi/Ag, *R* factor reduced significantly resulting 83% occupancy for Bi1 and 17% occupancy for Ag1 in 4*i* site in thick layer. Cu was found to partially occupy four different crystallographic sites yielding a final charge balanced formula, $Ag_{0.34}Bi_{4.54}Cu_{1.98}PbS_9$ (III). It is to be noted here that the use of split positions of Pb1 and Bi3 for III was evaluated against a model considering presence of anharmonic atomic displacement parameters (ADPs). The probability density function (P.D.F) of electrons was calculated from the refined anharmonic ADPs in the direct space to make sure that there were no termination effects in such maps. Such calculations indicated that the introduction of 4th order tensor leads to an unrealistic distribution of atoms in the Bi3/Pb1 site (Figure S2). On the other hand, the shape of the P.D.F with using only 3rd order term seemed to indicate split atom positions as we have used in our model (Figure S2). Moreover, it yielded a similar fit with the same number of refined parameters (Table S1). This means that we have a very reasonable support for split positions of Bi3/Pb1. The

crystal data and refinement parameters are given in Table 1, and selected bond lengths are listed in Table 2. Atomic coordinates, isotropic and anisotropic displacement parameters are given in Tables S2-S7. It is to be noted here that the final crystallographically-derived compositions are very close to the nominal compositions targeted and they are all charge balanced, $Ag_{0.72}Bi_{5.48}Cu_{0.88}S_9$ (I), $Ag_{0.70}Bi_{5.30}Cu_{1.3}S_9$ (II), and $Ag_{0.34}Bi_{4.54}Cu_{1.98}PbS_9$ (III).

2.3. POWDER X-RAY DIFFRACTION

To evaluate the bulk purity of the samples, the room temperature powder X-ray diffraction (PXRD) was carried out on hand ground polycrystalline samples using PANalytical X'Pert diffractometer assembled with Cu Kα anode and a linear array PIXcel detector over a 2θ range of 5 to 90° with an average scanning rate of 0.0472° s^{-1}. Powder diffraction patterns of the well-ground as-synthesized samples are provided in Figure 1 along with one-to-one matching of simulated patterns derived from atomic coordinates of I – III obtained from single-crystal structure solutions. To further verify the phase-purity, we have carried out Rietveld refinement of the PXRD patterns of the as-synthesized products using the single-crystal atomic coordinates. Good convergence between the calculated and the experimental patterns along with the low values of weighted profile residuals, Rwp, (Figure S3 and Table S8) confirm the correctness of the model. The refined unit cell parameters are in good agreement with the single-crystal structure solution (compare tables 1 and S8). Rietveld refinements also show absence of any discernable impurity phase(s) in I – III. PXRDs were also collected on the hot-pressed samples to see any phase transformations during the hot pressing (Figure S4).

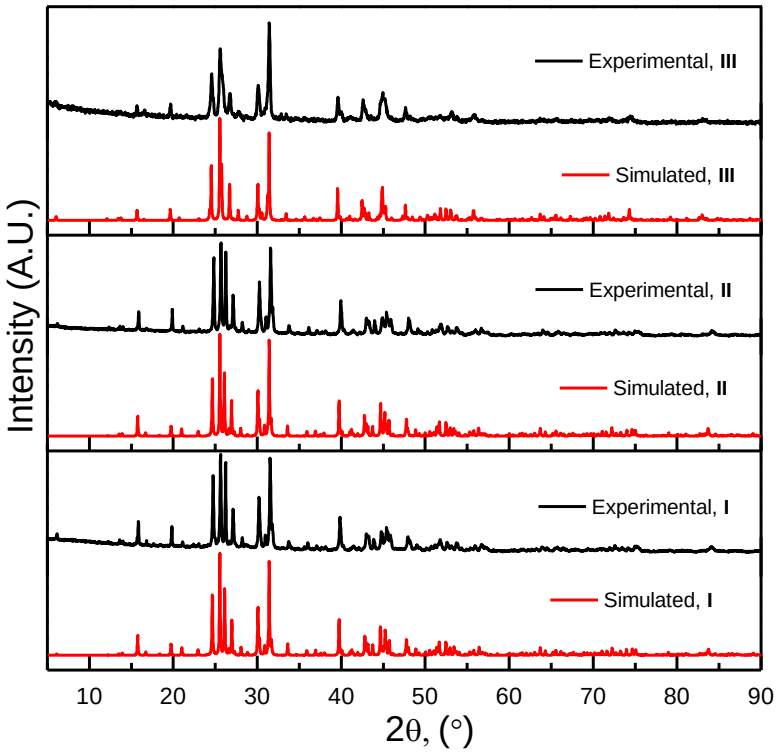

Figure 1. Comparison of experimental and simulated powder X-ray diffraction patterns for compounds $Ag_{0.72}Bi_{5.48}Cu_{0.88}S_9$ (I), $Ag_{0.70}Bi_{5.30}Cu_{1.3}S_9$ (II), and $Ag_{0.34}Bi_{4.54}Cu_{1.98}PbS_9$ (III).

2.4. OPTICAL BAND GAP MEASUREMENTS

Varian Cary 5000 UV-Vis-NIR spectrophotometer equipped with a praying mantis set up was used to measure the optical band gap using $BaSO_4$ powder (Fisher, 99.2%) as a reflectance standard. Diffuse reflectance spectroscopy was performed on compounds I – III in the wavelength range 200 – 2500 nm. Band gap values were estimated using a Tauc plot.[38] The equation $\alpha h\nu = A(h\nu - E_g)^m$ was employed to estimate the optical band gap, where α is absorption coefficient (Kubelka-Munk function),[39] $h\nu$ is the photon energy, and m = 2 and ½ depending on whether the transition is direct or indirect. Compounds I – III exhibit linearity in $h\nu$ *vs* $(\alpha h\nu)^{1/2}$ plot, suggesting that the samples possess indirect band gap. The band gap values are very narrow and below 0.5 eV as the curve was still riding

on the steep absorption edge at the lowest energy end of the measured wavelength (Figure 2).

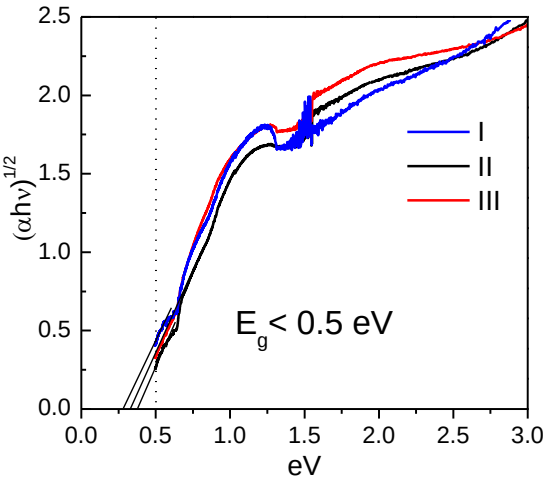

Figure 2. Diffuse reflectance spectra plotted as $h\nu$ *vs* $(\alpha h\nu)^{1/2}$ for compounds $Ag_{0.72}Bi_{5.48}Cu_{0.88}S_9$ (I), $Ag_{0.70}Bi_{5.30}Cu_{1.3}S_9$ (II), $Ag_{0.34}Bi_{4.54}Cu_{1.98}PbS_9$ (III).

2.5. THERMAL ANALYSIS

TGA-DSC data were collected simultaneously from room temperature to 1050 °C with scan rate of 10 °C/min under a high purity argon atmosphere on approximately 20-30 mg of synthesized powder using a TA Instrument Q600SDT. DSC plots for compounds I, II and III are presented in Figure S5. All three compounds have similar melting points in the range 925 – 950 K. Compound I displayed an endothermic peak at 540 K corresponding to a phase transition (Figure S5).

2.6. SAMPLE PREPARATION FOR PHYSICAL PROPERTY MEASUREMENTS

As-synthesized ingots were ground to fine powders using agate mortar in an argon filled glove box. The fine powders were loaded into a graphite die of 0.5 inch diameter. The die was placed in a hot press apparatus and the temperature was slowly raised to 500 °C using a load of 35 MPa under high purity argon atmosphere for 20 minutes. The furnace was slowly cooled to 250 °C over a course of 2 hours and then the load was withdrawn. Hard cylindrical disks were obtained with more than 95% of the crystallographic density.

2.7. SEEBECK AND ELECTRICAL RESISTIVITY MEASUREMENTS

Bars with dimensions ~10 mm x 2 mm x 1 mm were cut from the hot-pressed pellets using a Buehler diamond saw for high temperature resistivity and Seebeck coefficient measurements on a Linseis LSR-3. Measurements were done using a standard four-probe method under a helium atmosphere from 325 K to 475 K.

Low temperature electrical resistivity and Seebeck coefficients were measured for compound II from 5 – 300 K. Bars of dimension 4 mm x 1.5 mm x 10 mm were measured in a Quantum Design PPMS thermal transport option (TTO) using a standard four probe method. Room temperature Hall measurements were performed on the same polished bar for compounds II and III using the PPMS system. Hall coefficients were derived from a hall resistance (ρ_{xy}) versus magnetic field (B) plot (Figure S6). Carrier concentration was determined from the Hall coefficient (R_H) using the formula $R_H = 1/ne$, where n is the carrier density and e is the charge.

2.8. THERMAL CONDUCTIVITY MEASUREMENTS

Hot-pressed pellets were further polished and coated with graphite for thermal diffusivity $\alpha(T)$ measurements using the laser flash technique under high purity helium or argon atmosphere. Thermal diffusivity measurements were performed on compounds I – III from 300 to 475 K in Davis and from 475K to 800K for compounds II and III in Rolla. For compound I, our high temperature thermal diffusivity measurements failed as the pellet shattered after 540 K due to the presence of a phase transition at 540 K as evident from our DSC data (Figure S5). It is to be noted here that there is a slight mismatch of thermal conductivity data for compound III at 475 K (collected in two locations), presumably because of different pellets used from different batch of syntheses. Such differences may originate from small variations in stoichiometry and therefore carrier concentration due to human error during weighing of reactants for syntheses or slight differences in the density of hot-pressed pellets. Thermal conductivity was calculated using the formula $\kappa = \alpha(T).C_P.d$, where α(T) is thermal diffusivity, C_P is specific heat, d is the density. Specific heat (C_P) is estimated by Dulong-Petit limit, $C_P = 3R/M$ (where R = ideal gas constant, M = average molar mass of each element) and density of all the samples were measured from the dimensions and masses. The calculated densities are ~ 95% of the theoretical densities.

3. RESULTS AND DISCUSSION

3.1. STRUCTURE DESCRIPTION

Compounds, I – III, belong to the ^4P pavonite homologous series and are also known as makovickyites. These structures have complex 3-D networks composed of two types of alternating slabs stacking perpendicular to the *c*-axis. The thick slab is composed of BiS_6 octahedra resembling a NaCl lattice and is four octahedra thick along the diagonal direction. The thin slab consists of pairs of BiS_5 square pyramidal pillars interconnected by either AgS_6 octahedra or interstitial copper atoms, depending on how much Cu is substituted for Ag (Figure 3).

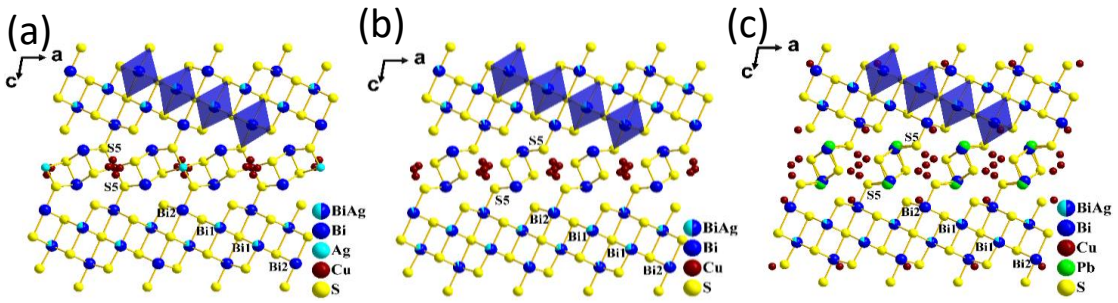

Figure 3. Makovickyite structures (^{4}P pavonites) with four octahedra thick incremental layer (thick) and one octahedra thick non-incremental layer (thin) of compounds (a) $Ag_{0.72}Bi_{5.48}Cu_{0.88}S_9$, I; (b) $Ag_{0.70}Bi_{5.30}Cu_{1.3}S_9$, II; (c) $Ag_{0.34}Bi_{4.54}Cu_{1.98}PbS_9$, III.

All the structures I, II, and III have three crystallographically unique Bi sites. Bi1 and Bi2 are present in slightly distorted octahedra within the thick layer, with the Bi1/2 – S bond lengths in the range 2.651(3) – 3.070(4) and 2.657(3) – 3.0294(7) Å, respectively, and the Bi1 site is mixed occupied by Ag and in case of II, Bi2 site is also mixed occupied with Ag . Bi3 is part of the thin layer and is coordinated to five S atoms in a square

pyramidal fashion, with four longer axial bonds in the range 2.8562(2) – 2.976(4) Å and a shorter equatorial bond from 2.546(4) – 2.595(3) Å. In III, Bi3 site is split between Bi3 and Pb1. because of the higher Ag content, some Ag is also present in the thin layer. In this case, Ag atoms adopt octahedral coordination and interconnect the $Bi3S_5$ square pyramidal pairs, with Ag2 – S bond distances ranging between 2.233(3) – 2.902(2) Å. Cu adopts linear and tetrahedral coordination in the makovickyite/cupromakovickyite structures. Accordingly, in compounds I and III, all the Cu atoms are tetrahedrally coordinated; however, in compound II, among four crystallographically distinct partially occupied Cu sites, Cu4 adopts linear coordination with a Cu4 – S distance of 2.251(3) Å, while Cu1, Cu2 and Cu3 adopt flattened tetrahedral coordination in the thin layer, with the Cu – S

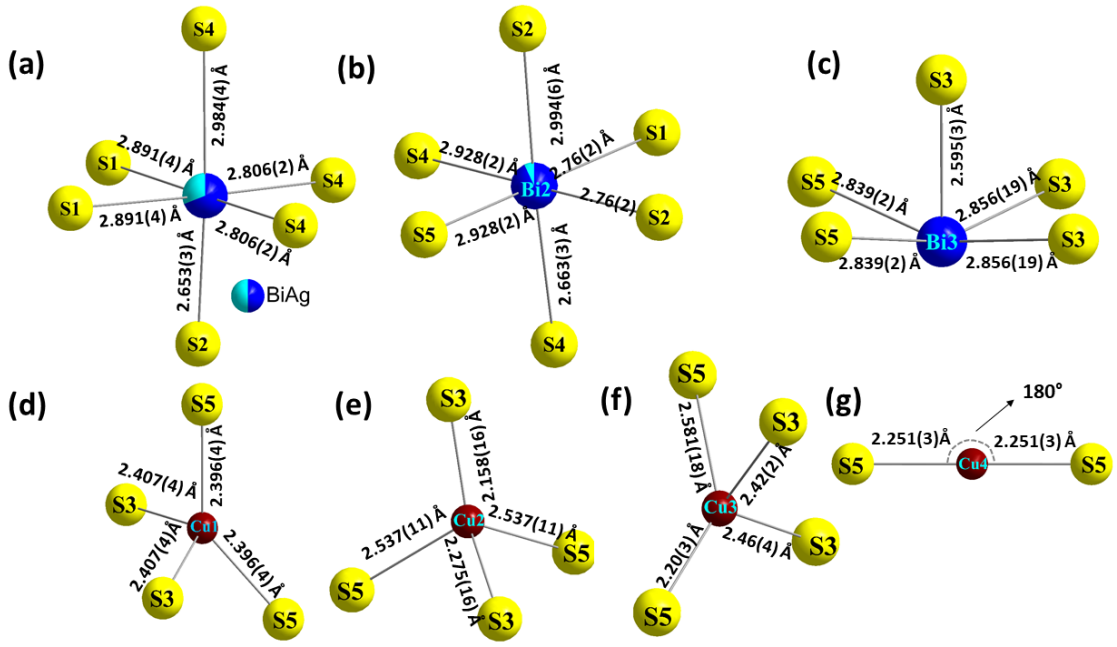

Figure 4. Coordination environments of Bi and Cu in $Ag_{0.70}Bi_{5.30}Cu_{1.3}S_9$ (II).

bond lengths in the range 2.158(16) – 2.581(18) Å. Local coordination environments for Bi and Cu for II are given in Figure 4. The thick and thin slabs are joined by a shared S5 atom resulting in a complex 3-D crystal structure. From the above discussion it is now amply clear that makovickyite structures offer excellent freedom in terms of tunable compositions and development of disorder as a function of Cu and Pb substitution, which enable independent tuning of the electrical and thermal properties and make them ideal candidates for thermoelectric applications.

3.2. TRANSPORT PROPERTIES

We selected one of the compositions to measure low temperature electrical conductivity and Seebeck coefficients. Thus, low temperature electrical conductivity and Seebeck coefficient measurements were performed on compound II in the temperature

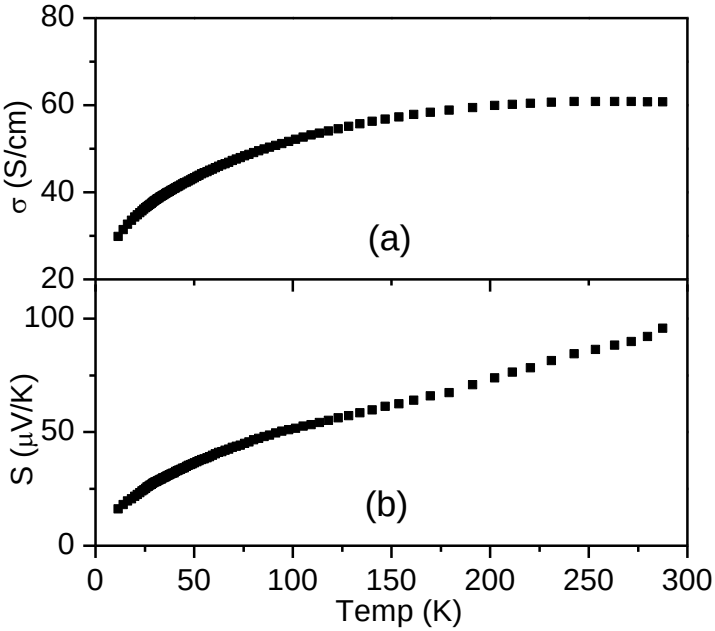

Figure 5. Low temperature charge transport measurements for compound $Ag_{0.70}Bi_{5.30}Cu_{1.3}S_9$, II (a) Electrical conductivity (b) Seebeck coefficient

range 5-300K (Figure 5). An increase in the electrical conductivity with temperature demonstrates the semiconducting nature of compound II. Compound II exhibits a moderate electrical conductivity of 60.7 S/cm at room temperature. Large negative Seebeck coefficients that increase linearly with temperature confirm the *n*-type charge carrier, reaching a value of 95 μVK^{-1} at 300 K. With these encouraging low-temperature transport properties we proceeded to investigate the high temperature TE properties of the three compositions.

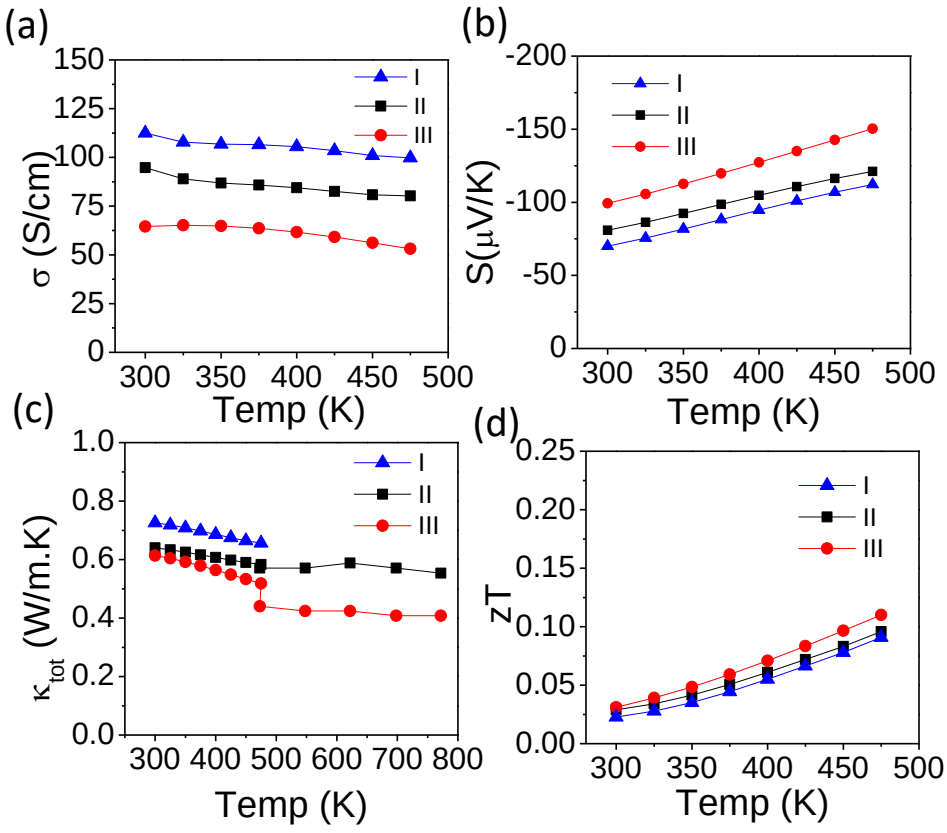

Figure 6. Temperature dependance of thermoelectric properties for compounds $Ag_{0.72}Bi_{5.48}Cu_{0.88}S_9$, I, $Ag_{0.70}Bi_{5.30}Cu_{1.3}S_9$, II, and $Ag_{0.34}Bi_{4.54}Cu_{1.98}PbS_9$, III; (a) Electrical conductivity, (b) Seebeck coefficient, (c) Thermal conductivity, (d) Figure of merit.

Figure 6 shows the temperature dependence of thermoelectric properties for compounds I – III in the temperature range 300 – 500 K. Compounds I, II, and III exhibit room temperature electrical conductivities of 112, 95, and 65 S/cm, respectively, as shown in Figure 6a. Electrical conductivities did not change much in the measured temperature range, though decreased monotonically as in degenerate semiconductor. The electrical conductivity values of I – III are comparable to many other pavonite compounds, for example 79 S/cm for $CdPb_2Bi_4S_9$ (n = 4)[16] and 42 S/cm for $AgBi_3S_5$ (n = 5) at 300K.[17] Note that for $CdPb_2Bi_4S_9$,[16] which is n =4 and structurally same as I – III also exhibit a monotonic decrease of electrical conductivity with temperature.

As observed in Figure 6b, the Seebeck coefficients for compounds I, II and III are negative and consistent with electrons being the dominant charge carriers. Seebeck coefficient of compound I is 70 μV/K at 300 K and increased to 112 μV/K at 500 K. The Seebeck coefficient of compound II is 81 μV/K at 300 K and increased to 121 μV/K at 500K whereas Seebeck coefficient of compound III is 100 μV/K at 300K and increased to 150 μV/K at 500K. The power factor ($PF = S^2\sigma$) as a function of temperature for all the three compounds are given in Figure 7a. The power factors are in the range of 0.6 – 1.2 $\mu W.cm^{-1}K^2$ for compounds I – III which are in good agreement with other pavonites, such as $CdPb_2Bi_4S_9$ (n = 4).[16] The trend observed in electrical conductivity and Seebeck coefficients can be correlated. The Hall coefficient-derived carrier concentration values are of the order of 1.025×10^{20} cm^{-3} for compound II and 1.55×10^{19} cm^{-3} for compound III. Slightly higher carrier concentration in compound II compared to compound III resulted in an increase in the electrical conductivity and decrease in the Seebeck coefficient, since the σ is directly proportional to the carrier concentration and *S* has an inverse relation with

carrier concentration. Small variations in the values of electrical conductivity and Seebeck coefficient are observed in the room temperature data between the low temperature and above room temperature measurements because of the use of different batch of samples.

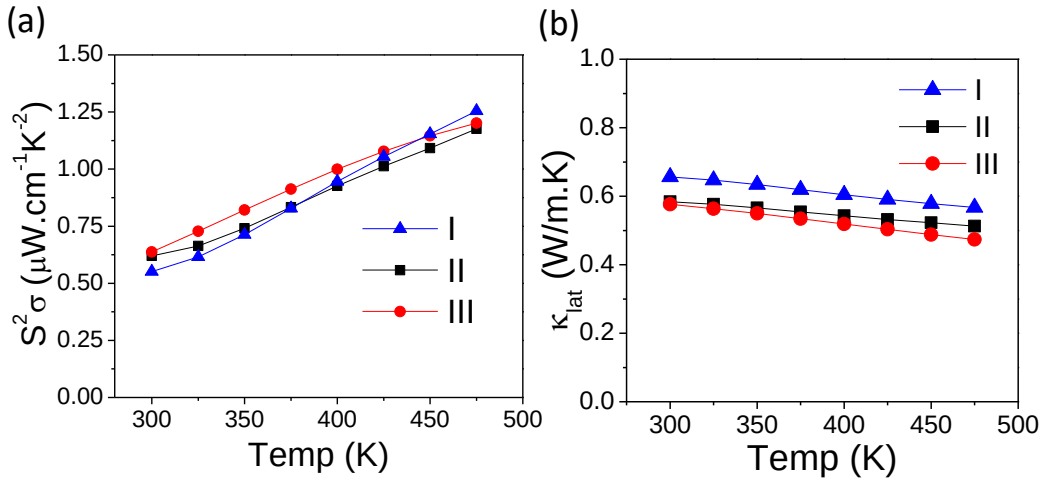

Figure 7. (a) Power factors (b) Lattice thermal conductivity (κ_{lat}) for $Ag_{0.72}Bi_{5.48}Cu_{0.88}S_9$, I, $Ag_{0.70}Bi_{5.30}Cu_{1.3}S_9$, II, and $Ag_{0.34}Bi_{4.54}Cu_{1.98}PbS_9$, III from 300 to 475K.

Figure 6c shows κ_{tot} in the temperature range 300 – 800 K for compounds II and III and 300 – 500 K for compound I. These compounds possess ultra-low thermal conductivities in the range of 0.51 – 0.72 $Wm^{-1}K^{-1}$. The room temperature thermal conductivities are 0.72 $Wm^{-1}K^{-1}$ for I, 0.64 $Wm^{-1}K^{-1}$ for II, and 0.61 $Wm^{-1}K^{-1}$ for III. These values are comparable to the other reported pavonite family compounds, for example, 0.8 $Wm^{-1}K^{-1}$ in $LiSn_2Bi_5S_{10,}$[15] 0.6 $Wm^{-1}K^{-1}$ in $AgBi_3S_5$,[17] 0.78 $Wm^{-1}K^{-1}$ in $CdPb_2Bi_4S_9$[16] and 0.67 – 1 $Wm^{-1}K^{-1}$ in MBi_4S_7 (M = Mn, Fe)[19] and as well as to many state of the art chalcogenide thermoelectric materials, for example, κ_{tot} <1 $Wm^{-1}K^{-1}$ in $Cu_{2-x}Se$, 0.46 – 0.68 $Wm^{-1}K^{-1}$ in SnSe.[40,41] The electronic contribution to the total thermal conductivity

can be calculated using $\kappa_{ele} = L\sigma T$ (Wiedemann–Franz law). κ_{lat} can be calculated by subtracting the electronic contribution from the total thermal conductivity ($\kappa_{tot} = \kappa_{ele} + \kappa_{lat}$). The Lorenz number L is calculated using the Seebeck coefficient via the equation $L = 1.5 + \exp\left[\frac{-|S|}{116}\right]$ where L is in 10^{-8} WΩK^{-2} and S is in μV/K.[42]

Lattice thermal conductivity, κ_{lat}, values for compounds, I – III, (Figure 7b) are close to the κ_{tot} values because of the negligible electronic contribution, which corroborates well with the low electrical conductivities. The room temperature κ_{lat} values are 0.65 Wm^{-1}K^{-1} for I, 0.58 Wm^{-1}K^{-1} for II, and 0.57 Wm^{-1}K^{-1} for III. Though there are significant differences in the electrical conductivity and Seebeck coefficient values of compounds II and III, the κ_{lat} values are similar, which suggest that there may be opportunities to improve the electrical conductivity without negatively affecting the thermal conductivity.

The ultra-low and temperature independent thermal conductivity could originate from the very large anisotropic thermal vibration of partially occupied, disordered copper atoms, especially Cu1, Cu3 in compound II and Cu1, Cu2 in compound III. Additionally, for III**,** strong vibrational anharmonicity due to the presence of stereo-active lone pairs on Pb results in the lowest lattice thermal conductivity amongst the three compounds. These extremely low κ_{lat} values can be attributed to a combination effect of the complex electronic structure, mixed and partial occupancies, large unit cell volumes, and vibrational anharmonicities within the lattice. The partially occupied Cu atoms in the interstitial positions in the thin layer may be considered as rattling of atoms in a cage-like structure and can act as a source of enhance phonon scattering.[43,44] However, to confirm this hypothesis, the nature of Cu atoms in the interstitial positions needs to be evaluated using phonon dispersion calculations. The *zT* values calculated using the above transport

properties are presented in Figure 6d. The *zT* values are 0.09 for I and II, 0.11 for III at 475K.

4. CONCLUSIONS

Three quaternary complex chalcogenides, $Ag_{0.72}Bi_{5.48}Cu_{0.88}S_9$ (I), $Ag_{0.70}Bi_{5.30}Cu_{1.3}S_9$ (II), $Ag_{0.34}Bi_{4.54}Cu_{1.98}PbS_9$ (III) were synthesized by substituting Cu and Pb for Bi in the makovickyite family with general formula $Ag^{ab}{}_{n-1}Bi^{a}{}_{4}Bi^{ab}Bi^{b}{}_{n+2}S_{2n+10}$. These materials are indirect-gap *n*-type semiconductors with band gaps < 0.5 eV. Inherent complex compositions and partial occupancies yield very low thermal conductivities < 0.75 $W.m^{-1}K^{-1}$. Ultra-low thermal conductivity coupled with a large Seebeck coefficient and moderate electrical conductivity yielded a promising zT of ~ 0.1 at 475K. These pavonite phases would be ideal candidates for substitutions with various divalent and trivalent metal atoms for Bi to increase carrier concentration and electrical conductivity, while adding additional disorder to further retain the lattice thermal conductivity. The amount of interstitial Cu can also be adjusted to tune the thermoelectric properties accordingly. Furthermore, once the role Cu atoms play in phonon suppression is understood, one can design an appropriate system with balanced electrical and thermal properties to achieve a higher *zT*.

ACKNOWLEDGEMENTS

The authors, AC and SB, acknowledge the funding for this work from National Science Foundation (NSF) under grant number DMR- 1809128. AH and SMK acknowledge the support from NSF (DMR-201156) for this work. AH also acknowledges NSF for her graduate fellowship.

SUPPLEMENTARY INFORMATION

Table S1. Table showing the similar fit with the same number of refined parameters indicating reasonable support for split positions Bi3/Pb1 and no additional benefit for the anharmonic refinements.

	R(obs)	wR2(obs)	R(all)	wR2(all)	GOF(all)	N(ref)	N(par)	ρ(max)	ρ(min)
Split-model	0.0394	0.1154	0.0446	0.1194	1.42	1064	71	2.61	-2.66
Anharm-3	0.0401	0.1160	0.0453	0.1196	1.43	1064	71	2.13	-2.81
Anharm-4	0.0346	0.1037	0.0393	0.1070	1.28	1064	80	1.75	-1.73

Table S2. Final atomic coordinates and equivalent isotropic displacement parameters of the atoms for compounds I. $U_{(eq)}$ = 1/3 of the trace of the orthogonalized U_{eq} tensor.

Atom	Wyckoff	S.O.F	x	Y	z	U(eq)
			$Ag_{0.72}Bi_{5.48}Cu_{0.88}S_9$ **I**			
Bi(1)	4i	0.74	0.3498(1)	0	0.4347(1)	0.0020(1)
Ag(1)	4i	0.26	0.3498(1)	0	0.4347(1)	0.0020(1)
Bi(2)	4i	1	0.0530(1)	0	0.3076(1)	0.0022(1)
Bi(3)	4i	1	0.7480(1)	0	0.1232(1)	0.0026(1)
Ag(2)	2a	0.20	0	0	0	0.0077(5)
Cu(1)	4g	0.35	0	0.1963(16)	0	0.0037(2)
Cu(2)	4i	0.07	0.0224(17)	0.5	0.0531(17)	0.0030(6)
Cu(3)	4i	0.02	0.0410(60)	0.5	0.0040(60)	0.0029(6)
S(1)	2c	1	0	0	0.5	0.0017(1)
S(2)	4i	1	0.4100(2)	0	0.2707(2)	0.0020(1)
S(3)	4i	1	0.3576(2)	0	0.0426(2)	0.0014(1)
S(4)	4i	1	0.2928(2)	0	0.6249(3)	0.0026(1)
S(5)	4i	1	0.1010(2)	0	0.1383(2)	0.0019(1)

Table S3. Final atomic coordinates and equivalent isotropic displacement parameters of the atoms for compounds II. $U_{(eq)}$ = 1/3 of the trace of the orthogonalized U_{eq} tensor.

Atom	Wyckoff	S.O.F	x	y	z	U(eq)
			$Ag_{0.70}Bi_{5.30}Cu_{1.3}S_9$ **II**			
Bi(1)	4i	0.72	0.3494(1)	0	0.4347(1)	0.0021(1)
Ag(1)	4i	0.28	0.3494(1)	0	0.4347(1)	0.0021(1)
Bi(2)	4i	0.93	0.0524(1)	0	0.3086(1)	0.0020(1)
Ag(2)	4i	0.07	0.0524(1)		0.3086(1)	0.0020(1)
Bi(3)	4i	1	0.7482(1)	0	0.1237(1)	0.0026(1)
Cu(1)	4g	0.34	0	0.2025(19)	0	0.0042(2)
Cu(2)	4i	0.09	0.0216(12)	0.5	0.0513(13)	0.0033(4)
Cu(3)	4i	0.1	0.270(20)	0	-0.0231(16)	0.0038(8)
Cu(4)	2a	0.24	0	0	0	0.0040(5)
S(1)	2c	1	0	0	0.5	0.0017(1)
S(2)	4i	1	0.4097(2)	0	0.2706(2)	0.0020(1)
S(3)	4i	1	0.3572(2)	0	0.0424(2)	0.0016(1)
S(4)	4i	1	0.2934(2)	0	0.6239(3)	0.0026(1)
S(5)	4i	1	0.1017(2)	0	0.1394(2)	0.0021(1)

Table S4. Final atomic coordinates and equivalent isotropic displacement parameters of the atoms for compounds III. $U_{(eq)}$ = 1/3 of the trace of the orthogonalized U_{eq} tensor.

Atom	Wyckoff	S.O.F	x	y	z	U(eq)
$Ag_{0.34}Bi_{4.54}Cu_{1.98}PbS_9$ **III**						
Bi(1)	4i	0.83	0.3493(1)	0	0.4336(1)	0.0020(1)
Ag(1)	4i	0.17	0.3493(1)	0	0.4336(1)	0.0020(1)
Bi(2)	4i	0.94	0.0520(1)	0	0.3092(1)	0.0020(1)
Cu(3)	4i	0.06	-0.002(30)		0.2570(30)	0.0045(7)
Bi(3)	4i	0.5	0.7547(3)	0	0.1166(2)	0.0027(1)
Pb(1)	4i	0.5	0.7437(4)	0	0.1387(2)	0.0049(1)
Cu(1)	4i	0.4	-0.0210(4)	0.5	-0.0762(7)	0.0059(3)
Cu(2)	4i	0.33	0.0487(5)	0	-0.0444(8)	0.0046(2)
Cu(2A)	4g	0.2	0	1780(40)	0	0.0064(5)
S(1)	2c	1	0	0	0.5	0.0019(1)
S(2)	4i	1	0.4094(2)	0	0.2707(2)	0.0020(1)
S(3)	4i	1	0.3575(2)	0	0.0406(2)	0.0018(1)
S(4)	4i	1	0.2933(4)	0	0.6258(2)	0.0026(1)
S(5)	4i	1	0.0980(2)	0	0.1417(2)	0.0020(1)

Table S5. Anisotropic displacement parameters ($Å^2 x\ 10^3$) for I. The anisotropic displacement factor exponent takes the form: $-2p^2[\ h^2 a^{*2} U^{11} + ... + 2\ h\ k\ a^*\ b^*\ U^{12}\ ]$

Atoms	U^{11}	U^{22}	U^{33}	U^{23}	U^{13}	U^{12}
$Ag_{0.72}Bi_{5.48}Cu_{0.88}S_9$, **I**						
Bi(1)	18(1)	18(1)	24(1)	0	4(1)	0
Ag(1)	18(1)	18(1)	24(1)	0	4(1)	0
Bi(2)	24(1)	22(1)	20(1)	0	4(1)	0
Bi(3)	29(1)	29(1)	18(1)	0	-2(1)	0
Ag(2)	91(9)	59(6)	59(6)	0	-57(6)	0
Cu(1)	20(2)	61(4)	30(3)	0	1(2)	0
Cu(2)	20(9)	58(8)	11(8)	0	3(8)	0
Cu(3)	18(14)	59(8)	7(11)	0	-4(11)	0
S(1)	17(2)	20(2)	14(2)	0	3(2)	0
S(2)	21(2)	18(2)	20(2)	0	1(1)	0
S(3)	18(1)	15(1)	11(1)	0	4(1)	0
S(4)	19(2)	18(2)	37(2)	0	0(1)	0

Table S6. Anisotropic displacement parameters ($Å^2 x\ 10^3$) for II. The anisotropic displacement factor exponent takes the form: $-2p^2[\ h^2 a^{*2} U^{11} + ... + 2\ h\ k\ a^*\ b^*\ U^{12}\ ]$

Atoms	U^{11}	U^{22}	U^{33}	U^{23}	U^{13}	U^{12}
			$Ag_{0.70}Bi_{5.30}Cu_{1.3}S_9$ **II**			
Bi(1)	20(1)	20(1)	21(1)	0	3(1)	0
Ag(1)	20(1)	20(1)	21(1)	0	3(1)	0
Bi(2)	24(1)	21(1)	16(1)	0	3(1)	0
Ag(2)	24(1)	21(1)	16(1)	0	3(1)	0
Bi(3)	31(1)	28(1)	16(1)	0	-3(1)	0
Cu(1)	21(3)	78(5)	27(3)	0	1(2)	0
Cu(2)	13(7)	64(7)	26(7)	0	14(6)	0
Cu(3)	29(12)	65(8)	17(5)	0	-2(7)	0
Cu(4)	24(10)	70(7)	23(6)	0	-3(6)	0
S(1)	18(2)	19(2)	14(2)	0	2(2)	0
S(2)	21(1)	21(2)	16(1)	0	0(1)	0
S(3)	19(1)	19(1)	10(1)	0	1(1)	0
S(4)	20(2)	19(2)	38(2)	0	-2(1)	0

Table S7. Anisotropic displacement parameters ($Å^2 x\ 10^3$) for III. The anisotropic displacement factor exponent takes the form: $-2p^2[\ h^2a^{*2}U^{11} + ... + 2\ h\ k\ a^*\ b^*\ U^{12}\ ]$

Atoms	U^{11}	U^{22}	U^{33}	U^{23}	U^{13}	U^{12}
$Ag_{0.34}Bi_{4.54}Cu_{1.98}PbS_9$ **III**						
Bi(1)	16(1)	19(1)	24(1)	0	2(1)	0
Ag(1)	16(1)	19(1)	24(1)	0	2(1)	0
Bi(2)	19(1)	20(1)	19(1)	0	1(1)	0
Cu(3)	59(15)	26(13)	51(15)	0	13(14)	0
Bi(3)	31(1)	27(1)	15(1)	0	-14(1)	0
Pb(1)	50(1)	24(1)	70(3)	0	6(2)	0
Cu(1)	32(3)	41(3)	94(5)	0	-14(3)	0
Cu(2)	31(3)	24(3)	74(5)	0	-17(3)	0
Cu(2A)	23(5)	110(10)	56(7)	0	-4(5)	0
S(1)	20(2)	15(2)	22(2)	0	2(2)	0
S(2)	17(2)	22(2)	20(2)	0	1(1)	0
S(3)	17(1)	18(1)	17(2)	0	0(1)	0
S(4)	15(2)	19(2)	41(2)	0	-5(1)	0

Table S8. Refined lattice constants and final Rietveld refinement parameters for compounds, I – III.

	I	II	III
Formula	$Ag_{0.72}Bi_{5.48}Cu_{0.88}S_9$	$Ag_{0.70}Bi_{5.30}Cu_{1.3}S_9$	$Ag_{0.34}Bi_{4.54}Cu_{1.98}PbS_9$
Unit cell	a = 13.1832(7)	a = 13.1887(8)	a = 13.3373(20)
	b = 4.04828(15)	b = 4.04196(16)	b = 4.0391(3)
	c = 14.6292(9)	c = 14.6176(10)	c = 14.7888(24)
	β = 99.401(3)	β = 99.501(4)	β = 99.822(9)
Volume	770.26(4)	768.54(4)	785.00(8)
Rw	6.819	6.744	7.301
RF^2	9.526	8.494	10.866

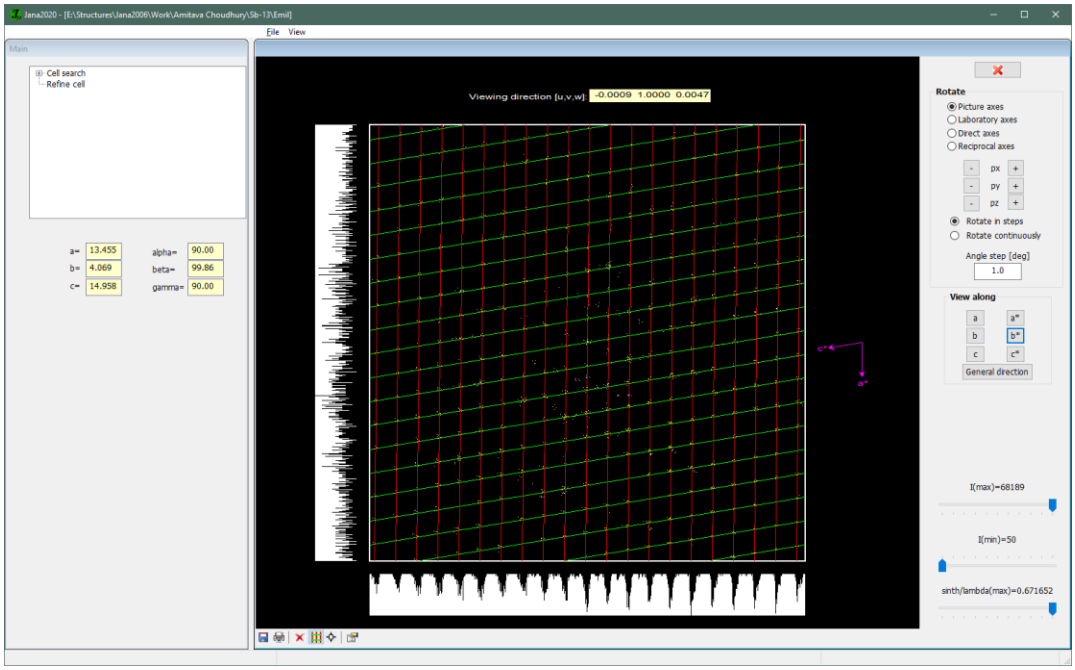

Figure S1. Diffraction pattern from the raw data frames projected on reciprocal lattice. The used cell, *a* = 13.45, *b* = 4.069, and *c* = 14.958, β = 99.86. It can be seen from the above figure that there are only a few additional spots. However, there are no systematic unaccounted spots that would call for a cell doubling along c-axis.

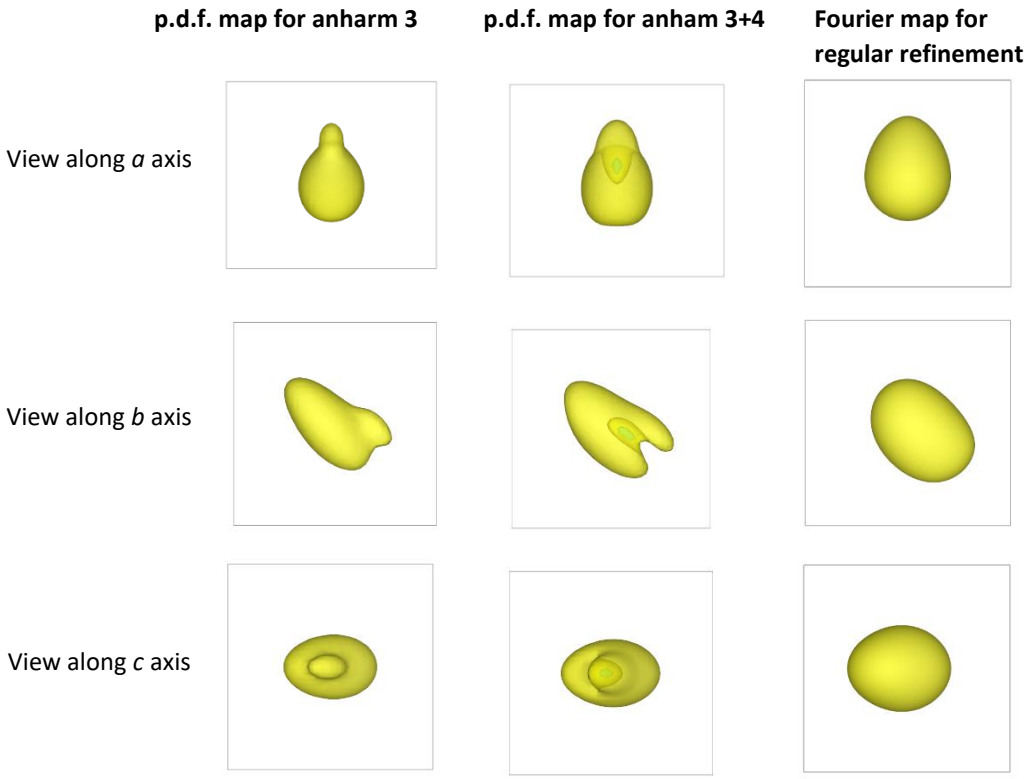

Figure S2. The probability density function p.d.f. is calculated from the refined anharmonic ADPs in the direct space (from a, b, and c-directions). This means that there are no termination effects in such maps. Introduction of 4th order tensor leads to an unrealistic distribution of atoms in the Bi3/Pd1 site. On the other hand, the shape of the p.d.f with using only 3rd term seems to indicate split atom positions as we have used in the regular model.

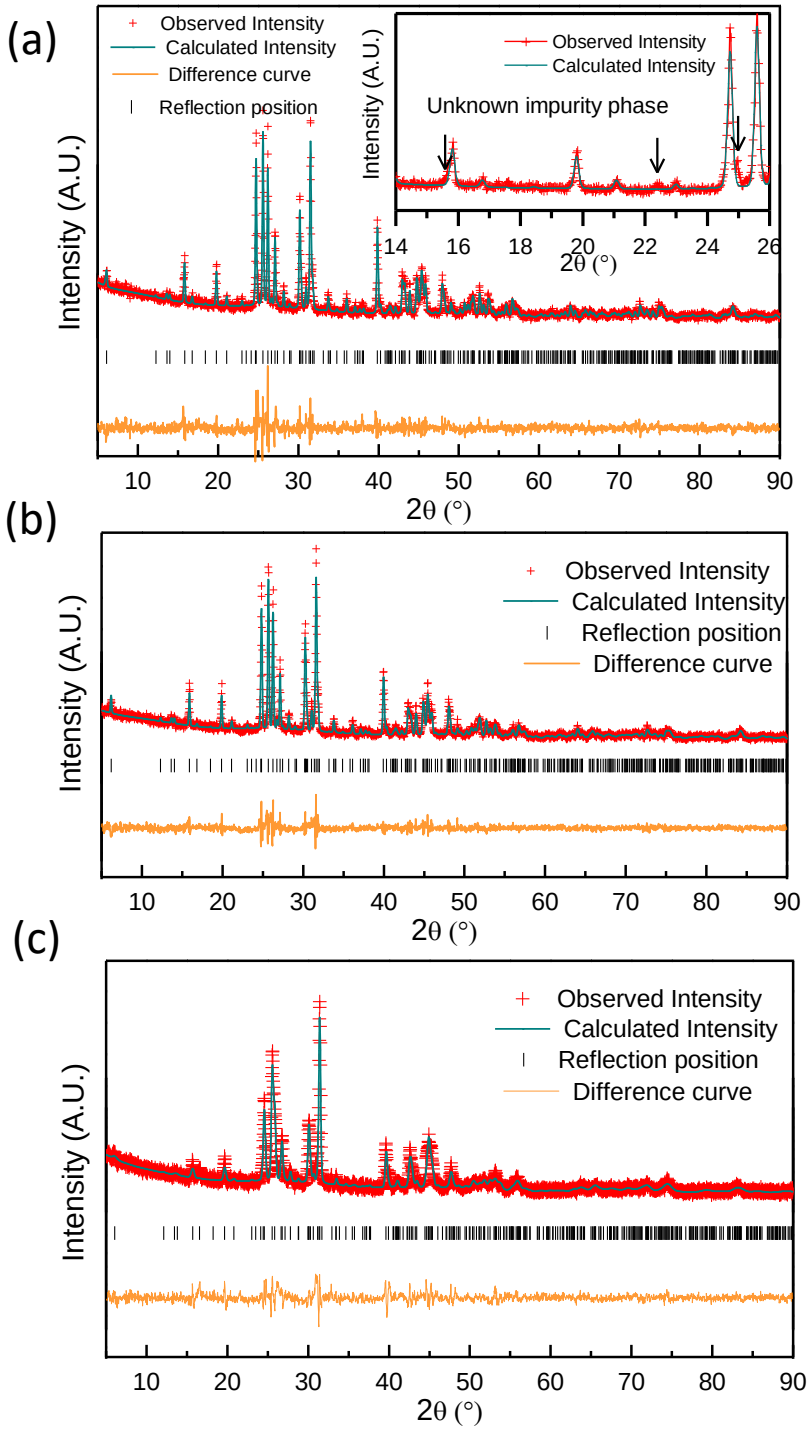

Figure S3. Rietveld refinement plots for (a) $Ag_{0.72}Bi_{5.48}Cu_{0.88}S_9$, I (b) $Ag_{0.70}Bi_{5.30}Cu_{1.3}S_9$, II (c) $Ag_{0.34}Bi_{4.54}Cu_{1.98}PbS_9$, III showing the observed, calculated and difference curve. Inset in (a) shows an enlarged view of the segment for 2θ = 14 to 26°. The arrows indicate the presence of minute quantity of an unknown impurity phase.

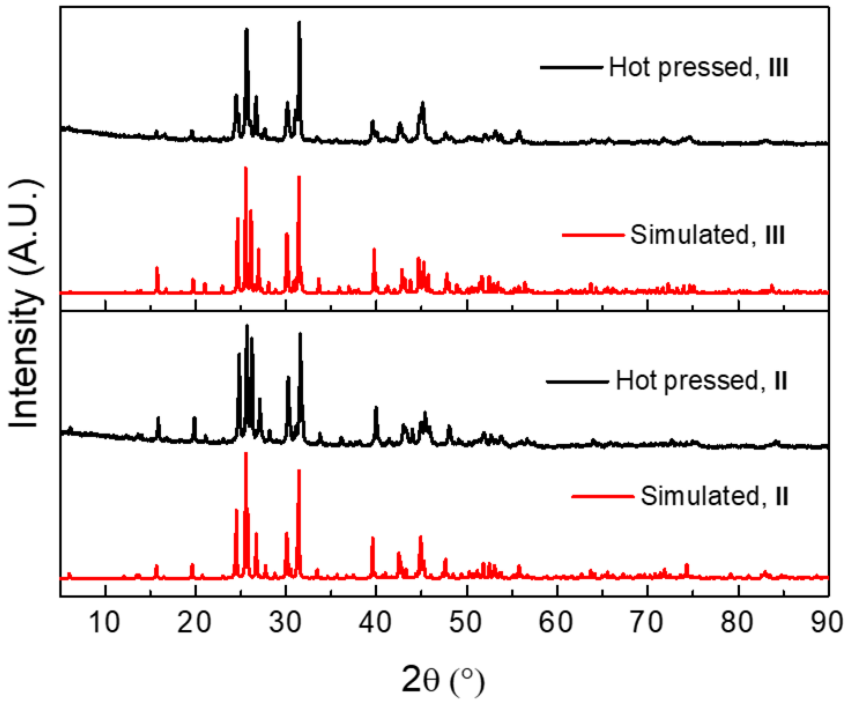

Figure S4. PXRD comparison with of hot-pressed samples with the simulated patterns for $Ag_{0.70}Bi_{5.30}Cu_{1.3}S_9$ (II), $Ag_{0.34}Bi_{4.54}Cu_{1.98}PbS_9$(III).

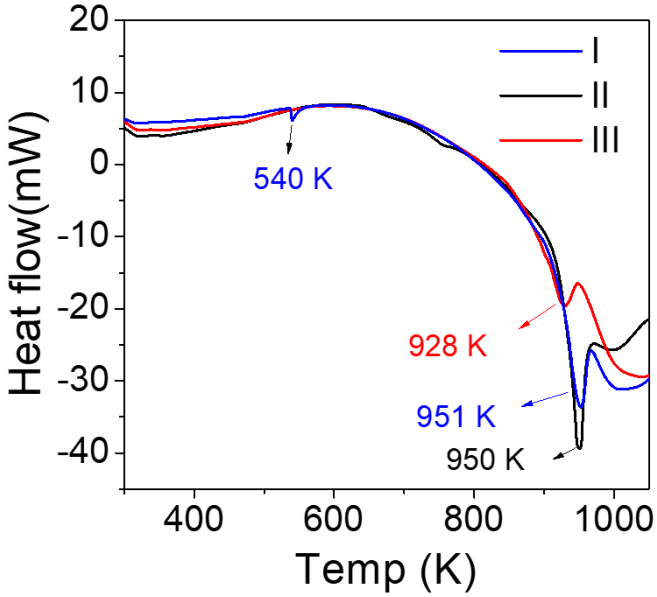

Figure S5. DSC curves for $Ag_{0.72}Bi_{5.48}Cu_{0.88}S_9$ (I), $Ag_{0.70}Bi_{5.30}Cu_{1.3}S_9$ (II), $Ag_{0.34}Bi_{4.54}Cu_{1.98}PbS_9$(III).

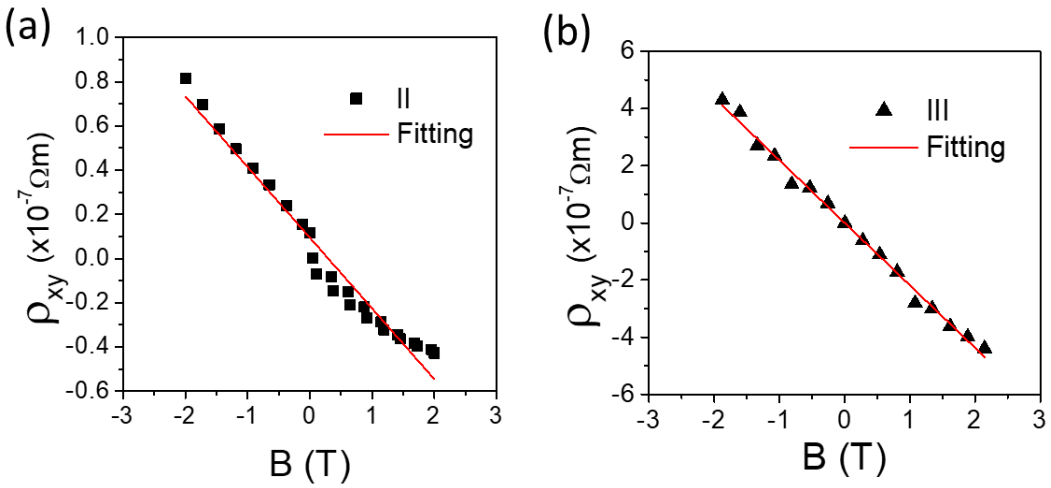

Figure S6. Magnetic field vs Hall resistivity (a) $Ag_{0.70}Bi_{5.30}Cu_{1.3}S_9$ II (b) $Ag_{0.34}Bi_{4.54}Cu_{1.98}PbS_9$ III.

REFERENCES

1. G. J. Snyder and E. S. Toberer, *Nat. Mater.*, 2008, 7, 105–114.
2. X. L. Shi, J. Zou and Z. G. Chen, *Chem. Rev.*, 2020, **120**, 7399–7515.
3. I.Terasaki, *Compr. Semicond. Sci. Technol.*, 2011, 326–358.
4. D. M. Rowe, *CRC handbook of thermoelectric*, 2018.
5. J. R. Sootsman, D. Y. Chung and M. G. Kanatzidis, *Angew. Chemie Int. Ed.*, 2009, **48**, 8616–8639.
6. E. J. Skoug and D. T. Morelli, *Phys. Rev. Lett.*, 2011, **107**, 235901.
7. M. D. Nielsen, V. Ozolins and J. P. Heremans, *Energy Environ. Sci.*, 2013, **6**, 570–578.
8. W. G. Mumme, *Neues Jahrb. Miner. Monatsh.*, 1990, 193–204.
9. W. Zak, L.; Fryda, L.; Mumme, W.G.; Paar, *Neues Jahrb. fuer Mineral. - Abhandlungen*, 1994, **168**, 147–169.
10. J. M. Perez-Mato, L. Elcoro, E. Makovicky, D. Topa, V. Petříček and G. Madariaga, *Mater. Res. Bull.*, 2013, **48**, 2166–2174.

11. Z. Z. Luo, C. S. Lin, W. D. Cheng, W. L. Zhang, Y. B. Li, Y. Yang, H. Zhang and Z. Z. He, *Cryst. Growth Des.*, 2013, **13**, 4118–4124.

12. P. F. P. Poudeu and M. Ruck, *Acta Cryst. C*, 2005, **61**, i41-i43.

13. C. Anglin, N. Takas, J. Callejas and P. F. P. Poudeu, *J. Solid State Chem.*, 2010, **183**, 1529–1535.

14. S. Nakhal, D. Wiedemann, B. Stanje, O. Dolotko, M. Wilkening and M. Lerch, 2016, **238**, 60–67.

15. J. F. Khoury, S. Hao, C. C. Stoumpos, Z. Yao, C. D. Malliakas, U. Aydemir, T. J. Slade, G. J. Snyder, C. Wolverton and M. G. Kanatzidis, *Inorg. Chem.*, 2018, **57**, 2260–2268.

16. J. Zhao, S. Hao, S. M. Islam, H. Chen, G. Tan, S. Ma, C. Wolverton and M. G. Kanatzidis, *Chem. Mater.*, 2019, **31**, 3430–3439.

17. G. Tan, S. Hao, J. Zhao, C. Wolverton and M. G. Kanatzidis, *J. Am. Chem. Soc.*, 2017, **139**, 6467–6473.

18. J. Zhao, S. M. Islam, S. Hao, G. Tan, X. Su, H. Chen, W. Lin, R. Li, C. Wolverton and M. G. Kanatzidis, *Chem. Mater.*, 2017, **29**, 8494–8503.

19. J. Labégorre, A. Virfeu, A. Bourhim, H. Willeman, T. Barbier, F. Appert, J. Juraszek, B. Malaman, A. Huguenot, R. Gautier, V. Nassif, P. Lemoine, C. Prestipino, E. Elkaim, L. Pautrot-d'Alençon, T. Le Mercier, A. Maignan, R. Al Rahal Al Orabi and E. Guilmeau, *Adv. Funct. Mater.*, 2019, **29**, 1904112.

20. M. Ruck and P. F. Poudeu, *Zeitschrift fur Anorg. und Allg. Chemie*, 2008, **634**, 475–481.

21. K. G. S. Ranmohotti, H. Djieutedjeu, J. Lopez, A. Page, N. Haldolaarachchige, H. Chi, P. Sahoo, C. Uher, D. Young and P. F. P. Poudeu, *J. Am. Chem. Soc.*, 2015, **137**, 691–698.

22. K. G. S. Ranmohotti, H. Djieutedjeu and P. F. P. Poudeu, *J. Am. Chem. Soc.*, 2012, **134**, 14033–14042.

23. M. F. Wang, S. M. Jang, J. C. Huang and C. S. Lee, *J. Solid State Chem.*, 2009, **182**, 1450–1456.

24. W. G. Mumme and J. A. Watts, *Acta Crystallogr. Sect. B Struct. Crystallogr. Cryst. Chem.*, 1980, **36**, 1300–1304.

25. W. Choe, S. Lee, P. O'Connell and A. Covey, *Chem. Mater.*, 1997, **9**, 2025–2030.

26. S. Qu, J. Zhao, Z. Jiang, D. Jiang and Y. Wang, *Mater. Chem. Front.*, 2021, **5**, 1283–1294.

27. J. Y. Cho, H. Mun, B. Ryu, S. Il Kim, S. Hwang, J. W. Roh, D. J. Yang, W. H. Shin, S. M. Lee, S. M. Choi, D. J. Kang, S. W. Kim and K. H. Lee, *J. Mater. Chem. A*, 2013, **1**, 9768–9774.

28. J. Y. Hwang, M. W. Oh, K. H. Lee and S. W. Kim, *J. Mater. Chem. C*, 2015, **3**, 11271–11285.

29. M. Ohmasa, *M. Jahrb. Mineral. Monatsh.* ,1973, 227

30. K. Tomeoka, M. Ohmasa and R. Sadanaga, *Mineral. J.*, 1980, **10**, 57–70.

31. D. Topa and W. H. Paar, *Can. Mineral.*, 2008, **46**, 503–514.

32. D. Topa, E. Makovicky and T. Balić-Žunić, *Can. Mineral.*, 2008, **46**, 515–523.

33. M. Nagashima, T. Armbruster, Y. Izumino and K. Nakashima, *Neues Jahrb. fur Mineral. Abhandlungen*, 2013, **191**, 75–81.

34. Bruker- SMART. Bruker AXS Inc., Madison, Wisconsin, USA. 2002.

35. Bruker-SAINT and SADABS, and SHELXTL. Bruker AXS Inc., Madison, Wisconsin, USA, 2008

36. G. M. Sheldrick, Acta Crystallogr. Sect. A Found. Crystallogr., 2008, 64, 112–122.

37. C. B. Hübschle, G. M. Sheldrick and B. Dittrich, J. Appl. Crystallogr., 2011, 44, 1281–1284.

38. J. Tauc, *Mater. Res. Bull.*, 1968, **3**, 37–46.

39. P. Kubelka and F. Z. Munk, *Tech. Phys*., 1931, **12**, 593–601

40. H. Liu, X. Shi, F. Xu, L. Zhang, W. Zhang, L. Chen, Q. Li, C. Uher, T. Day and G. Snyder Jeffrey, *Nat. Mater.*, 2012, **11**, 422–425

41. L. D. Zhao, S. H. Lo, Y. Zhang, H. Sun, G. Tan, C. Uher, C. Wolverton, V. P. Dravid and M. G. Kanatzidis, *Nature*, 2014, **508**, 373–377.

42. H. S. Kim, Z. M. Gibbs, Y. Tang, H. Wang and G. J. Snyder, *APL Mater.*, 2015, **3**, 041506.

43. G. S. Nolas, D. T. Morelli and T. M. Tritt, *Annu. Rev. Mater. Sci.*, 1999, **29**, 89–116.

44. K. Suekuni, C. H. Lee, H. I. Tanaka, E. Nishibori, A. Nakamura, H. Kasai, H. Mori, H. Usui, M. Ochi, T. Hasegawa, M. Nakamura, S. Ohira-Kawamura, T. Kikuchi, K. Kaneko, H. Nishiate, K. Hashikuni, Y. Kosaka, K. Kuroki and T. Takabatake, *Adv. Mater.*, 2018, **30**, 10–15

VIII. DISORDER INDUCED ULTRALOW LATTICE THERMAL CONDUCTIVITY IN AIKINITE STRUCTURE FAMILY

*Srikanth Balijapelly,[a] Ashlee Hauble,[b] Jeremy Lee Watts,[c] Susan Kauzlarich,[b] Aleksandr V. Chernatynskiy[d] and Amitava Choudhury[a,] **

[a]Department of Chemistry, Missouri University of Science and Technology, Rolla, MO 65409, USA

[b]Department of Chemistry, One Shields Avenue, University of California, Davis, California 95616, United States

[c]Department of Materials Science and Engineering, Missouri University of Science and Technology, Rolla, MO 65409, USA

[d]Department of Physics, Missouri University of Science and Technology, Rolla, MO 65409, USA

ABSTRACT

Herein we report the synthesis and characterization of three complex quaternary chalcogenide compounds, $Cu_xPb_xBi_{2-x}S_3$ (x = 0.2 (I), 0.33(II), 1.0(III)) in the bismuthinite (Bi_2S_3) – aikinite ($CuPbBiS_3$) solid solution series. All the compounds in this solid solution series can be generated by replacing Bi and a vacancy by Pb and Cu. Compositions in between the end members of the series possess complex crystal structures with mixed occupied Bi/Pb and partially occupied Cu/vacancy sites. These intrinsic structural attributes lead to ultralow thermal conductivities < 0.65 W m^{-1} K^{-1} from 300 – 700 K. All the compounds exhibit narrow band gap below 1.0 eV confirmed by diffuse reflectance measurements. DFT band structure analysis shows that the band gap tends to decrease with increasing amount of Cu and Pb substitution due to increased contribution of the Cu *d* states to the valence band. High temperature charge transport properties are consistent with

electrons being dominant charge carriers with low electrical conductivities and large Seebeck coefficients. A promising figure of merit, *zT*, of 0.21 for II has be achieved at 475 K.

1. INTRODUCTION

One of the key strategies to boost the thermoelectric performance is to minimize the total thermal conductivity, since the efficiency of thermoelectric materials is defined by the figure of merit, $zT = \frac{S^2 \sigma T}{\kappa_{total}}$, where S is Seebeck coefficient, σ is electrical conductivity, κ_{total} is total thermal conductivity and T is the absolute temperature.[1-3] It is challenging to reduce the thermal conductivity without adversely affecting the electrical properties.[3,4] However, it is possible to suppress the lattice thermal conductivity by introducing defects, grain boundaries, and nano structuring, which are all in the hands of synthetic solid state chemists. In this scenario, it is also important to find materials with intrinsically low thermal conductivities with a room to tune the composition to further improve the electrical properties. Not every family of compounds are bestowed with the freedom to create disorder or vacancies, as it depends on the thermodynamic stabilities of both end members of the series. Hence, the doping strategy is limited to few specific dopants for which the coordination and bonding requirements must be satisfied. There exists a plethora of mineral compositions possessing complex crystal structures on which substitutional disorders and creation of vacancies are essential to tune the electronic and thermal components independently. For example, homologous series of lillianite, cannizzarite,[5-7] and pavonite, gives the freedom to tune the electrical properties as a

function of slab thickness.[8-10] Recently, our group investigated Cu substitution in makovickyite family of compounds and found that the lattice thermal conductivity can be suppressed by introducing Cu^{+} ions in the interstitial void spaces, which effectively scatter the phonons.[10] All of these intrinsic assets make complex chalcogenide based minerals, a potential platform for tunable compositions.

Recently, working on a similar concept we sought to synthesize bismuthinite (Bi_2S_3) – aikinite ($CuPbBiS_3$) series of complex composition through substitution of Bi with Pb and Cu, where Cu can take up interstitial site. The systematic substitution of Pb and Cu for Bi generates several compositions $Cu_xPb_xBi_{1-x}S_3$ (x = 0 to 1) across the solid solution series with varied amount of Cu and Pb for Bi. For example, bismuthinite (Bi_2S_3, x = 0), pekoite ($Cu_{0.2}Pb_{0.2}Bi_{1.8}S_3$, x = 0.2), gladite ($Cu_{0.33}Pb_{0.33}Bi_{1.66}S_3$, x = 0.33), hammarite ($Cu_{0.66}Pb_{0.66}Bi_{1.33}S_3$, x = 0.66) and aikinite ($CuPbBiS_3$, x = 1).[11-15] Aikinite, an end member of the series, $CuPbBiS_3$, can be generated by completely replacing one Bi and vacancy by Pb and Cu to maintain the charge neutrality, where both Pb and Cu occupy ordered independent position.[16,17] Any other composition with 1>x>0 will have disorder between Cu and vacancy as well as between Bi and Pb. This solid solution series has structural complexity, compositional flexibility and disorder to become potential thermoelectric material, however, not much work has been done in this direction. A promising figure of merit $zT \approx 0.42$ at 723 K was reported by Liang *et al.* for the gladite, $CuPbBi_5S_9$, resulting from low Debye temperature, low average velocity, and large Grüneisen parameters.[18] While we were preparing our manuscript, another extensive report thermoelectric properties appeared in bismuthinite (Bi_2S_3) – aikinite ($CuPbBiS_3$) series.[19] In this recent article, Maji *et al.* showed that the synthetic gladite is disordered in contrast

to the natural gladite which is an ordered structure. A high thermoelectric figure of merit *z*T in the range of 0.30 and 0.43 at 700 K has been achieved by tuning the carrier concentration of gladite phase ($CuPbBi_5S_9$, x = 0.33) by replacing the S with Cl and Br.[19] These investigations by Liang *et al* and Maji *et al* reiterates the potential as thermoelectric materials in the bismuthinite – aikinite solid solution series and the opportunities to tune the compositions to achieve high *z*T. Therefore, it is important to investigate each composition within the solid solution series and understand the interplay between the composition and thermoelectric properties. As both recent reports are mainly focused on gladite (x = 0.33) structure, we sought to investigate pekoite (x = 0.2). In this work, we have synthesized three different compositions $Cu_xPb_xBi_{2-x}S_3$ (x = 0.2(I), 0.33(II), 1(III)) using high temperature solid state reaction. Measurements of physical properties exhibited ultralow thermal conductivities (< 0.65 $Wm^{-1} K^{-1}$) for all the phases, while high Seebeck coefficient value, and low electrical conductivity of I (x = 0.22) yielded a good *z*T at moderately low temperatures. The origin of low lattice thermal conductivity is further evaluated from DFT-based phonon dispersion calculations.

2. EXPERIMENTAL

2.1. SYNTHESIS

Compounds I-III are derivatives of Bi_2S_3 structure. In our synthesis we targeted different amounts of Cu and Pb substitution for Bi in Bi_2S_3 with the nominal compositions, $Cu_{0.2}Pb_{0.2}Bi_{1.8}S_3$ (I), $Cu_{0.33}Pb_{0.33}Bi_{1.66}S_3$ (II), and $CuPbBiS_3$ (III). Compounds I-III were synthesized by melting stoichiometric combinations of high purity Cu (Aldrich 99%), Bi

(Cominco electronic materials), Pb (Alfa Aesar 99.9%), and S (Alfa Aesar 99.99%) powders. All the powder precursors were weighed accordingly and loaded into 12 mm diameter quartz ampoule (total weight of 3 g) in an argon filled glove box (O_2 < 0.1ppm). The loaded ampoules were taken out with the help of an adapter and flame sealed under vacuum. The sealed ampoules were heated to 700 °C at a rate of 20 °C h^{-1} and dwelled for four days before cooling down to room temperature at a rate of 35 °C h^{-1}. A silvery single ingot was obtained in all cases. Well-ground powder samples were used for the evaluation of bulk purity and further characterization.

2.2. POWDER X-RAY DIFFRACTION

Bulk purity of the samples is evaluated using powder X-ray diffraction (PXRD) on hand-ground polycrystalline samples using PANalytical X'Pert diffractometer assembled with Cu Kα anode over a 2θ range of 5 to 90° with an average scanning rate of 0.0472° s^{-1}. The crystal structures of compounds II and III, were reported in the ICSD 197450,[14] ICSD 9120,[16] hence, we compared the simulated PXRD patterns of the reported structures with our as-synthesized powder samples. Comparison of simulated and experimental PXRD patterns of compounds I-III were provided in Figure 1. To further asses the phase purity, we carried out the Rietveld refinements of the PXRD patterns of as-synthesized products using single crystal atomic coordinates from the reported structures, ICSD 197450 (gladite)[14] for compound I, II, and ICSD 9120 (aikinite)[16] for compound III. The refinements were performed using GSAS II software.[20] Good convergence between the calculated and the experimental patterns along with the low values of weighted profile residuals, R_{wp}, (Figure S1) confirm the correctness of the model. The refined unit cell

parameters are in good agreement with the reported solutions. Rietveld refinements also show absence of any discernable impurity phase(s) in I–III. PXRDs were also collected on the hot-pressed samples to see any phase transformations during the hot pressing (Figure S2). No structural change or phase transition has been observed after the hot-pressing process.

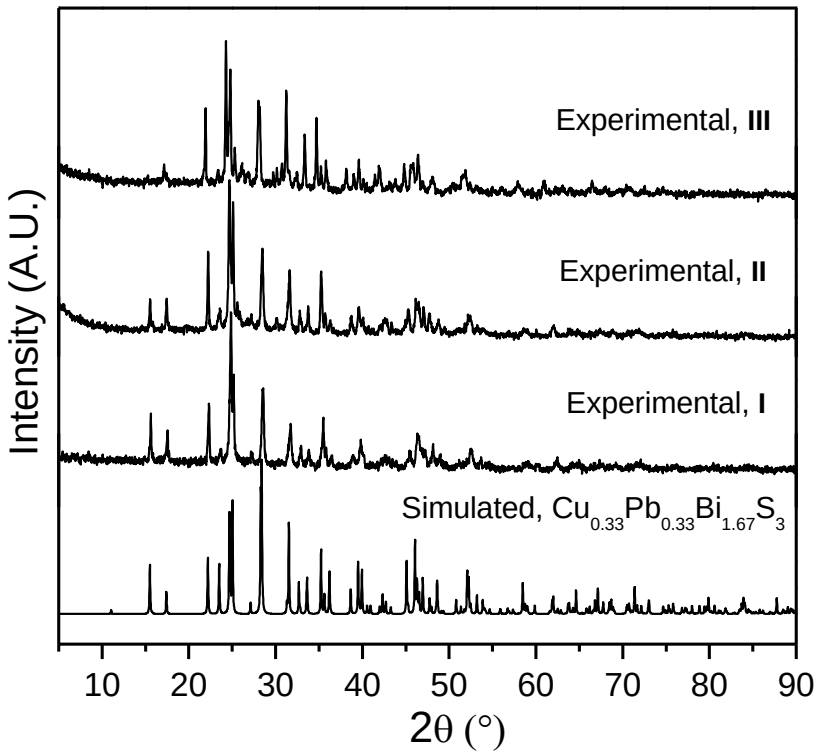

Figure 1. Comparison of simulated ($Cu_{0.33}Pb_{0.33}Bi_{1.67}S_3$), ICSD 197450[14] with experimental and powder X-ray diffraction patterns for compounds $Cu_{0.2}Pb_{0.2}Bi_{1.8}S_3$ (I), $Cu_{0.33}Pb_{0.33}Bi_{1.66}S_3$ (II), and $CuPbBiS_3$ (III).

2.3. OPTICAL BAND GAP MEASUREMENTS

Varian Cary 5000 UV-Vis-NIR spectrophotometer equipped with a praying mantis set up was used to measure the optical band gap using $BaSO_4$ powder (Fisher, 99.2%) as a 100% reflectance standard. Diffuse reflectance spectroscopy was performed on

compounds I–III in the wavelength range 200–2500 nm. Band gap values were estimated using a Tauc plot. The equation $\alpha h\nu = A(h\nu - E_g)^m$ was employed to estimate the optical band gap, where α is absorption coefficient (Kubelka–Munk function),[21] $h\nu$ is the photon energy, and m = 2 and 1/2 depending on whether the transition is indirect or direct. Compounds I–III exhibit linearity in $h\nu$ *vs.* $(\alpha h\nu)^{1/2}$ plot, suggesting that the samples possess indirect band gap. An indirect band gap of 0.98 eV for compound I, 0.87 eV for compound II, and 0.83eV for compound III was obtained. A band gap of 0.87 eV for gladite composition (II) is in very good agreement with the band gap value of 0.89 eV reported for $CuPbBi_5S_9$ by Maji et al.[19] It is evident that as the amount of Cu and Pb increases in the composition, the optical band gap decreases as observed in compound I through III.

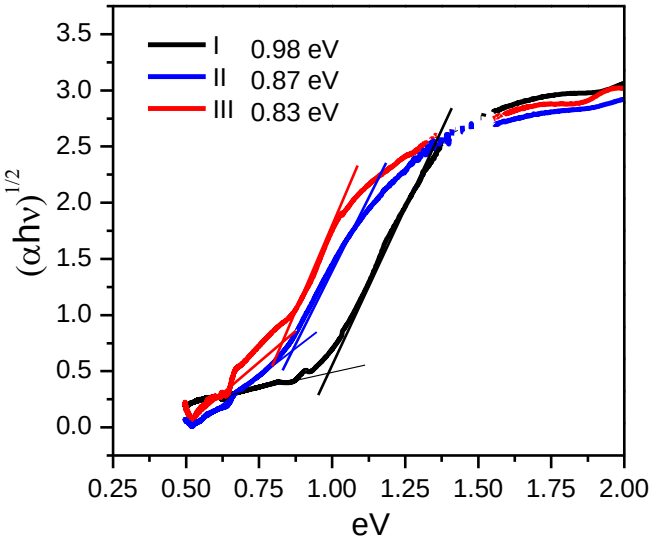

Figure 2. Diffuse reflectance spectra plotted as $h\nu$ *vs.* $(\alpha h\nu)^{1/2}$ for compounds $Cu_{0.2}Pb_{0.2}Bi_{1.8}S_3$ (I), $Cu_{0.33}Pb_{0.33}Bi_{1.66}S_3$ (II), and $CuPbBiS_3$ (III).

2.4. TRANSPORT PROPERTIES

Bars with dimensions ~10 mm × 2 mm × 1 mm were cut from the hot-pressed pellets using a Buehler diamond saw for high temperature resistivity and Seebeck coefficient measurements on a Linseis LSR-3. Measurements were done using a standard four-probe method under a helium atmosphere from 300 to 475 K. Compounds II and III were found to be too resistive to measure electrical resistivity on Linseis LSR-3. Hence, Seebeck, electrical resistivity measurements were performed only on compound I.

Hot-pressed pellets were further polished and coated with graphite for thermal diffusivity $\alpha(T)$ measurements using the laser flash technique under high purity helium or argon atmosphere. Thermal diffusivity measurements were performed on compounds I–III from 300 to 475 K in Davis and from 475 to 700 K in Rolla. Thermal conductivity was calculated using the formula $\kappa = \alpha(T)\cdot C_P \cdot d$, where $\alpha(T)$ is thermal diffusivity, C_P is specific heat, d is the density. Specific heat (C_P) is estimated by Dulong–Petit limit, $C_P = 3R/M$ (where R = ideal gas constant, M = average molar mass of each element) and density of all the samples were measured from the dimensions and masses. The calculated densities are ~95% of the theoretical densities.

2.5. THEORETICAL CALCULATIONS

Electronic band structure calculations were carried out using the density functional theory as implemented in the Vienna Ab-initio computational Package (VASP).[22-25] We employed the revised Perdew–Burke–Ernzerhof generalized gradient approximation (PBESol) to the density functional and used Projected Augmented Wave (PAW) pseudopotential to describe the effect of the core electrons. Kinetic energy cut off was set

to 520 eV and Monkhorst-pack[26] *k*-point grid size of 4×6×5 was used for Brillouin zone integration. For structure optimization, convergence threshold of 10^{-6} eV for total energy and 10^{-3} eV/Å for the maximum force was used.

3. RESULTS AND DISCUSSION

3.1. STRUCTURE DESCRIPTION

Compounds I – III can be described as ordered derivatives of Bi_2S_3, with incremental Bi + vacancy → Pb + Cu substitution in a general formula, $Cu_{1-x}\square_xPb_{1-x}Bi_{1+x}S_3$.[11-17] To understand the crystal structure of the solid solution, it is necessary to understand the crystal structure of one of the end members, Bi_2S_3. The crystal structure of Bi_2S_3 consists of ribbons of Bi4S6 with two distinct metal sites Bi1 and Bi2. Bi1 adopts 6-coordination distorted octahedral and Bi2 site adopts five coordination with S atoms in square pyramid fashion and edge-sharing between these polyhedra forms ribbons of Bi4S6.

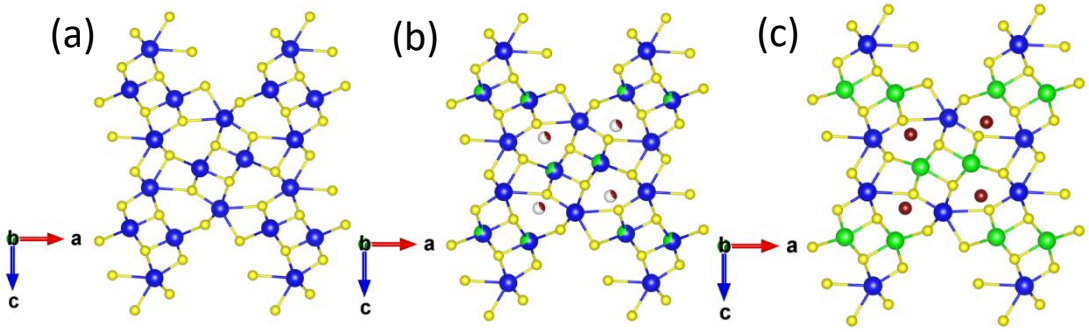

Figure 3. Framework structure showing the occupancy of Cu in tetrahedral holes and mixed occupancy of Bi2/Pb1 compared to pristine Bi_2S_3 structure (a) Bi_2S_3, ICSD 171864;[35] (b) $Cu_{0.33}Pb_{0.33}Bi_{1.68}S_3$, ICSD 197450 (II);[14] (c) $CuPbBiS_3$ (III), ICSD 9120.[15]

These ribbons are stacked along *a*-axis and held together through weaker Bi – S bonds with longer Bi – S distances (Bi1 – S ~3.38 and Bi2 – S ~ 3.32 Å). The inter-ribbon space is empty (a vacant site) in pure Bi_2S_3. As one starts to substitute Pb^{2+} and Cu^{+} for Bi^{3+}, the Cu starts to fill up the empty tetrahedral site in the inter-ribbon space connecting the two individual ribbons and Pb^{2+} starts to share Bi2 site. A series of solid solutions are thus formed until Bi2 is fully replaced by a Pb and Cu to form another end member, the aikinite, $CuPbBiS_3$. Figure 3 illustrates increase in the Cu occupancy in the inter ribbon space by replacing Bi by Cu and Pb. Although the natural and synthetic analogues of bismuthinite – aikinite series are compositionally similar, there exists differences in their long-range ordering. The synthetic analogues tend to form disordered structure between Cu/vacancy and Pb/Bi compared to naturally occurred compositions.[19] Similar situation was observed in makovickyite type compound $Ag_{0.34}Bi_{4.54}Cu_{1.98}PbS_9$, the naturally occurred composition has ordered structure, whereas the synthetic analogue has disordered structure.[10] These slight structural differences are obvious due to the high temperature synthesis procedure adopted in the laboratory compared to slow natural crystal growth process. From the above discussion it is now clear that bismuthinite – aikinite solid solution series offers an exceptional freedom to tune the composition and band gap for the optimum thermoelectric performance.

3.2. BAND STRUCTURE ANALYSIS

Electronic band structure calculations were performed on Bi_2S_3 and $CuPbBiS_3$ (III) to understand the effect of Cu and Pb in modifying the states near valence and conduction band. A calculated band gap of 1.2 eV for Bi_2S_3 is in good agreement with other reported

values using GGA method[27] and slightly lower than the experimental band gap value of 1.35 eV.[28] The band gap of $CuPbBiS_3$ (III) was calculated for the first time and the calculated band gap of 0.5 eV is slightly lower than the experimental value of 0.83 eV. As shown in Figure 4, the band structure of Bi_2S_3 has major contribution from S *p* states in the valence band with Bi *p* and S *p* states in the conduction band. Upon substitution with Cu and Pb, the contribution of Cu *d* states to the valence band becomes predominant with Bi *p* admixed with S *p* states forming the conduction band. Narrowing of band gap upon substitution with Cu and Pb for Bi is observed from DFT calculations which is consistent with experimental band gap values calculated from diffuse reflectance method. Strong overlap of Cu *d* states and S *p* states raises the Fermi level, thus narrowing the band gap.

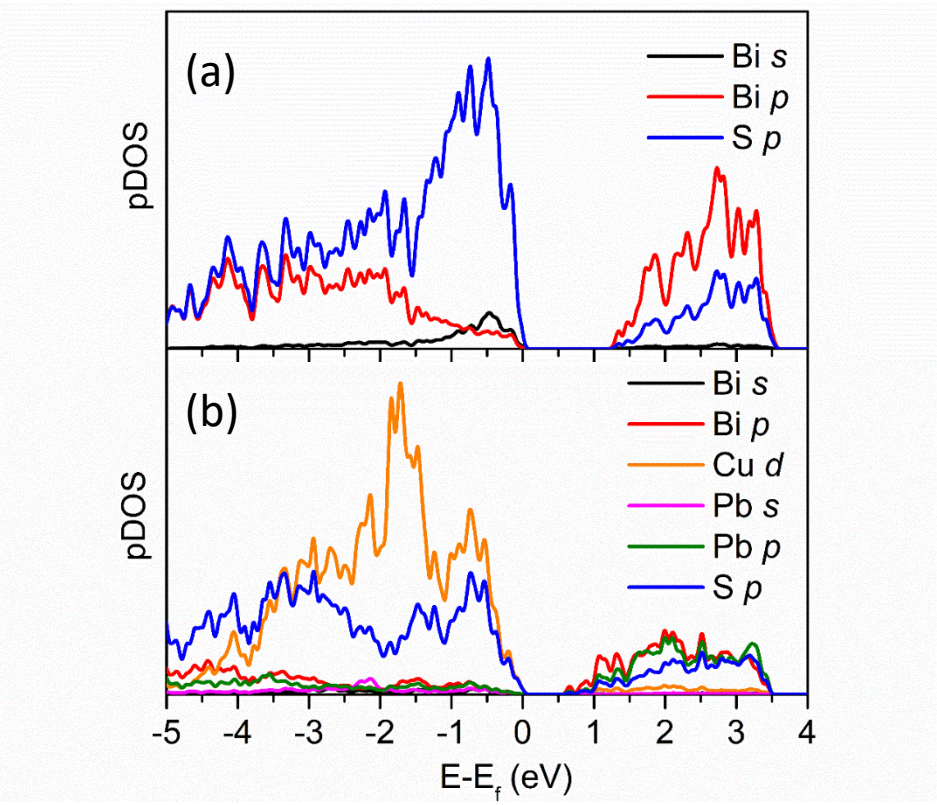

Figure 4. Density of states (a) Bi_2S_3, atomic coordinates are taken from ICSD 171864,[35] (b) $CuPbBiS_3$ (III), atomic coordinates are taken from ICSD 9120[19].

3.3. TRANSPORT PROPERTIES

Figure 5 shows temperature dependence of thermoelectric properties of compound I between room temperature to 475 K, and thermal conductivity data for compounds, I – III between room temperature to 700 K.

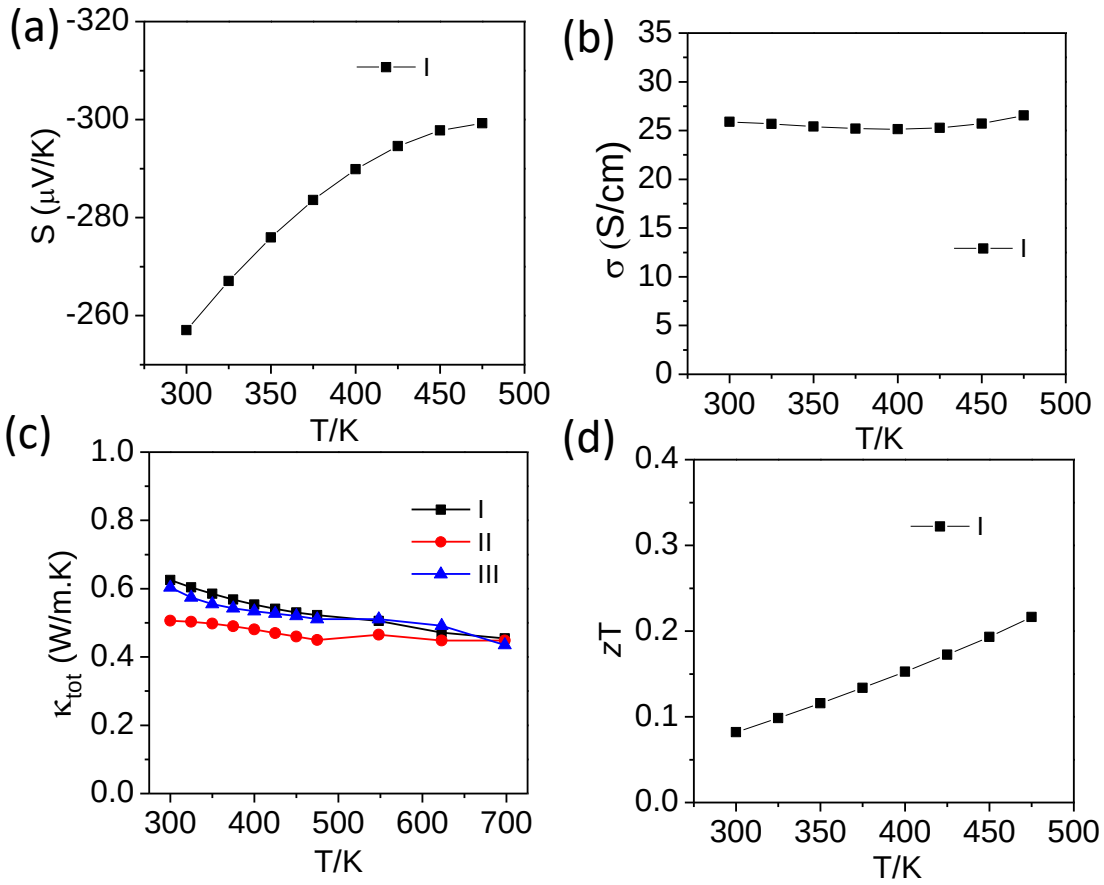

Figure 5. Temperature dependance of thermoelectric properties for compounds $Cu_{0.2}Pb_{0.2}Bi_{1.8}S_3$, I, $Cu_{0.33}Pb_{0.33}Bi_{1.66}S_3$, II, and $CuPbBiS_3$, III; (a) electrical conductivity, (b) Seebeck coefficient, (c) thermal conductivity, (d) figure of merit.

Compound I exhibits room temperature electrical conductivity of 25.9 S/cm as shown in Figure 5a. For compound I, Electrical conductivity did not change much in the measured temperature range indicating degenerate semiconducting nature. As shown in

Figure 5b, very large negative Seebeck coefficient values are observed for compound I, indicating electrons being the dominant charge carriers. Seebeck coefficient of compound I is 257 μV K^{-1} at 300 K and increased to 300 μV K^{-1} at 475 K. Recently reported TE properties on compound $CuPbBi_5S_9$,[18] which is isostructural to compound II has very low electrical conductivity of 2.85×10^{-4} S/cm and very large negative Seebeck coefficient value, $S = -1370$ μV K^{-1}, at 375 K due to very low carrier concentration. However, for similar composition Liang *et al* reported a range of Seebeck coefficients and electrical conductivity values, highly dependent on the mode of synthesis adapted.[18] These differences could arise due to slight nonstoichiometry in the composition and subsequent presence of various number of defects. Hence, it is now clear that highly resistive nature of compounds II and III may be resulted from very low charge carrier concentration indicative of a charge balanced compositions. In compound I, the large Seebeck coefficients are in consistent with low electrical conductivity values, indicative of low concentration of charge carriers. The power factors are in the range of 1.71–2.37 μW cm^{-1} K^{-2} for compound I in the measured temperature range.Figure. 5c shows the plot of κ_{tot} in the temperature range 300–700 K for compounds I – III. These compounds possess ultralow thermal conductivities in the range of 0.45–0.62 Wm^{-1} K^{-1}. The room temperature thermal conductivities are 0.62 Wm^{-1} K^{-1} for I, 0.5 Wm^{-1} K^{-1} for II, and 0.6 Wm^{-1} K^{-1} for III. These values are in good agreement with the data reported by Liang *et al* (0.44 W $m^{-1}K^{-1}$ at 298 K)[18] and Maji *et al* (0.59 W m^{-1} K^{-1} at 300 K)[19] for pristine $CuPbBi_5S_9$. These values are also comparable to many low thermal conductivity complex chalcogenide-based systems. For example, 0.6 Wm^{-1} K^{-1} in $AgBi_3S_5$,[29] 0.67–1 Wm^{-1} K^{-1} in MBi_4S_7 (M = Mn, Fe),[30] and 0.61 Wm^{-1} K^{-1} in makovickyite type compound

$Ag_{0.34}Bi_{4.54}Cu_{1.98}PbS_9$.[10] The electronic contribution to the total thermal conductivity can be calculated using $\kappa_{ele} = L\sigma T$ (Wiedemann–Franz law). κ_{lat} can be calculated by subtracting the electronic contribution from the total thermal conductivity ($\kappa_{tot} = \kappa_{ele} + \kappa_{lat}$). The Lorenz number L is calculated using the Seebeck coefficient *via* the equation $L = 1.5 + \exp\left[\frac{-|S|}{116}\right]$ where L is in 10^{-8} WΩ K^{-2} and S is in μV K^{-1}. Room temperature lattice thermal conductivity, κ_{lat}, value (0.61 Wm^{-1} K^{-1}) for compound I is very close to the κ_{tot} value (0.62 Wm^{-1} K^{-1}) because of the negligible electronic contribution, which corroborates well with the low electrical conductivities.

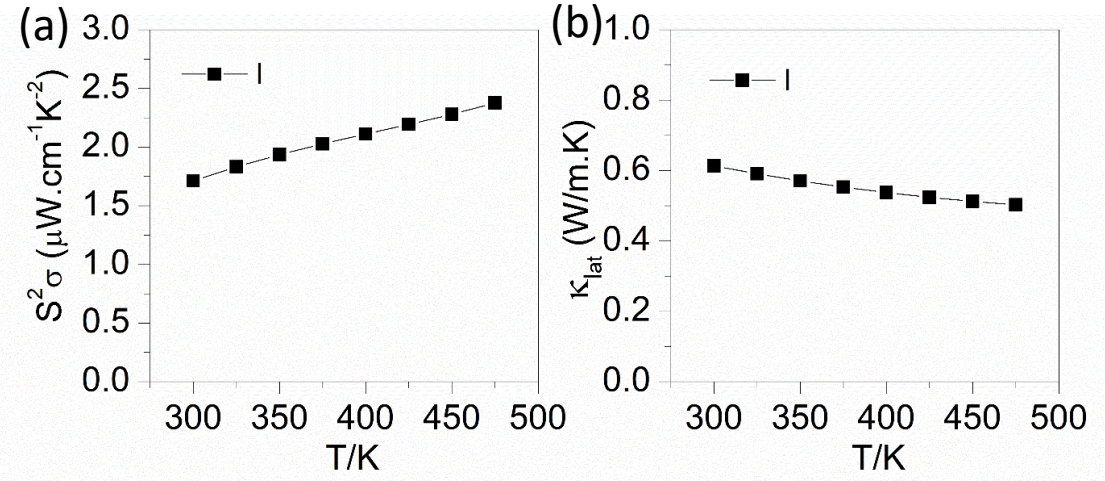

Figure 6. (a) Power factors (b) Lattice thermal conductivity (κ_{lat}) for $Cu_{0.2}Pb_{0.2}Bi_{1.8}S_3$, I from 300 to 475K.

It needs to be pointed out here that the room temperature thermal conductivity of compounds I – III is two to three times lower than the bulk Bi_2S_3 compound.[28] Among compounds I – III, compound II has intermediate composition between compounds I and III but showed lowest thermal conductivity of 0.5 Wm^{-1} K^{-1} at room temperature. It is clear that the lattice thermal conductivity is drastically suppressed by introducing Cu and Pb in

the structure, however, there may be an optimum Cu/vacancy ratio to display lowest thermal conductivity since further increase in the amount of Cu and Pb did not show a significant change. These insights will help in optimizing the electrical properties without affecting the low lattice thermal conductivity. Anharmonic rattling behavior of partially occupied interstitial Cu^{+} ions is critical in effectively scattering the acoustic phonon modes as it was observed in Cu intercalated TiS_2 and $Cu_{1.6}Bi_{4.8}S_8$ and .[31.32]

Low thermal conductivity, large Seebeck coefficient values coupled with low electrical conductivity yielded a promising *z*T of 0.21 at 475 K for compound I. Note that Maji *et al* reported a *z*T value of 0.04 at 700 K for pristine $CuPbBi_5S_9$, which was further increased to 0.43 upon Cl doping. However, in this work a *z*T value of 0.21 has been achieved at moderate temperature of 475 K without any additional doping. Hence, compound I, $Cu_{0.2}Pb_{0.2}Bi_{1.8}S_3$ would be an ideal candidate for further aliovalent doping to increase the carrier concentration which will ultimately increase the *z*T.

4. CONCLUSION

Three quaternary complex chalcogenides, $Cu_xPb_xBi_{2-x}S_3$ (x = 0.2 (I), 0.33(II), 1(III)), are successfully synthesized in the bismuthine – aikinite solid solution series. These materials are indirect *n*-type narrow band gap semiconductors with band gaps in the range if 0.6 – 0.8 eV. Ultralow thermal conductivities < 0.65 $Wm^{-1} K^{-1}$, which are two to three times lower than pristine Bi_2S_3 compound suggest the critical role of interstitial Cu ions and stereochemical lone pairs on Pb in suppressing the lattice thermal conductivity. A promising *z*T of 0.21 at 475 K for compound I warrants further investigation to tune the

thermoelectric properties especially in increasing the electrical conductivity through monovalent anion doping.

SUPPLEMENTARY INFORMATION

Table S1. Refined lattice constants and final Rietveld refinement parameters for compounds, I – III**.**

	I	II	III
Formula	$Cu_{0.2}Pb_{0.2}Bi_{1.8}S_3$	$Cu_{0.33}Pb_{0.33}Bi_{1.68}S_3$	$CuPbBiS_3$
Unit cell	a = 11.3579	a = 11.4314	a = 11.6167
	b = 3.99676	b = 4.00661	b = 4.04342
	c = 11.17939	c = 11.19316	c = 11.33351
Volume	507.486	512.66	532.349
Rw	10.543	8.394	7.732
RF^2	13.8	19.2	16.95

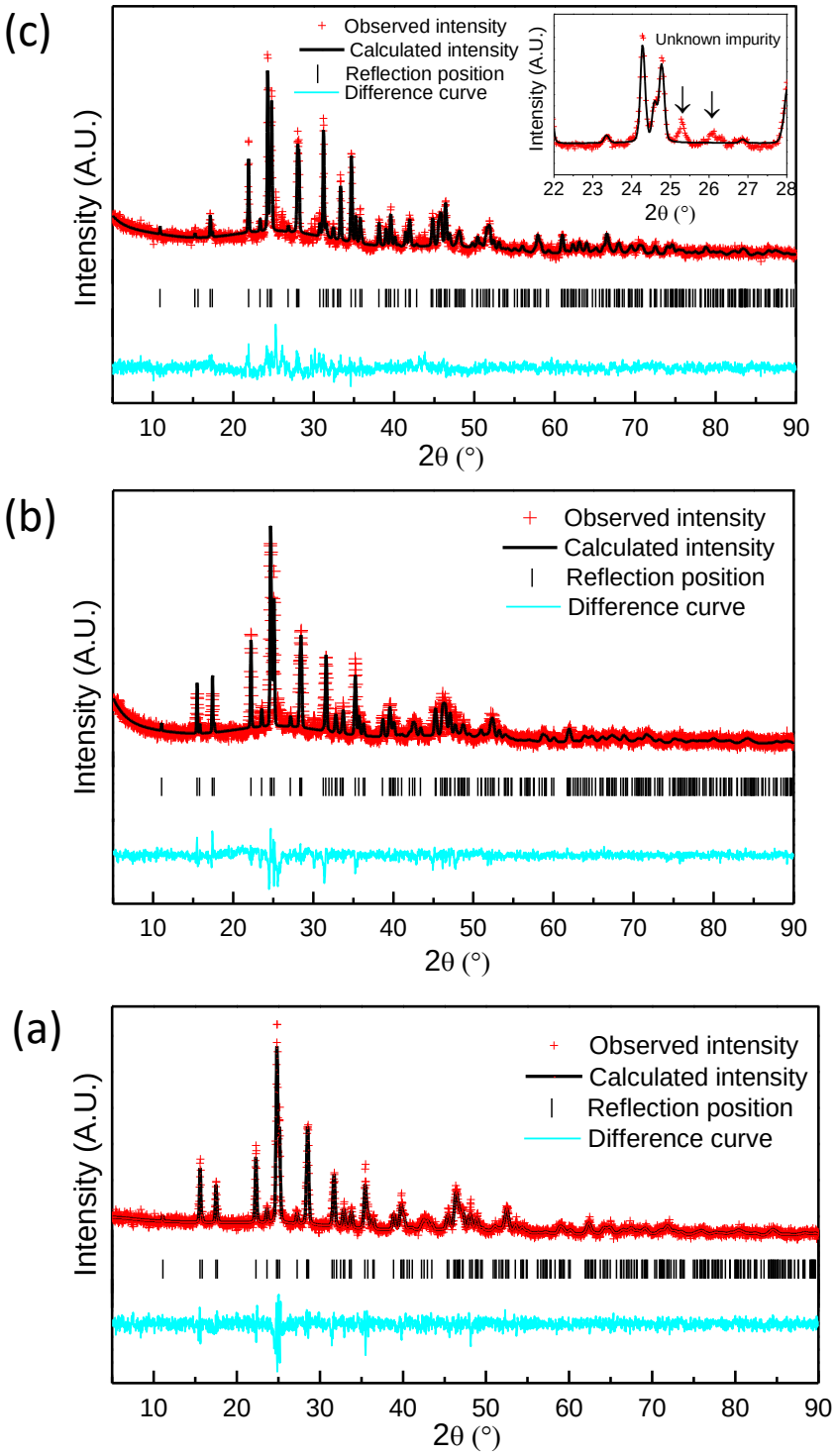

Figure S1. Rietveld refinement plots for (a) $Cu_{0.2}Pb_{0.2}Bi_{1.8}S_3$, I (b) $Cu_{0.33}Pb_{0.33}Bi_{1.68}S_3$, II (c) $CuPbBiS_3$, III, showing the observed, calculated and difference curve. Inset in (c) shows an enlarged view of the segment for $2\theta = 22$ to 28°. The arrows indicate the presence of minute quantity of an unknown impurity phase

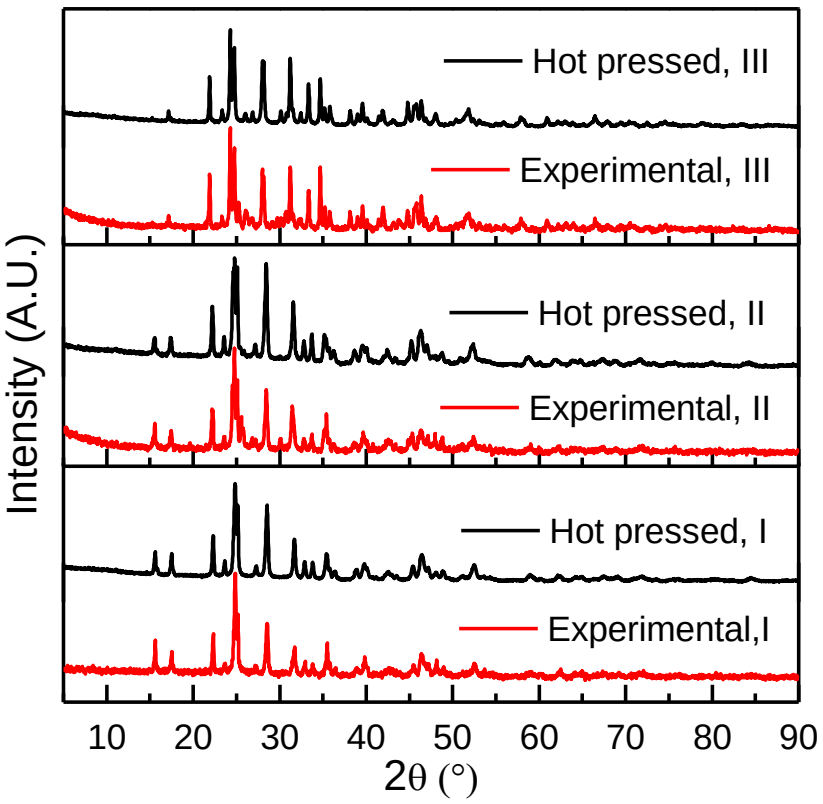

Figure S2. PXRD comparison with of hot-pressed samples with the experimental patterns for $Cu_{0.2}Pb_{0.2}Bi_{1.8}S_3$, I; $Cu_{0.33}Pb_{0.33}Bi_{1.68}S_3$, II; $CuPbBiS_3$, III**.**

REFERENCES

1. Snyder, G. J.; Toberer, E. S. Complex Thermoelectric Materials. Nature Materials. February 2008, pp 105–114. https://doi.org/10.1038/nmat2090.

2. Shi, X. L.; Zou, J.; Chen, Z. G. Advanced Thermoelectric Design: From Materials and Structures to Devices. Chem. Rev. 2020, 120 (15), 7399–7515. https://doi.org/10.1021/acs.chemrev.0c00026

3. I.Terasaki. Thermal Conductivity and Thermoelectric Power of Semiconductors. *Compr. Semicond. Sci. Technol.* **2011**, 326–358

4. Rowe, D. M. *CRC Handbook of Thermoelectric*; 2018

5. Ohta, M.; Chung, D. Y.; Kunii, M.; Kanatzidis, M. G. Low Lattice Thermal Conductivity in $Pb_5Bi_6Se_{14}$, $Pb_3Bi_2S_6$, and $PbBi_2S_4$: Promising Thermoelectric Materials in the Cannizzarite, Lillianite, and Galenobismuthite Homologous Series. *J. Mater. Chem. A.* **2014**, *2*, 20048– 20058, DOI: 10.1039/c4ta05135a

6. A Lillianite Homologue with Promising Thermoelectric Properties. *Inorg. Chem.* **2015**, *54*, 746– 755, DOI: 10.1021/ic501327u

7. Casamento, J.; Lopez, J. S.; Moroz, N. A.; Olvera, A.; Djieutedjeu, H.; Page, A.; Uher, C.; Poudeu, P. F. P. Crystal Structure and Thermoelectric Properties of the ^{7,7}L Lillianite Homologue $Pb_6Bi_2Se_9$. *Inorg. Chem.* **2017**, *56*, 261– 268, DOI: 10.1021/acs.inorgchem.6b02118

8. Zhao, J.; Hao, S. Q.; Islam, S. M.; Chen, H. J.; Tan, G. J.; Ma, S. L.; Wolverton, C.; Kanatzidis, M. G. Six Quaternary Chalcogenides of the Pavonite Homologous Series with Ultralow Lattice Thermal Conductivity. *Chem. Mater.* **2019**, *31*, 3430– 3439, DOI: 10.1021/acs.chemmater.9b00585

9. Qu, S. Q.; Zhao, J.; Jiang, Z. M.; Jiang, D. Q.; Wang, Y. G. Pavonite homologues as potential n-type thermoelectric materials: crystal structure and performance. *Mater. Chem. Front.* **2021**, *5*, 1283– 1294, DOI: 10.1039/D0QM00662A

10. Balijapelly, S., Hauble, A., Pollard, M., Poupon, M., Petříček, V., Watts, J.L., Hor, Y.S., Kauzlarich, S.M., Choudhury, A. Ultralow thermal conductivity through the interplay of composition and disorder between thick and thin layers of makovickyite structure **J. Mater. Chem. C**, 2021,**9**, 11207-11215. DOI: 10.1039/d1tc02173g

11. Petříček, V.; Makovicky, E. Interpretation of Selected Structures of the Bismuthinite - Aikinite Series as Commensurately Modulated Structures. *Can. Mineral.* **2006**, *44* (1), 189– 206, DOI: 10.2113/gscanmin.44.1.189

12. Mumme, W. G.; Watts, J. A. Pekoite, $CuPbBi_{11}S_{18}$, A New Member of the Bismuthinite-Aikinite Mineral Series: Its Crystal Struture and Relationship with Naturally- and Synthetically-Formed Members. *Can. Mineral.* **1976**, *14*, 322– 333

13. Syněcek, V.; Hybler, J. The Crystal Structure of Krupkaite, $CuPbBi_3S_6$, and of Gladite, $CuPbBi_5S_9$, and the Classification of Superstructures in the Bismuthinite- Aikinite Group. *Neues Jahrb. Miner. Monatsh.* **1974**, 541– 560

14. Kohatsu, I.; Wuensch, B. J. The Crystal Structure of Gladite, $PbCuBi_5S_9$, a Superstructure Intermediate in the Series Bi_2S_3-$PbCuBiS_3$ (Bismuthinite-Aikinite). *Acta Crystallogr. Sect. B Struct. Crystallogr. Cryst. Chem.* **1976**, *32* (8), 2401– 2409, DOI: 10.1107/S0567740876007851

15. Topa, D.; Balić-Žunić, T.; Makovicky, E. The Crystal Structure of $Cu_{1.6}Pb_{1.6}Bi_{6.4}S_{12}$, a New 44.8 Å Derivative of the Bismuthinite-Aikinite Solid-Solution Series. *Can. Mineral.* **2000**, *38*, 611– 616, DOI: 10.2113/gscanmin.38.3.611

16. Kohatsu, I.; Wuensch, B. J. The Crystal Structure of Aikinite, $PbCuBiS_3$. *Acta Crystallogr. Sect. B Struct. Crystallogr. Cryst. Chem.* **1971**, *27* (6), 1245– 1252, DOI: 10.1107/S0567740871003819

17. Ohmasa, M.; Nowacki, W. A Redetermination of the Crystal Structure of Aikinite $[BiS_2|S|Cu^{IV}Pb^{VII}]$. *Z. Kristallogr.* **1970**, *132*, 71– 86, DOI: 10.1524/zkri.1970.132.1-6.71

18. Liang, H.; Guo, J.; Zhou, Y. X.; Wang, Z. Y.; Feng, J.; Ge, Z. H. $CuPbBi_5S_9$ Thermoelectric Material with an Intrinsic Low Thermal Conductivity: Synthesis and Properties. *J. Mater.* **2022**, *8*, 174– 183, DOI: 10.1016/j.jmat.2021.03.016

19. Maji, K.; Lemoine, P.; Le Renaud, A.; Zhang, B.; Zhou, X.; Carnevali, V.; Candolfi, C.; Raveau, B.; Al, R.; Al Orabi, R.; Fornari, M.; Vaqueiro, P.; Pasturel, M.; Prestipino, C.; Guilmeau, E. A Tunable Structural Family with Ultralow Thermal Conductivity: Copper-Deficient Cu1–x□xPb1–xBi1+xS3, *J. Am. Chem. Soc*. **2022**. https://doi.org/10.1021/JACS.1C11998

20. Toby, B. H.; Von Dreele, R. B. GSAS-II: the genesis of a modern open-source all-purpose crystallography software package. *J. Appl. Crystallogr.* **2013**, *46*, 544– 549, DOI: 10.1107/S0021889813003531

21. Kubelka, P.; Munk, F. Ein Beitrag Zur Optik Der Farbanstriche. Z. Techn. Phys., 12 (1931), pp. 593-601

22. Kresse, G. Hafner, J. Ab initio molecular dynamics for liquid metals. Phys. Rev. B, 47 (1993), pp. 558-561, 10.1103/PhysRevB.47.558

23. Kresse, G.; Furthmüller, J. Efficiency of ab-initio total energy calculations for metals and semiconductors using a plane-wave basis set. Comput. Mater. Sci., 6 (1996), pp. 15-50, 10.1016/0927-0256(96)00008-0

24. Kresse, G.; Furthmüller, J**.** Efficient iterative schemes for ab initio total-energy calculations using a plane-wave basis set. Phys. Rev. B, 54 (1996), pp. 11169-11186, 10.1103/PhysRevB.54.11169

25. Joubert, D. **R**om ultrasoft pseudopotentials to the projector augmented-wave method. Phys. Rev. B, 59 (1999), pp. 1758-1775, 10.1103/PhysRevB.59.1758

26. Monkhorst, H.J.; Pack, J.D. Special points for brillonin-zone integrations. Phys. Rev. B., 13 (1976), pp. 5188-5192, 10.1103/PhysRevB.13.5188

27. Larson, P.; Greanya, V. A.; Tonjes, W. C.; Liu, R.; Mahanti, S. D.; Olson, C. G. Electronic Structure of Bi_2X_3 (X = S, Se, T) Compounds: Comparison of Theoretical Calculations with Photoemission Studies. *Phys. Rev. B: Condens. Matter Mater. Phys.* **2002**, *65*, 085108, DOI: 10.1103/PhysRevB.65.085108

28. Biswas, K.; Zhao, L. D.; Kanatzidis, M. G. Tellurium-Free Thermoelectric: The Anisotropic n -Type Semiconductor Bi_2S_3. *Adv. Energy Mater.* **2012**, *2* (6), 634– 638, DOI: 10.1002/aenm.201100775

29. Tan, G.; Hao, S.; Zhao, J.; Wolverton, C.; Kanatzidis, M. G. High Thermoelectric Performance in Electron-Doped $AgBi_3S_5$ with Ultralow Thermal Conductivity. *J. Am. Chem. Soc.* **2017**, *139* (18), 6467– 6473, DOI: 10.1021/jacs.7b02399

30. Labégorre, J. B.; Virfeu, A.; Bourhim, A.; Willeman, H.; Barbier, T.; Appert, F.; Juraszek, J.; Malaman, B.; Huguenot, A.; Gautier, R.; Nassif, V.; Lemoine, P.; Prestipino, C.; Elkaim, E.; Pautrot-d'Alençon, L.; Le Mercier, T.; Maignan, A.; Al Rahal Al Orabi, R.; Guilmeau, E. XBi_4S_7 (X = Mn, Fe): New Cost-Efficient Layered n-Type Thermoelectric Sulfides with Ultralow Thermal Conductivity. *Adv. Funct. Mater.* **2019**, *29* (48), 1904112– 1904124, DOI: 10.1002/adfm.201904112

31. Guilmeau, E.; Bréard, Y.; Maignan, A. Transport and Thermoelectric Properties in Copper Intercalated TiS_2 Chalcogenide. *Appl. Phys. Lett.* **2011**, *99* (5), 052107– 052109, DOI: 10.1063/1.3621834

32. Bhui, A.; Dutta, M.; Mukherjee, M.; Rana, K. S.; Singh, A. K.; Soni, A.; Biswas, K. Ultralow Thermal Conductivity in Earth-Abundant $Cu_{1.6}Bi_{4.8}S_8$: Anharmonic Rattling of Interstitial Cu. *Chem. Mater.* **2021**, *33*, 2993– 3001, DOI: 10.1021/acs.chemmater.1c00659

33. Li, C.; Zhao, J.; Hu, Q.; Liu, Z.; Yu, Z.; Yan, H. Crystal Structure and Transporting Properties of Bi_2S_3 under High Pressure: Experimental and Theoretical Studies. *J. Alloys Compd.* **2016**, *688*, 329– 335, DOI: 10.1016/J.JALLCOM.2016.06.276

34. Liu, Z. H.; Pei, Y. L.; Geng, H. Y.; Zhou, J. C.; Meng, X. F.; Cai, W.; Liu, W. S.; Sui, J. H. Enhanced thermoelectric performance of Bi_2S_3 by synergistical action of bromine substitution and copper nanoparticles. *Nano Energy* **2015**, *13*, 554– 562, DOI: 10.1016/j.nanoen.2015.03.036

35. Kyono, A.; Kimata, M. Structural variations induced by difference of the inert pair effect in the stibnite-bismuthinite solid solution series $(Sb, Bi)_2S_3$. *American Mineralogist*. **2004** *89*, 932-940

SECTION

3. CONCLUSIONS

In the first part of the dissertation, it is demonstrated that the building block approach can be used as a synthetic toolbox to systematically design new quaternary complex chalcogenides in a predictive manner. *In operando* synchrotron powder X-ray diffraction experiments demonstrated instantaneous product formation during the reaction without the destruction of the building block. This building block approach involves no change in the oxidation state of the elements during the reaction, making it a more predictive and rational in nature compared to traditional exploratory based synthesis approach. Several new quaternary complex chalcogenide compounds were discovered employing building block approach, which were shown to exhibit interesting physicochemical properties for application in solid electrolytes, magnetic semiconductors, and nonlinear optics. This unique synthesis approach can pave the way for new materials discovery with target compositions and specified properties.

In the second part of the dissertation, it is demonstrated that complex chalcogenide minerals can be engineered through the interplay of composition and disorder to tune thermoelectric properties. Accordingly, we have demonstrated that by varying the ratio of Cu and Pb in place of Bi, ultra-low thermal conductivities (<0.7 W/m.K) can be achieved in makovickyite type structure. This strategy has been successfully applied to another complex chalcogenide system bismuthinite – aikinite where different amount of Cu/Pb substitution for Bi in Bi_2S_3 generates a series of

structures, $Cu_xPb_xBi_{2-x}S_3$ (x = 0.2, 0.33, 1), with ultralow thermal conductivity (<0.6 W/m.K) conducive to achieve high *z*T (thermoelectric figure of merit) at moderately high temperatures.

BIBLIOGRAPHY

1. Spaldin, N. Fundamental materials research and the course of human civilization, VSH-Bulletin Nr. 2, **2017**, 11-15.

2. B. Dunn, H. Kamath, J.-M. Tarascon, Electrical energy storage for the grid: a battery of choices *Science*, **2011**, 334, 928-935, 10.1126/science.1212741

3. Baliga, B. J. Trends in power semiconductor devices, *IEEE Trans. Electron Devices*, **1996,** *43*, 10, 1717-1731.

4. Government, U. Materials Genome Initiative National Science and Technology Council

5. Committee on Technology Subcommittee on the Materials Genome Initiative JUNE **2014**. Whitehouse.Gov.

6. Saal, J. E., Kirklin, S., Aykol, M., Meredig, B. Wolverton, C. Materials design and discovery with high-throughput density functional theory: The open quantum materials database (OQMD). **2017**, *65*, 1501–1509

7. Zunger, A. Inverse design in search of materials with target functionalities. Nat Rev Chem, **2018**, *2*, 1–16.

8. Jansen M. A. Concept for Synthesis Planning in Solid-State Chemistry, *Angew. Chem., Int. Ed.*, **2002**, *41*, 3746 —3766.

9. Kanatzidis, M. G. Discovery-Synthesis, Design, and Prediction of Chalcogenide Phases. *Inorg. Chem.* **2017**, *56*, 3158– 3173, DOI: 10.1021/acs.inorgchem.7b00188

10. Szczypiński, F. T.; Bennett, S.; Jelfs, K. E. Can We Predict Materials That Can Be Synthesised?. *Chem. Sci.* **2021**, *12*, 830, DOI: 10.1039/D0SC04321D

11. Sootsman, J. R.; Chung, D. Y.; Kanatzidis, M. G. New and Old Concepts in Thermoelectric Materials. *Angew. Chem., Int. Ed*. **2009**, *2*, 8616–8639. https://doi.org/10.1002/anie.200900598

12. Kanatzidis, M. G. New Directions in Synthetic Solid State Chemistry: Chalcophosphate Salt Fluxes for Discovery of New Multinary Solids. *Curr. Opin. Solid State Mater. Sci.* **1997**, *2*, 139– 149 DOI: 10.1016/S1359-0286(97)80058-7

13. Bugaris, D. E.; zur Loye, H. C. Materials Discovery by Flux Crystal Growth: Quaternary and Higher Order Oxides. *Angew. Chem., Int. Ed*. **2012**, 51, 3780– 3811 DOI: 10.1002/anie.201102676

14. Vasylenko, A.; Gamon, J.; Duff, B. B.; Gusev, V. V.; Daniels, L. M.; Zanella, M.; Shin, J. F.; Sharp, P. M.; Morscher, A.; Chen, R.; Neale, A. R.; Hardwick, L. J.; Claridge, J. B.; Blanc, F.; Gaultois, M. W.; Dyer, M. S.; Rosseinsky, M. J. Element Selection for Crystalline Inorganic Solid Discovery Guided by Unsupervised Machine Learning of Experimentally Explored Chemistry. *Nat. Commun.* **2021**, *12* (1), 1–12. https://doi.org/10.1038/s41467-021-25343-7

15. Yaghi, O. M.; O'Keeffe, M.; Ockwig, N. W.; Chae, H. K.; Eddaoudi, M.; Kim, J. Reticular Synthesis and the Design of New Materials. *Nat.* **2003**, *423* (6941), 705–714. https://doi.org/10.1038/nature01650

16. Stein A, Keller SW, Mallouk TE. Turning down the heat: design and mechanism in solid-state synthesis. *Science*. **1993**, 259(5101):1558-64. doi: 10.1126/science.259.5101.1558.

17. Aykol, M.; Montoya, J. H.; Hummelshøj, J. S.; Aykol, M.; Montoya, J. H.; Hummelshøj, J. Rational Solid-State Synthesis Routes for Inorganic Materials. *J. Am. Chem. Soc.* **2021**, *143*, 9244, DOI: 10.1021/jacs.1c04888

18. Alberi, K.; Nardelli, M. B.; Zakutayev, A.; Mitas, L.; Curtarolo, S.; Jain, A.; Fornari, M.; Marzari, N.; Takeuchi, I.; Green, M. L.; Kanatzidis, M.; Toney, M. F.; Butenko, S.; Meredig, B.; Lany, S.; Kattner, U.; Davydov, A.; Toberer, E. S.; Stevanovic, V.; Walsh, A.; Park, N.-G.; Aspuru-Guzik, A.; Tabor, D. P.; Nelson, J.; Murphy, J.; Setlur, A.; Gregoire, J.; Li, H.; Xiao, R.; Ludwig, A.; Martin, L. W.; Rappe, A. M.; Wei, S.-H.; Perkins, J. The 2019 materials by design roadmap. *J. Phys. D: Appl. Phys.* **2018**, *52*, 013001 DOI: 10.1088/1361-6463/aad926

19. Tan, G.; Zhao, L. D.; Kanatzidis, M. G. Rationally Designing High-Performance Bulk Thermoelectric Materials. *Chem. Rev.* **2016**, *116*, *19*, *12123–12149*. https://doi.org/10.1021/acs.chemrev.6b00255

20. Chung, I.; Kanatzidis, M. G. Metal Chalcogenides: A Rich Source of Nonlinear Optical Materials. *Chem. Mater.* **2014**, *26* (1), 849– 869, DOI: 10.1021/cm401737s

21. Gottlieb, M.; Singh, N. B.; Hopkins, R. H.; Mazelsky, R. Noncollinear Acoustooptic Tunable Filter - Thallium Phosphorus Selenide System. *Opt. Eng*. **1994**, 33, 2503– 2508 DOI: 10.1117/12.176513

22. Eggleton, B., Luther-Davies, B. & Richardson, K. Chalcogenide photonics. *Nature Photon*, **2011**, **5,** 141–148. https://doi.org/10.1038/nphoton.2011.309

23. Kato, Y., Hori, S., Saito, T. *et al.* High-power all-solid-state batteries using sulfide superionic conductors. *Nat Energy*, **2006**, 1, 16030. https://doi.org/10.1038/nenergy.2016.30

24. Sheldrick, W. S.; Wachhold, M. Chalcogenidometalates of the Heavier Group 14 and 15 Elements. *Coord. Chem. Rev.* **1998**, *176* (1), 211– 322, DOI: 10.1016/S0010-8545(98)00120-9

25. Abudurusuli, A.; Huang, J.B.; Wang, P.; Yang, Z.H.; Pan, S.L.; Li, J.J. $Li_4MgGe_2S_7$: the first alkali and alkaline-earth diamond-like infrared nonlinear optical material with exceptional large band gap. *Angew. Chem. Int. Ed*., **2021,** *60*, 24131-24136

26. Grabar, A. A.; Kedyk, I. V.; Gurzan, M. I.; Stoika, I. M.; Molnar, A. A.; Vysochanskii, Y. M. Enhanced Photorefractive Properties of Modified $Sn_2P_2S_6$ *Opt. Commun*. **2001**, 188, 187– 194 DOI: 10.1016/S0030-4018(00)01119-6

27. Gottlieb, M.; Singh, N. B.; Hopkins, R. H.; Mazelsky, R. Noncollinear Acoustooptic Tunable Filter - Thallium Phosphorus Selenide System *Opt. Eng*. **1994**, *33*, 2503– 2508 DOI: 10.1117/12.176513

28. Balijapelly, S.; Zhang, Q.; Sandineni, P.; Adhikary, A.; Mohapatra, S.; Sundaramoorthy, S.; Gerasimchuck, N.; Chernatynskiy, A.V.; Choudhury, A. High Sodium-Ion Conductivity in Interlocked Quaternary Chalcogenides Built with Supertetrahedral Building Units. *ACS Appl. Energy Mater*. **2021**, *4*, 8, 7942–7951

29. Murayama, M.; Sonoyama, N.; Yamada, A.; Kanno, R. Material Design of New Lithium Ionic Conductor, thio-LISICON, in the Li_2S-P_2S_5 System *Solid State Ionics* **2004**, *170*, 173– 180 DOI: 10.1016/j.ssi.2004.02.025

30. Ellis, B. L.; Nazar, L. F. Sodium and sodium-ion energy storage batteries. *Curr. Opin. Solid State Mater. Sci.* **2012**, *16*, 168– 177, DOI: 10.1016/j.cossms.2012.04.002

31. Kamaya, N.; Homma, K.; Yamakawa, Y.; Hirayama, M.; Kanno, R.; Yonemura, M.; Kamiyama, T.; Kato, Y.; Hama, S.; Kawamoto, K.; Mitsui, A. A Lithium Superionic Conductor. *Nat. Mater*. **2011**, *10*, 682– 686 DOI: 10.1038/nmat3066

32. Kanatzidis, M. G.; Park, Y. Polychalcogenide Synthesis in Molten-Salts - Novel One-Dimensional Compounds in the K/Cu/S System Containing Exclusively S_4^{2-} Ligands. *J. Am. Chem. Soc*. **1989**, *111*, 3767– 3769 DOI: 10.1021/ja00192a055Shoemaker, D.

33. Shoemaker, D. P.; Chung, D. Y.; Mitchell, J.; Bray, T. H.; Soderholm, L.; Chupas, P. J.; Kanatzidis, M. G. Understanding fluxes as media for directed synthesis: In situ local structure of molten potassium polysulfides. *J. Am. Chem. Soc.* **2012**, *134*, 9456, DOI: 10.1021/ja303047e

34. Kanatzidis, M. G. Molten Alkali-Metal Polychalcogenides as Reagents and Solvents for the Synthesis of New Chalcogenide Materials. *Chem. Mater*. **1990**, 2, 353– 363 DOI: 10.1021/cm00010a009

35. Parkin, I. P. Solid state metathesis reaction for metal borides, silicides, pnictides and chalcogenides: ionic or elemental pathways *Chem. Soc. Rev.* **1996**, *25*, 199−207

36. Gillan, E. G.; Kaner, R. B. Synthesis of refractory ceramics via rapid metathesis reactions between solid-state precursors. *Chem. Mater*. **1996**, *8*, 333−343

37. Treece, R. E.; Gillan, E. G.; Kaner, R. B. Materials Synthesis Via Solid-State Metathesis Reactions. *Comments Inorg.Chem.* **1995**, *16*, 313-337. https://doi.org/10.1080/02603599508035775

38. Meyer, H.-J. Solid state metathesis reactions as a conceptual tool in the synthesis of new materials *Dalton Trans*. **2010**, *39*, 5973– 5982 DOI: 10.1039/c001031f

39. Martinolich, A. J.; Neilson, J. R. Toward Reaction-by-Design: Achieving Kinetic Control of Solid-State Chemistry with Metathesis. *Chem. Mater.* **2017**, *29* (2), 479– 489, DOI: 10.1021/acs.chemmater.6b04861

40. Larcher, D.; Tarascon, J.-M. Towards greener and more sustainable batteries for electrical energy storage. *Nat. Chem.* **2015**, *7*, 19– 29, DOI: 10.1038/nchem.2085

41. Janek, J.; Zeier, W. G. A solid future for battery development. *Nat. Energy* **2016**, *1*, 16141, DOI: 10.1038/nenergy.2016.141

42. Tarascon, J. M.; Armand, M. Issues and Challenges Facing Rechargeable Lithium Batteries. *Nature* **2001**, *414*, 359– 367, DOI: 10.1038/35104644

43. Manthiram, A., Yu, X. & Wang, S. Lithium battery chemistries enabled by solid-state electrolytes. *Nat Rev Mater,* **2017**, *2***,** 16103 https://doi.org/10.1038/natrevmats.2016.103

44. Goodenough, J. B.; Singh, P. Review—Solid Electrolytes in Rechargeable Electrochemical Cells. *J. Electrochem. Soc.* **2015**, *162*, A2387– A2392, DOI: 10.1149/2.0021514jes

45. Dudney, N. J.; West, W. C.; Nanda, J. *Handbook of Solid State Batteries*. Second. World Scientific, **2016**

46. Banerjee, A.; Wang, X.; Fang, C.; Wu, E. A.; Meng, Y. S. Interfaces and Interphases in All-Solid-State Batteries with Inorganic Solid Electrolytes. *Chem. Rev.* **2020**, *120*, 6878– 6933, DOI: 10.1021/acs.chemrev.0c00101

47. Bachman, J. C.; Muy, S.; Grimaud, A.; Chang, H.-H.; Pour, N.; Lux, S. F.; Paschos, O.; Maglia, F.; Lupart, S.; Lamp, P.; Giordano, L.; Shao-Horn, Y. Inorganic Solid-State Electrolytes for Lithium Batteries: Mechanisms and Properties Governing Ion Conduction. *Chem. Rev.* **2016**, *116*, 140– 162, DOI: 10.1021/acs.chemrev.5b00563

48. Wang, Y.; Zhou, D.; Palomares, V.; Shanmukaraj, D.; Sun, B.; Tang, X.; Wang, C.; Armand, M.; Rojo, T.; Wang, G. Revitalising Sodium-Sulfur Batteries for Non-High-Temperature Operation: A Crucial Review. *Energy Environ. Sci.* **2020**, *13*, 3848– 3879, DOI: 10.1039/d0ee02203a

49. Jia, H.; Peng, L.; Yu, C.; Dong, L.; Cheng, S.; Xie, J. Chalcogenide-Based Inorganic Sodium Solid Electrolytes. *J. Mater. Chem. A* **2021**, *9*, 5134– 5148, DOI: 10.1039/D0TA10994K

50. Seino, Y.; Ota, T.; Takada, K.; Hayashi, A.; Tatsumisago, M. A sulphide lithium super ion conductor is superior to liquid ion conductors for use in rechargeable batteries. *Energy Environ. Sci.* **2014**, *7*, 627– 631, DOI: 10.1039/c3ee41655k

51. Ohno, S.; Banik, A.; Dewald, G. F.; Kraft, M. A.; Krauskopf, T.; Minafra, N.; Till, P.; Weiss, M.; Zeier, W. G. Materials Design of Ionic Conductors for Solid State Batteries. *Prog. Energy* **2020**, *2*, 022001, DOI: 10.1088/2516-1083/ab73dd

52. Tian, Y.; Zeng, G.; Rutt, A.; Shi, T.; Kim, H.; Wang, J.; Koettgen, J.; Sun, Y.; Ouyang, B.; Chen, T.; Lun, Z.; Rong, Z.; Persson, K.; Ceder, G. Promises and Challenges of Next-Generation ″Beyond Li-ion″ Batteries for Electric Vehicles and Grid Decarbonization. *Chem. Rev.* **2021**, *121*, 1623– 1669, DOI: 10.1021/acs.chemrev.0c00767

53. Tritt, T., Subramanian, M. Thermoelectric Materials, Phenomena, and Applications: A Bird's Eye View. *MRS Bulletin,* **2006**, *31*(3), 188-198. doi:10.1557/mrs2006.44

54. Nolas, G.S.; Sharp, J.; Goldsmid, H.J. Thermoelectrics: Basic Principles and New MaterialsDevelopments. Springer-Verlag, Berlin, **2001**

55. Sootsman, J. R.; Chung, D. Y.; Kanatzidis, M. G. New and Old Concepts in Thermoelectric Materials. *Angew. Chem., Int. Ed.* **2009**, *48* (46), 8616– 8639, DOI: 10.1002/anie.200900598

56. Paradiso, J. A.; Starner, T. Energy Scavenging for Mobile and Wireless Electronics. *IEEE Pervasive Computing*. **2005**, 18–27. https://doi.org/10.1109/MPRV.2005.9

57. Terasaki, I. *Compr. Semicond. Sci. Technol.*, **2011**, 326 —358

58. Seebeck, T.J.Abh. K. Akad. Wiss. (Berlin, 1823) p.265

59. Sales, B. C.; Mandrus, D.; Williams, R. K. Filled Skutterudite Antimonides: A New Class of Thermoelectric Materials. *Science* **1996**, *272* (5266), 1325– 1328, DOI: 10.1126/science.272.5266.1325

60. Graf, T.; Felser, C.; Parkin, S. S. P. Simple rules for the understanding of Heusler compounds. *Prog. Solid State Chem.* **2011**, *39* (1), 1– 50, DOI: 10.1016/j.progsolidstchem.2011.02.001

61. He, J., Liu, Y. & Funahashi, R. Oxide thermoelectrics: The challenges, progress, and outlook. *Journal of Materials Research,* **2011**, *26***,** 1762–1772. https://doi.org/10.1557/jmr.2011.108

62. Kauzlarich, S. M.; Brown, S. R.; Jeffrey Snyder, G. Zintl Phases for Thermoelectric Devices. *J. Chem. Soc. Dalt. Trans.* **2007**, *21*, 2099–2107. https://doi.org/10.1039/b702266b.

63. Yu, Y.; Cagnoni, M.; Cojocaru-Mirédin, O.; Wuttig, M. Chalcogenide Thermoelectrics Empowered by an Unconventional Bonding Mechanism. *Adv. Funct. Mater.* **2020**, *30*, 1904862 DOI: 10.1002/adfm.201904862

64. Snyder, G. J.; Toberer, E. S. Complex Thermoelectric Materials. *Nature Mater*. **2008**, *7*, 105–114. https://doi.org/10.1038/nmat2090

65. Brown, S. R.; Kauzlarich, S. M.; Gascoin, F.; Jeffrey Snyder, G. $Yb_{14}MnSb_{11}$: New High Efficiency Thermoelectric Material for Power Generation. *Chem. Mater.* **2006**, *18* (7), 1873–1877. https://doi.org/10.1021/cm060261t

66. Moëlo, Y., Makovicky, E., Mozgova, N.N., Jambor, J.L., Cook, N., Pring, A., Paar, W., Nickel, E H.; Graeser, S; Karup-Møller, Sven; Balic-Žunic, T; Mumme, W G.; Vurro, F; Topa, Dan ; Bindi. L., Bente K. and Shimizu M. Sulfosalt systematics: a review. Report of the sulfosalt sub-committee of the IMA Commission on Ore Mineralogy. *Eur. J. Mineral* **2008**, *20*, 7–46.

67. Craig, J.R. Phase relations and mineral assemblages in the Ag-Bi-Pb-S system. *Mineral. Deposita,* **1967**, 1, 278–306. https://doi.org/10.1007/BF00205202

68. Deiseroth, H. J.; Kong, S. T.; Eckert, H.; Vannahme, J.; Reiner, C.; Zaiß, T.; Schlosser, M. Li_6PS_5X: A Class of Crystalline Li-Rich Solids with an Unusually High Li+ Mobility. *Angew. Chemie - Int. Ed.* **2008**, *47* (4), 755–758. https://doi.org/10.1002/anie.200703900.

69. Moessner, R. Magnets with Strong Geometric Frustration. *Can. J. Phys.* **2001**, *79* (11–12), 1283–1294. https://doi.org/10.1139/p01-123.

70. Shiomi, Y.; Nomura, K.; Kajiwara, Y.; Eto, K.; Novak, M.; Segawa, K.; Ando, Y.; Saitoh, E. Spin-Electricity Conversion Induced by Spin Injection into Topological Insulators. *Phys. Rev. Lett.* **2014**, *113*, 196601 https://doi.org/10.1103/PhysRevLett.113.196601

71. Nielsen, M. D.; Ozolins, V.; Heremans, J. P. Lone Pair Electrons Minimize Lattice Thermal Conductivity. *Energy Environ. Sci.* **2013**, *6* (2), 570– 578, DOI: 10.1039/C2EE23391F

72. Tan, G.; Hao, S.; Zhao, J.; Wolverton, C.; Kanatzidis, M. G. High Thermoelectric Performance in Electron-Doped $AgBi_3S_5$ with Ultralow Thermal Conductivity. *J. Am. Chem. Soc.* **2017**, *139* (18), 6467– 6473, DOI: 10.1021/jacs.7b02399

73. Jae-Yeol Hwang, Min-Wook Oh, Kyu Hyoung Lee, Sung Wng Kim. Strong correlation between the crystal structure and the thermoelectric properties of pavonite homologue $Cu_{x+y}Bi_{5-y}Ch_8$ (Ch = S or Se) compounds. *J. Mater. Chem. C*, **2015**, *3*, 11271-11285 https://doi.org/10.1039/C5TC02388B

74. Maji, K.; Lemoine, P.; Le Renaud, A.; Zhang, B.; Zhou, X.; Carnevali, V.; Candolfi, C.; Raveau, B.; Al, R.; Al Orabi, R.; Fornari, M.; Vaqueiro, P.; Pasturel, M.; Prestipino, C.; Guilmeau, E. A Tunable Structural Family with Ultralow Thermal Conductivity: Copper-Deficient $Cu_{1-x}\square_xPb_{1-x}Bi_{1+x}S_3$, *J. Am. Chem. Soc.* **2022**. https://doi.org/10.1021/JACS.1C11998

VITA

Srikanth Balijapelly was born in Kamalapoor, a village in the state of Telangana, India. In May 2015, he received his Integrated Masters (BS-MS) in Chemistry from Kakatiya University, Warangal, India. He carried out his master's thesis work titled "Synthesis and Characterization Fe(II) and Mn(II) metal complexes of NNN Pincer ligands for CO_2 activation" at Department of Chemistry, Indian Institute of Technology, Bombay, India. Later from April 2016 to November 2017, he worked in Asian Paints Ltd. Hyderabad, India, as a Quality Officer. To further accomplish his goals, he came to United States in Spring 2018 to pursue a Ph.D. in the Department of Chemistry, Missouri University of Science and Technology, Rolla, Missouri, USA. In May 2022, he received his Doctor of Philosophy in Chemistry from Missouri S&T under the guidance of Dr. Amitava Choudhury, for his work on "Design, Synthesis, and Characterization of Complex Chalcogenides for Energy Storage and Energy Conversion Applications".